CARBON NANOTUBES AS STRUCTURAL TEMPLATES WITHIN POLY(VINYL ALCOHOL) COMPOSITE FIBERS

A Dissertation
Presented to
The Academic Faculty

by

Ericka Nicole Johnson Ford

In Partial Fulfillment
of the Requirements for the Degree
Polymer, Textile and Fiber Engineering in the
SCHOOL OF POLYMER, TEXTILE AND FIBER ENGINEERING

Georgia Institute of Technology
December 2012

CARBON NANOTUBES AS STRUCTURAL TEMPLATES WITHIN POLY(VINYL ALCOHOL) COMPOSITES

Approved by:

Professor Satish Kumar, Advisor
School of Materials Science and Engineering
Georgia Institute of Technology

Professor Fred Cook
School of Materials Science and Engineering
Georgia Institute of Technology

Dr. Meisha Shofner
School of Materials Science and Engineering
Georgia Institute of Technology

Dr. Kyriaki Kalaitzidou
School of Mechanical Engineering
Georgia Institute of Technology

Dr. Tao Liu
High-Performance Materials Institute
Florida State University

Date Approved: November 8, 2012

But God hath chosen the small things of the world to confound the wise…
I Corinthians 1:27

ACKNOWLEDGEMENTS

I would like to begin by expressing my gratitude to the faculty and staff of the Georgia Institute of Technology (Georgia Tech) School of Polymer, Textile and Fiber Engineering. I was inspired by them to continue on with the post-baccalaureate study of polymers and fibers. I am grateful to Professor Satish Kumar (within the School of Materials Science and Engineering, MSE) for allowing me work within his research group, his guidance, and assistance with this research. This research was sponsored by grants from the National Science Foundation (NSF-CMMI 0826221), the Air Force Office of Scientific Research, and the Southern Regional Education Board's Doctoral Scholars program. Furthermore, I would like to thank my committee members for their contributions of time and expertise, which have led to the successful completion of this dissertation and published works: Professor Fred Cook (MSE), Dr. Kyriaki Kalaitzidou (School of Mechanical Engineering), Dr. Meisha Shofner (MSE), and Dr. Tao Liu (Industrial and Manufacturing Engineering at Florida State University).

I also want to recognize these collaborators and to thank them for their contributions to manuscripts that have been published or are in the advanced stages of preparation: Dr. Marilyn Minus, furnished the fibers used in the study of carbon nanotube (CNT)-directed molecular orientations and provided training on fiber testing and fabrication; Dr. Tao Liu, rendered his expertise for the analysis of spectroscopic data; Drs. Seung Soon Jang and Ji Il Choi, performed computational models of charge transfer between CNTs and functional molecules; Drs. Meisha Shofner and Tracy R. Brown characterized the rheology of polymer solutions and CNT/polymer dispersions; Dr.

Roman Popil (Institute of Paper Science and Technology) advised on the preparation of breathable corrugated box liners; and Dr. Sudahkar Jagannathan tested the pore size of electrosprayed box liners.

I appreciate the invaluable help that I have received from my current and former co-workers within Professor Kumar's group. Drs. Rahul Jain and Smitha Nair helped with the analysis of scanning electron micrographs, and Laura Lanier helped with the preparation and testing of samples. Dr. Swapan Bhattacharya, Dr. Asif Rasheed, Dr. Han Gi Chae, Dr. Young Ho Choi, Dr. Yaodong Lui, Dr. Prabhakar Gulgunje, Dr. Kishor Gupta, Dr. Jon Baek, Dr. Dhriti Nepal, Dr. Xiangyang 'Jacobson' Hao, Dr. Manjeshwar Kamath, Dr. Arup Bhattacharyya, Dr. Merlin Theodore, Beom-Jin Yoon, An-Ting Chien, Kevin Lyons, Brad Newcomb, Dawei Gao, Kenneth McDonald, Andrew Goreman, and Joshua Gomberg have all provided various forms of laboratory assistance, training, and constructive input for the betterment of this research.

I am also grateful for the instrument training, resources, and coaching from (former and current) members of the broader Georgia Tech community. Professor Mohan Srinivasarao permitted the use of his lab's Raman spectrometer and optical microscope, which was supervised by Dr. Xuxia Yao and Dr. Min Sang Park, respectively; Drs. Jasmeet Kaur, Wei Zhang, and Ian Winters provided thermal analysis training; Dr. Michelle Schlea provided imaging assistance on the scanning electron microscope; Dr. Richard Harper provided access to the water distiller; Professor Athanasios Nenes and Terry Lathem (with the School of Earth and Atmospheres Science) allowed the use of a pendant drop tensionmeter. This recognition list also includes Dr. Rosario Gerhardt, Dr. Davis Lee, Dr. Tolecia Clark, Dr. Michelle Gaines, Dr.

Ramasubramani ‘Ram’ Thanumoorthy, Dr. Kevin Worrell, and Sarang Deodhar because of their support, mentoring, and general laboratory assistance.

My academic education and professional development was enhanced by my participation within graduate traineeships. I have learned several dos and don’ts for interdisciplinary teamwork and technology commercialization from Professor Marie Thursby, Ms. Margi Berbari, Ben Hill, Ann Reiter, and Dr. Renita Anderson, while participating in the Technology Innovation: Generating Economic Results (TI:GER) program, which was a NSF sponsored Integrative Graduate Education and Research Traineeship (IGERT).

I learned how to become an academic mentor and educator while participating in the NSF K-12 program (sponsored by grant #0338261) called the Georgia Tech Student Teacher Enhancement Partnership (GT-STEP). Dr. Donna Llewellyn with the Center for the Enhancement of Teaching and Learning; Dr. Marion Usselman with the Center for Education Integrating Science, Mathematics, and Computing (CEISMC); and Mrs. Yvette Gilbert (chemistry and physical science teacher at Miller Grover High School in Lithonia, GA) were my role models for engaging students within science and engineering courses. Furthermore, I would like to recognize the influential roles of Mrs. Leslie Bayor and Ms. Patricia Glore, from whom I have acquired a sincere love of engineering education and outreach while at Georgia Tech.

I have been privileged to receive loving support, encouragement, and counsel from my family and sharers of like-precious faith: namely, my husband Arris Ford; mother Gloria Gates; brother Eric and Betty Johnson; uncle James and aunt Tyereon Johnson; cousin Kanetra Ingram; my in-laws George, Mary, and Alexis Ford; Pastors

Gerald and Wendi Wyatt; Pastors Franz and Tricia Todman; and members of the Body of Christ Worship Center and Destiny Ministries International. I thank God for you all and this great accomplishment.

TABLE OF CONTENTS

	Page
ACKNOWLEDGEMENTS	iv
LIST OF TABLES	xiii
LIST OF FIGURES	xv
LIST OF SCHEMES	xx
LIST OF SYMBOLS	xxi
LIST OF ABBREVIATIONS	xxvii
SUMMARY	xxxi
CHAPTER	
1 INTRODUCTION	1
1.1. High Performance Fibers	1
1.1.1. Properties of High Performance Fibers	1
1.1.2. Gel Fiber Spinning Technique	3
1.1.2.1. Role of Chain Entanglements	4
1.1.2.2. Polymer Gelation	6
1.1.2.3. Models of Gel Structure	8
1.1.2.4. Gel-spun UHMWPE Fiber	10
1.2. Gel-spinning PVA Fibers	11
1.2.1. Structure of PVA	11
1.2.2. Processing PVA	13
1.2.3. Aging PVA Gel	17
1.3. Filler Reinforced PVA	18
1.3.1. Polymer Reinforcement	19

1.3.2. Nucleation-and-Growth of Filler Polymer 20

1.3.3. Filler Reinforced PVA Composites 21

1.4. Carbon Nanotube Reinforced Polymer 25

1.4.1. Carbon Nanotubes 25

1.4.2. CNT Morphology 26

1.4.3. Non-covalently Bonded CNTs 29

1.4.4. CNTs as Nucleating Agents 30

1.5. SWNT Reinforced PVA Fibers 34

1.6. Thesis Objectives 37

2 EFFECTS OF CARBON NANOTUBES ON THE MICROSTRUCTURE OF DRAWN FIBERS 38

2.1. Introduction 38

2.2. Experimental Section 38

2.2.1. Fiber Preparation 38

2.2.2. Mechanical Testing 40

2.2.3. Thermal Analysis 40

2.2.3.1. Thermal Shrinkage 40

2.2.3.2. DSC 41

2.2.3.3. TGA 41

2.2.4. WAXD Analysis 42

2.2.5. Spectroscopic Analysis 42

2.2.5.1. Raman Spectroscopy 42

2.2.5.2. IR Spectroscopy 43

2.2.6. Molecular Modeling 44

2.3. Results and Discussion 45

2.3.1. Mechanical Properties 45

2.3.2. PVA Microstructure 47

2.3.3. IR Spectroscopy of PVA Fibers 51

2.3.4. SWNT Influenced Molecular Orientations 57

2.3.4.1. Orientation of Embedded SWNTs 57

2.3.4.2. Orientation of PVA Chain Conformations 58

2.3.4.3. Orientation of Pendant Hydroxyl Groups 59

2.3.4.4. Orientation of Carbonyl Moieties 62

2.3.4.5. Orientation of Imbibed Water 63

2.3.4.6. Orientation of Imbibed DMSO 65

2.4. Conclusions 65

3 KINETIC MECHANISMS OF GEL CRYSTALLIZATION WITHIN POLY(VINYL ALCOHOL) AND CARBON NANOTUBE DISPERSIONS 67

3.1. Introduction 67

3.2. Experimental Section 69

3.2.1. Sample Preparation 69

3.2.2. Viscosity Measurements 71

3.2.3. DSC 72

3.3. Results and Discussion 74

3.3.1. Sample Characterization at RT 74

3.3.1.1. DP_w Related Elution Time for Sonicated Polymer 74

3.3.1.2. DP_w of Polymers within CNT Dispersions 75

3.3.1.3. Complex Viscosity of PVA Solutions and CNT Dispersions 78

3.3.2. Cryo-gelation of PVA Solutions 79

3.3.3. Cryo-gelation of PVA/CNT Dispersions 83

3.3.4. Cryo-transformation Mechanisms of PVA Solutions 84

3.3.5. Cryo-transformation Mechanisms of CNT Dispersions 91

3.3.6. Cryo-transformation Kinetics 93

3.4. Conclusions 98

4 EFFECT OF GEL AGING ON THE STRUCTURE AND PROPERTIES OF POLY(VINYL ALCOHOL)/ CARBON NANOTUBE FIBERS 99

4.1. Introduction 99

4.2. Experimental 100

4.2.1. Spinning dopes of PVA and PVA/CNT 100

4.2.2. Fiber Gel-spinning 101

4.2.3. Mechanical Testing 102

4.2.4. WAXD 103

4.2.5. Thermal Analysis 103

4.3. Results and Discussion 104

4.3.1. Optimizing the Circularity of Gel-spun PVA-10000 Fibers 104

4.3.2. Aging Gels of PVA-10000 105

4.3.2.1. Drawn 4P10000 Fibers from Gels Aged in MeOH 105

4.3.2.2. 4P10000 Gel Fiber Aged in MeOH 112

4.3.2.3. Drawn 4P10000 Fibers from Gels Aged in MeOH/Water 119

4.3.2.4. 4P10000 Gel Fiber Aged in MeOH/Water 122

4.3.2.5. Drawn 4P10000 Fibers after Extensive Gel Aging in MeOH/Water 127

4.3.3. Aging PVA/SWNT Gel of PVA-8900 129

4.3.3.1. Drawn PS4P10000 Fibers from Gel Aged in MeOH 129

4.3.3.2. PS4P10000 Gel Fiber Aged in MeOH 130

4.3.3.3. Drawn PS4P10000 Fibers from Gels Aged in MeOH/Water 134

4.3.3.4. PS4P10000 Gels Aged in MeOH/Water 140
4.3.4. Aging Gels of PVA-4000 144
4.3.4.1. Drawn 10P4000 Fibers from Gels Aged in MeOH/Water 144
4.3.5. Aging PVA/FWNT Gels of PVA-3700 155
4.3.5.1. Drawn PF10P4000 Fibers from Gels Aged in Solvent 155
4.3.5.2. PF10P4000 Gels Aged in Solvent 163
4.3.6. Stiffening of 10P4000 and PF10P4000 Fibers 169
4.4. Conclusions 171
5 CONCLUSIONS AND RECOMMENDATIONS 174
5.1. Conclusions 174
5.1.1. Chapter 2 174
5.1.2. Chapter 3 175
5.1.3. Chapter 4 176
5.2. Recommendations 179
APPENDIX A: RESCALED PLOTS OF THE EFFECTIVE ACTIVATION ENERGY 181
APPENDIX B: FWNT/SOLVENT DISPERSIONS 182
APPENDIX C: LOSS MODULUS OF GEL FIBERS 185
REFERENCES 188

LIST OF TABLES

Page

Table 1.1: Mechanical Properties of Fiber Classes. 2

Table 1.2: Mechanical Properties of PVA and PVA/SWNT Fibers. 36

Table 2.1: Mechanical Properties of PVA and PVA/SWNT Fibers with Sequential Drawing. 46

Table 2.2: WAXD Characterization of PVA and PVA/SWNT Fibers. 48

Table 2.3: Identification of FTIR peaks in PVA-Based Fibers. 53

Table 2.4: PVA and SWNT Orientation Parameters. 58

Table 2.5: Fraction of Molecular Moieties Perfectly Aligned Along the Fiber Axis. 61

Table 3.1: Relative DP_w of Dilute PVA/DMSO Solution (0.45 wt.% PVA) at 31 °C versus Sonication Time. 75

Table 3.2: Rheology of PVA Solutions and PVA/CNT Dispersions. 77

Table 3.3: Effects of Annealing Temperature on the Cryo-behaviors of Hermetically Sealed PVA Solutions and PVA/CNT Dispersions. 81

Table 3.4: Thermal Properties of Hermetically Sealed 80/20 DMSO/Water. 82

Table 3.5: Avrami Fit Parameters to Cryo-transformations Upon Cooling at 2 °C/min. 95

Table 4.1: PVA-10000 Fiber Cross-sections. 104

Table 4.2: Mechanical Properties of Drawn 4P10000 Fibers from Gels Aged in MeOH. 106

Table 4.3: WAXD Characterization of Drawn 4P10000 Fibers from Gels Aged in MeOH. 111

Table 4.4: WAXD Characterization of 4P10000 Gel Fibers Aged in MeOH. 115

Table 4.5: Mechanical Properties of Drawn 4P10000 Fibers from Gels Aged in MeOH/Water. 120

Table 4.6: WAXD Characterization of Drawn 4P10000 Fibers from Gels Aged in MeOH/Water. 122

Table 4.7: WAXD Characterization of 4P10000 Gel Fibers Aged in MeOH/Water. 125

Table 4.8: Mechanical Properties of Drawn 4P10000 Fibers from Gels Extensively Aged in MeOH/Water. 127

Table 4.9: WAXD Characterization of Drawn 4P10000 Fibers from Gels Extensively Aged in MeOH/Water. 129

Table 4.10: WAXD Characterization of PS4P10000 Gel Fibers Aged in MeOH. 133

Table 4.11: Mechanical Properties of Drawn PS4P10000 Fibers from Gels Aged in MeOH/Water. 135

Table 4.12: WAXD Characterization of PS4P10000 Fibers Drawn from Gels Aged in MeOH/Water. 139

Table 4.13: WAXD Characterization of PS4P10000 Gel Fibers with MeOH/Water Aging Time. 142

Table 4.14: Mechanical Properties of Drawn 10P4000 Fibers from Gels Aged in MeOH/Water. 145

Table 4.15: WAXD Characterization of Drawn 10P4000 Fibers from Gels Aged in MeOH/Water. 148

Table 4.16: WAXD Characterization of 10P4000 Gel Fibers Aged in MeOH/Water. 153

Table 4.17: Mechanical Properties of Drawn PF10P4000 Fibers from Gels Aged in MeOH. 156

Table 4.18: Mechanical Properties of Drawn PF10P4000 Fibers from Gels Aged in MeOH/Water. 156

Table 4.19: WAXD Characterization of Drawn PF10P4000 Fibers from Gels Aged in MeOH. 162

Table 4.20: WAXD Characterization of Drawn PF10P4000 Fibers from Gels Aged in MeOH/Water. 163

Table 4.21: WAXD Characterization of PF10P4000 Gel Fibers Aged in MeOH. 167

Table 4.22: WAXD Characterization of PF10P4000 Gel Fibers Aged in MeOH/Water. 167

Table B.1: Preparation of FWNT/Solvent Dispersions. 182

Table B.2: Thermal Properties of FWNTs Dispersed in Solvents 184

LIST OF FIGURES

Page

Figure 1.1: Unit cell models of PVA by a) Bunn and b) Sakurada. 11

Figure 2.1: Fabrication of gel-spun fibers. 39

Figure 2.2: Effects of drawing stages on the thermal shrinkage of a) PVA and b) PVA/SWNT fibers. 45

Figure 2.3: MDSC thermograms of a) PVA and b) PVA/SWNT fibers: i) total heat flow, ii) R-heat flow, and iii) NR-heat flow. 49

Figure 2.4: Thermographs of a) solvent evaporation from as-received PVA powder, control PVA, and PVA/SWNT fibers that were drawn at 7.5 X and 7.3 X, respectively, and b) 80/20 DMSO/water evaporation. 49

Figure 2.5: IR spectra of PVA powder (P) and fiber (F). Both the powder and the fiber samples were heated from RT to 100 and 200 °C at 10 °C/min in nitrogen, cooled to RT, and made into pellets of KBr. 51

Figure 2.6: Gaussian deconvolutions of IR Spectra had ranged from 950-1175 cm^{-1}: a) as-received PVA powder, b) S4/290 PVA fiber, and c) S4/290 PVA/SWNT fiber. 52

Figure 2.7: Spectra of a) PVA and b) PVA/SWNT 4/290 drawn fibers with IR polarization angles of 0, 5, 10, 20, 30, 40, 50, 60, 70, 80, 85, and 90° from the fiber axis. 56

Figure 2.8: Polarized Raman of PVA/SWNT fibers a) SWNT G^{+}-band intensities as a function of Raman polarization angles for samples having different *DR* values, and b) Raman spectra for S4/290 fiber at polarization angles of 0, 30, 60, and 90°. 57

Figure 2.9: Polarized IR of a) crystalline and b) amorphous conformations of PVA. 59

Figure 2.10: Orientation of hydroxyl and carbonyl functionalities within PVA and PVA/SWNT fibers. 60

Figure 2.11: Atomistic models of (6,6) CNT with aligned PVA groups: a) PVA oligomer 1,3,5-hexane triol and b) PVAc oligomer 1,3,5-hexane triacetate. 62

Figure 2.12: Polarized IR intensities of solvent molecules in PVA and PVA/SWNT fibers: water (H-O-H bending) and DMSO (S=O stretching). 64

Figure 2.13: Water bending vibrations normal to the SWNT fiber axis, where hydrogen atoms are a) adjacent to or b) away from the SWNT axis. 64

Figure 3.1: Rheology of PVA solutions and PVA/CNT dispersions heated to 80 °C for 1 hr, cooled to T_{anneal}=30, 55, and 70 °C for 2 hrs (where each color represents an annealing temperature), and conditioned at 22 ± 3 °C for 2 hrs prior to testing. 76

Figure 3.2: Hermetically sealed 80/20 DMSO/water, PVA/CNT dispersions, and PVA solutions containing a) PVA-10000 and b) PVA-4000 for T_{anneal}=30, 55, and 70 °C prior to 2 °C/min cooling, c) their exothermic transitions upon 2 °C/min heating for T_{anneal}=30 °C, d) thermograms of 4PBlend at 2 °C/min cooling from annealing temperature. 80

Figure 3.3: 4P10000 was annealed at 30 °C for 2 hrs prior to cooling: a) exothermic reactions upon cooling at β_i=1, 2, and 5 °C/min and b) plots used to determine E_α using the maximum rate theory. 85

Figure 3.4: Influence of T_{anneal} on the values of E_α for PVA solutions and PVA/CNT dispersions. 86

Figure 3.5: Change in the conformational entropy of cryo-transformations. 90

Figure 3.6: Proposed phases within a) blend of low and high *DP* polymers (A and B) and b) CNT/polymer dispersions. 90

Figure 3.7: Example plots for determining isoparametric rate constant ($\ln k_{iso}$) and temperature (T_{iso}). 94

Figure 3.8: Avrami fits to $g(\alpha)$ for PVA solutions annealed at 30, 55, and 70 °C, where the cooling rate 2 °C/min. 96

Figure 4.1: Cross-sections of fibers spun from solutions of a) 3.5, b) 4, and c) 5 wt.% PVA-10000. 105

Figure 4.2: Cross-sections of drawn 4P10000 fibers from gels aged in MeOH for a) 1 and b) 22 days. 107

Figure 4.3: MDSC thermograms of drawn 4P10000 fibers from gels aged in MeOH. 108

Figure 4.4: WAXD analysis from radial scans of drawn 4P10000 fibers from gels aged in MeOH for a) 1 and b) 22 days. 110

Figure 4.5: Storage modulus of 4P10000 gel fibers aged in MeOH. 112

Figure 4.6: 4P10000 gel fibers aged in MeOH: a) TGA and b) DTGA at 10 °C/min in nitrogen. 115

Figure 4.7: 4P10000 gel fiber with aging time a) 0, b) 1, c) 22, and d) 30 days in MeOH. 116

Figure 4.8: Cross-sections of 4P10000 fibers drawn from gels aged in MeOH/water for a) 1, b) 69, c) 120, and d) 155 days. 120

Figure 4.9: MDSC thermograms of drawn 4P10000 fibers from gels aged in MeOH/water. 121

Figure 4.10: Storage modulus of 4P10000 gel fibers aged in MeOH/water. 123

Figure 4.11: 4P10000 gel fibers aged in MeOH/water: a) TGA and b) DTGA at 10 °C/min in nitrogen. 124

Figure 4.12: WAXD analysis of 4P10000 gel fibers with aging time a) 0, b) 1, c) 69, d) 122, and e) 155 days in MeOH/water. 126

Figure 4.13: Stress-strain curves of drawn 4P10000 fibers from gels aged in MeOH/water for 1 day and extensively aged for 18 months. 128

Figure 4.14: Cross-sections of drawn 4P10000 fibers from gels aged in MeOH/water for a) 1 day and b) extensively aged for 18 months. 128

Figure 4.15: Cross-sections of PS4P10000 fiber drawn from gels aged in MeOH for 1 day. 130

Figure 4.16: Storage modulus of PS4P10000 gel fibers aged in MeOH. 131

Figure 4.17: PS4P10000 gel fiber aged in MeOH: a) TGA and b) DTGA at 10 °C/min in nitrogen. 132

Figure 4.18: WAXD analysis of PS4P1000 gel fibers with aging time a) 0, b) 1, and c) 30 days in MeOH. 134

Figure 4.19: Cross-sections of drawn PS4P10000 fibers from gels aged in MeOH/water for a) 1, b) 30, c) 60, d) 123 days with cold drawing, and e) 219 days without cold drawing. 136

Figure 4.20: MDSC thermograms of drawn PS4P10000 fibers from gels aged in MeOH/water. 138

Figure 4.21: Storage modulus of PS4P10000 gel fibers aged in MeOH/water. 140

Figure 4.22: PS4P10000 gel fibers aged in MeOH/water: a) TGA and b) DTGA at 10 °C/min in nitrogen. 141

Figure 4.23: WAXD analysis of PS4P10000 gel fibers with aging time a) 0, b) 1, c) 30, d) 60, e) 123, and f) 218 days in MeOH/water. 143

Figure 4.24: Cross-sections of 10P4000 drawn from gels aged in MeOH/water for a) 1, b) 16, c) 46, d) 60, and ei) 120 days with cold drawing, eii) 120 and f) 155 days without cold drawing stage. 146

Figure 4.25: MDSC thermograms of drawn 10P4000 fibers from gels aged in MeOH/water. 147

Figure 4.26: Storage modulus of 10P4000 gel fibers aged in MeOH/water. 150

Figure 4.27: 10P4000 gel fibers aged in MeOH/water a) TGA and b) DTGA at 10 °C/min in nitrogen. 151

Figure 4.28: WAXD analysis of 10P4000 gel fibers with aging time a) 0, b) 1, c) 15, d) 46, e) 60, f) 122, and g) 152 days in MeOH/water. 154

Figure 4.29: Stress-strain curves of PF10P4000 fibers drawn from gels aged in a) MeOH and b) MeOH/water. 155

Figure 4.30: Cross-sections of PF10P4000 fibers drawn from gels aged in MeOH for a1) 1, b1) 120, c1) 218, and d1) 263 days and MeOH/water for a2) 1, b2) 122, c2) 215, and d2) 265 days. 158

Figure 4.31: SEM characterization of FWNTs within PF10P4000 fiber drawn from gel aged in MeOH/water for 219 days. 159

Figure 4.32: MDSC thermograms of PF10P4000 fibers drawn from gels aged in a) MeOH and b) MeOH/water. 161

Figure 4.33: Storage modulus of PF10P4000 gel fibers aged in a) MeOH and b) MeOH/water. 165

Figure 4.34: TGA of PF10P4000 gel fibers aged in a) MeOH and b) MeOH/water at 10 °C/min in nitrogen. 165

Figure 4.35: WAXD analysis of PF10P4000 gel fibers aged in MeOH for a) 0, b) 1, c) 15, d) 122, e) 215, and f) 256 days. 168

Figure 4.36: WAXD analysis of PF10P4000 gel fibers aged in MeOH/water for a) 0, b) 1, c) 122, d) 215, and e) 256 days. 168

Figure 4.37: Stress-strain curves of drawn PF10P4000-215 fiber at S5/180 and S6/210. 170

Figure A.1: Rescaled E_α plots for select samples to demonstrate nonlinear increases in E_α with conversion. 181

Figure B.1: FWNTs sonicated in organic solvent for a total of 24 hrs. 183

Figure C.1: Loss modulus of 4P10000 gel fibers aged in MeOH. 185

Figure C.2: Loss modulus of 4P10000 gel fibers aged in MeOH/water. 185

Figure C.3: Loss modulus of PS4P10000 gel fibers aged in MeOH. 186

Figure C.4: Loss modulus of PS4P10000 gel fibers aged in MeOH/water. 186

Figure C.5: Loss modulus of 10P4000 gel fibers aged in MeOH/water. 187

Figure C.6: Loss modulus of PF10P4000 gel fibers aged in a) MeOH and b) MeOH/water. 187

SCHEMES

Page

Scheme 1.1: Synthesis of PVA from PVAc. 14

Scheme 3.1: Proposed parallel cryo-transformation pathway for homopolymer PVA solutions. 87

SYMBOLS

%/sec	%/sec Means Strain Rate
$<P_2(cos\psi)>$	$<P_2(cos\psi)>$ Means Second Order Orientation Parameter
°C	°C Means Degrees Celsius
°C/min	°C/min Means Degrees Celsius per minute
2θ	2θ Means Diffractometer Angle
A	A Means Pre-exponential Factor
A_b	A_b Means the Branching Coefficient
A_α	A_α Means Effective Pre-exponential Factor
A_θ	A_θ Means Polarized Infrared Absorbance
b	b Means Breath of the Linear Elastic Region
CI	CI Means Circularity Index
cm	cm Means Centimeters
cm^{-1}	cm^{-1} Means Per Centimeters; Wavenumber
D	D Means Dichroic Ratio
DP	DP Means Degree of Polymerization
DP_w	DP_w Means the Weight Average Degree of Polymerization
DP_v	DP_v Means the Viscosity Average Degree of Polymerization
DR	DR Means the Cumulative Heat Draw Ratio
dE_α/dT_α	dE_α/dT_α Means Differential Change in Activation Energy with Respect to Temperature
dL	dL Means Deciliters
dQ/dt	dQ/dt Means Differential Heating With Respect to Time; Heat flow
dT/dt	dT/dt Means Differential Temperature With Respect to Time

dX_c/dV_{fCNT}	dX_c/dV_{fCNT} Means Differential Volume Fraction of Crystalline Polymer with Respect to the Volume Fraction of Carbon Nanotubes
dY/dV_{fCNT}	dY/dV_{fCNT} Means Differential Young's Modulus with Respect to the Volume Fraction of Carbon Nanotubes
$E'(f)$	$E'(f)$ Means Storage Modulus in Tension
$E''(f)$	$E'(f)$ Means Loss Modulus in Tension
E_α	E_α Means Effective Activation Energy
$E_{Adsorbate}$	$E_{Adsorbate}$ Means the Energy of Adsorbate
E_{SWNT}	E_{SWNT} Means Energy of SWNT
eV	eV Means Electronvolts
f_b	f_b Means *b*-axis Orientation of PVA Crystals
f_c	f_c Means Orientation of Crystalline PVA Chain Conformations
g	g Means Grams
$g(\alpha)$	$g(\alpha)$ Means Experimental Transformation Model
$G(\omega)$	$G(\omega)$ Means Shear Modulus
g/cm^3	g/cm^3 Means Grams per Centimeters Cubed
g/den	g/den Means Grams per Denier
g/dL	g/dL Means Grams per Deciliter
$G'(\omega)$	$G'(\omega)$ Means Shear Storage Modulus
$G''(\omega)$	$G''(\omega)$ Means Shear Loss Modulus or Viscous Response
GPa	GPa Means Gigapascals
h	h Means the Height of a Gaussian Peak Fit
hr(s)	hr(s) Means Hour(s)
Hz	Hz Means Hertz
$I(\kappa)$	$I(\kappa)$ Means X-ray Diffraction Intensity at Angle κ
$I(\psi)$	$I(\psi)$ Means Raman Intensity; $y(\psi)$-$y0$

J/g	J/g Means Joules per Grams
k(T)	*k(T)* Means Rate Constant as a Function of Temperature
K/min	K/min Means Kelvin per Minute
kbar	kbar Means Kilobar
kg	kg Means Kilograms
$kJ \cdot mol^{-1} \cdot K^{-1}$	$kJ \cdot mol^{-1} \cdot K^{-1}$ Means Kilojoules per Mole per Kelvin
kV	kV Means Kilovolts
L	L Means Liter
L	*L* Means Liquid Solvent
$\ln k_{iso}$	$\ln k_{iso}$ Means Logarithmic Isoparametric Rate Constant
m	*m* Means Negative Slope of Shear Thinning Region
mA	mA Means Milliamperes
M_e	M_e Means Molecular Weight Between Chain Entanglements
mg	mg Means Milligram
mg/L	mg/L Means Milligrams per Liter
mL	mL Means Milliliters
mL/min	mL/min Means Milliliters per Minute
mm	mm Means Millimeters
mm/s	mm/s Means Millimeters per Second
mm/s^2	mm/s^2 Means Millimeters per Seconds Squared
MPa	MPa Means Megapascals
mS	mS Means Millisiemens
mW	mW Means Milliwatts
M_x	M_x Means Means Molecular Weight Between Crosslinks
nm	nm Means Nanometers

P_{gel}	P_{gel} Means Polymer Gelation
phi	*phi* Means the WAXD Angle that is Perpendicular to 2θ
P_{homo}	P_{homo} Means Homopolymer
R	R Means Universal Gas Constant
R^2	R^2 Means the Goodness of Fit Parameter
rad/s	rad/s Means Radians Per Second
s	s Means Second
S	S Means Solid, Frozen Solvent
$S(T_f)$-$S(T_i)$	$S(T_f)$-$S(T_i)$ Means Change in Conformational Entropy
T	T Means Temperature
t	t Means Time
T_{anneal}	T_{anneal} Means Annealing Temperature
T_{evap}	T_{evap} Means the Peak Temperature for Solvent Evaporation
T_{exo}	T_{exo} Means the Peak Temperature for an Exothermic Transition
T_f	T_f Means Freezing Temperature
T_g	T_g Means Glass Transition Temperature
T_{iso}	T_{iso} Means the Isoparametric Temperature
T_m	T_m Means Melting Temperature
TM	*TM* Means Tensile Modulus
TPa	TPa Means Terapascal
TS	*TS* Means Tensile Strength
T_α	T_α Means the Conversion Dependent Temperature
V/m	V/m Means Voltage per Meter
v/v	*v/v* Means Volume Fraction
V_{fCNT}	V_{fCNT} Means Means Volume Fraction of Carbon Nanotubes

w	w Means Full Width at Half Maximum
w_f	w_f Means Weight of Fiber
w_x	w_x Means Weight Fraction
X	X Means Times
x	x Means Fraction of Oriented Functional Groups
X_c	X_c Means the Volume Fraction of Crystalline Polymer
XS	XS Means Crystal Size
v_2	v_2 Means Volume Fraction of Polymer
v_{2r}	v_{2r} Means Memory Parameter
v_e	v_e Means Density of Molecular Chain Entanglements
v_{in}	v_{in} Means the Feed Velocity
v_{out}	v_{out} Means the Output Velocity
v_s	v_s Means Stretching Vibration
v_x	v_x Means Crosslink Density
v_δ	v_δ Means Bending Vibration
Y_{eff}	Y_{eff} Means Effective Young's Modulus
α	α Means Conversion
β	β Means Heating Rate
$\beta_<$	$\beta_<$ Means Angle of the PVA Unit Cell
ΔE	ΔE Binding Means Binding Energy
ΔH_f	ΔH_f Means Enthalpy of Freezing
ΔH_m	ΔH_m Means Enthalpy of Melting
ΔT	ΔT Means Difference Between the Peak Melting and Freezing Temperatures; Degree of Supercooling
$\eta^*(\omega)$	$\eta^*(\omega)$ Means Complex Viscosity
η_0	η_0 Means Zero Shear Viscosity

θ	θ Means Orientation Angle Relative to the Optical Axis
κ	κ Means the Azimuthal Angle for X-ray diffraction
λ	λ Means Characteristic Time
μm	μm Means Micrometers
ρ_1	ρ_1 Means the Density of Solvent
ρ_2	ρ_2 Means the Density of Dry Polymer
φ_f	φ_f Means Diameter of Fiber
ψ	ψ Means the Polarization Angle About the Optical Axis for Raman Spectroscopy
ψ_c	ψ_c Means Corrected Raman Polarization Angle
$\dot{\gamma}$	$\dot{\gamma}$ Means Shear Strain Rate

LIST OF ABBREVIATIONS

10P4000	Ten Weight Percent Polymer Blend of Poly(Vinyl Alcohol) Polymer Having a Degree of Polymerization Equal to 4,000
3.5P10000	Three and One-half Weight Percent Polymer Blend of Poly(Vinyl Alcohol) Polymer Having a Degree of Polymerization Equal to 10,000
4P10000	Four Weight Percent Polymer Blend of Poly(Vinyl Alcohol) Polymers Having Degrees of Polymerization Equal to 10,000 and 4,000
4PBlend	Four Weight Percent Polymer Blend of Poly(Vinyl Alcohol) Polymers Having Degrees of Polymerization Equal to 10,000 and 4,000
5P10000	Five Weight Percent Polymer Blend of Poly(Vinyl Alcohol) Polymer Having a Degree of Polymerization Equal to 10,000
a-	Atactic; for example a-PVA is atactic PVA
AFM	Atomic Force Microscopy
C=O	Carbonyl Group
C_2H_3OO	Acetate Group
CB	Carbon Black
C-C	Carbon-Carbon Backbone
$CH_3COO^-K^+$	Potassium Acetate
CNT	Carbon Nanotube
Cryo-	Cryogenic
G´-bands	2nd Harmonic of the D-band
D-band	Raman Mode Disorder Bands from Carbon Nanotubes
DFT	Density Functional Theory
DMA	Dynamic Mechanical Analysis

DMSO	Dimethyl Sulfoxide
DNP	Double Numerical Plus Polarization
DSC	Differential Scanning Calorimetry
DTGA	Differential Thermogravimetric Analysis
ECC	Extended Chain Conformation
EDA	Electron Donor-Acceptor Complex
EDWG	Electron Donating and Withdrawing Group
F	Fiber
FCC	Folded Chain Conformation
FWNT	Few-walled Carbon Nanotubes
G^+-bands	Raman Mode Axial Vibration from Carbon Nanotubes
GGA	Generalized Gradient Approximation
HiPCO	High Pressure Carbon Monoxide
H-O-H	Water Bending Mode
Hydrol	Hydrolysis
i-	Isotactic; for example i-PVA means isotactic PVA
IR	Infrared
JSR	Jet Stretch Ratio
KBr	Potassium Bromide
M/W	Methanol/Water
MDSC	Modulated Differential Scanning Calorimetry
MeOH	Methanol
MMT	Montmorillonite
MWNT	Multi-walled Carbon Nanotubes
NR-Heat Capacity	Non-reversing Heat Capacity

NR-Heat Flow	Non-reversing Heat Flow
O-coordination	Oxygen Coordination
-OH	Hydroxyl Group
P	Powder
PAN	Poly(Acrylonitrile)
PBE	Perdew-Burke-Ernzerhof
PE	Polyethylene
PEO	Polyethylene Oxide
PF10P4000	Ten Weight Percent Polymer Blend of Poly(Vinyl Alcohol) Polymer
PMMA	Poly(Methyl Methacrylate)
PP	Polypropylene
PS	Polystyrene
PS4P10000	Four Weight Percent Polymer Blend of Poly(Vinyl Alcohol) Polymer Having a Degree of Polymerization Equal to 10,000 Consists of 0.25 Weight Percent Few-walled Carbon Nanotubes
PVA	Poly(Vinyl Alcohol)
PVA-10000	Poly(Vinyl Alcohol) Polymer Having a Weight Average Degree of Polymerization Equal to 10,000
PVA-3700	Poly(Vinyl Alcohol) Polymer Having a Weight Average Degree of Polymerization Equal to 3,700
PVA-4000	Poly(Vinyl Alcohol) Polymer Having a Weight Average Degree of Polymerization Equal to 4,000
PVA-8900	Poly(Vinyl Alcohol) Polymer Having a Weight Average Degree of Polymerization Equal to 8,900
PVAc	Poly(Vinyl Acetate)
PVP	Poly(Pyrrolidone)
RBM	Radial Breathing Mode
R-Heat Capacity	Reversing Heat Capacity

R-Heat Flow	Reversing Heat Flow
RT	Room Temperature
s-	Syndiotactic; For Example s-PVA Means Syndiotactic PVA
S#/#	Drawing Sequence/Temperature of Drawing in ℃; For Example S1/100
S=O	Sulfoxide Group
SDS	Sodium Dodecyl Sulfate
SEM	Scanning Electron Microscopy
SWNT	Single-walled Carbon Nanotube
TMA	Thermal Mechanical Analysis
TEM	Transmission Electron Microscopy
TGA	Thermogravimetric Analysis
UHMWPE	Ultrahigh Molecular Weight Polyethylene
UV-vis	Ultraviolet Visible
VH	Verticle-Horizontal
VV	Verticle-Verticle
WAXD	Wide Angle X-ray Diffraction
Wt.%	Weight Percent

SUMMARY

The main objectives of this study were to enhance the mechanical performance of gel-spun poly(vinyl alcohol), PVA, fibers by using process steps that would 1) increase the cumulative draw ratio (*DR*) of carbon nanotube (CNT) embedded fibers and 2) enable CNTs to nucleate phases of ordered PVA. Because the gel-spinning process has the potential to yield fibers of high strength and high modulus, this technique was employed to construct continuous filaments of PVA/CNT. A gel aging technique was employed with the goal of increasing the *DR* for composite fibers and for promoting the development of crystalline PVA, having higher temperatures of melting. Changes within the crystalline and amorphous phases of PVA fibers were characterized as a function of CNT incorporation, the weight average degree of polymerization (DP_w) for PVA polymers, fiber *DR*, and aging conditions for the pre-cursor gel fiber. Since residual solvent can lower the mechanical properties of drawn fibers, solvent phases of water and dimethyl sulfoxide (DMSO) within the drawn fibers were also characterized. PVA was loaded with CNTs at ≤1 weight percent (wt.%) of polymer. Low weight fractions of CNTs were used to aid their dispersion, exfoliation, and adhesion with matrix polymer and to minimize the raw material costs from using expensive CNTs.

Chapter 1 is a review of fiber microstructures and processing steps that could promote properties of high strength and high modulus within polymers and their composites. Such properties are promoted by the drawing of highly ordered and aligned polymer microstructures. The drawing of fibers to high values of *DR* could be achieved by reducing the number of molecular chain entanglements and by reducing the hydrogen

bonding between PVA chains. By loading nanofillers (such as CNTs) into the polymer, the mechanical strength, thermal resistance, and chemical resistance of the composite would surpass the properties of neat films/fibers. The stretching of composite fibers to high values of *DR* is also important to achieve high mechanical properties among composite fibers. For CNTs to structurally reinforce polymers, they must be well-dispersed throughout the matrix polymer and have good interfacial adhesion with the polymer. The development of an ordered polymer interphase along CNTs will help to strengthen the overall performance of the composite.

Chapter 2 describes the influence of CNTs on the structure/property relationships of PVA fibers and the microphases that exist within gel-spun fibers. Composite fibers consisted of 1 wt.% single-walled carbon nanotubes (SWNTs) and PVA having a DP_w of 18,000. Both neat and filled fibers were prepared with four consecutive stages of elevated-temperature drawing; such that the drawing sequences/temperatures in Celsius degrees were called S1/100, S2/160, S3/200, and S4/290. Neat and CNT loaded fibers were stretched to similar values of *DR*; however, the incorporation of SWNTs did not improve the mechanical strength of PVA. But, SWNTs did help to reduce the susceptibility of drawn fibers to thermal shrinkage. PVA fibers had consisted of crystalline and amorphous polymer. An additional interphase of ordered polymer and solvent was believed to exist along the SWNTs of composite fibers, based on spectroscopic evidence. As embedded SWNTs were uniaxially aligned along the drawn fibers' axes; they were found to induce preferential alignment among the side groups of PVA chains and residual solvent. The alignment of PVA side groups in parallel with SWNTs was attributed to charge transfer between the SWNT interface and PVA

hydroxyl and/or residual acetate carbonyl groups. Based on infrared analysis, nearly 40% of the imbibed water had constituted the solvent interphase along SWNTs. The thermogravimetric analysis of PVA/SWNT fibers had given additional evidence of a water interphase along SWNTs; as such the water within composite fibers had evaporated at a higher temperature and slower rate than water within unfilled PVA fibers. Therefore, the complete removal of solvent from gel-spun PVA/SWNT is expected to improve the adhesive interphase between polymer and filler, while enhancing the overall mechanical strength of gel-spun composites.

Dispersions of PVA mixed with ~0.25 wt.% CNTs were prepared for the investigation of the gel aging technique. CNT-polymer dispersions were prepared from a sonicated solution of CNT/PVA/DMSO and an unsonicated solution of PVA/DMSO/water. Chapter 3 describes the cryogenic (cryo-) transformation of PVA solutions and CNT-polymer dispersions that were later gel-spun. Chapter 4 discusses the structure/property relationships for fibers prepared by the gel aging technique, which was used in conjunction with the process of stage drawing.

In Chapter 3, the mechanisms and kinetics of cryo-gelation and solvent freezing within PVA/CNT dispersions are discussed. Samples were annealed at 30, 55, and 70 °C prior to rheological measurments at room temperature (RT) and being cooled to subzero temperatures within the instrument for differential scanning calorimetry (DSC). $G'(\omega)/G''(\omega) \approx 1.5$ for each sample; therefore, the bulk heterogeneity of CNT dispersions at RT had been primarily influenced by the matrix polymer in solution. PVA/CNT dispersions had values of complex viscosity that were lower than those reported for their corresponding homopolymer solutions (which had a DP_w of either 10,000 or 4,000). The

DP_w of PVA was reduced by sonication, as implied by study of capillary elution time versus sonication time for PVA/DMSO solutions at 0.5 g/dL. Therefore, the blending of sonicated polymer with unsonicated polymer had reduced the DP_w and complex viscosity of polymers constituting the CNT dispersions.

The kinetic mechanisms of subzero transformations were interpreted from the isoconversional analysis of non-isothermal, DSC data. Few-walled carbon nanotubes (FWNTs) had nucleated gel crystallization within dispersions of PVA (having a DP_w of 3,700); SWNTs had nucleated solvent freezing within dispersions of PVA (having a DP_w of 8,900). The nucleation-and-growth kinetics of most samples had fitted the Avrami model; these transformations were believed to proceed by parallel or serial pathways.

Chapter 4 investigates the use of the gel aging technique to increase the mechanical strength of gel-spun ~99.75:0.25 PVA/CNT fibers. The goals for applying this technique were to draw PVA/CNT fibers to higher *DR* with gel aging and to induce the molecular ordering of PVA along CNTs with drawing. Structure/property relationships were characterized in terms of DP_w, CNT incorporation, and aging conditions. As-spun gels were aged in solvent systems of 10 °C methanol (MeOH) or MeOH/water for several months. Afterwards, fibers were drawn in four stages: S1/100, S2/160, S3/200, and S4/220; some gels that were aged in MeOH/water were also drawn cold, coagulated in MeOH for 24 hrs, and then drawn in four stages. Neat PVA fibers, which had the highest values of mechanical strength, came from gels that were aged in MeOH for 1 day and MeOH/water for 18 months (this polymer had a DP_w of 10,000). The maximum reported values of tensile strength (*TS*) and tensile modulus (*TM*) were 1.01 ± 0.07 GPa and 36 ± 4 GPa, respectively, from PVA fiber having a diameter of 31

μm and circularity index (*CI*) of 0.9- with 1 representing a perfect circle. The MeOH/water aging of PVA/CNT gels for ≥215 days had resulted in drawn fibers that had *TS* values that were greater than 1 GPa and *TM* values that were greater than 20 GPa. Their fiber diameters ranged from 23-29 μm, and the *CI* values of their cross sections ranged from 0.8-0.9. After a treatment of high temperature annealing at 220 ℃, the *TM* of PVA/FWNT fiber had increased from 24 to 33 GPa; nevertheless, the *TS* decreased from 1.33 to 1.06 GPa. The incorporation of FWNTs was believed to inhibit the excessive relaxation of polymer chains upon high temperature drawing, which would have greatly decreased the tensile strength of the fibers.

Gel aging was shown to increase the *DR* of drawn PVA/FWNT fibers from 5 to 8 X; as a result, an additional peak for high temperature melting was observed among the more highly drawn fibers. The development of the higher temperature melting peak was attributed to the draw induced ordering of PVA along FWNTs. The scanning electron micrograph of a fractured PVA/FWNT fiber had shown FWNTs coated with PVA; the thickness of those coated FWNTs was 22 ± 5 nm.

The glass transition temperatures, T_g, of fibers drawn from aged gels were significantly lower than the T_g of dried PVA. The presence of water within the amorphous phase had reduced the T_g and limited the modulus values of drawn fibers. DSC transitions that were indicative of water evaporation had shifted to higher temperatures and were less intense for drawn PVA/CNT fibers that had *TS* values of 1.0-1.3 GPa. The aging of gels had resulted in the enthalpic relaxation of polymer constituting drawn fibers; this transition was shown to increase to slightly higher temperatures with the gel aging time of some samples.

The storage modulus of aged gel was a function of solvent diffusion, which changed with aging time. DMSO was found to more readily diffuse from the network of aged gel than water. Solvent diffusion from gels had increased the storage modulus, but the counter-diffusion of DMSO/water into gels had lowered the storage modulus, as predicted by mechanical models of gels. The responses of $E'(f)$ for PVA gels were shown to be more reproducible within CNT composite; therefore, CNTs must have stabilized the gel network and nucleated the ordering of PVA chains.

The PVA chains within as-spun gels were believed to organize within sheet geometries, because only two axes of molecular ordering could be determined from the wide angle X-ray diffraction (WAXD) analysis. Further, the PVA chains within these sheets were believed to be intercalated by water molecules, which would explain the shorter d-spacing along the *a*-axis of as-spun gels (0.63-0.66 nm) than for the aged gels (~0.76 nm). The solvent phase within as-spun gel was manifest as a peak at 2θ=21.7°. The $(10\bar{1})$/(101) planes pertained to hydrogen bonding between atactic PVA chains. In this study, their values of d-spacing (~0.45 nm) had indicated the presence of water between the ordered chains of gel and drawn fibers. Based on the WAXD analysis of PVA gels and drawn fibers, as-spun gel exhibited PVA ordering according to the Sakurada unit cell model; whereas aged gels and drawn fibers prescribed to the Bunn model.

CHAPTER 1

INTRODUCTION

1.1 High Performance Fibers

1.1.1 Properties of High Performance Fibers

Terms like ‘textile’ or ‘commodity’, ‘industrial’, and ‘high performance’ describe categories for natural and synthetic fibers. Applications for commodity fibers include clothing and fashion; cotton and polyester fibers are in the highest demand for this group of fibers. Industrial fibers are used in the automotive industry, home furnishings, as geotextiles, and in packaging and filtration. The physical properties and price of fibers will dictate their use within industrial applications.[1] Within Table 1.1, fibers were categorized in terms of their mechanical properties and applications.[1-2]

‘High performance’ describes fibers that have extraordinary properties, which would make them ideal materials for the aerospace industry, military, and electronics industry.[1-2] Specialty fibers will typically have some combination of high strength, stiffness, heat resistance, chemical inertness, thermal conductivity, and electrical conductivity, and they offer weight reductions, especially when they are used to replace inorganic materials. The commercial price of high performance fibers exceed that of industrial fibers, in that they are priced at ≥$20/kg.[1]

Table 1.1. Mechanical Properties of Fiber Classes.

	Tensile Strength	**Tensile Modulus**
Textile Fibers	Up to 7 g/den < 1 GPa	10-30 g/den < 10 GPa
Industrial Fibers	7 to 10 g/den > 1 GPa	30-100 g/den > 10 GPa
High Performance Fibers	20-50 g/den 3-6 GPa	200-2500 g/den 50-600 GPa

Data in Table 1.1.[1-3]

The mechanical properties of polymeric fibers are greatly influenced by their microstructure. High performance fibers will consist of well-ordered and highly aligned polymer chains.[1-3] The poor alignment of polymer chains, defect structures, and the loose packaging of molecular chains have been known to adversely affect the mechanical properties of fibers.[2] Fibers are drawn from polymer melts or solutions having a critical concentration of polymer chain entanglements; however, an excessive number of chain entanglements will impede the drawing of a highly ordered microstructure. Therefore, the molecular disentanglement of polymer chains is important for the drawing of highly aligned microstructures that are also densely packed. The formation of microvoids within the fiber microstructure can be avoided as long as fibers have not been over-drawn. By limiting the introduction of foreign particles and dangling chain ends within the fiber, the packing density and structural integrity of fibers can also be improved.[1-2, 4]

The semi-crystalline microstructure of textile and industrial fibers has typically consisted of folded-chain crystals (FCC) that are randomly dispersed within a matrix of amorphous polymer. The mechanical properties of these fibers are influenced by percent crystallinity, crystal size and form, and the orientation of crystalline regions. The

formation of extended chain crystals (ECC) has been essential to the development of high performance fibers from synthetic polymers.[1]

The microstructures of main chain, liquid crystalline polymers have been archetypes for high performance fibers. For example, Kevlar® polymer consists of rigid rod para-aramids, which can hydrogen bond with parallel chains. Kevlar® fiber is also highly crystalline, and the polymer chains are highly oriented along the fiber axis. The processing of Kevlar® fibers was made possible with the development of dry-jet wet spinning. The nematic ordering of backbone mesogens will begin in the air gap component of this process. The lyotropic phase of crystalline polymer is aligned within 12-15° of the fiber axis upon removing the fiber from the coagulation bath. The process of drawing will further aid the aligning of rigid rod polymers along the fiber axis. The alignment of crystalline polymer is further accompanied by the enlargement of polymer crystals and the development of a more uniform fiber structure.[1] The tensile strength (*TS*) and tensile modulus (*TM*) values of Kevlar® (29 and 49 yarns by Dupont) are 3 GPa and 70-112 GPa, respectively.[5]

1.1.2. Gel Fiber Spinning Technique

Aliphatic polymers are attractive raw materials for preparing high performance fibers. In comparison to poly(aramids), aliphatic polymers have greater availability, lower prices, and they are less dense.[1] The method of gel-spinning has been used to manufacture strong fibers from vinyl polymers, such as polyethylene (PE), poly(acrylonitrile) (PAN), and poly(vinyl alcohol) (PVA). Gel-spun fibers can be more highly drawn than melt and solution spun fibers, thus rendering a stronger fiber.[1-2]

1.1.2.1. Role of Chain Entanglements

The molecular weight and concentration of polymer will influence the density of polymer chain entanglements (v_e). Molecular entanglements will occur at the junction of overlapping chains, such that physical hooks are formed within a three-dimensional space. The value of v_e within molten polymer or polymer solutions will influence the ability to extrude and draw fiber; therefore, v_e must be sufficiently higher than the critical overlap concentration to continuously extrude polymer from solution. Below the critical overlap concentration of a polymer in solution, individual chains will not physically interact with one another.[6-7]

The nucleation-and-growth of FCC and ECC phases within polymer has been influenced by the mechanism of chain disentanglement at elevated temperatures. According to Hikosaka et al., polymer crystals will form from segments of disentangled chains.[8] As polymer crystals grow, chain entanglements are thereby excluded and confined to regions outside of crystalline domains. ECC phases were believed to grow directly from amorphous polymer. The growth of three dimensional crystals from regions of highly aligned/extended chains is therefore characterized by the process of sliding chain diffusion and the disentanglement of polymer. Polymers yielding phases of FCC are less mobile than polymers that yield phases of ECC.

The following parameters will influence the molecular mobility of polymer chains and thus the number of chain entanglements: temperature, annealing time, internal/external stresses, and the method of polymer processing.[9] For instance, changes to the conformation of polymer chains can occur at temperatures above the glass transition temperature (T_g) of that polymer. Above the T_g, covalently bonded segments of

the carbon-carbon (C-C) backbone can rotate. As segments of the polymer chain change their direction, molecular kinks will result in the formation of molecular chain entanglements.[9] Above melting temperature (T_m), the density of chain entanglements increases with annealing time and polymer chains will adopt random coil conformations. As the crystallinity of polymer is reduced and the relaxation of polymer chains occur at temperatures above the T_m, the melt memory of semi-crystalline polymer will have a lesser affect on polymer processing steps.[8]

In conjunction with temperature, internal and external stresses can reduce the number of chain entanglements. As polymer chains are relaxed from internal stresses, the molecular disentanglement of chains can also occur and enable the formation of crystalline polymer.[8] Rees and Bassett applied an external stress to PE to promote the crystallization of the ECC phase.[10] The ECC phase was believed to persist from the FCC phase under conditions of high pressure and at temperatures near the melting temperature. PE maintained at 227 ℃ and external pressures of >4 kbar exhibited an ECC phase upon cooling. PE melts that were exposed to external pressures of 2-4 kbar had shown elements of FCC and ECC phases upon cooling.

Polymer processes, such as mechanical shearing and stretching, involve the application of external stresses which in turn causes the molecular disentanglement of polymer chains.[8-9] Processes of high temperature drawing, as used in fiber spinning, will enable chain disentanglement and further the growth and alignment of crystalline domains.[8]

According to Qian et al., the preparation of polymer solutions can influence the concentration of chain entanglements, as indicated by changes in polymer viscosity.[8]

Two solutions of PAN polymer at 5 g/dL were made by (1) dissolving the appropriate mass of PAN in dimethylformamide (DMF) solvent and (2) removing excess DMF from a 2 wt.% solution. The solution prepared by method (1) had twice the viscosity of the solution prepared by vacuum distillation at 50 ℃. Therefore, solution (2) was believed to have fewer chain entanglements than solution (1).[9]

Melt and solution spinning techniques will influence the value of v_e differently. Molten polymer is known to have the highest concentration of entangled chains versus polymer in solution; whereas the process of dissolving polymer in a good solvent will decrease the number of molecular entanglements in comparison to a poor solvent. Therefore, polymer processed from polymer solutions will have lower values of v_e than molten polymer.[6]

1.1.2.2. Polymer Gelation

The nucleation-and-growth of polymer gels is especially important to the development of high performance fibers produced by the gel-spinning technique.[9, 11-12] Vinyl polymers such as polypropylene (PP), poly(methyl methacrylate) (PMMA), PAN, and PVA have been investigated as candidates for gel-spun high performance fibers. Gel-spinning promotes the development of fiber properties that cannot be achieved with melt spinning.[2] Gel-spun fibers are prepared from lower concentrations of polymer than those prepared from traditional methods of melt or wet spinning; therefore, the value of v_e is much lower for gel-spun fiber. As a result, the molecular chains of gel-spun fibers have the potential to be drawn to higher values of draw ratio (*DR*) than the melt-spun polymers.

A physical gel is comprised of flexible chains that are adjoined by clusters of associating chains. These associations may occur through non-covalent, intermolecular attractions, physical aggregation, or molecular ordering. The transformation of a polymer solution into a physical gel is often stimulated by changes in temperature.[13-15] These temperature induced transformations have often proceeded from phase separation phenomenon; such as, spinodal decomposition into polymer-rich and solvent rich phases,[16-17] the bi-continuous formation of frozen solvent and concentrated polymer phases,[18] gelation-induced separation of polymer from phases of continuous solvent,[19] and the spinodal decomposition of blended polymers prior to gelation.[20] The development of thermally-induced gel structures is often time dependent. Also, thermoreversible gels have been shown to revert back into polymer solutions at temperatures above their gel melting temperature.[16, 21]

Studies by Berghams et al. reported supercooling effects for thermoreversible s-PMMA gels, where cryogenic (cryo-) gelation had occurred below the temperature of gel melting.[16, 21] The rheological characteristic of isothermal gelation was the gradual increase in the storage modulus.[16] Gels prepared from isotactic (i-)PS and syndiotactic (s-)PMMA evolved from a 2-step mechanism of 1) random coil to trans-trans conformation of molecular chain segments and 2) the aggregation of ordered sequences.[22]

Solution properties- such as the polymer's degree of polymerization (*DP*),[16, 23] polymer concentration, and solvent composition-[16, 19, 24] will influence gel development and crosslink density. For instance, the thermally-induced conversion of polymer solution to gel depends on the critical overlap concentration of the polymer

solution.[6, 23] As the concentration of polymer exceeds the overlap concentration, the gel network becomes highly crosslinked. At low polymer concentrations, a two-phase system of polymer solution and gel will exist.[6, 23] Gel-phases that are initiated upon cooling from elevated temperatures[24] can occur by means of refrigeration[25] or immersion into a chilled coagulating solvent.[12]

Several studies have reported on the influence of temperature and solvent system on the gel structure.[2, 16, 22, 24-25] For instance, s-PMMA gels that were formed at temperatures of 25-130 ℃ were opaque, but transparent gels of s-PMMA were observed from solutions cooled below 20 ℃.[16] Berghmans et al. and Hoshino et al. had determined that the opacity of gels was influenced by the form of crystals within the gel phase.[16, 24] In Hoshino et al., the ratio of DMSO/water was shown to affect the structure of PVA gel crystals as well.[24] As solutions of 60-70% DMSO were chilled from 90 to 23 °C, opaque gels of fibrillar crystals had formed. PVA solutions of <60% DMSO required relatively longer times to form opaque gels of fibrillar crystals at 23 °C.

1.1.2.3. Models of Gel Structure

Equation 1.1 is a mechanical model for a well-defined polymer network; such that, the microscopic arrangement of adjoined chains is consistent throughout the bulk structure. The shear modulus (G) will depend on the density of the dry network (ρ_2), temperature (T), gas constant (R), and the molecular weight between junctions. M_e stands for the chain lengths between physical entanglements and M_x represents the chain lengths between crosslinks. As the DP (or molecular weight) of polymer increases, the number of entanglements will also increase. Further, an increase in either the number of molecular entanglements or crosslinks will increase the network modulus.[15]

$$G \approx \rho_2 RT\left(\frac{1}{M_x} + \frac{1}{M_e}\right) \quad (1.1)$$

The shear modulus (G) of a fully developed, polymer network is measured by the use of dynamic mechanical analysis (DMA); wherein, the shear storage modulus, $G'(\omega)$, of the gel network is represented by the frequency independent storage modulus.[15, 26] This characteristic plateau modulus has occurred within the low frequency regime of an oscillating strain.[26] The loss modulus (or viscous response, $G''(\omega)$) lags behind the storage modulus by a phase shift of $\pi/2$. The behavior of $G''(\omega)$ represents the mechanical response from dangling chain ends and unconfined polymer strands.

Equation 1.2 is an expanded version of Equation1.1, it accounts for the effects of solvent on the network modulus (G). Parameters v_x is the crosslink density, v_{2r} is the volume fraction of the pre-swollen network, and v_2 is the volume fraction of polymer. The value of A_b=1 would exist in the case of nodal branching that is greater than 2 (Equation 1.2).

$$G = A_b RT v_x v_{2r}^{2/3} v_2^{1/3}; \quad (1.2)$$

The molecular weight between junctions of the adjoined chains (M_x) would reflect interactions between flexible chains and solvent molecules in the gel. The molecular weight between adjoined chains (M_x in Equation 1.3) has been accounted for in Equation 1.2; in which parameter ρ_2 is density of the dry network.

$$M_x = \frac{\rho_2}{v_x} \quad (1.3)$$

Since the modulus of a swollen gel is significantly influenced by the volume fraction of polymer within the as-prepared gel; term v_{2r} was included as a memory parameter. The value of v_{2r}=1 exists for gels prepared from a dry network.[27-28]

Structural changes within the gel microstructure (as it pertains to the number of junction points, polymer crystallinity, crystal size, and/or the pore size of swollen gels) would all influence the value of v_x. An increase in the size or number of physical junction points would then result in the development of a stiffer gel.

The volume fraction of polymer (v_2) in a gel is inversely related to the value of solvent swelling (Q) (Equation 1.3). Parameters ρ_2 and ρ_1 represent the density of polymer and swelling solvent, respectively.

$$v_2 = \left(1 + \frac{\rho_2 Q}{\rho_1} \right)^{-1} \tag{1.4}$$

Through the relationship between parameters v_2 and Q; solvent swelling will adversely affect the plateau shear modulus (G) of a gel network (Equation 1.2). Parameter Q is determined gravimetrically, according to Equation 1.5.

$$Q = \frac{w_{solvent}}{w_{polymer}} \tag{1.5}$$

1.1.2.4. Gel-spun UHMWPE Fibers

The synthesis of PE polymer, having molecular weights of 10^6 g/mol, was essential to the spinning of high performance PE fibers. Gel-spun fibers were fabricated from solutions of 1-2 wt. % UHMWPE in decalin.[2, 11] The gel fiber formed as the polymer jet of >100 ℃ was spun through a bath of cold water. The *DR* for UHMWPE gel fiber can be ≥30 X.[2, 11] The highly drawn microstructures of gel-spun UHMWPE fiber consists of densely aligned ECC phases.

1.2. Gel-spinning PVA Fibers

1.2.1. Structure of PVA

Like PE, PVA can exhibit trans-trans chain conformations, which are conducive to the formation of the ECC phase. The atactic form of vinyl polymers (having this molecular formula, $-CH_2-CHX-_n$) typically do not crystallize; however, atactic (a-) PVA does crystallize. Pendant hydroxyl groups do not disrupt the process of crystallization.[7, 29] As a result of hydrogen bonding, PVA has a higher T_m than PE and offers a higher operating temperature.

The monoclinic arrangement of the a-PVA unit cell has the following lattice parameters along the *a*-axis, *b*-axis, and *c*-axis: 0.778, 0.549, and 0.254 nm, respectively; $\beta_<$ has a value of 91.7°, according to the Bunn model in Figure 1.1.a.[29-30] The molecular axis for the monomer unit of PVA occurs along the *b*-axis. Monomer units within the Bunn and Sakurada unit cell models of PVA are stacked differently; such that intermolecular hydrogen bonding influences the *c*-axis parameters of the Bunn model, in contrast to the *a*-axis parameters of the Sakurada model. Furthermore, van der Waals bonding occurs along the *a*-axis of the Bunn model and the *c*-axis of the Sakurada model.

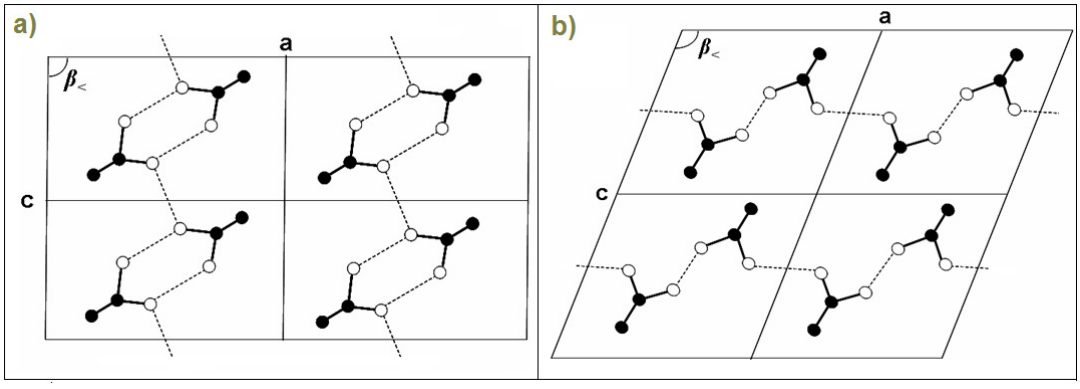

Figure 1.1. Unit cell models of PVA by a) Bunn and b) Sakurada.[29-30]

The theoretical modulus of PVA is between 230-250 GPa, as determined from strain measurements of its crystalline lattice.[12, 31-32] As previously discussed, the polymer microstructure has a significant influence on the ultimate performance properties of fibers; as such, the mechanical properties of manufactured PVA fibers are less than their theoretically determined projections of strength.

Suzuki et al. have demonstrated how the alignment of crystalline and amorphous chain conformations will ultimately influence the mechanical strength of gel-spun PVA fibers. Crystalline chain conformations were shown to more readily align along the axis of gel-spun PVA fibers than amorphous chain conformations. Measurements of chain orientation by birefringence microscopy had revealed the orientation of crystalline PVA (f_c) within fibers drawn by 15 and 25 X were similar (f_c=0.96); whereas, the orientation of amorphous PVA (f_a) within these drawn fibers was considerably different: f_a=0.69 and f_a=0.95 for *DR* values of 15 X and 25 X, respectively.[33]

Hydrogen bonding between PVA chains can hinder the disentanglement of PVA and thus the growth of crystalline PVA at temperatures near T_m. Endo et al. reported conditions for the melt crystallization of PVA (having a *DP* of 2,700); wherein, the thermal degradation of PVA chains was suppressed at temperatures near that of crystalline melting. The crystallization of PVA was studied from films that were prepared from aqueous PVA solutions, degassed and heated under high pressure, and annealed at crystallization temperatures of 208-221 ℃ from the melt.[34] Lamellar thickening within molten PVA was observed; nevertheless, the crystal sizes reported for PVA were considerably smaller than crystal sizes found within PE. The authors

concluded that the thickening of crystalline PVA by the process of sliding chain diffusion was restricted by hydrogen bonding.

Solvent has been shown to influence the amorphous and crystalline microphase of PVA.[29, 35] For instance, solvent can form hydrogen bonds with PVA chains, and saturate amorphous polymer. Sakurada has observed that solvent can influence the lattice parameters of ordered PVA, just as water can expand the (101) planes of water-cellulose.[29] The overall crystallinity of PVA increases during the process of gel drying.[36] As solution cast films of semi-crystalline polymer undergo drying, film shrinkage and the crystallization of polymer can also occur. Furthermore, solvent can freely reside within the PVA gel, in a state that is not bound to PVA by intermolecular forces.[37] For instance, free water has been shown to reside in the porous walls of PVA hydrogels and amorphous polymer.

1.2.2. Processing PVA

PVA, having a low degree of polymerization (*DP*), is polymerized from the solution of vinyl acetate in methanol (MeOH) (≤4000 *DP*). High *DP* polymers of (10,000-18,000 repeat units) have been prepared by suspension/emulsion polymerization. Scheme 1 depicts the synthesis of a-PVA, which is derived from poly(vinyl acetate) (PVAc).[29] The deacytalation of PVAc is performed in the presence of methanol (MeOH). Sodium hydroxide (NaOH) catalyzes the methanolysis of the reaction, and the presence of water can result in the formation of sodium acetate.

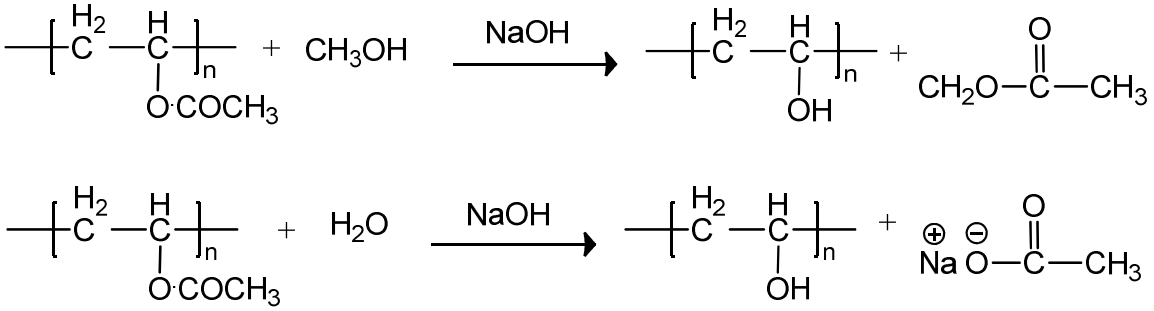

Scheme 1.1. Synthesis of PVA from PVAc.

Industrial applications of PVA include its use in adhesives, textile sizing, and packaging to name a few.[38] Staple PVA fibers (of 6-30 mm in length by 24-660 μm in diameter, φ_f) have been used to reinforce concrete. Crack propagation within structural concrete is impeded by the dispersion of staple PVA fibers through the cement matrix. Further, hydroxyl groups along PVA promote molecular adhesion between wet cement and the embedded fibers. Commercial manufactures of PVA staple fibers for concrete reinforcement include Kuraray and Nycon.[38-39] The mechanical properties of these fibers range from 0.8-1.6 GPa in *TS* and 23-40 in *TM*.

The wet spinning technique is commonly used to spin industrial fibers from solutions of 14-16 wt.% PVA, having *DP* values of ~2,000; whereby aqueous solutions of PVA have been coagulated into baths of aqueous salts or alkali solutions.[29] The method of coagulating fiber in aqueous sodium hydroxide has yielded high tenacity fiber of 14-18 g/den (where the highest value corresponds to a *TS* of 2 GPa). The cross sections of these high tenacity fibers are fairly circular in comparison to those obtained by coagulation in aqueous salts.

High performance PVA fibers have been gel-spun from polymers having a *DP* of ≥5,000.[29] Fibers having tenacity and modulus values of 20-22 g/den and 480-550

g/den have been reported. Ideally, this process could be used to prepare fibers that are suitable for tire cords. Organic solvents are typically used to process these fibers. In contrast to the wet spinning process, fibers prepared by the gel spinning process are fabricated from lower concentrations of polymer, thus resulting in a lower degree of molecular entanglements.

Researchers have applied variations to the gel-spinning process, in hopes of improving the mechanical integrity of drawn fibers. Literature has reported the effects of polymer architecture, solvent(s) within the PVA solution, gelation temperature, and freeze-thawing on the structure/property relationships of films and fibers derived from gels. A technique of sequential drawing has been used to improve the mechanical integrity of gel-spun PVA as well.

The molecular architecture of PVA polymers can influence the structure, properties, and processing of gel-spun fibers. The atactic form of PVA is the hydrolysis product of PVAc.[29] Isotactic (i-) PVA has been synthesized from poly(t-butylvinyl ether), poly(benzyl vinylether), and poly(vinyl trimethylsilylether).[29, 40] PVA polymers containing diad sequences that are indicative of syndiotactic polymer have been prepared from the hydrolysis of poly(vinyl pivalate), poly(vinyl trifluoroacetate), and poly(vinyl formate). Research on the drawability of microfibrils, prepared from atactic and syndiotactic polymers (having a *DP* of 8,000), had shown that the content of racemic (r)-diads influenced the optimum *DR* of those fibers.[41] The maximum *DR* values of those microfibrils decreased from 13 to 5 X upon increasing the r-diad content from 56 to 65% r-diad. Microfibrils of s-PVA polymer also exhibited higher values of f_c than microfibrils

of a-PVA, which were stretched to similar values of *DR*. The T_m of s-PVA microfibrils was higher than that of a-PVA microfibrils.

DMSO and water mixtures have been used to influence the development of PVA gels and gel-spun fibers. Solvent mixtures of water and >60 % DMSO were shown to yield high strength, high modulus fibers.[12, 33] High performance fibers were prepared from 6 wt.% PVA (having a *DP* of 5,000) that was dissolved in 80/20 volume ratio (*v/v*) DMSO/water. PVA gel that was coagulated within MeOH at -20 ℃ had yielded transparent gel, which could undergo a tensile strain of 950%.[12] Coagulation within 18 ℃ MeOH yielded an opaque gel that extended to a lower tensile strain of 650%. The *TS* and *TM* values of gel-spun fibers, where the gel was formed within -20 ℃ MeOH, were 2.8 GPa and 64 GPa, respectively.

High performance fibers have been prepared by the sequential drawing of dried or swollen gels at increasingly higher temperatures. Heating elements and oil baths have been used to bring fibers to the desired temperature for drawing.[12, 33] The high strength, high modulus fibers by Cha et al. were produced by two stages of drawing: at 160 and 200 ℃.[12] The transition of crystalline relaxation enables the drawing of PVA chains, which would have been inhibited by hydrogen bonding.[35] As fibers are drawn at sequentially higher temperatures, this transition temperature can increase. Therefore, PVA fibers have been strengthened through the processing of drawing at temperatures near or above T_m and for brief periods of time.[42-43] Gel-spun PVA fibers, from polymer having a *DP* of 18,000, were drawn at stage/drawing temperatures of S1/100, S2/160, S3/200, and S4/290. The resulting *TS* and *TM* of these PVA fibers were 1.6 GPa and 47 GPa, respectively.[33] The highest tensile modulus that has been reported for a

PVA fiber is 115 GPa, where the *DP* value of PVA was 11,800.[43] The preparation of such fiber was described in Kunugi et al.; wherein, dried as-spun gel fibers (having a diameter of 184 μm) were drawn sequentially at stage/temperature (°C) S1/255, S2/210, S3/220, and finally heated from room temperature (RT) to 230 °C with an oscillating frequency of 110 Hz.[43] Crystalline PVA had enlarged upon molecular chain relaxation and the stretching of molten polymer. As discussed earlier, the relaxation of polymer chains is important for the removal of chain entanglements and for the growth of ECC phases.

1.2.3. Aging PVA Gels

The cyclical freezing and thawing of PVA hydrogels have been used to improve their mechanical strength. The swelling ratio of the dried gels will decrease as the result of repeated freezing and thawing. Upon freeze-thawing, the number of network junctions and polymer crystallinity will increase; also, unbound solvent diffuses from the gel microstructure as the polymer network becomes denser.[25, 36-37]

As observed with the process of freeze-thawing, the aging of cryo-gel can lead to gel strengthening. Cryo-gels were prepared from 10 wt.% solutions of PVA (having a *DP* of 2,600) that were chilled to -34 °C for 1 day and subsequently aged at 30 °C. The compression modulus of aged gels was shown to increase with aging time. PVA gels that were prepared from solutions of 60/40 (*v/v*) DMSO/water had exhibited a modulus of 1 GPa after 500 days of RT aging.[44]

The gel aging technique was also included as a process step for preparing high strength, high modulus PVA tapes. Tanigami et al. was able to achieve *TS* and *TM* values of 2.8 GPa and 72 GPa, respectively. The cryo-gelation of PVA, dissolved in

80/20 (*v/v*) DMSO/water, occurred under refrigeration at -34 ℃. Afterwards, gels were heat pressed, submerged within aging solvents (of water or 50:50 (*v/v*) DMSO/water) for several months at 10°C, vacuum dried, and finally drawn at 200 ℃. Aging time and aging solvent had influenced the drawability of aged gels. The *DR* of dried gels had increased from ~11 X to 23 X after gel aging in 10 ℃ water for 4 months.[32]

Structural differences between aged gels were observed. The original, cryogenically-induced gel exhibited a single endothermic peak ranging from 40-90 ℃. The single endothermic peak of the original cryo-gel was also observed within the thermograms of aged gels, along with additional peaks. The increased drawability of aged gels was then attributed to these structural changes. The melting temperatures for highly drawn tapes had ranged from 220-260 ℃, and several tapes had exhibited twin melting peaks.[32] Cha et al. had also reported the occurrence of double melting peaks for high strength PVA fibers.[12] The intensity of the highest melting temperature peak/shoulder had become more pronounced with *DR*.[12, 32]

1.3. Filler Reinforced PVA

Nano-micro size fillers have been used to improve the physical properties of polymers; such as their mechanical strength, thermal resistance, barrier properties against chemical agents, and electrical conductivity. The overall performance properties of the composite are influenced by the polymer microstructure, filler morphology, and the molecular adhesion between polymer and filler. Mechanisms for polymer reinforcement were introduced prior to the discussion of PVA composites.

1.3.1. Polymer Reinforcement

The mechanical properties of polymeric materials can be enhanced through the addition of organic or inorganic fillers. Nevertheless, filler incorporation can incur structural macro- and microscopic heterogeneities within the polymer.[45] For instance, the physical properties of polymer along the filler's surface can microscopically differ from the bulk polymer. At the filler's surface, the packing density, molecular conformation, and supramolecular arrangement of polymer chains can differ from that of the bulk polymer. This region of microscopic heterogeneity is known as the polymer interphase. Microscopic heterogeneities can also occur within polymer blends and in composites comprising two different filler geometries.

Filled polymers can be strengthened by the inherent strength of the filler and the polymer interphase.[45] The dispersion and exfoliation of laminated fillers throughout the matrix polymer will promote interfacial adhesion between the polymer and filler. The thickness of the interphase, or adhesion layer, alludes to the attraction between the matrix polymer and filler. Poor adhesion between the matrix polymer and filler will decrease the modulus of the overall composite; whereas, good adhesion between polymer and filler will yield a composite that is stiffer than the neat polymer. Just as the thickening of the polymer interphase can strengthen the overall composite, defects and impurities within the interphase can weaken the strength of the composite.[45] The interphase thickness can result from the physical adsorption of solvated polymer onto filler or by the phase-separation polymer. The term 'perfect' interphase suggests the interfacial layer of polymer along the filler does not debond from the filler under large shear stresses.[46] Modes of mechanical failure within the composite can result from the delamination of the

interphase from the filler, fractures at some distance from the interphase, or cracks between the interphase and bulk polymer.[45]

The surface of fillers will confine the molecular mobility of polymer chains and restrict the number of conformations by which polymer chains can arrange themselves. The change in conformational entropy will decrease at the surface of the filler.[45] As a result of the interphase, the T_g of amorphous polymer will increase. Further, the shear modulus and the molecular relaxation time for polymer are greatest at the interphase.

1.3.2. Nucleation-and-Growth of Filled Polymer

Because fillers are capable of influencing the local density of polymer, they can also nucleate the molecular ordering of polymer chains.[45] In response to filler loading, the isothermal crystallization of supercooled polymer may occur at even lower temperatures. Conformational changes to the structure of polymer chains are either incited or hindered by mechanisms of molecular attraction between the polymer and filler. Moderate affinity between fillers and polymer chains can incur the heterogeneous nucleation of crystalline polymer from the surface of fillers. Morphologies of transcrystalline polymer have resulted from the epitaxal growth of crystalline polymer along the long axis of the filler. Also, the physical adsorption of polymer to the filler surface can induce the assembly of micro-ordered domains that could in turn nucleate polymer crystallization. Non-interacting fillers are not expected to exert any influence on the crystallization of polymer.

The loading of polymer with filler can be optimized to achieve the highest rates of polymer nucleation for crystal growth.[45] Typically, the highest rates of nucleation are associated with low weight fractions of filler. High loadings of filler within polymer can

inhibit polymer crystallization; this is due to the decreased mobility of polymer chains for crystallization. Further, the crystallization of polymer chains can be impeded by the presence of the polymer interphase.[45]

1.3.3. Filler Reinforced PVA Composites

In this section, the structure/property relationships for several filled systems of PVA are discussed. The dimensions of fillers were on the order of microns and nanometers.

In the work by Lozinsky et al., the dimensions of spherical fillers had influenced the mechanical, thermal, and structural reinforcement of PVA hydrogels. Hydrogels of aqueous PVA (having a viscosity average degree of polymerization, DP_v, of 1,900) were filled with different size distributions of crosslinked dextran, gels beads. Overall, cryo-gels of the smaller bead sizes had exhibited higher temperatures of gel melting and values of shear modulus at similar weight fractions of filler. Micrographs of dried PVA/dextran gels had shown surface coatings of PVA around the beads of 30-100 μm; however, the composite of slightly larger beads (50-150 μm) did not have surface layers of polymer along its beads. Therefore, the PVA gels of the smallest beads were structurally reinforced by an interphase of polymer at the surface of the embedded beads. At 20 wt.% dextran gel, PVA gels that were loaded with beads of 30-100 μm in diameter were twice as stiff and melted at 6 K higher temperature than composites containing beads of 50-150 μm in diameter.

PVA has been reinforced with silica to prepare stiff, optically clear composites. The thermal and mechanical properties of PVA/silica composites, in the study by Nakane et al., were described in relation to the morphology of embedded silica.[47] Composite

films of PVA/silica were prepared from blended solutions of aqueous PVA (having a *DP* of 1,700) and tetraethoxysilane catalyzed with hydrochloric acid. The reduced solubility and swelling behavior of composites films in 20 ºC water was suggestive of good adhesion between the PVA and silica. At loadings of less than 30 wt.%, the morphology of silica was proposed to exist as dispersed particles, but an interconnected network of silica was believed to form at even higher loadings of silica. Although the RT storage modulus of PVA/silica composites had increased with higher loadings of silica, it became apparent that the stiffness of composites having >30 wt.% silica were less influenced by the presence of polymer. The tensile stress-strain curves of PVA/silica composites did not exhibit a yield stress indicative of plastic deformation as the composites of up to 30 wt.% silica. As a result, the T_g and crystallization of the polymer was significantly inhibited within composites of >30% silica.

Imogolite filler (i.e. tubes of alumina-silicate having diameters of 2.5 nm) has been used to mechanically reinforce drawn films of ultra-high molecular weight, s-PVA (having a *DP* of 12,300).[48] The *TS* of drawn PVA/imogolite films (at 9 wt.% imogolite) exceeded the strength of homopolymer PVA films (1.8 GPa versus 1.4 GPa, respectively). However, the *TM* for corresponding composite films was inferior to that of the neat PVA film (19.8 GPa versus 25.2 GPa, respectively). Crystalline PVA was more highly aligned within the PVA/imogolite film than in the neat film of PVA; nevertheless, the presence of imogolite hindered the conformational alignment of amorphous PVA. The packing density of crystalline PVA was also hindered by the presence of imogolite. Choi et al. observed the melting temperatures of PVA crystals within imogolite films were lower than the values reported for homopolymer although films were stretched to

similar *DR* values. This behavior suggests the addition of imogolite had hindered the chain mobility for crystal growth.

Strawhecker and Manias studied the structure/property relationships of PVA (having a *DP* of ~900) films that were loaded with layered silicate, namely sodium montmorillonite (MMT).[49] The loading of 4 wt.% MMT was shown to increase the thin film modulus of PVA by 300%, and the water permeability of nanocomposite films had decreased by more than 40% upon the addition of 2-6 wt.% MMT. Testing by transmission electron microscopy (TEM) and wide angle X-ray diffraction (WAXD) analysis provided evidence that the nanocomposites of less than 20 wt.% MMT consisted of exfoliated layers and polymer intercalated silicates. As a result, nanocomposites of 4 and 10 wt.% MMT were optically transparent to 400-700 nm light just as the neat films. Intercalated silicates were observed at loadings of ≥40 wt.%. The distance between intercalated layers had decreased from 5 to 2 nm at higher loadings. The T_m and T_g of PVA residing in composites of >60 wt.% MMT were not measurable. At such high loadings of MMT, the molecular mobility of amorphous PVA was restricted by the presence of MMT. Melting from two distinct phases of crystalline PVA were observed in the differential scanning calorimetry (DSC) thermograms of samples consisting of 2-40 wt.% MMT. The second, higher T_m peak was attributed to the development of PVA crystals of a different molecular conformation.[49] s-PVA and i-PVA are known to have higher melting temperatures than a-PVA.[50] Therefore, the exfoliated layers of silicate were believed to template PVA conformations that would yield higher melting temperatures.

Hydrophilic polymers have been loaded with electrically conductive fillers to make electroactive materials. In the study by Chuangchote et al, PVA was filled with carbon black (CB)- a low cost, colloidal filler of amorphous carbon-. Filler particles had a diameter of ~29 nm. The loading of CB into PVA (having a DP_w value of 1,600) was shown to affect the storage modulus of PVA fiber mats. CB was dispersed within aqueous PVA using 10 min of sonication. It was shown that the viscosity of the untreated 10 wt.% solution of PVA was 25% higher than the viscosity of the same solution that was exposed to 10 min of sonication. The viscosity of the unsonicated PVA solution was also greater than the values reported for CB filled solutions of 10 wt.% PVA. The electrical conductivity of aqueous PVA/CB dispersions was measured as a function of CB loading (up to 10 wt.%). The unfilled PVA solutions of sonicated and unsonicated polymer had the same values of electrical conductivity; whereas, the electrical conductivity of the PVA solution increased upon loading 10 wt.% CB (from 1.011 to 1.024 mS/cm, respectively).[51]

The diameter of CB-filled electrospun fibers were ~160 nm regardless of CB loading.[51] The average diameter of fibers spun from the sonicated solution of 10 wt.% PVA was 169 nm, and the average diameter of fibers prepared from the unsonicated solution of PVA was 285 nm. The surfaces of unfilled fibers were smooth; whereas, the surfaces of CB containing fibers were irregular. Irregularities within the diameter of CB filled fibers were attributed to the heterogeneous dispersion of CB within the fiber matrix. The *TS* of PVA fibers decreased from 7.4 MPa to 4.5 MPa upon the incorporation of 8 wt.% CB; nevertheless, the modulus values of electrospun mats had doubled upon the

incorporation of 8 wt.% CB. The storage of modulus (at 0.1 rad/s) of the 8 wt.% filled mats was more than twice the storage modulus of PVA mats (at ~0.1 GPa).

1.4. Carbon Nanotube Reinforced Polymer

1.4.1. Carbon Nanotubes

Carbon based nanocomposites offer the potential to create materials that have greater structural integrity, range of operating temperature, and electrical/thermal conductivity.[52] Furthermore, these materials can be incorporated in polymers, to create composites of high performance. Nano-structured allotropes include fullerenes (i.e. buckyballs),[53-54] capped tubes of a single or multiple walls,[52, 54] and graphene. In comparison to carbon black, the aforementioned materials are highly crystalline. The high aspect ratios and surface areas of carbon nanotube (CNTs), make them ideal fillers for polymers.[52]

CNTs are known to exhibit properties of gigapascal strength (13-53 GPa), terapascal modulus (0.6-5 TPa),[55] and good electrical conductivity.[52] The molecular architecture of CNTs has been known to influence its physical properties. CNTs are composed of sp^2 covalently bonded carbons, which are arranged as hexagonal rings along the backbone of CNTs. The diagonal arrangement of planar rings, i.e. chirality,[54] is used to distinguish metallic single walled carbon nanotubes (SWNTs) from semi-conducting SWNTs.[56]

CNTs are manufactured from the carbon-arch discharge method, laser ablation, and the process of high pressure carbon monoxide (HiPCO).[52, 57] The bulk of CNTs are produced by the catalytic chemical vapor deposition method.[57] The cost of SWNTs is ~$1000/kg; the purity of SWNTs will greatly influence this price.[58]

SWNTs have characteristic Raman bands which allow researchers to infer the molecular structure of as-received or treated SWNTs. The radial breathing mode, which occurs in the range of 100-500 cm^{-1}, is indicative of nanotube diameter.[56] The use of a single Raman laser is limited in its ability to detect the presence of all SWNT diameters and electronic states within a mixed sample of semi-conducting and metallic SWNTs.[56, 59] The diameter of SWNTs typically ranges from ~1-7 nm.[54-55] Multi-walled carbon nanotubes (MWNTs) having large diameter tubes do not feature radial breathing mode (RBM) bands.[56] However, the inner tubes of double walled carbon nanotubes tubes (DWNTs) have exhibited RBM bands.

The G^+-band at ~1580 cm^{-1} represents axial vibrations along the CNTs.[56] The G^+-band is accompanied by a lower frequency shoulder called the G^--band. The disorder band (D-band) is indicative of bonding defects. The frequency of the D-band depends on the wavelength of the Raman laser. A 2.4 eV Raman laser can produce a D-band peak at 1350 cm^{-1}, which is known to shifts from 1350 cm^{-1} in increments of 50 cm^{-1} per 1 eV change in laser energy.[56] The frequencies of the D-band, G-band, and the G′-band (at ~2500 cm^{-1}) are influenced by mechanical deformation,[60-61] thermal treatment,[62] and the chemical environment of the SWNTs.[56] Chemical environments that reduce the sp^2 character of SWNTs will in turn increase the intensity of the D-band. Repair of the sp^2 structure will result in a decline in the D-band intensity.[63]

1.4.2. CNT Morphology

CNTs have been used to improve the mechanical performance of synthetic fibers and films.[52] The achievement of impressive *TS* and *TM* reinforcement by CNTs has been attributed in part to the successful transfer of load between the matrix polymer and

CNTs. These characteristics of CNT morphology within matrix polymer- such as dispersion quality, exfoliation, and interfacial adhesion- will influence the efficacy of load transfer and molecular adhesion between CNTs and polymer. These following factors, which are inherent to samples of CNTs, should also be considered when choosing reinforcing filler: percent purity, length, and the diameter distribution of CNTs.

CNTs, namely SWNTs, readily aggregate into bundles that are bonded by van der Waals forces. The surface area of CNTs is reduced upon aggregation; furthermore, their interaction with matrix polymer is limited upon this occurrence. Surfactants, good solvents, and the covalent functionalization of CNTs are techniques for dispersing CNTs in polymers.[64] The sonication of CNTs in a good solvent or polymer solution also aids the mixing of CNTs; unfortunately, sonication can damage SWNTs.[65] Intermolecular, non-covalent bonding between the matrix polymer and π-electrons along unmodified CNTs can enable the integration of CNTs in polymer as well.[64]

Because the CNT aggregation will reduce the aspect ratio and surface area of CNTs for polymer reinforcement, the assessment of CNT exfoliation within the matrix polymer is of interest to those that study CNT reinforced polymers. Aggregation within mixtures of CNT/solvent or CNT/polymer/solvent has been investigated with ultraviolet-visible (UV-vis) spectroscopy. Semi-conducting materials, having a high aspect ratio, are known to exhibit van Hove singularities within the UV-vis absorbance spectrum; wherein each peak will represent the transition between valence and conduction bands.[66] Strong van Hove transitions are qualitative indicators of exfoliated CNTs.

In the study by Zhang et al., the aqueous dispersion of SWNT, sodium dodecyl sulfate (SDS), and poly(pyrrolidone) (PVP) (of 45, 16, and 75 mg/L, respectively) each

was processed with sonication and centrifugation to achieve isolated SWNTs, as noted by the van Hove transitions.[67] Changes in the aggregated structure of dispersed SWNTs were shown to influence the intensities and absorbance wavelengths of van Hove transitions. For example, films consisting of SWNT/SDS/PVP/PVA (at 1 and 5 wt.% SWNTs) exhibited van Hove transitions that were broader than those observed within the aqueous SWNT/SDS/PVP dispersion. This behavior suggests the SWNTs had aggregated within the PVA film. A similar behavior of SWNT re-aggregation had occurred as the dispersion of exfoliated SWNTs had undergone processing into as-spun fiber, according to Chae et al.[68] The presence of exfoliated SWNTs, within the PAN/DMF dispersion, was represented by van Hove transitions; nevertheless the SWNT composite of as-spun, undrawn fiber did not show forth any van Hove transitions. PAN/SWNT fiber that was stretched 16 X its length did exhibit an UV-vis spectrum of van Hove transitions. Therefore, the re-aggregation of exfoliated SWNTs can re-occur within solvent cast or coagulated composites.

CNTs were observed to axially align as the polymer composite was deformed to higher values of tensile strain; this was the result of stress transfer from the matrix polymer to embedded CNTs. Within the cast film of SWNT/SDS/PVP/PVA by Zhang et al., the frequency of the Raman G′-band varied with tensile strain as tensile stress would vary with the elongation of the bulk polymer. This behavior was suggestive of good load transfer between polymer and CNTs.[67]

The Herman's orientation parameter[7] has also been used to describe the molecular alignment of polymer crystals and the axial alignment of CNTs (namely, SWNTs) within stretched polymer composites or bulky paper of only carbon

nanotubes.[69-70] The Herman orientation factor for aligned SWNTs has been determined from the Gaussian or Lorentzian distribution models of vertical-vertical (VV) polarized, G^+-band intensities over 0 to 180º.[71]

1.4.3. Non-covalently Bonded CNTs

The molecular composition of polymers,[64, 72] the solubility parameters of solvents, [73] and the hydrophilic to lipophilic balance of surfactants[72, 74] have been used to manipulate the homogeneity of SWNTs within polymer solutions and composites. The review article by Bose et al. described studies of molecular π-π, π-cation, and CH-π bonding between carbon nanotubes and surfactants within matrix polymer. UV-Vis spectroscopy, Raman spectroscopy, IR spectroscopy, and X-ray photoelectron spectroscopy have been used to analyze changes in the electronic structure of CNTs that result from non-covalent interactions between SWNTs and their molecular environment.[63, 75] Polycyclic aromatic ring structures (such as SWNTs) have assumed the roles of π-acceptor and π-donor within a charge transfer complex.[76-77] Metallic SWNTs were shown to be more susceptible to charge transfer between themselves and the electron donating and withdrawing groups (EDWGs) of several aromatic/aliphatic solvents than semi-conducting SWNTs[63].

According to the WAXD analysis of SWNTs in the presence of anhydrous sulfuric acid, a crystalline interphase of sulfuric acid molecules formed along the SWNT axis at low temperatures.[78] SWNTs had influenced the preferential alignment of solvent molecules, was suggestive of hydrogen bonding between SWNTs and the adjacent molecules of sulfuric acid. Polarized IR spectroscopy has been used to investigate the orientation of functional groups, polymer chains within polymeric films

[79-81], fibers [82] and drawn nanocomposites.[83-84] Yuan et al. utilized IR dichroism to study the effects of MWNTs, within drawn composite films, on the preferential alignment of molecular groups that were characteristic of the matrix polymer. MWNTs were observed to impede the preferential alignment of main chain methylene groups and the pendant benzene rings of syndiotactic polystyrene along the film stretch direction.[83]

1.4.4. CNTs as Nucleating Agents

Further, CNTs have been shown to template polymer interphases and crystalline polymer (within sheared solutions, fibers, and oriented films).[42, 85-87] The crystallization kinetics of polymer melts is also affected by CNT incorporation.[71] This section will discuss literature on CNT/polymer interfaces, the nucleation-and-growth of crystalline polymer from the melt, and solution-gel transformations in response to CNT loading.

According to Coleman et al, the presence of CNTs nucleated the ordering of the polymer interphase, which happens to be a major contributor to the stiffness of CNT reinforced PVA.[88] In their study, PVA films (having a *DP* of 680-1,600) were embedded with different types of CNTs at low volume fractions of filler, V_{fCNTs}, ($\leq$1 wt.% CNTs). Both the Young's modulus (Y) and crystallinity (X_c) of PVA composites had scaled linearly with the V_{fCNT} of each CNT-type.[88] This behavior suggests the volume fraction of CNTs had affected the nucleation of ordered PVA. Further, the calculated thickness of the polymer interphase along different CNTs, which was calculated from plots of X_c versus V_{fCNT}, was shown to agree with the experimentally determined values of interphase thickness. The differential modulus and differential crystallinity of PVA with respect to the volume fraction of CNTs (dY/dV_{fCNT} and

dX_c/dV_{fCNTs}, respectively) had scaled linearly with each other, irrespective of CNT-type. Therefore, the structural reinforcement of polymers was attributed to the ability of CNTs to nucleate an ordered interphase of polymer.

Filler aggregation and imperfect interphases along the filler's surface will have an adverse effect on the modulus of CNTs/polymer composites.[89] Karevan et al. used phase imaging atomic force microscopy to investigate phases within composites of PP/CNTs and PP/exfoliated graphite nanoplatelets. The stiffness of the polymer interphase, between agglomerated filler and matrix polymer, was shown to decrease gradually along its width. In some instances, voids were detected in the region between the bulk polymer and filler interface. The aggregation of CNTs and voids both prevented the realization of CNT reinforcement, as predicted by mechanical models that assumed a perfect contact between exfoliated filler and polymer.

In the work by van Hutten et al., the crystalline morphology of gel-spun UHMWPE was transformed from shish-kebabs to densely packed fibrils of extended chain polymer as the incremental fiber draw ratio was increased from 5.6 to 80 X.[90] Gel-spun fibers that were prepared from 5 wt.% solutions of UHMWPE in paraffin oil had shown shish-kebab morphologies (i.e. PE fibrils decorated with periodic layers of lamellar PE) once they were hot-drawn by 5.6 X. Interestingly, shish-kebab morphologies have also formed within stationary dispersions of PE/MWNTs/p-xylene and nylon 6,6/MWNTs/glycerin.[91] For instance, isolated MWNTs behaved as rigid shish that were capable of nucleating the growth of lamellar PE crystals within PE/MWNT/p-xylene dispersions held at 103 ºC for 30 min. The periodic growth of

lamellar crystals along the axis of exfoliated CNTs had resulted in structures called nanohybrid shish-kebabs.[91-92]

The presence of CNTs has been shown to influence the temperature of isothermal crystallization and the conformation of polymer. Polyamide 6/MWNT composites were melt blended at 250 °C for 6 minutes under nitrogen and using a mixing rate of 200 rpm, in the work by Brosse et al.[93] The incorporation of 0-10 wt.% MWNTs into polyamide 6 caused the formation of crystals that would melt at higher temperatures and another crystalline form. The homogeneous dispersion of MWNTs was necessary to observe melting from two forms of crystalline polymer and the intense peak of higher T_m. The higher T_m peak was attributed to the perpendicular growth of lamellar polyamide 6 chains from the axis of MWMTs.

The nucleation-and-growth of crystalline PVA within dispersions and films of SWNTs has also been reported in the literature.[86, 88, 94] A solution of 1 wt.% PVA in 80/20 v/v DMSO/water and the corresponding 99:1 PVA/SWNT dispersion were sheared with 500 to 800 rpm at 55 ℃ for several hours.[86] PVA was shown to assemble into fibers of several microns that were composed of nanoscale fibrils. Fibrils observed within the fibers of homopolymer were on the order of 100-800 nm; whereas, fibrils from the PVA/SWNT dispersion were on the order of 10-100 nm. The molecular axis of crystalline PVA was reported to align itself at 36° off of the SWNT axis. The crystallinity of PVA within the PVA/SWNT system was 36% greater than the value reported for the homopolymer solution.

Probst et al. studied the effects of SWNT incorporation on the crystallization of molten PVA (DP_w of 3,400).[94] SWNTs, stabilized with the sodium salt of

decylbenzenesulfonic acid, were dispersed in aqueous solutions of PVA at 0.1 and 1 wt.% and subsequently sonicated for 3 hr. Samples were held at 235 ℃ for 1 min prior to cooling and nonisothermal crystallization. The PVA composite of 0.1 and 1 wt.% SWNTs exhibited crystallization temperatures that were ~5 ℃ higher than those observed for the neat PVA. Growth rates for crystalline PVA were highest among the composite of 0.1 wt.% SWNTs than for the neat film and sample of 1 wt.% SWNTs. The melting temperatures of 1 wt.% SWNTs films that were cooled from 235 ℃ at different rates were slightly lower than the values reported for films of homopolymer. Also, the thermal degradation of PVA, at temperatures near crystalline melting, was more pronounced in the composite of 1 wt.% SWNTs. In this study, the loading of 1 wt.% SWNTs catalyzed the thermal degradation of PVA and reduced the growth rate of crystalline polymer.

CNTs have also shown to influence the sol-gel transformation of precursor gels in preparing fibers and films. It has been shown that the type of CNTs within PVA polymer can influence the freezing temperature of solvent imbibed within the developing gel network. PVA gel fiber containing 1 wt.% SWNTs had shown evidence of solvent freezing post immersion into -25 °C MeOH; however, gels of 1 wt.% MWNTs and unfilled PVA did not exhibit any evidence of solvent freezing within MeOH chilled to -40 ℃.[42] In the Wang and Chen study of SWNT hydrogels (containing 0.01 to 0.2 wt.% SWNTs), CNTs appeared to hasten the RT gelation of Pluronic block copolymer in combination with cyclodextrin.[95] The rapid inclusion of polyethylene oxide (PEO) blocks of Pluronic copolymers into cyclodextrin linkers was accredited to the pre-organization of PEO blocks along SWNTs, which seemingly resulted from the sonication

and centrifugation of CNT/polymer dispersions. Polymer crystallization within UHMWPE/MWNTs was proposed to ensue from the surface of MWNTs.[96] Regions of gel polymer were believed to be adjoined by CNTs. However, in the same study, MWNTs were observed to decrease the rate of UHMWPE gelation.

1.5. SWNT Reinforced PVA Fibers

Researchers have investigated areas of PVA gel formation,[24, 44] fiber drawing, [12, 32, 43] and composite fibers of CNTs [97-99] to influence the microstructure and overall properties of gel-spun PVA fibers. SWNTs have been incorporated into polymer to behave as load bearing fillers for high strength, high modulus fibers. Upon the addition of 0.3-3 wt.% SWNTs to the matrix polymer, several researchers have reported overall enhancements in the mechanical performance of gel-spun PVA fibers. These property enhancements have been attributed in part to the dispersion and orientation of carbon nanotubes (CNTs) within fully drawn fibers and the interfacial crystallization of polymer along aligned CNTs.[68, 97]

The mechanical properties and gel-spinning conditions of some unfilled PVA fibers and SWNT embedded fibers are listed in Table 1.2. Xu et al. prepared high strength PVA/SWNT fibers of 2.2 GPa using 0.3 wt.% SWNTs and PVA, having a *DP* of 1,500.[98] High strength and high modulus SWNT composite fibers (of 2.6 GPa and 70 GPa, respectively) were prepared by Minus et al., using PVA having a *DP* of 18,000 and 1 wt.% SWNTs.[97] Fibers in both studies were composed of uniaxially aligned SWNTs, and each study gave evidence in support of strong interfacial adhesion between the PVA and SWNTs.

For instance in Xu et al., Raman spectra of PVA/SWNT dispersions, comprising 0.05, 0.1, and 0.3 wt.% SWNTs, revealed an upshift in the frequency of the SWNT G^+-band from that of pristine SWNTs.[98] Charge transfer between the PVA/DMSO carrier and SWNTs was acknowledged as the cause of that shift. Because of the adhesion between PVA and SWNTs, repeat washings of PVA-coated SWNTs with distilled water at RT could not remove PVA from the surface of SWNTs.[98]

In Minus et al., PVA fibers of high mechanical strength were shown to dissolve within DMSO at 85 °C; whereas the high strength, high modulus fibers of 99:1 PVA/SWNT were not completely dissolved in DMSO at 85 °C.[97] Further, TEM micrographs of the insoluble PVA/SWNT matter had revealed PVA fibrils along the surface of SWNTs. The wet shrinkage of 99:1 PVA/SWNT fiber in boiling water for 30 min was 11%, which is three times less than the shrinkage that was reported for neat fiber under the same conditions.[97]

Although the *TS* and *TM* of fibers reported in the study by Zhang et al. were lower than those observed in the studies by Minus et al. and Xu et al., their study did show evidence that the embedded SWNTs had mechanically and structurally reinforced gel-spun PVA fibers.[97-99] The *TS* and *TM* of gel-spun PVA/SWNT fibers, containing 3 wt.% SWNTs, were 1.1 GPa and 35.8 GPa, respectively.[99] These values were higher than the corresponding *TS* and *TM* of neat PVA fibers, which were 0.9 GPa and 25.6 GPa, respectively. The T_g and *alpha*-relaxation of crystalline polymer occurred at higher temperatures within the PVA/SWNT fibers than within the neat PVA fibers. These behaviors suggested the molecular mobility of PVA chains were constrained by the presence of SWNTs. The SEM micrographs had revealed bundles of SWNTs that were

coated with PVA, at the fracture tip of the composite fiber. The width of PVA coated SWNTs were ~20 nm in diameter.

Table 1.2. Mechanical Properties of PVA and PVA/SWNT Fibers.

PVA-Fiber Techniques	**Hydrolysis (%)**	***DP***	**Total DR**	***TS*** [a] **(GPa)**	***TM*** [b] **(GPa)**
10 wt. % PVA in 80/20 DMSO:H_2O; Gelation in MeOH at -20 ℃; Drawn at S1/160 [c] and then S2/200 [12]	99.5	5,000	50	2.8	64
3 wt. % PVA in 80/20 DMSO:H_2O; Gelation in MeOH (MeOH) at -70 ℃; Coagulation in MeOH for 24 hrs at -70 ℃; Drawn at S1/00, S2/160, S3/200, S4/290[97]	98.4	18,000	6.9 [d]	1.6	47
10 wt. % PVA in 100 % DMSO; Gelation in MeOH at ~ -10 ℃; Coagulation in MeOH for 24 hrs at RT; Drawn at 220 ℃[98]	99.9	1,500	26	1.7	28
PVA/SWNT Fiber Techniques	**Hydrolysis (%)**	***DP***	**Total DR**	***TS*** **(GPa)**	***TM*** **(GPa)**
99:1 PVA:SWNT 3 wt. % PVA in 80/20 DMSO:H_2O Gelation at -70 ℃ in MeOH Coagulation in MeOH for 24hrs at -70 ℃; Drawn at S1/100, S2/160, S3/200, S4/290 [97]	98.4	18,000	14 [d]	2.6	70
99.7:0.3 PVA:SWNT 10 wt. % PVA in 100% DMSO Gelation ~-10 ℃ in MeOH; Coagulation in MeOH for 24 hrs at RT; Drawn 220 ℃[98]	99.9	1,500	23	2.2	36

a) *TS* = tensile strength, b) *TM* = tensile modulus, c) S#/# = sequence of stage drawing and its temperature in Celsius degrees, and d) *DR* = cumulative heat draw ratio.

1.6. Thesis Objectives

Interestingly, researchers have revealed marked improvements in the mechanical properties of gel-spun PVA/CNT fibers (having loadings of ≤1 wt. % SWNTs).[97-99] Due to the high price of CNTs, the formation of high performance fibers from low weight fractions of CNTs would be ideal. The process of gel fiber aging was integrated into the gel-spinning method in an attempt to increase the *DR* of PVA/CNT fibers and to induce the formation of microphases that would be conducive to the fabrication of strong fibers. The use of gel aging to prepare high strength, high modulus tapes of neat PVA has been published;[32] however, the publication of any work that has attempted to prepare PVA/CNT fibers by the gel aging technique is currently unknown. The ability of CNTs to nucleate the ordering of polymer upon gelation and fiber drawing was studied throughout this investigation as well.

The goals of this study were to

1. Identify phases residing in PVA/CNT composite fibers and specify the effects of CNTs on the microstructure/properties of drawn fibers.
2. Investigate the nucleating effects of CNTs on the gelation of PVA/CNT dispersions at subzero temperatures.
3. Understand the effects of CNTs on the structure/properties/processing of fibers drawn from aged gels.

CHAPTER 2

EFFECTS OF CARBON NANOTUBES ON THE MICROSTRUCTURE OF DRAWN FIBERS

2.1. Introduction

Several stages of elevated temperature drawing were applied to the fabrication of gel-spun PVA fibers,[12, 43] as well as their CNT composites[97]. The mechanical reinforcement of polymer using CNTs has been attributed to the transfer of mechanical stress from the matrix polymer onto inherently strong CNTs and the structural reinforcement of polymer by CNTs.[88]

This chapter explores the mechanical properties of composite fibers and the development of fiber microstructure, with respect to SWNT incorporation and sequential drawing. Gel-spun PVA and PVA/SWNT fibers were stretched in 2-4 stages of elevated temperature drawing and to similar values of *DR*. Furthermore, the effects of SWNT orientation on the preferential alignment of PVA functional groups and imbibed solvent have been studied. The molecular adhesion between SWNTs and functional groups within the matrix polymer were investigated using spectroscopy and the density functional theory.

2.2. Experimental Section

2.2.1. Fiber Preparation

Spinning dopes were prepared from 3 wt.% aPVA that was dissolved in a mixture of DMSO (Aldrich) and deionized water at ≈85 °C. PVA had a *DP* of 18,000 and was 98.4% hydrolyzed (lot # 636837 by Kuraray Co. Ltd). SWNTs (lot # P0247 by CNI

having a purity of >98%) were sonicated in DMSO (at 0.4 mg SWNTs per mL of DMSO) using the Fisher Scientific bath at 43 kHz and 150 W for 24 hrs. SWNT dispersions were blended into PVA solutions by means of mechanical stirring. The overall v/v of DMSO/water within the final PVA and PVA/SWNT spinning dopes was 80/20. The weight ratio of PVA to SWNT within the composite fiber was 99:1.

The spinning dope was pumped through the 18 gauge (i.e. 1 mm diameter) syringe that was placed 2-5 mm above the chilled MeOH spinning bath. Gel-fiber was spun in the -20 °C MeOH bath, taken-up, and subsequently stored in a MeOH coagulation bath at -78 °C for 24 hrs. Batches of gel-spun fiber were drawn in the following sequence of stages/hotplate temperatures: S1/100, S2/160, S3/200, and S4/290. The draw ratio was determined as the speed of the take-up roller divided by the speed of the feed roller. The reported cumulative *DR* was actually the product of draw ratios from each stage of drawing.

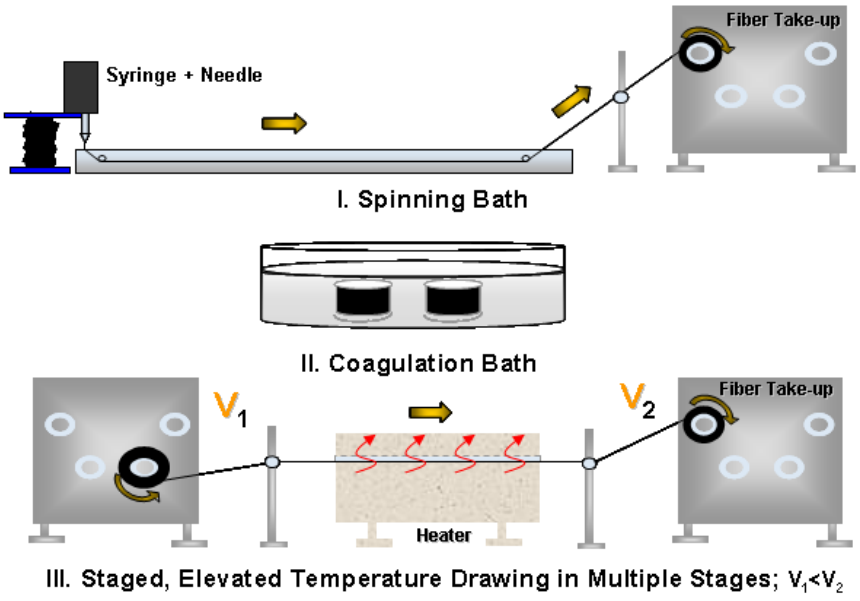

Figure 2.1. Fabrication of gel-spun fibers.

2.2.2. Mechanical Testing

The *TS*, *TM*, and strain at break of PVA and SWNT composite fibers were measured using the rheometrics solids analyzer, RSA III by Rheometics Scientific Co. Mechanical testing was performed at RT using a gauge length of 25.4 mm and at a strain rate of 0.1 %/sec.

The effective fiber diameters (φ_f) were determined from measurements of fiber density. Values of fiber weight (w_f) were taken from predetermined lengths (l) of at least 300 cm of fiber. The value of X_c was determined from the WAXD analysis of bundled fibers. The densities of amorphous and crystalline PVA were ρ_a=1.269 and ρ_c=1.345 g/cm^3, respectively.[97] The values of the aforementioned parameters were substituted into Equation 2.1, to calculate φ_f. An error of ≈10% was associated with the calculation of fiber diameter.

$$\varphi_f = \left[\frac{4w_f}{\pi l} \left(\frac{X_c}{\rho_c} + \frac{1 - X_c}{\rho_a} \right) \right]^{1/2} \qquad (2.1)$$

2.2.3. Thermal Analysis

The following tests were used to conduct the thermal analysis: thermomechanical analysis (TMA) on the TMAQ400, DSC on the DSC Q200, and thermogravimetric analysis (TGA) on the TGA 5000 (all from TA Instruments).

2.2.3.1. Thermal Shrinkage

The thermal shrinkage of PVA and PVA/SWNT fibers, as a function of drawing stage, was performed on the TMA. Fibers were heated from RT to 200 ºC at 5 ºC/min and with a constant stress of 2.5 MPa in argon. The applied stress was below the yield

stress of each tested fiber. The yield stress of fibers was determined from stress-strain curves.

2.2.3.2. DSC

Fiber bundles of 0.4 to 1 mg were prepared in aluminum standard pans for DSC analysis. Modulated differential scanning calorimetry (MDSC) experiments were performed to resolve overlapping transitions through the application of cyclical heating and/or cooling [100-101]. Reversing (R-) heat flow curves revealed transitions in which the applied heating rate ($\beta=dT/dt$) was directly related to the total heat flow (dQ/dt); e.g., the T_g and crystalline melting [100-102]. The subtraction of R-heat flow from total heat flow had given the non-reversing (NR-) heat flow. NR-heat flow was derived from kinetic events- which are functions of absolute temperature and time; e.g., evaporation, crystallization, and degradation [100-101].

MDSC experiments were conducted as follows: equilibration at -20 ℃, modulation of ± 0.796 ℃ of the average temperature every 60 seconds, and a temperature ramp up to 300 ℃. The average rate of heating was 5 ℃/min in nitrogen. The presented thermograms were all from the first heating cycle of a DSC run. The T_g of fibers was obtained from the first heating cycle of the reversing heat flow curve.

2.2.3.3. TGA

Gel-spun fiber, PVA powder, and 80/20 DMSO/water (at 0.85-1.5 mg) were prepared for TGA. Samples were tested in a platinum holding pan. Heating was performed at 10 ℃/min in nitrogen gas. Differential thermogravimetric analysis (DTGA) had assisted the tracking of weight loss that was due to solvent evaporation and polymer degradation.

2.2.4. WAXD Analysis

WAXD was performed on the Micro Max 002 X-ray generator and R-axis VI++ detector by Rigaku. Instrument settings included 45 kV power and a current of 0.66 mA. Fiber bundles of 15 or more fibers were used for WAXD analysis. The unit cell orientation of crystalline PVA (f_b) within PVA and PVA/SWNT fibers was determined according to methods described in Minus et al. and Wilchinsky; wherein azimuthal scans of the (200) and (101) diffraction planes (for $-90 \leq \kappa \geq 90$) were used to calculate the values of $<\cos^2\kappa>$, and $I(\kappa)$ represented the intensity of X-ray diffraction at angle κ (see Equations 2.2 and 2.3).[86, 103]

$$f_b = \frac{3}{2} < \cos^2 \kappa > -\frac{1}{2} \tag{2.2}$$

$$< \cos^2 \kappa >= \frac{\int_{-\pi/2}^{\pi/2} I(\kappa)\cos^2 \kappa \sin \kappa d\kappa}{\int_{-\pi/2}^{\pi/2} I(\kappa)\sin \kappa d\kappa} \tag{2.3}$$

2.2.5. Spectroscopic Analysis

2.2.5.1. Raman Spectroscopy

The polarized Raman spectrometer (by Kaiser Optical Systems Inc.) equipped with a 1.58 eV (785 nm) laser was used to analyze fibers of PVA/SWNT. Spectra were collected with laser power of 60 mW at 1 s exposure times, and 40 spectral accumulations. Fiber bundles were rotated from -90 to +90º about the optical axis in VV mode. The fiber axis was initially placed perpendicular to the optical axis.

The polarized Raman intensities of SWNT G^+-bands were normalized by the highest Raman intensity and fitted according to Equation (2.4) using Origin Pro 8.1. In Equation (2.4), the Raman G^+-band intensities were given as a function of polarization,

I(ψ)- represented the difference between the recorded Raman intensity (*y(ψ)*) and constant background (y_0). *I(ψ)* was fitted by a Gaussian distribution having peak height (*h*) and full width at half maximum (*w*). The *w* was used to describe the orientation of SWNTs from Gaussian fits. The misalignment of the fiber/SWNT axis of symmetry, with respect to the polarization direction of the incident laser beam, was corrected with ψ_c.

$$y(\psi) - y_0 = h \cdot \exp \frac{(\psi - \psi_c)^2}{2w} \tag{2.4}$$

2.2.5.2. IR Spectroscopy

The AutoIMAGE System and gold wire grid polarizer- L186-0408 (by Perkin Elmer Instruments) was used to perform polarized IR analysis. Spectra were collected using 256 scans at a resolution of 4 cm^{-1}. The collected spectra were subjected to constant baseline subtraction and normalized to the 1456 cm^{-1} peak[104-105] for further analysis. The dichroic ratio (*D*) was experimentally determined from polarized absorbance values (*A*) at 0 and 90º, as given in Equation (2.5).

$$D = \frac{A_{\theta=0^\circ}}{A_{\theta=90^\circ}} \tag{2.5}$$

The fraction of molecular moieties that exhibited preferential alignment was described using Fraser's relationship (Equation 2.6), between the dichroic ratio (*D*) and the fraction of functional groups (*x*), having a transition moment along the angle (θ) relative to the fiber axis. The polarized beam for θ=0º was assumed to be in parallel with the fiber/optical axis.[103] The remaining functional groups (1-*x*) were assumed to be unoriented.

$$D(\theta, x) = \frac{x\cos^2\theta + \frac{1}{3}(1-x)}{\frac{1}{2}x\sin^2\theta + \frac{1}{3}(1-x)} \quad (2.6)$$

IR measurements were also performed on as-received PVA powder, unfilled PVA fibers, and PVA/SWNT composite fibers that were thermally treated and pelletized in potassium bromide (KBr). Thermal treatments were performed using the TGA.

2.2.6. Molecular Modeling

The interactions between SWNTs and functional groups were studied using the spin-unrestricted density functional theory (DFT) by employing the generalized gradient approximation (GGA), Perdew-Burke-Ernzerhof (PBE) functional,[106] and the double numerical plus polarization (DNP) basis set in DMol^3[107-108] under periodic boundary conditions.

First, a single metallic (6,6) SWNT, having a diameter of 0.814 nm, was placed in the presence of one molecule of either 1,3,5-hexane triol, 1,3,5-hexane triacetate, water, or DMSO. Then, energy minimization was performed to optimize the structure of the SWNT-adsorbate complex, to calculate the charge transfer, and determine the binding energy. The charge transfer was calculated using the Mulliken population analysis,[109] which divides the electrons to the basis functions of the atoms connected through the bonds. The binding energy ($\Delta E_{binding}$) was determined by Equation 2.7. $E_{SWNT-adsorbate}$, E_{SWNT}, and $E_{adsorbate}$ denoted the energy of the entire system in which the adsorbate molecule was bound onto the SWNT, the energy of bare SWNT, and the energy of adsorbate, respectively. Thus, the adsorption was favorable if $\Delta E_{binding} < 0$.

$$\Delta E_{binding} = E_{SWNT-adsorbate} - (E_{SWNT} + E_{adsorbate}) \quad (2.7)$$

2.3. Results and Discussion

2.3.1. Mechanical Properties

The mechanical properties of gel-spun PVA and SWNT composite fibers (prepared according to Figure 2.1) were listed in Table 2.1. The series of PVA fibers had showed a greater resistance to mechanical deformation with additional drawing; also, the cross sections of PVA fibers had decreased with sequential drawing. The mechanical properties of PVA/SWNT S4/290 drawn fibers were counter-intuitive; higher strength and modulus values typically correlate with higher values of *DR*. This behavior will be discussed upon the determination of PVA/SWNT S4/290's fiber microstructure.

The incorporation of SWNTs and sequential drawing also influenced the thermal shrinkage of gel-spun fibers, as shown in Figure 2.2. PVA/SWNT fibers had exhibited less shrinkage than PVA fibers that were drawn to similar values of *DR*. Therefore, SWNTs must inhibit the relaxation of PVA chains at elevated temperatures; this behavior of SWNTs was similarly reported in Zhang et al. and Minus et al.[97, 99]

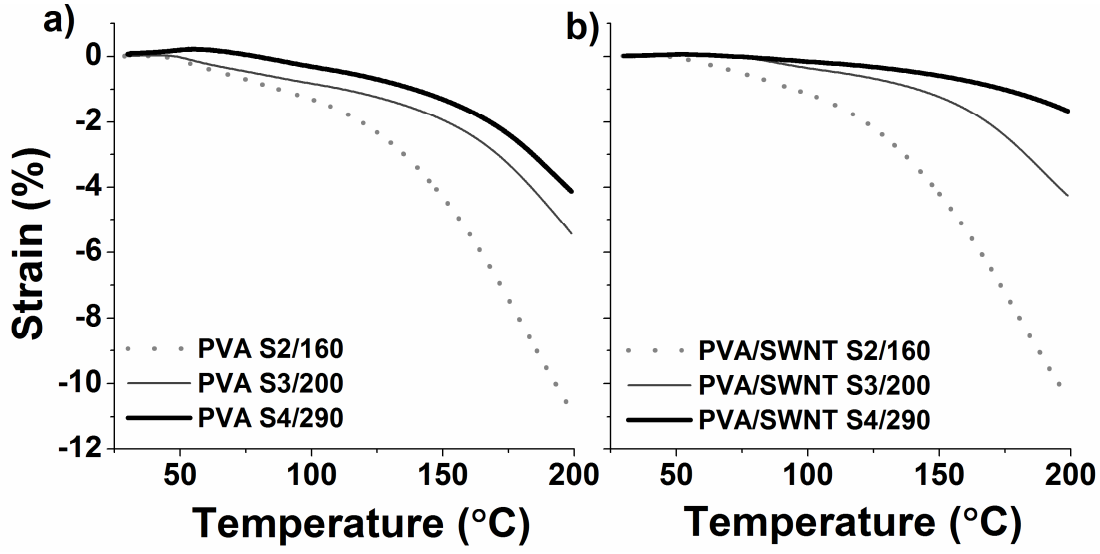

Figure 2.2. Effects of drawing stages on the thermal shrinkage of a) PVA and b) PVA/SWNT Fibers.

Table 2.1. Mechanical Properties of PVA and PVA/SWNT Fibers with Sequential Drawing.

Sample Designation		**PVA Fibers (Drawn In Series)**			**PVA-SWNT Fibers (Drawn In Series)**		
Processing	**Total Draw Stages/ Final Draw Temp (°C)**	**S2/160**	**S3/200**	**S4/290**	**S2/160**	**S3/200**	**S4/290**
	DR **[a)]**	4.1	5.2	7.5	3.7	4.5	7.3
Properties	φ_f **[b)] (μm)**	25	23	19	29	24	24
	TS **[c)] (GPa)**	0.81 ± 0.04	0.94 ± 0.05	1.0 ± 0.01	0.61 ± 0.05	0.68 ± 0.06	0.55 ± 0.05
	TM **[d)] (GPa)**	26 ± 2	29 ± 2	31 ± 2	24 ± 3	21 ± 2	18 ± 2
	Strain at Break (%)	6.3 ± 0.4	5.7 ± 0.5	5.9 ± 0.6	5.3 ± 0.4	4.8 ± 0.4	5.3 ± 0.4

a) $DR = DR_{Stage1} \times DR_{Stage2} \times DR_{Stage3} \times DR_{Stage4}$ and the cumulative heat draw ratio, b) φ_f = the diameter of fibers, c) *TS* = tensile strength, and d) *TM* = tensile modulus.

2.3.2. PVA Microstructure

The crystalline microstructures of unfilled and CNT composite fibers were characterized to understand the effects of stage drawing on the mechanical properties of gel-spun fibers (as reported in Table 2.1 and Figure 2.2). The crystalline phase within gel-spun fiber was characterized by WAXD (Table 2.2). The size of PVA crystals were shown to grow with sequential drawing. The growth of PVA crystals with stage drawing had led to the increase in mechanical properties and the fiber's resistance to thermal shrinkage. Cappacio similarly observed less thermal shrinkage from UHMWPE fibers that were drawn to higher values of *DR* and possessed thicker crystals.[110] The crystal size (*XS* in Table 2.2) of PVA crystals had increased with *DR*, but the X_c decreased for unknown reasons.

The measurements of T_m for stage-drawn PVA and PVA/SWNT fibers were similar, ≈229 °C (according to total heat flow and R-heat flow curves in Figure 2.3). The crystallinity of fibers was not calculated from DSC thermograms due to thermal degradation of PVA that can occur at temperatures above 200 ℃ (as observed from TGA curves in Figure 2.4a). WAXD analysis was used instead to calculated values of X_c (Table 2.2.). High temperature shoulders along the prominent melting peak became more noticeable with higher values of *DR*. Suzuki et al. had observed a high temperature shoulder along the prominent melting peak of gel-spun PVA fibers. In that study, the PVA used had a *DP* of 7,000 and fibers were stretched to a *DR* value of 20 X[33]. Cha et al. and Tanigami et al. also reported double melting peaks and melting temperatures above 230 °C among high strength and high modulus fibers [12, 32]. Therefore, the high

temperature shoulders that were observed among S4/290 fibers were associated with the formation of ECC[33].

Table 2.2. WAXD Characterization of PVA and PVA/SWNT Fibers.

Sample Designation	**PVA Fibers (Drawn in Series)**			**PVA/SWNT Fibers (Drawn in Series)**		
Total Draw Stages/ Final Draw Temp (°C)	S2/160	S3/200	S4/290	S2/160	S3/200	S4/290
DR [a] **(X)**	4.1	5.2	7.5	3.7	4.5	7.3
X_c [b] **(%)**	61	54	56	56	51	47
	XS [c] **(nm)**					
(100)	4	5	6	5	5	7
(001)	8	8	13	8	8	13
(110)	5	11	11	5	11	12
(111)	5	8	10	5	8	9
(211)	5	6	7	5	6	7

a) *DR* = the cumulative heat draw ratio, b) X_c = the volume fraction of crystalline polymer, and c) *XS* = crystal size.

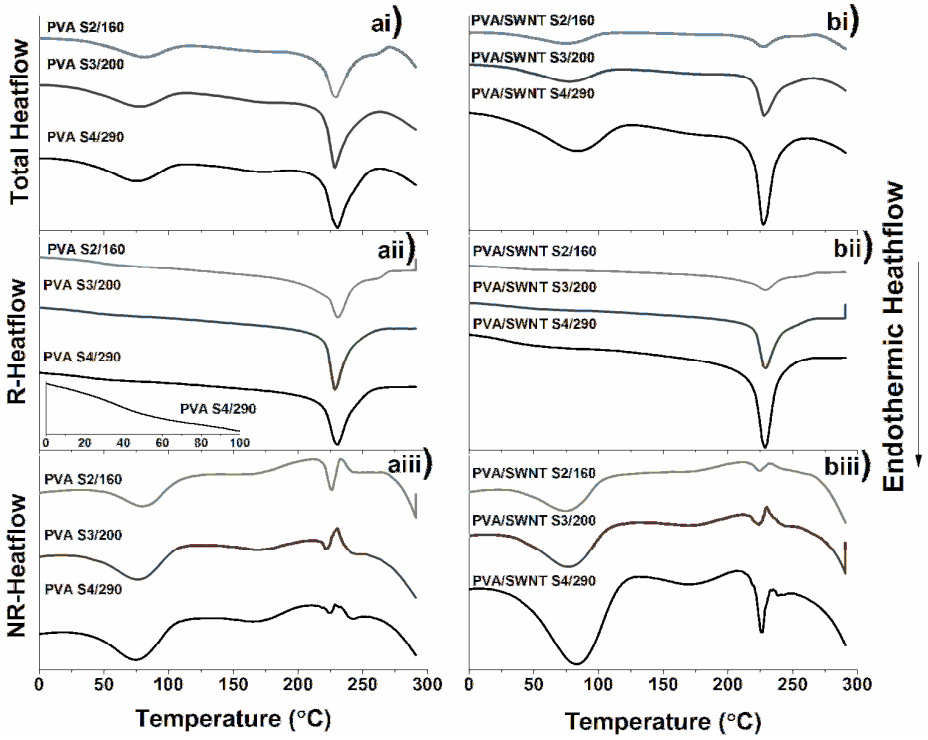

Figure 2.3. MDSC thermograms of a) PVA and b) PVA/SWNT fibers: i) total heat flow, ii) R-heat flow, and iii) NR-heat flow.

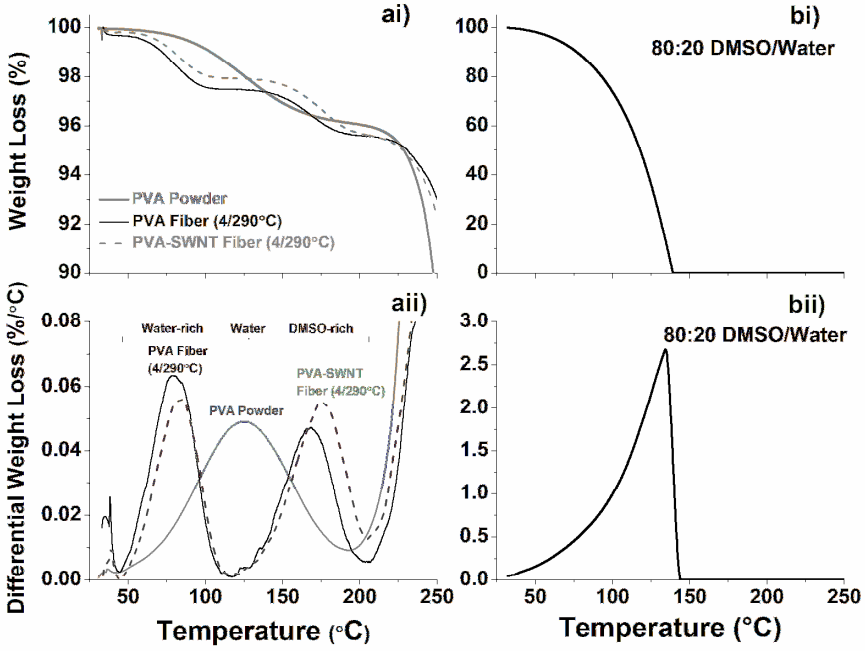

Figure 2.4. Thermographs of a) solvent evaporation from as-received PVA powder, control PVA, and PVA/SWNT fibers that were drawn at 7.5 X and 7.3 X, respectively, and b) 80/20 DMSO/water evaporation by i) TGA and ii) DTGA.

PVA and PVA/SWNT fibers had lost ~4.5% of their weight when heated up to 200 ℃, regardless of drawing stage. The evaporation of solvent from S4/290 fibers had revealed two mechanisms of weight loss (from 25-200 °C in Figure 2.4a); whereas, the 80/20 solution of DMSO/water had a single mode of evaporation, whose rate had peaked at 134 ℃ (Figure 2.4b). The evaporation of solvent from fibers represented two distinct phases of solvent: a water-rich phase[111] and a DMSO-rich phase. These phases evaporated at peak temperatures of ~82 ℃ and ~172 ℃, respectively according to DTGA in Figure 2.4aii. Endothermic peaks from the total and NR-heat flow thermograms (Figure 2.3) coincided with those DTGA transitions. Guerrini et al. attributed a similar endothermic peak, which ranged from 4 to 129 ℃, to the evaporation of water from PVA [112]. Although, the weight fractions of residual water and DMSO did not change with draw ratio, the heat capacities of these transitions did change with draw ratio (Figure 2.3). Therefore, endothermic peaks below 200 ℃ were believed to include the relaxation of polymer chains upon solvent evaporation.

The reversing mode enabled clear delineation of the polymer's T_g. Due to the presence of solvent within amorphous PVA, T_g values ranged from 32-45 ℃ (Figure 2.3aii). The reported T_g of dry PVA was ~ 85 °C.[35, 113]

2.3.3. IR Spectroscopy of PVA Fibers

Crystalline and amorphous PVA absorbed in the 950-1175 cm^{-1} frequency range (Figure 2.5, 2.6 and Table 2.3). Gaussian peak deconvolution was used to separate contributions from the PVA conformations in crystalline and amorphous domains. The deconvoluted results were shown in Figure 2.6, where the fitted peaks at 1141 cm^{-1} and higher were attributed to crystalline chain conformations of PVA and the fitted peaks at 1087-1097 cm^{-1} represented amorphous PVA (Table 2.3).[40, 114-115] The remaining deconvoluted peaks in Figure 2.6 were identified in Table 2.3.

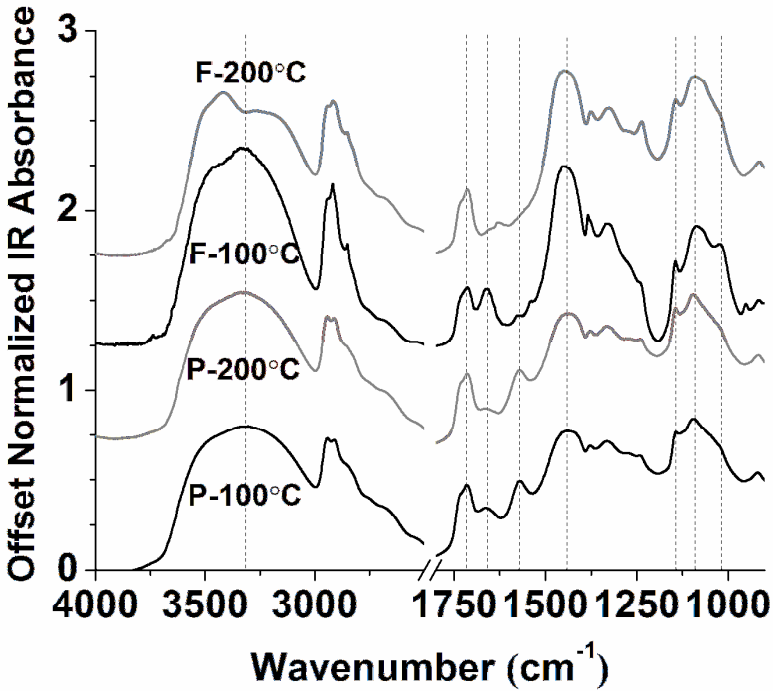

Figure 2.5. IR spectra of PVA powder (P) and fiber (F). Both the powder and the fiber samples were heated from RT to 100 and 200 °C at 10 °C/min in nitrogen, cooled to RT, and made into pellets of KBr.

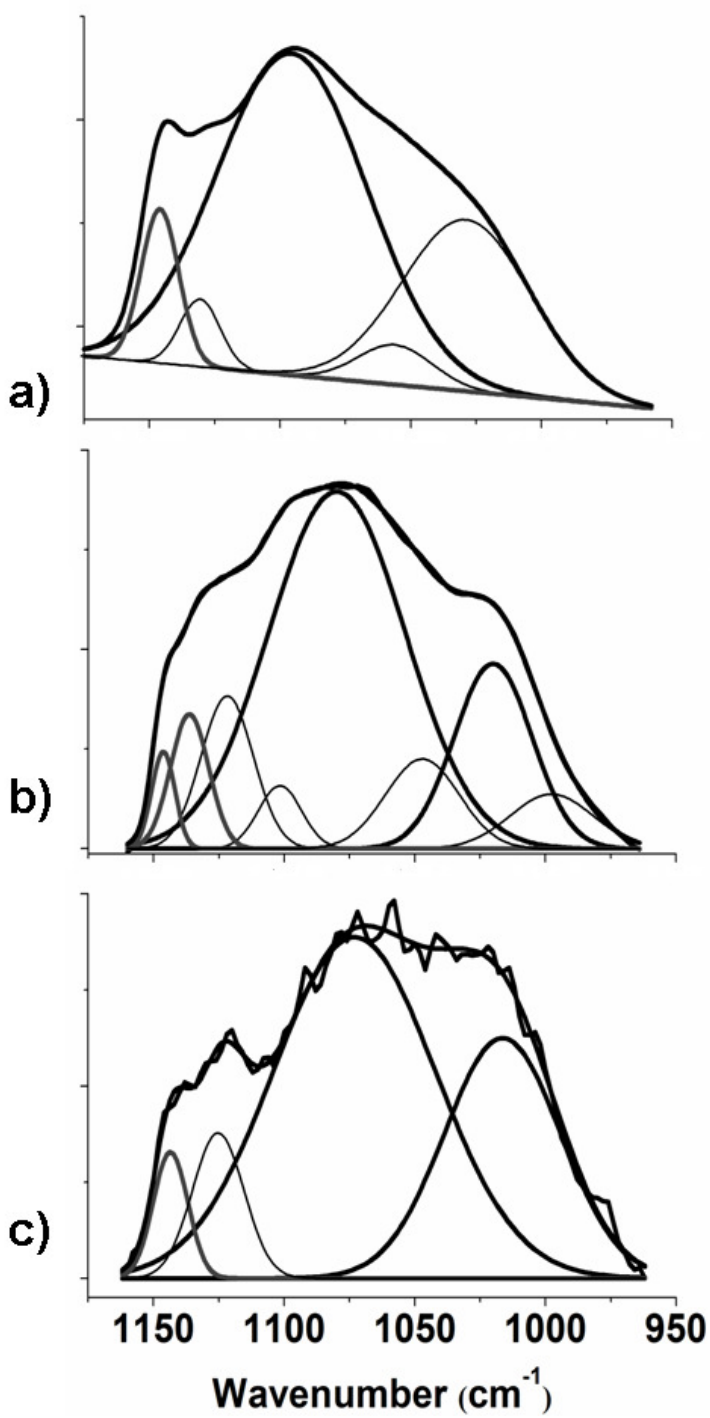

Figure 2.6. Gaussian deconvolutions of IR Spectra had ranged from 950-1175 cm^{-1}: a) as-received PVA powder, b) S4/290 PVA fiber, and c) S4/290 PVA/SWNT fiber. For the b) and c) spectra, IR beam was polarized perpendicular to the fiber axis. Heavily outlined, absorbance peaks represented crystalline PVA conformations (≥ 1141 cm^{-1}), amorphous PVA conformations (1073-1096 cm^{-1}), and DMSO (1016, 1020 cm^{-1}).

Table 2.3. Identification of FTIR peaks in PVA-Based Fibers.

Wavenumber (cm^{-1})	Peak Identification	Comments
3000-3750	(vs, -OH)	The observed absorbance was due to –OH stretching from water, PVA, and hydrogen bonding between –OH groups. Free –OH groups, which were not engaged in hydrogen bonding and will absorb at higher wavenumbers. [116-118]
~1721	(sh, C=O) Stretching	The absorbance shoulder along the 1714 cm^{-1} peak was indicative of acetate groups.[117, 119-120]
1714	(s, C=O) Stretching	Carbonyl absorbance was due to presence of acetic acid impurities or possibly molecular oxidation[111] in the as-received PVA powder[117, 121].
1656-1665	(s, H-O-H) Water Bending	H-O-H bending vibration from imbibed water was influenced by hydrogen bonding and the formation of molecular complexes.[117, 122] Water removal was evident upon heating PVA from 100 to 200 ºC, as shown by the depression or disappearance of the H-O-H bending vibration in Figure 2.5.
~1560	(s,$CH_3COO^-K^+$)	Coordination between residual acetic acid in the PVA powder and potassium ions of the KBr matrix yielded potassium acetate. [116-117]
1456	(vs, -CH_2-)	CH_2 and possibly OH bending band among alcohols[104]
1141-1144, 1150	(sh, PVA Chain)	Indicative of the conformation of PVA chains in the crystalline region.[40, 114-115]
1073-1125	(s, PVA Chain)	The conformation of PVA chains in the amorphous region was affected by solvation and orientation.[40, 114-115]
1014-1058	(sh, S=O) Stretching	-S=O stretching originated from residual DMSO contained within drawn fibers. IR absorbance ranging from 1045 - 1014 cm^{-1} was indicative of intermolecular bonding between DMSO and other chemicals; concentrated DMSO molecules absorbed at higher wavenumbers.[123] DMSO removal was evident upon heating fiber from 100 to 200 ºC, was shown in Figure 2.5 by the depression of S=O stretching vibration features in Figure 2.5.
998-1056	(sh, -CH_2-)	Skeletal vibrations[124]

Peak intensities were described as vs for very strong, sh for shoulder, and s for strong.

The IR absorbance from pendant PVA hydroxyl groups, ν_s(-OH), occurred between 3000-3750 cm^{-1}. The -OH stretching peak from PVA powder had narrowed upon heating from 100 to 200 ℃ (Figure 2.5). The absorbance shoulder at ~1721 cm^{-1} in Figure 2.5 has been attributed to the presence of unhydrolyzed acetate carbonyl side-groups.[120] The stretching vibration of acetate carbonyl groups at ~1721 cm^{-1} has also been used to suggest hydrogen bonding between these functional groups and proton donors.[119] The carbonyl peak for pendant acetate groups (C_2H_3OO) shouldered a more intense peak (ranging from 1714-1716 cm^{-1}), which has been identified as acetic acid (CH_3COOH). Acetic acid was an impurity from the conversion of PVAc into PVA (Scheme 1.1). Absorbance at ~1714 cm^{-1} has suggested acetic acid was engaged in molecular complexes.[116-117, 121] Hydrogen bonding between acetic acid and other molecules may have caused its evaporation temperature to increase. Acetic acid remained in the PVA powder and fibers above its boiling temperature, as evidenced by the spectra in Figure 2.5. Spectra of PVA powder in KBr showed absorbance peaks at ~1560 cm^{-1}, which were not observed in the KBr pellets of fibers. Since carboxylic acid can form potassium carboxylate when pelletized in KBr,[116] that peak was attributed to the formation of potassium acetate. Acetic acid in the core of PVA fiber would be less susceptible to complex formation with KBr, as confirmed by the spectra in Figure 2.5.

Imbibed water and DMSO have been identified from IR spectra in Figures 2.5 and 2.6. The absorbance peaks for imbibed water occurred around 1656-1665 cm^{-1} and for DMSO around 1016-1047 cm^{-1}, respectively. The intensities of these peaks diminished upon heating gel-spun fiber PVA S4/290 from 100 to 200 ℃, as shown in Figure 2.5. The vibrational frequencies of water and DMSO were influenced by hydrogen bonding

and molecular complexing with metal ions or EDWGs.[125] The bending frequency of water, v_δ(H-O-H), imbibed within PVA powder occurred at ~1650 cm^{-1};[117] however, spectra of gel-spun PVA fibers have shown the bending frequency for water at 1665 cm^{-1}. Therefore, the bending frequency of water was influenced by the presence of a co-solvent; the complexing of water with DMSO has been reported to exhibit an IR peak at 1663 cm^{-1}.[122] Molecular interactions between water molecules and PVA were also believed to influence the IR frequency of imbibed water.

Intermolecular bonding between DMSO and proton donating groups was confirmed by the 1016 and 1020 cm^{-1} absorbance frequencies (Figure 2.6b,c). These frequencies have been indicative of hydrogen bonding via the oxygen atom of the sulfoxide group, i.e. O-coordination.[123, 125] According to Bertoluzza *et al*, the sulfoxide stretching frequency, v_s(S=O), shifted to lower frequencies from 1058 cm^{-1} as DMSO dimers were diluted with water. When the water/DMSO molar ratios ranged from 1 to 20, the sulfoxide stretching frequency gradually shifted from 1014 to 1045 cm^{-1}.[123] The deconvoluted IR spectra of gel-spun PVA and PVA/SWNT fibers (in Figure 2.6b,c) gave evidence of O-coordination by DMSO.

IR spectra of PVA and SWNT composite fibers (Figure 2.7) revealed that the intensities of several IR bands exhibited anisotropy about the fiber axis. The following sections will explore molecular anisotropy as a function of fiber drawing and SWNT orientation.

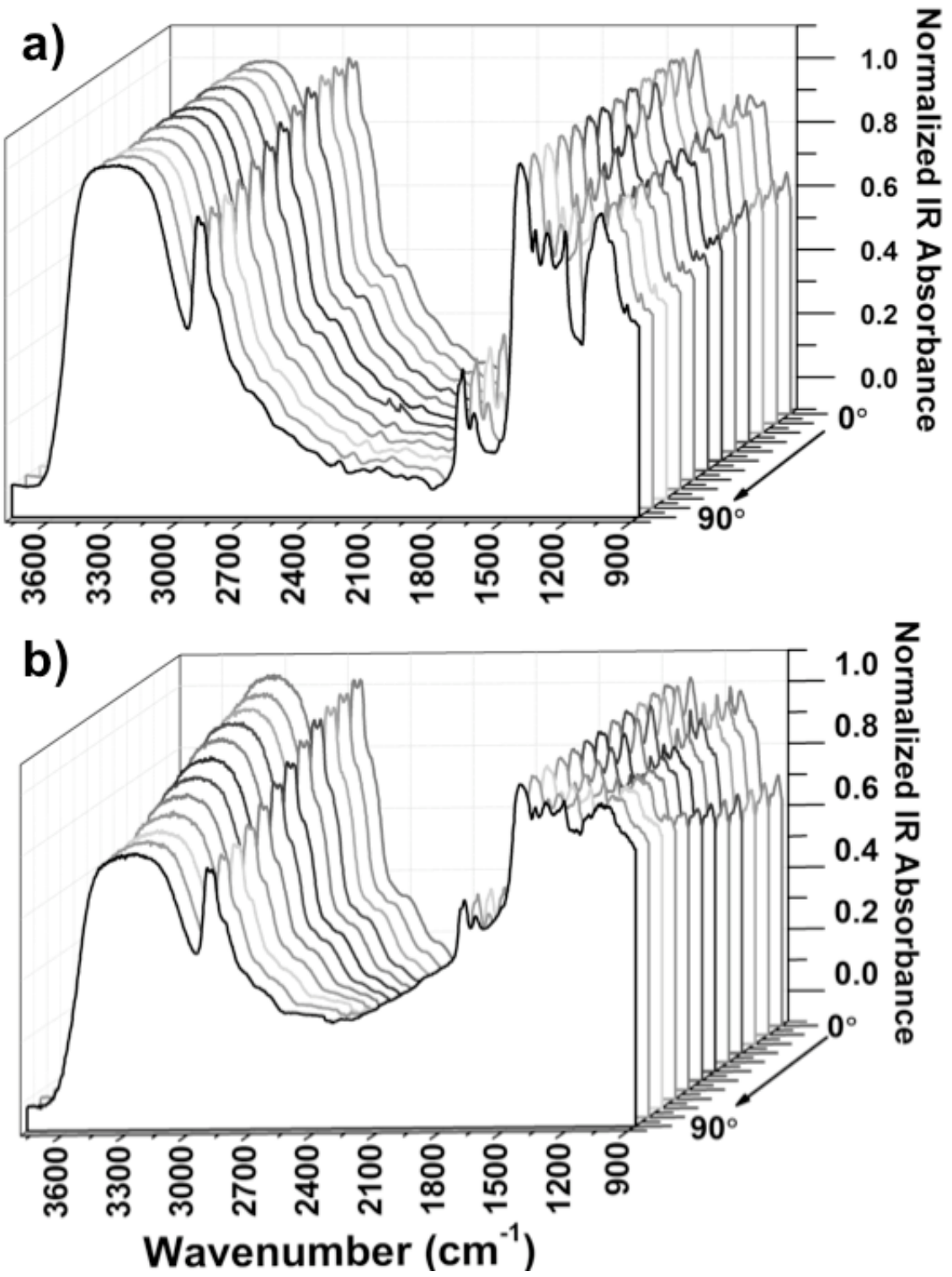

Figure 2.7. Spectra of a) PVA and b) PVA/SWNT 4/290 drawn fibers with IR polarization angles of 0, 5, 10, 20, 30, 40, 50, 60, 70, 80, 85, and 90° from the fiber axis.

2.3.4. SWNT Influenced Molecular Orientations

2.3.4.1. Orientation of Embedded SWNTs

The Raman G^+-band intensities for SWNT orientation, as fitted with Equation (2.4), were shown in Figure 2.8. The Gaussian fit parameters, which describe the alignment of embedded SWNTs, were listed in Table 2.4. The orientation of embedded SWNTs had increased with consecutive stages of drawing, as noted by decreasing values of *w*.

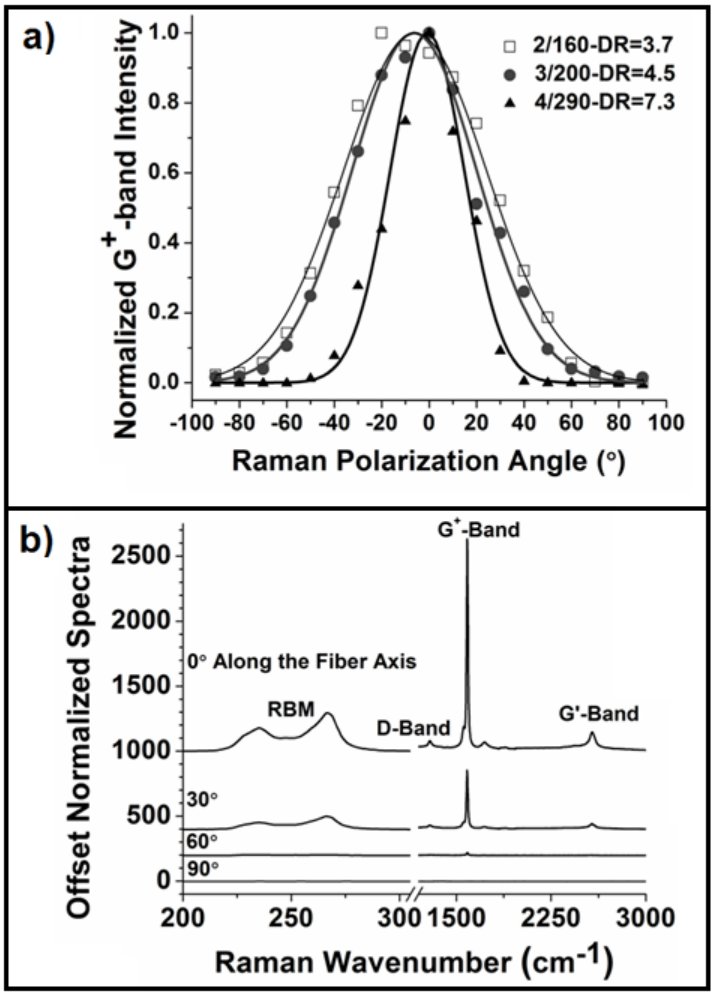

Figure 2.8. Polarized Raman of PVA/SWNT fibers a) SWNT G^+-band intensities as a function of Raman polarization angles for samples having different *DR* values, and b) Raman spectra for S4/290 fiber at polarization angles of 0, 30, 60, and 90°.

Table 2.4. PVA and SWNT Orientation Parameters.

	Total Draw Stages/ Final Draw Temp (°C)	S2/160	S3/200	S4/290
PVA	***DR*** [a] **(X)**	4.1	5.2	7.5
	φ_f [b] **(μm)**	25	23	19
	f_b [c]	0.82	0.88	0.89
PVA/SWNT	***DR*** **(X)**	3.7	4.5	7.3
	φ_f **(μm)**	29	24	24
	f_b	0.77	0.87	0.87
	w [d] **(°)**	71	62	37

a) *DR* = cumulative heat draw ratio, b) φ_f = the diameter of drawn fiber according to density measurements, c) f_b = PVA *b*-axis orientation per WAXD, and d) w = the full width at half maximum and the orientation parameter of embedded SWNTs by Raman spectroscopy.

2.3.4.2. Orientation of PVA Chain Conformations

The alignment of crystalline and amorphous chains at various values of *DR*, as characterized by polarized IR spectroscopy, was shown in Figure 2.9. Polarized IR absorbance from 1132-1146 cm^{-1} and 1071-1095 cm^{-1} for crystalline and amorphous conformations, respectively, were normalized by the peak intensity at 0° polarization. As expected, the IR data in Figure 2.9a was in qualitative agreement with the WAXD data in Table 2.4. Overall, crystalline PVA was oriented along the axes of control and composite fibers. The misalignment of crystalline chain conformations within PVA/SWNT S4/290 fiber was believed to have reduced the tensile strength of that fiber in comparison to that of PVA/SWNT S3/200 fiber. The alignment of amorphous PVA in both the control and composite fibers were relatively low (Figure 2.9b).

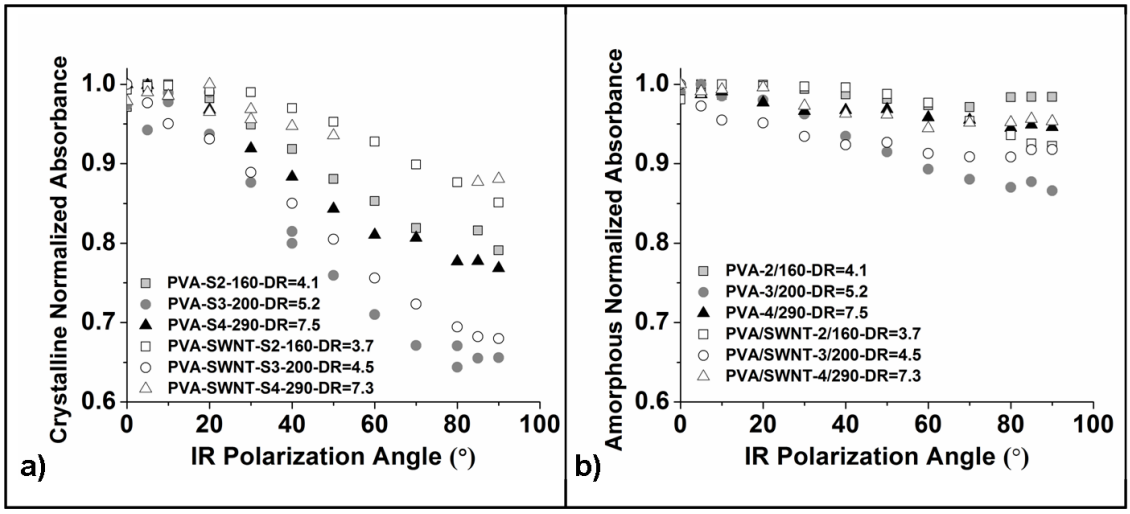

Figure 2.9. Polarized IR of a) crystalline and b) amorphous conformations of PVA.

2.3.4.3. Orientation of Pendant Hydroxyl Groups

The orientation of PVA hydroxyl groups was investigated from strong -OH absorbance peaks at 3320 cm^{-1} (Figure 2.7).[116] It is noteworthy to mention that the breadth of this -OH absorbance peak was influenced by hydrogen bonding.[118] The stretching vibration for pendant hydroxyl groups was normalized by the highest polarized peak intensity and plotted as a function of polarization angle (Figure 2.10). This data has shown the greatest alignment of hydroxyl groups to occur within PVA/SWNT fibers. Since neat PVA fibers were shown to possess the greatest amount of axially aligned crystalline conformations with *DR* (Figure 2.9), differences between the preferential alignment of hydroxyl groups within neat and composite fibers were attributed to SWNT incorporation and the interaction of SWNTs with hydroxyl groups.

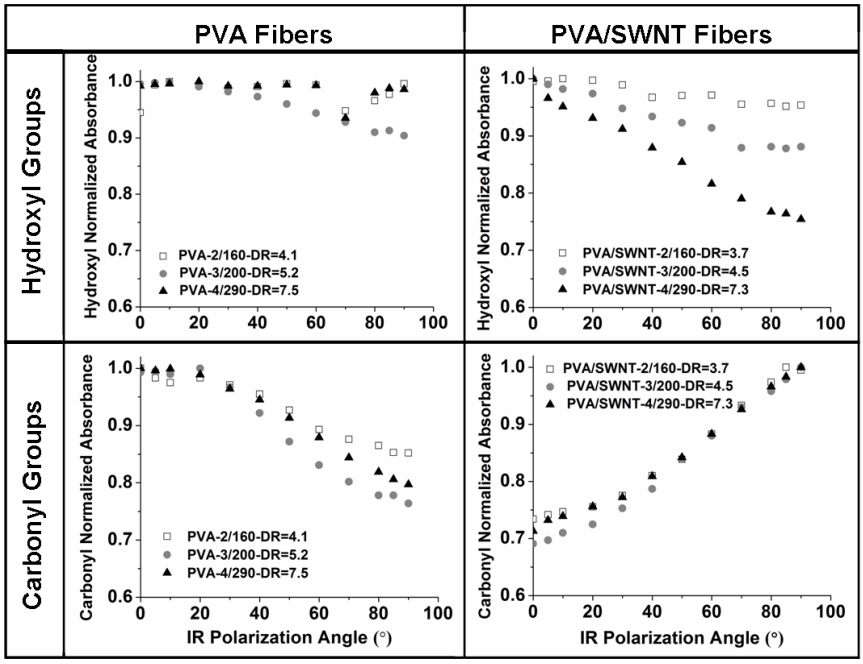

Figure 2.10. Orientations of hydroxyl and carbonyl functionalities within PVA and PVA/SWNT fibers.

The quantitative effects of SWNT incorporation on the preferential alignment of hydroxyl and other functional groups were described as the fraction of molecular moieties, $x(\theta)$, that were preferentially aligned either parallel (θ=0°) or perpendicular (θ=90°) to the fiber axis (Equation 2.6).[105] The value of D (in Equation 2.4) for PVA S2/160 fiber was 0.945, because $A_{0°} < A_{90°}$, the fraction of groups that were perfectly aligned in parallel with the fiber axis, $x(0°)$, could not be calculated (see Equation 2.6). Among PVA S3/200 drawn fibers, 3% of the hydroxyl groups were aligned in parallel to the fiber axis. The fraction of hydroxyl groups that were aligned in parallel to the fiber axis of PVA S4/290 fiber was negligible (Table 2.5). In contrast, the fraction of hydroxyl groups that were perfectly aligned in parallel to the fiber axes of PVA/SWNT fibers had increased from 1 to 10% with increasing *DR*.

Table 2.5. Fraction of Molecular Moieties Perfectly Aligned Along the Fiber Axis.

	DR [a]	**Hydroxyl** ***x(0°)*** [b]	**Carbonyl** ***x(0°)***	**H-O-H** ***x(0°)***	**Sulfoxide** ***x(0°)***
PVA	4.1	-	5.5%	1.5%	2.3%
	5.2	3.3%	9.1%	1.0%	9.8%
	7.5	0.0%	7.8%	-	4.8%
	DR	**Hydroxyl** ***x(0°)***	**Carbonyl** ***x(90°)*** [c]	**H-O-H** ***x(90°)***	**Sulfoxide** ***x(90°)***
PVA/SWNT	3.7	1.4%	19%	37%	1.6%
	4.5	4.3%	23%	41%	4.7%
	7.3	9.8%	21%	43%	7.2%

a) *DR* = cumulative heat draw ratio, b) $x(\theta=0^o)$ = the fraction of groups perfectly aligned along the fiber axis, and c) $x(\theta=90^o)$ = the fraction of groups perfectly aligned normal to the fiber axis.

Non-covalent bonding between hydroxyl groups and SWNTs would account for the anisotropy of hydroxyl groups about the fiber axes of PVA/SWNT fibers. SWNTs were expected to interact with pendant hydroxyl groups and form electron donor-acceptor (EDA) complexes, because lone pair electron donors (such as on hydroxyl groups) are capable of interacting with the π-bonds of aromatic compounds.[126] Weak hydrogen bonding could also occur between the hydroxyl groups and π-bonds of SWNTs.[126-128] The energy minimization of PVA oligomer 1,3,5-hexane triol in the presence of metallic SWNTs supported the feasibility of having hydroxyl groups adjacent to the SWNT surface. The atomistic model of pendant PVA hydroxyl groups in the vicinity of SWNT

was shown in Figure 2.11a. The modeling study confirmed electron charge transfer from the PVA oligomer to the SWNT.

2.3.4.4. Orientation of Carbonyl Moieties

Molecular absorbance from pendant carbonyl acetate groups (1721 cm^{-1}) exhibited similar dependency with IR polarization angle as the stronger carbonyl peak at ~1714 cm^{-1} coming from acetic acid (Figure 2.7). Therefore, the preferential alignment of carbonyl groups was characterized using the ~1714 cm^{-1} peak (Figure 2.10). The absorbance intensities for carbonyl moieties were normalized by the highest polarized peak intensity. Carbonyl stretching vibrations within the control PVA fibers were directed in parallel to the fiber axis upon drawing. The alignment of carbonyl moieties within drawn PVA/SWNT fibers had changed by 90° in comparison to their alignment within PVA fibers. At most, 9% of these carbonyl moieties aligned along the axes of control PVA fibers, but ~20% of the carbonyl moieties had aligned normal to the PVA/SWNT fiber axis (Table 2.5).

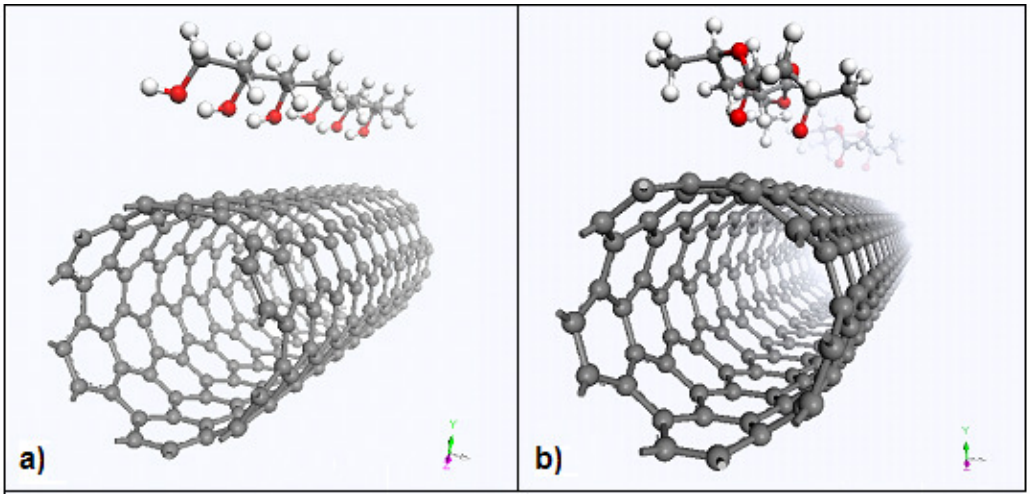

Figure 2.11. Atomistic models of (6,6) CNT with aligned PVA groups in: a) PVA oligomer 1,3,5-hexane triol and b) PVAc oligomer 1,3,5-hexane triacetate.

Non-covalent interactions between SWNTs and carbonyl moieties were believed to have caused the preferential alignment of those moieties normal to the fiber axis. The carbonyl moieties of acetate side groups were expected to respond to SWNT incorporation just as acetic acid carbonyl groups. DMol^3 analysis affirmed non-covalent binding between pendant acetate groups of the PVAc oligomer and SWNTs. Carbonyl moieties were directed toward the surface of the SWNT, and charge transfer had persisted from 1,3,5-hexane triacetate to SWNT. The molecular modeling and IR analysis have implied the formation of EDA complexes via the carbonyl oxygen. The DMol^3 model of this behavior was presented in Figure 2.11b. Therefore, the alignment of acetate side groups has also responded to the aligning of embedded CNTs.

2.3.4.5. Orientation of Imbibed Water

The orientation of water molecules was characterized by the IR polarization of the ~1660 cm^{-1} peak; polarized intensities were normalized by the highest intensity peak. H-O-H bending peaks from control PVA fibers were mostly independent of *DR*. Intensity ratios were above 0.9 for all the polarization angles (Figure 2.12). However, the preferential alignment of water molecules was very evident in the SWNT containing fibers. The $x(\theta=90°)$ for H-O-H bending in PVA/SWNT fibers was in the range of 37 to 43% (Table 2.5). The binding energies for water bending, where either the oxygen atom or the hydrogen atoms were directed toward the SWNT axis (as depicted in Figure 2.13), were comparable.

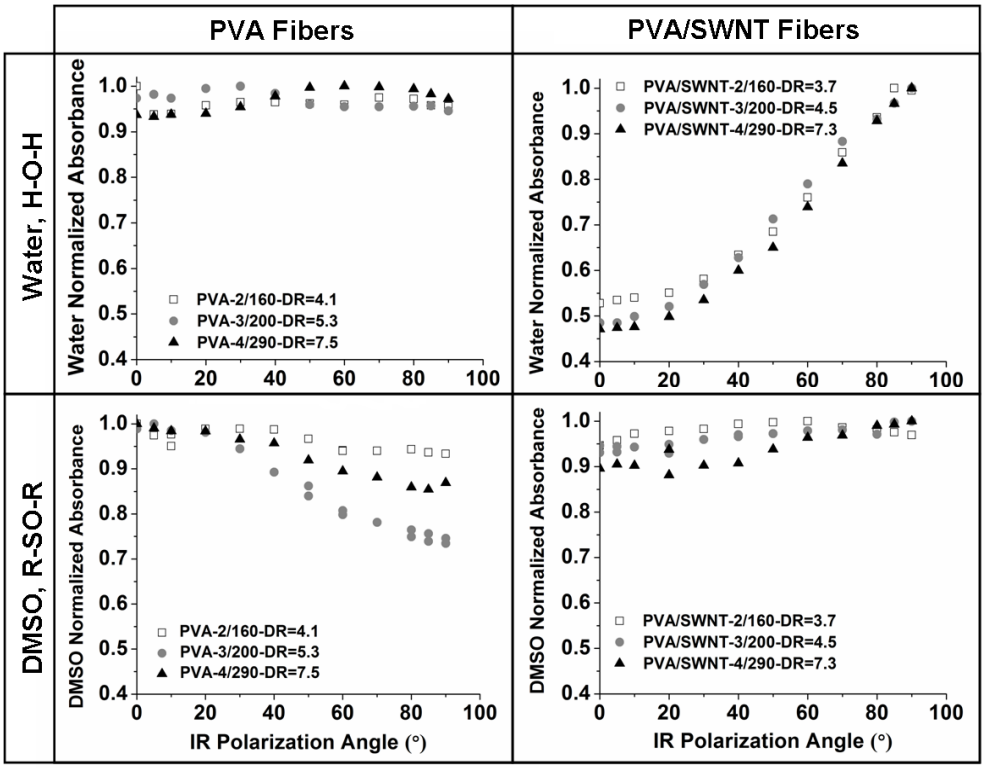

Figure 2.12. Polarized IR intensities of solvent molecules in PVA and PVA/SWNT fibers: water (H-O-H bending) and DMSO (S=O stretching).

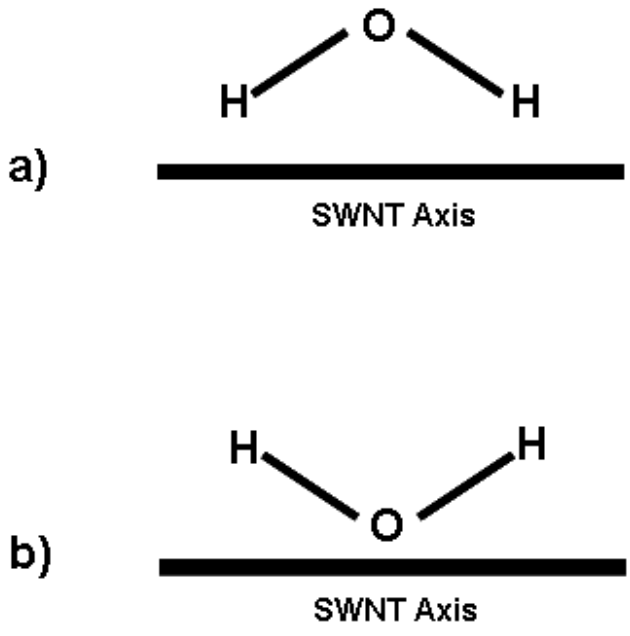

Figure 2.13. Water bending vibrations normal to the SWNT fiber axis, where hydrogen atoms are a) adjacent to or b) away from the SWNT axis.

2.3.4.6. Orientation of Imbibed DMSO

IR absorbance peaks for DMSO sulfoxide groups were deconvoluted in the range of 1014-1025 cm^{-1}. This frequency range was indicative of O-coordination between DMSO and proton donors. Sulfoxide groups were preferentially aligned in parallel with the fiber axes of neat PVA fibers (as shown in Figure 2.12). The fraction of complexed sulfoxide groups, which were perfectly parallel to the fiber axis had increased from 2 to 10% as *DR* increased from 4.1 to 5.3 X (i.e. from S2/160 to S3/200 drawing). The fraction of axially aligned sulfoxide groups had decreased upon S4/290 drawing although the *DR* increased from 5.3 to 7.5 X. PVA hydroxyl groups were misaligned during the process of S4/290 drawing (shown in Figure 2.10), which could account for the misalignment of non-covalently bonded groups.[129] Sulfoxide groups of DMSO exhibited alignment that was normal to the PVA/SWNT fiber axis (Figure 2.12); this was attributed to the charge transfer between SWNTs and DMSO.

2.4. Conclusions

According to thermo-mechanical plots of fiber shrinkage, SWNTs had hindered the thermal shrinkage of the matrix polymer at high temperatures. This behavior was attributed in part to the dispersion and adhesion of SWNTs within the matrix polymer. Polarized IR spectroscopy was used to observe the influence of SWNTs on the preferential alignment of polymer side groups and solvent within drawn fibers. The preferential alignment of ~10% of the PVA hydroxyl groups was influenced by the presence of 1 wt.% SWNTs in the fiber. The remainder of the polymer functional groups had resided within the bulk crystalline and amorphous regions of the polymer making them inaccessible to SWNT. The exfoliation, dispersion, and weight fraction of SWNTs

should be optimized to increase the molecular interaction between PVA and SWNTs. Additionally, the drawing of composite fibers was shown to aid the charge transfer between solvent molecules and SWNTs and the ordering of solvent molecules along SWNTs. About 40% of the water molecules within the composite fibers had exhibited preferential alignment. The SWNT-induced alignment of water molecules was believed to form an interphase of water along SWNTs. The presence of low molar mass impurities (water, acetic acid, DMSO, etc.) on the SWNT surface would negatively affect the interfacial adhesion between PVA and SWNTs. Therefore, the removal of such low molar mass impurities will be important for making mechanically robust polymer/CNT composites.

The temperature of 290 ℃ has enabled the drawing of PVA and PVA/SWNT fibers to *DR* values of 7.5 and 7.3 X, respectively; however, the misalignment of polymer conformations may also occur. The relaxation and melting of crystalline PVA can occur if fiber is not held under sufficient tension at temperatures $\geq T_m$ or if the polymer is exposed to such high temperatures for too long.[35] The method of gel aging was proposed as a technique for enhancing the *DR* of PVA/CNT fibers at temperatures less than T_m. The preparation of CNT dispersions for the gel aging study was discussed in Chapter 3; the structure/property/processing relationships for the prepared PVA/CNT fibers were described in Chapter 4.

CHAPTER 3

KINETIC MECHANISMS OF GEL CRYSTALLIZATION WITHIN POLY(VINYL ALCOHOL) AND CARBON NANOTUBE DISPERSIONS

3.1. Introduction

The goal of this study was to determine the effects of CNTs on the cryo-transformations of PVA gel crystallization and solvent freezing per thermal analysis. Homopolymer solutions of PVA were prepared at concentrations that were appropriate for gel spinning fibers, as discussed in Chapter 4. PVA/CNT dispersions were prepared to contain the same weight percent of polymer and 80/20 (*v/v*) DMSO/water as in the neat solutions of PVA. CNT-dispersions must also undergo the process of sonicating CNTs with PVA to disperse them within the concentrated solutions of polymer. The molecular structure and physical properties of CNTs are dissimilar from that of the polymer; therefore, the incorporation of CNTs is believed to influence the gelation of hybrid spinning dopes. Such changes to the nucleation-and-growth behaviors of gel crystallization and solvent freezing may also influence the process of gel-spinning PVA and the microstructure of the resulting fiber.

The presence of CNTs has been shown to influence the nucleation-and-growth of PVA crystals within supercooled melts[94] and the gelation of UHMWPE [96] (which were previously discussed in the Introduction). In the work by Minus, solvent freezing was reported to turn gels brittle and to reduce the drawability of the as-spun gel fiber within the spinning bath. [42] Further, PVA gels containing 1 wt.% SWNTs were

prone to solvent freezing when submerged into MeOH at -25 °C although neat PVA gels would not exhibit solvent freezing even at -40 °C.[42]

Just as SWNTs could nucleate solvent freezing within PVA gel, they may also nucleate the growth of gel crystals, and the nucleation of gel crystals by CNTs could in turn influence the structure of the polymer gel. Nevertheless, this study will focus on the use of DSC to characterize the nucleation-and-growth mechanisms of gel crystallization and solvent freezing within PVA/CNT dispersions. Chapter 4 will explore the effects of aging time on the microstructures of PVA and PVA/CNT gels and drawn fibers.

Ideally, the method for analyzing thermal data should yield information about the kinetics and mechanisms of transformation. An isoconversional analysis of thermal data was chosen for this study, because it has been used to analyze complex transformations; such as epoxy curing,[130] drug crystallization,[131] and the gelation of aqueous gelatin[132] from DSC data. According to the isoconversional approach, mechanisms of complex transformation could be deduced from plots of the effective activation energy (E_α), wherein activation energy varies with conversion (α).[130, 132] The DSC study of epoxy-amine curing had attributed discontinuous trends in E_α to distinct pathways for solid state transformation[130]. The E_α plots, from supercooled gelatin upon heating, were fitted with the modified Fisher-Turnbull model, and the findings had shown that gelation constrained the molecular diffusion of polymer chains.[132] Therefore, the isoconversional analysis of DSC data may also provide useful information about the kinetics of solution to gel conversion within filled systems.

Since the processes of molecular crosslinking[132] and fillers[45] may influence the molecular mobility of polymer chains during cryo-transformation, changes in

conformational entropy were calculated from values of dE_α/dT_α.[133-135] Experimental models of transformation ($g(\alpha)$ as determined by the isoconversional approach) were fitted to a suitable model, so that the kinetics of solid state transformation could be described. The cryo-transformations and RT rheology of PVA and PVA/CNT dispersions were also investigated as a function of annealing temperature (T_{anneal}); wherein samples were annealed at 10, 25, and 50 ℃ below their clearing temperature of 80 ℃.

3.2. Experimental Section

3.2.1. Sample Preparation

PVA solutions and PVA/CNT dispersions were made for this study. PVA powders, having two different values of DP_w ± 15% were obtained from Kuraray.[136] PVA homopolymer, having a DP_w value of 10,000, was termed PVA-10000. PVA homopolymer, having a DP_w value of 4,000, was termed PVA-4000. The hydrolysis values of these aPVA polymers were 98%. CNTs of SWNTs and FWNTs were obtained from CNI. SWNTs from lot# P0247 had a purity that was > 98%, and FWNTs from lot# X0122UA had a purity of 99%. The mixture of DMSO and distilled water was used to dissolve polymer and disperse CNTs.

PVA was dissolved in 80/20 (*v/v*) DMSO/water at ≈85 ℃ and under constant stirring for several hours. The solution of 4 wt.% PVA-10000 was termed 4P10000. The solution of 10 wt.% PVA-4000 was termed 10P4000. PVA/CNT dispersions were also prepared to have the same weight percent of polymer, 80/20 (*v/v*) DMSO/water, and ~0.25 wt.% CNTs. The PVA/SWNT dispersion was prepared from PVA-10000 and was

termed PS4P10000. The PVA/FWNT dispersion was prepared from PVA-4000 and was termed PF10P4000.

The sonication of CNTs in the presence of dissolved polymer was used to disperse CNTs within concentrated solutions of PVA. Since sonication is known to reduce the average length of CNTs in solvent,[65, 137] sonication could have reduced the DP_w value of polymer. For this reason, a shorter sonication time was applied to the CNT dispersion of PVA-4000 than to the dispersion of PVA-10000 polymer.

Sample PS4P10000 was a dispersion of 99.75:0.25 PVA/SWNT; it was prepared from a dispersion of PVA/SWNT/DMSO and a PVA/DMSO/water solution. 17.63 mg SWNTs were dispersed in 100 ml DMSO and then sonicated for 4 hrs in a Branson 3510 (42 kHz and 100 W) bath sonicator to prepare the PVA/SWNT/DMSO dispersion. 3.5 g PVA was dissolved in 150 ml of DMSO at 60 ℃ and under constant stirring. This 2 wt.% PVA solution was then added to the SWNT/DMSO dispersion and later sonicated for 20 hrs. 180 ml DMSO were removed from the PVA/SWNT/DMSO dispersion with vacuum distillation to achieve the desired concentration of polymer. 3.8 g of PVA were dissolved in 34 ml of distilled water and 68 ml of DMSO at ≈85 ℃ under constant stirring. The PVA/SWNT/DMSO dispersion was gradually added to the 3.4 wt.% PVA solution in DMSO and water.

Sample 10P4000 was a dispersion of 99.76:0.24 PVA/FWNT; it was prepared from a dispersion of PVA/FWNT/DMSO and a PVA/DMSO/water solution. The FWNT/DMSO dispersion (of 52 mg FWNTs per 250 ml DMSO) was sonicated for 26 hrs before adding the PVA/DMSO solution (of 11 g PVA per 300 ml DMSO). Afterwards, the PVA/FWNT/DMSO dispersion was sonicated for 8 hrs. 460 ml of

DMSO were removed by vacuum distillation to prepare the concentrated dispersion of FWNTs. 11 g of PVA were dissolved in 90 ml of DMSO and 35 ml of water to prepare the PVA solution. The FWNT dispersion was gradually blended into PVA solution.

A blend of PVA polymers, having two different values of DP_w, was prepared to model the effects of polymer blending on cryo-transformations. The blend of 4wt.% PVA was comprised of 2 wt.% PVA-10000 and 2 wt.% PVA-4000; therefore this sample was termed 4PBlend. To prepare 4PBlend, polymers were dissolved in 80/20 (*v/v*) DMSO/water at ≈85 ℃ for several hours.

3.2.2. Viscosity Measurements

The effect of sonication time on the value of DP_w for PVA polymers was estimated from measurements of kinematic viscosity (υ), which is a function of capillary elution time (t) and constant C (Equation 3.1 from ASTM D446-07 and D445-11a).

$$\upsilon = t \cdot C \qquad (3.1)$$

Samples were prepared from 0.5 g PVA dissolved in 100 mL DMSO at ≈85 ℃. PVA/DMSO solutions were sonicated for 0-48 hrs. Prior to capillary testing, the samples were conditioned at 40 ℃. Flow times were recorded from the Ubbelohde viscometer (size #1 having C=0.01 mm^2/s^2) at 31 ℃. This viscometer was appropriate for measurements of $2 \leq \upsilon \leq 10$ mm^2/s^2 (ASTM D446-07).

The complex viscosity ($\eta^*(\omega)$) of PVA solutions and PVA/CNT dispersions were measured using an ARES Rheometric Scientific rheometer equipped with a parallel plate fixture. Samples were conditioned at 80 °C for 1 hr (to erase thermal history) and annealed in an oven for two hrs (at 30 °C, 55 °C, and 70 °C). Oven temperatures had decreased to the desired temperature within a period of 30 min. After annealing, samples

were stored at RT (23 ± 2 °C) for 2 hrs prior to testing. Once loaded with sample, the 25 mm in diameter rheometer plates were set at a gap width of 1 mm. The edges of exposed sample were coated with a thin layer of silicon oil to prevent the loss of solvent. Dynamic measurements were conducted with angular frequencies of 1 rad/s to 300 rad/s at 5% strain amplitude, which was in the linear viscoelastic region. The average complex viscosities from two measurements were reported and fitted with the modified Carreau model (Equation 3.2) by adjusting the following parameters: η_0 (zero shear viscosity), λ (characteristic time of molecular chain relaxation), $\dot{\gamma}$ (shear strain rate), b (breadth of linear elastic region), and m (negative slope of the shear thinning regime).[138]

$$\eta^*(\omega) = \eta_0 \left[1 + (\lambda\dot{\gamma})^b\right]^{-m/b} \tag{3.2}$$

3.2.3. DSC

The cryo-transitions of PVA/CNT dispersions were measured using MDSC on the Q200 instrument (TA Instruments). PVA/CNT dispersions, having sizes ranging from 7-13 mg, were hermetically sealed in aluminum T-zero pans (TA Instruments). The DSC sample chamber was purged with nitrogen gas at 50 ml/min. Samples of homopolymer PVA, PVA/CNT dispersions, and blended PVA were equilibrated to 80 ℃ for 30 min and cooled to annealing temperatures of 30, 55, or 70 ℃ within 1, 0.5, and 0.2 min, respectively. After 2 hours of annealing, samples were cooled at the desired cooling rate of 1, 2, and 5 ℃/min. The cryo-transformation of dispersion PS4P10000 annealed at 70 ℃ and 5 ℃/min required cooling beyond the limits of the DSC cooling accessory (which was -90 ℃); therefore, cooling rates of 1, 2 and 3 ℃/min were used to characterize that sample.

A minimum of three heating rates were necessary to calculate E_α using the first order maximum rate equation (Equation 3.3):[130, 139] E_α (kJ/mol) was the effective activation energy with conversion (α), A_α was the effective pre-exponential factor or the cumulative frequency of transforming interactions, β_i equaled the heating rate (K/min), $T_{\alpha,i}$ was the temperature (in Kelvins, K) at α and β_i, and the gas constant (R=0.008314 $kJ \cdot mol^{-1} \cdot K^{-1}$). The value of E_α was determined from the slope of $\ln(\beta_i/T_{\alpha,i}^{\ 2})$ versus $1/T_{\alpha,i}$.

$$ln\left(\frac{\beta_i}{T_{\alpha,i}^2}\right) = ln\left(\frac{A_\alpha \cdot R}{E_\alpha}\right) - \left(\frac{-E_\alpha}{R \cdot T_{\alpha,i}}\right) \tag{3.3}$$

The values of β_i, E_α, and A_α were used to calculate the values of the experimental transformation model ($g(\alpha)$ in Equation 3.4), which provided a relationship between the effective Arrhenius parameters (E_α and A_α), heating rate (β), temperature (T_α), and the gas constant (R).[140] The kinetics of the experimental transformation model was determined from the fit parameters of a known model for solid state transformation.[140] Origin Pro 8.5.1 was used to determine fit parameters.

$$g(\alpha) = \left(\frac{A_\alpha}{\beta}\right)\int_{T_0}^{T_\alpha} \exp\left(\frac{-E_\alpha}{RT}\right) dT_\alpha \tag{3.4}$$

The value of A_α was derived from the iso-kinetic relationship (IKR in Equation 3.5).[140-141] According to IKR, the logarithm of parameter A_α is a function of parameter E_α and isoparametric rate constants, $\ln k_{iso}$ and T_{iso}.[140-141]

$$\ln A_\alpha = \ln k_{iso} + \left(-\frac{1}{RT_{iso}}\right)E_\alpha \tag{3.5}$$

80/20 DMSO/water (*v/v*) mixtures, having sample sizes of 13-25 mg, were hermetically sealed in aluminum T-zero pans (by TA Instruments). The DSC sample

chamber was purged with nitrogen gas at 50 ml/min. The freezing and melting behaviors of the DMSO/water solvent system were characterized with MDSC, over 3-4 runs and at rates of 1-5 °C/min. MDSC runs at rates of 1, 2, 3 and 5 °C/min had corresponding modulation amplitudes of ± 0.16, 0.32, 0.48, and 0.80 °C/min.

3.3. Results and Discussion

3.3.1. Sample Characterization at RT

3.3.1.1. DP_w Related Elution Time for Sonicated Polymer

As described in the Experimental Section, CNTs were dispersed in DMSO using PVA polymer and sonication. According to Zhang *et al*, this method of preparing a PVA/CNT dispersion produces an optically homogeneous dispersion of CNTs within a mixture of DMSO and water;[99] nevertheless, sonication of the PVA/CNT/DMSO dispersion may reduce the DP_w of polymer, which is related to polymer viscosity. Surawut et al. sonicated carbon black (CB) in aqueous PVA (having a DP_w of 1,600) for 10 min to prepare dispersions for electrospun mats. Brookfield viscometer measurements of sonicated PVA/CB dispersions, sonicated PVA in solution, and unsonicated PVA in solution had shown the viscosity values from the sonicated sample of aqueous PVA and the PVA/CB dispersions (of up to 10 wt.% in loading) to be lower than the viscosity of unsonicated PVA.

The relationship between sonication time and capillary elution time was used to estimate the relative DP_w of polymers in this study. ASTM D2502-04 "Standard Test for Estimation of Mean Relative Molecular Mass of Petroleum Oil from Viscosity Measurements" has been used to estimate the molecular mass of petroleum oil from kinematic viscosity measurements that were taken at 38 °C and 100 °C. ASTM D2502-

04 consists of tabulated data that were obtained from numerous experiments and were fit to mathematically expressions.[142] Solutions of 0.45 wt.% PVA-10000 in DMSO and 0.45 wt.% PVA-4000 in DMSO were sonicated and tested with an Ubbelohde viscometer. The elution times for unsonicated PVA-10000 in DMSO and unsonciated PVA-4000 in DMSO were proportional to their values of DP_w (Table 3.1). Therefore, elution times were used to estimate the relative DP_w of sonicated polymers. Measurements of elution time implied that the DP_w of PVA-10000 was reduced by 22% after 20 hrs of sonication, and the DP_w of PVA-4000 was reduced by 15% after 8 hrs of sonication.

Table 3.1. Relative DP_w of Dilute PVA/DMSO Solution (0.45 wt.% PVA) at 31 °C versus Sonication Time.

	Sonication Time (hrs)	**Elution Time (min)**	**υ (mm^2/s)**	**PVA-10000 Relative DP_w**	**Relative DP_w PVA-4000**
PVA-10000	0	16.15	9.69	10,000	9,627
	20	12.65	7.59	7,832	7,540
	48	6.97	4.18	4,315	4,154
PVA-4000	0	6.71	4.03	4,154	4,000
	8	5.69	3.41	3,523	3,391
	24	5.28	3.17	3,269	3,147
	48	4.95	2.97	3,065	2,950

Relative DP_w = the relative weight average degree of polymerization based on the ratio of υ for sonicated and unsonicated reference polymers.

3.3.1.2. DP_w of Polymers within CNT Dispersions

According to Figure 3.1, the values of $\eta^*(\omega)$ for CNT/polymer dispersions (PS4P10000 and PF10P4000) were lower than the values reported for homopolymer solutions (4P10000 and 10P4000) that were composed of the same weight fraction of

polymer. As reported in Table 3.1, sonication reduced the values of elution time, which is related to DP_w. Therefore, the blending of sonicated polymer into unsonicated polymer had caused the low values of $\eta^*(\omega)$ to be observed among the CNT/polymer dispersions.

The rheological effects of blending two polymers, having different values of DP_w but the same weight percent of polymer, were observed with sample 4PBlend. As a result of blending PVA-10000 with PVA-4000, the values of $\eta^*(\omega)$ for sample 4PBlend were lower than those values reported for sample 4P10000. The DP_{wb} value for blended polymers within sample 4PBlend was calculated according to Equation 3.6.[143]

$$DP_{wb} = w_1 \cdot DP_{w1} + w_2 \cdot DP_{w2} \tag{3.6}$$

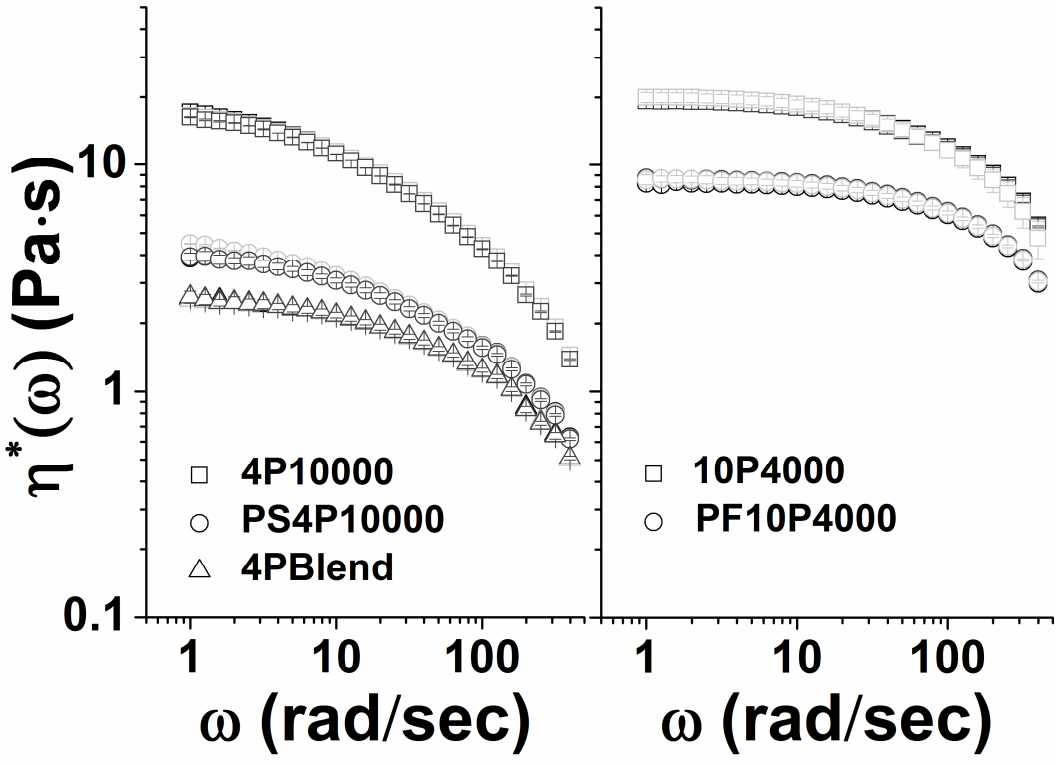

Figure 3.1. Rheology of PVA solutions and PVA/CNT dispersions heated to 80 °C for 1 hr, cooled to T_{anneal}=30, 55, and 70 °C for 2 hrs (where each color represents an annealing temperature), and conditioned at 22 ± 3 °C for 2 hrs prior to testing.

Sonicated PVA/CNT/DMSO dispersions contained 1.3 wt.% PVA-10000 and 1.8 wt.% PVA-4000. Equation 3.2 was used to determine the relative DP_{wb} of CNT dispersions that were comprised of sonicated and unsonicated polymer. Sonicated polymers within the PVA/CNT/DMSO dispersions were assumed to have the same relative DP_w values as those polymers within 0.45 wt.% PVA/DMSO solutions that were sonicated for similar periods of sonication time (Table 3.1). The estimated values of relative DP_{wb} for polymers within the PVA/CNT dispersions were reported in Table 3.2.

Table 3.2. Rheology of PVA Solutions and PVA/CNT Dispersions.

Sample Designation	DP_w **or** DP_{wb} [a]	**Modified Carreau Model**					$G'(\omega)/G''(\omega)$ **Linear Regression**	
		η_0 [b] **(Pa·s)**	λ [c] **(s)**	m [d]	b [e]	R^2 [f]	**Slope (Pa/Pa)**	R^2
4P10000	10,000	20.5	0.0223	1	0.577	1.000	1.6	1.000
PS4P10000	8,900	4.3	0.0076	1	0.600	0.997	1.5	1.000
4PBlend	7,000	2.7	0.0058	1	0.658	0.998	1.5	0.999
10P4000	4,000	20.1	0.0049	1	0.844	0.999	1.7	1.000
PF10P4000	3,700	8.4	0.0038	1	0.991	0.999	1.7	0.997

Samples were conditioned at 80 ℃ for 1 hr, followed by 2 hrs at 30 ℃, and then RT for 2 hrs prior to testing. a) DP_w or DP_{wb} = weight average degree polymerization for homopolymer and blended polymer, respectively b) η_0 = experimental zero shear viscosity, c) λ = characteristic time of polymer relaxation, d) m = slope of shear thinning behavior, e) b = breadth of linear elastic region, f) R^2 = 'goodness of fit' parameter. The slope of logarithmic $G'(\omega)/G''(\omega)$, was linear over two orders of angular velocity.

3.3.1.3. Complex Viscosity of PVA Solutions and CNT Dispersions

The complex shear viscosities of PVA solutions and CNT/polymer dispersions were independent of annealing temperature, as illustrated by the overlapping data points in Figure 3.1. The repeatability of these curves[144] at RT further suggests the bulk morphologies of these samples (of homopolymer, blended polymer, and CNTs) were uniform. Table 3.2 shows the properties of test samples annealed at 30 ℃ prior to testing. Insight into the spatial heterogeneity of polymeric solutions can be inferred from the slopes of shear storage modulus, $G'(\omega)$, plotted against shear loss modulus, $G''(\omega)$, for several magnitudes of angular velocity.[145] Slopes having values lower than two signify microscopic heterogeneity.[145] All the samples used within this study had similar levels of spatial heterogeneity,[145-146] where $G'(\omega)/G''(\omega)\approx1.5$ in Table 3.2.

In this study, PVA/CNT dispersions (having ~0.25 wt.% CNTs) had RT rheological behaviors that were dominated by the characteristics of the matrix polymer, as observed in the case of measuring $G'(\omega)/G''(\omega)$. Each sample of PVA and PVA/CNT was also shown to exhibit a value of m=1 (in Table 3.2); these values have suggested that the molecular interactions between solvated polymer chains[138] were all similar, and m was dominated by the behavior of matrix polymer.

The value of η_0 was calculated according to the modified Carreau model (Equation1)[138]. Samples of 4P10000 and 10P4000 had values of $\eta_0\approx20$ Pa·s at RT (Table 3.2). The weight fractions of PVA-10000 and PVA-4000 within these concentrated samples of polymer were chosen so as to gel-spin fibers, having fairly circular cross sections (see Chapter 4). The η_0 value for PS4P10000 was lower than the η_0 value reported for 4P10000 although fillers have been known to increase the viscosity

of matrix polymer[45]. The η_0 value for PF10P4000 was also shown to be lower than the η_0 value reported for 10P4000. According to Huang et al., the dynamic viscosities of MWNT/polydimethylsiloxane dispersions that were produced with high speed mixing, were higher than the values of unfilled polymer mixed under similar conditions.[144] The η_0 for sample 4PBlend was also lower than the value reported for sample 4P10000. Therefore, the values of DP_{wb} have also influenced the η_0 of CNT dispersions.

Trends pertaining to λ and b were mostly influenced by DP_w. For instance, the blending of PVA-4000 with PVA-10000 within sample 4PBlend has resulted in a λ that was lower than the value observed for sample 4P10000. Sample PS4P10000 also had a shorter value of λ than sample 4P10000; this was due to the blending of sonicated polymer with PVA-10000. The values of each sample's λ for molecular relaxation decreased with smaller values of DP_w (Table 3.2). The breadth of the linear elastic region for 10P4000 was broader than the region of linear elasticity as depicted for 4P10000 (Figure 3.1 and Table 3.2); this is a common trend for DP_w dependent $\eta^*(\omega)$.[147] Further, the parameter b became increasingly larger as the DP_w had decreased across all samples of PVA and PVA/CNT (Table 3.2).

3.3.2. Cryo-gelation of PVA Solutions

Heating and cooling thermograms of PVA solutions and dispersions, taken at 2 ℃/min, were given in Figure 3.2. Exothermic transitions occurred upon cooling (in Figure 3.2a,b,d). The exothermic transition from sample 4P10000 occurred between -32 and -42 °C; whereas exothermic transitions from sample 10P4000 occurred at even lower temperatures, between -45 and -57 °C. The cryo-transformation of 4PBlend, upon cooling, was shown to occur between -42 and -50 ℃ (Figure 3.2d).

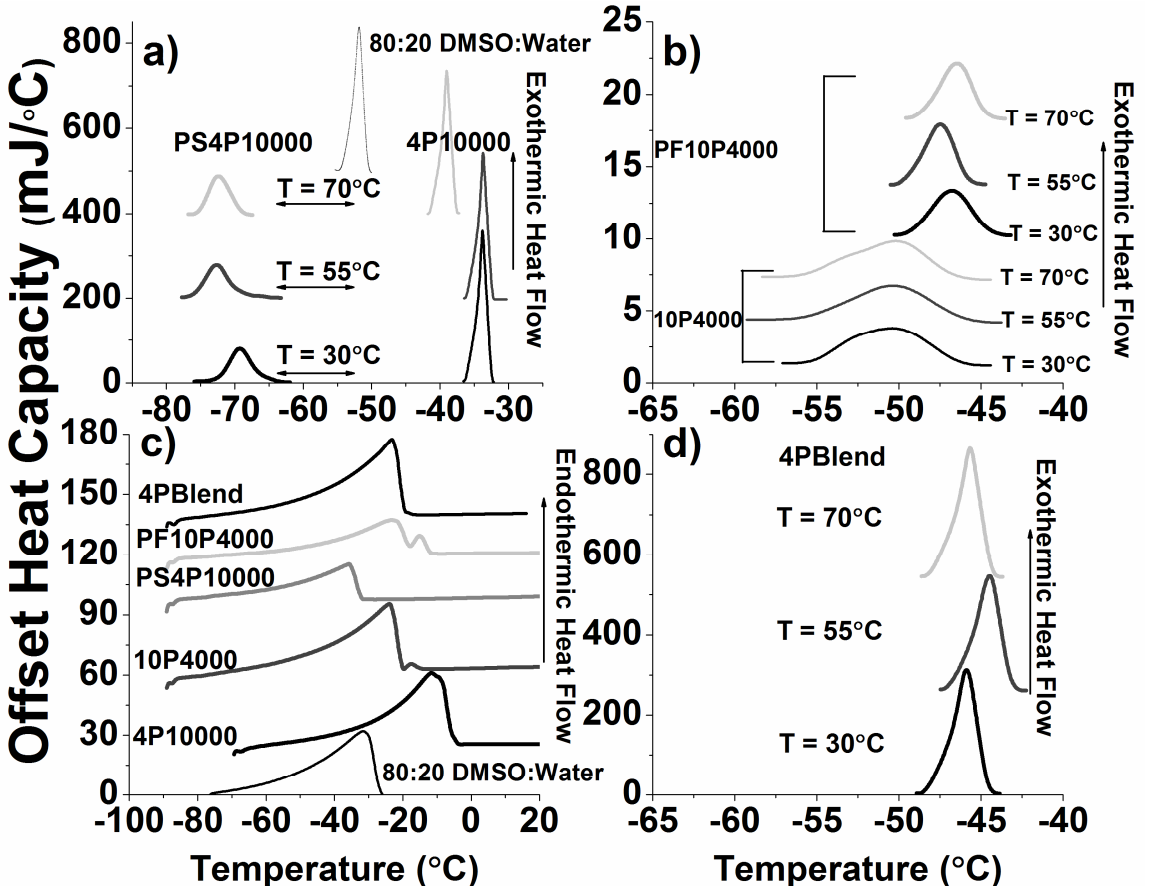

Figure 3.2. Hermetically sealed 80/20 DMSO/water, PVA/CNT dispersions, and PVA solutions containing a) PVA-10000 and b) PVA-4000 for T_{anneal}=30, 55, and 70 °C prior to 2 °C/min cooling, c) their exothermic transitions upon 2 °C/min heating for T_{anneal}=30 °C, d) thermograms of 4PBlend at 2 °C/min cooling from annealing temperature.

Sample 4P10000 exhibited cooling enthalpies (of ~90 J/g at 2 °C/min) that were considerably more than the enthalpy values from 10P4000, 4PBlend, and solvent freezing (Table 3.3). Gel crystallization was believed to occur within sample 4P10000, because its enthalpy of transformation was much greater than the enthalpy of solvent freezing (Table 3.3 and 3.4). The enthalpy of freezing 80/20 (*v/v*) DMSO/water was ~41 J/g (Table 3.4) and the enthalpy of fusion for crystalline PVA was 156 J/g.[148]

Upon heating at 2 °C/min, the peak endothermic temperature for sample 4P10000 had occurred at higher temperatures than those observed for 10P4000 and 4PBlend

(whose bulk temperatures occurred at ~-25 °C in Figure 3.2c). A small high temperature melting peak (near -20 °C) occurred along the dominant endothermic peak of sample 10P4000. A similar high temperature transition was not observed for sample 4PBlend (Figure 3.2c).

Table 3.3. Effects of Annealing Temperature on the Cryo-behaviors of Hermetically Sealed PVA Solutions and PVA/CNT Dispersions.

	Cooling Rate (℃/min)	**T_{anneal} [a] = 30 ℃**		**T_{anneal} = 55 ℃**		**T_{anneal} = 70 ℃**	
		T_{exo} [b] (℃)	**ΔH [c] (J/g)**	**T_{exo} (℃)**	**ΔH (J/g)**	**T_{exo} (℃)**	**ΔH (J/g)**
4P10000	**1**	-32	118	-35	121	-37	121
	2	-34	97	-34	91	-39	92
	5	-47	73	-45	80	-45	71
PS4P10000	**1**	-70	38	-67	35	-69	36
	2	-69	35	-73	36	-72	36
	3 † or 5 ‡	-71 ‡	35 ‡	-71 ‡	26 ‡	-61 †	33 †
10P4000	**1**	-49	35	-51	38	-48	36
	2	-50	36	-50	37	-50	36
	5	-58	42	-59	45	-59	44
PF10P4000	**1**	-40	31	-46	41	-43	36
	2	-47	39	-47	42	-46	40
	5	-49	40	-50	41	-50	42
4PBlend	**1**	-44	52	-46	58	-44	54
	2	-46	46	-44	44	-46	46
	5	-49	45	-49	44	-44	38

a) T_{anneal} = annealing temperature, b) T_{exo} = temperature peak for an exothermic transformation, and c) ΔH = enthalpy of the exothermic transformation.

Table 3.4. Thermal Properties of Hermetically Sealed 80/20 DMSO/Water.

	T_f [a]	ΔH_f [b]	T_m [c]	ΔH_m [d]	ΔT [e]
	(°C)	(J/g)	(°C)	(J/g)	(°C)
1 °C/min	-53 ± 5	50 ± 11	-32 ± 2	44 ± 4	21 ± 5
2 °C/min	-55 ± 4	45 ± 10	-34 ± 3	41 ± 5	21 ± 4
3 °C/min	-54 ± 3	41 ± 5	-32 ± 1	40 ± 3	23 ± 4
5 °C/min	-55 ± 1	43 ± 1	-29 ± 1	38 ± 3	26 ± 0

a) T_f = temperature of solvent freezing, b) ΔH_f = enthalpy of freezing, c) T_m = solvent melting upon heating, d) ΔH_m = enthalpy of melting, and e) ΔT = difference between peak temperatures of solvent freezing and solvent melting.

Homopolymer PVA solutions exhibited exothermic behaviors upon heating, which occurred at temperatures higher than those observed for 80/20 DMSO/water (Figure 3.2c and Table 3.4). Therefore, the high temperature melting, as observed within PVA solutions, was attributed to PVA gelation. The endothermic peak profiles for PVA solutions, in comparison to the profile for DMSO/water, also inferred the likelihood of solvent melting in the range of -25 to -80 °C (Figure 3.2c and Table 3.3). These factors gave ample reason to believe that singular exothermic peaks, as observed upon cooling, could actually represent multiple transformations (such as polymer gelation and solvent freezing)[18].

The endothermic peak for sample 4P10000 (in Figure 3.2c) was suggestive of high melting temperature gel crystals. Gel melting within 4P10000 occurred at higher temperatures than those observed for sample 10P4000 and 4PBlend. Chain segments within 4P10000 may have more readily aggregated to form gel crystals than the lower DP_w polymer of 10P4000 at low temperatures. Double endothermic peaks were observed

upon heating 10P4000. A phase of larger crystals has been attributed to peak of high melting temperature. Interestingly, the blending of polymer (as in sample 4PBlend) had inhibited the growth of high melting temperature gel crystals (Figure 3.2d). Gel crystallization appeared to be dominated by the nucleation-and-growth of 10,000 DP_w polymer, as inferred from the heat capacity measurements of cooling thermograms(Figure 3.2c). The exothermic transformation of PVA-10000 in 4Blend occurred at lower temperatures than within homopolymer sample 4P10000.

3.3.3. Cryo-gelation of PVA/CNT Dispersions

The exothermic transformation of sample PS4P10000 (Figure 3.2a) occurred at temperatures (-62 to -78 °C) that were much lower than those observed from sample 4P10000 (-32 to -42 °C) and sample 4PBlend (-42 to -49 °C) although the value of DP_{wb} for PVA in PS4P10000 was between the values of $DP_{w(b)}$ for both solutions. The cooling and heating of sample PS4P10000 resembled the freezing and melting of the binary solvent system (Figure 3.2a,c). Therefore, the temperature of solvent freezing has been depressed within sample PS4P10000, and the formation of gel crystals has been suppressed. In contrast, polymer gelation dominated the subzero transitions of sample 4P10000.

In contrast to sample PS4P10000, polymer gelation has occurred upon cooling sample PF10P4000. The onset of cryo-transformation has also occurred at higher temperatures for PF10P4000 than for 10P4000 (Figure 3.2b), which suggests the incorporation of FWNTs has nucleated cryo-transformation. Since the bulk of sample PF10P4000 melted at ~-25 °C, which is above the transition for solvent melting, the peak temperature for endothermic transformation within sample PF10P4000 has been

attributed to polymer gelation (Figure 3.2c). The endothermic transition for sample PF10P4000 (in Figure 3.2c) also exhibited two melting peaks for heating rates of 1 and 2 °C/min. A similar observation has been reported for the melting of PE and PE/MWNTs gels.[96] The narrow endothermic peak above -20 °C (Figure 3.2c) has been attributed to the melting of crystals nucleated by CNTs.

3.3.4. Cryo-transformation Mechanisms of PVA Solutions

Figure 3.3 gives an example of curves that have been used to determine the values of temperature dependent conversion (α_T) for different values of β_i. $-E_\alpha$ values were observed from plots of Equation 3.2, as was shown in Figure 3.3b. Negative values of activation energies have also been reported in literature for thermal gelation.[14]

The plots of E_α (in Figure 3.4) were used to describe transformation mechanisms (the trends of several curves have been enlarged within Appendix A), and the direction of dE_α/dT_α values were used to interpret mechanisms of nucleation-and-growth. For instance, solid state crystallization within inorganic materials has occurred by simple atomic diffusion when $dE/dT=0$, from stable nuclei when $dE/dT>0$, or from local heterogeneities that exist among atomic species when $dE/dT< 0$.[133]

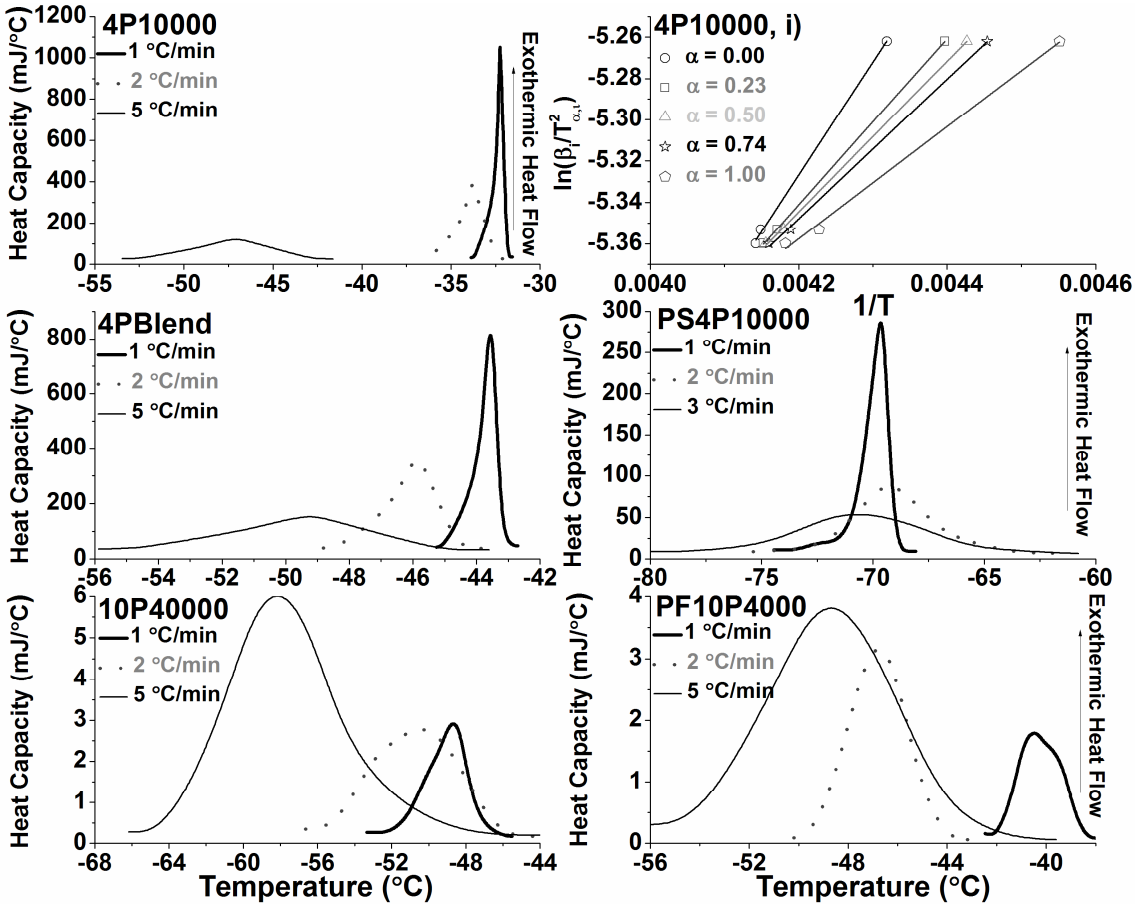

Figure 3.3. 4P10000 was annealed at 30 °C for 2 hrs prior to cooling: a) exothermic reactions upon cooling at β_i=1, 2, and 5 °C/min and b) plots used to determine E_α using the maximum rate theory.

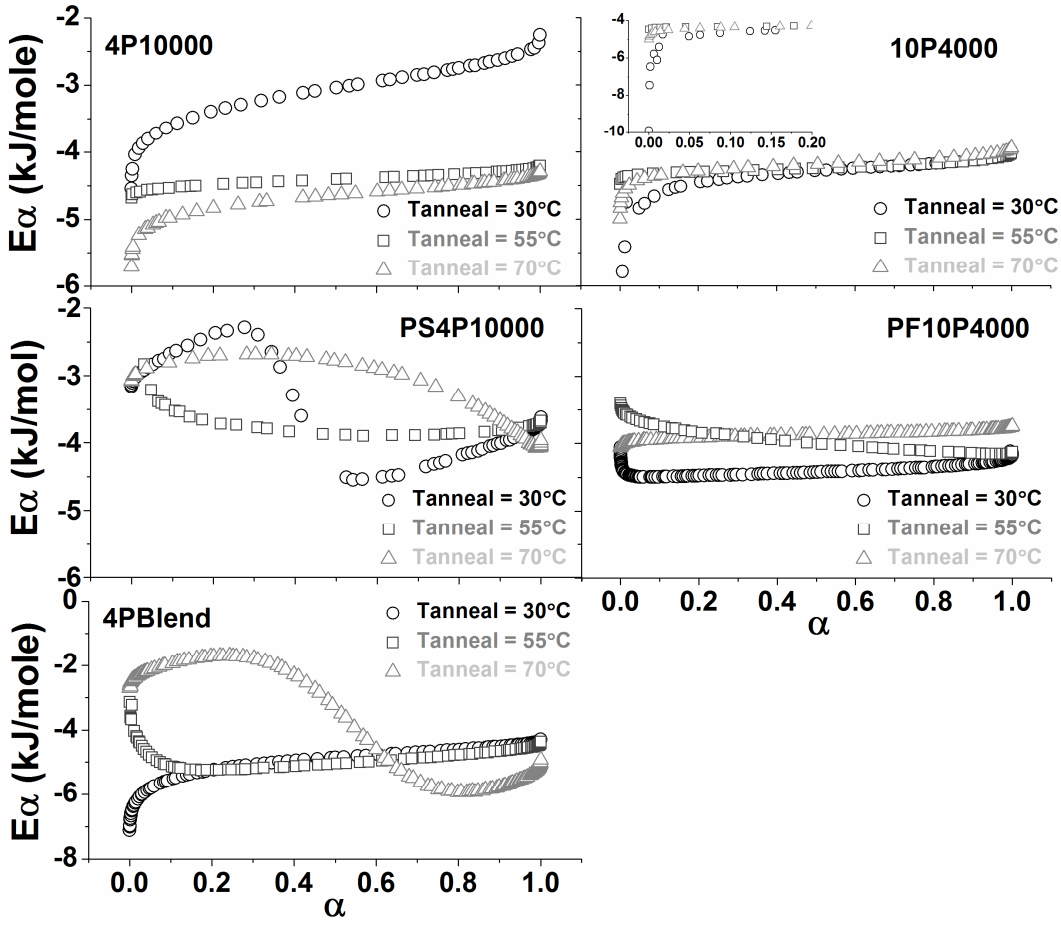

Figure 3.4. Influence of T_{anneal} on the values of E_α for PVA solutions and PVA/CNT dispersions.

Annealing temperature and DP_w did not seem to influence the mechanism of cryo-transformation within homopolymer solutions; E_α steadily increased with α for these samples and $dE_\alpha/dT_\alpha > 0$ was observed. Trends of increasing E_α were characteristic of parallel transformations.[133, 149-150] The term parallel has suggested that several kinetic processes can take place independently and simultaneously.[151] Nevertheless, T_{anneal} did influence the E_α of sample 4P10000 (Figure 3.4). The values of E_α for sample 4P10000 became increasingly more negative after annealing at higher temperatures. The E_α values for 10P4000 solutions were less susceptible to the influence of annealing

temperature, especially for values of $\alpha \geq 0.3$. Scheme 3.1 has illustrated parallel transformations of gel crystallization and solvent freezing within samples of 4P10000 and 10P4000. Solvated homopolymer (P_{homo}) associated at rate constant, $k_1(T)$, to nucleate-and-grow gel (P_{gel}) at low temperatures. Further, the liquid solvent system (L) had proceeded to freeze (S) on its own.

$$P_{homo} \xrightarrow{k_1(T)} P_{gel}$$

$$L \xrightarrow{k_2(T)} S$$

Scheme 3.1. Proposed parallel cryo-transformation pathway for homopolymer PVA solutions.

The subzero conversion of 4PBlend annealed at 30 °C had proceeded by unrelated processes of nucleation-and-growth, as was also observed for homopolymer solutions (Figure 3.3 and Scheme 3.1). However, the transformation mechanisms of 4PBlend for T_{anneal} values of 55 and 70 °C differed from the behavior observed for T_{anneal}=30 °C. The values of E_α at the onset of cryo-transformation- for T_{anneal} =55, 70 °C- were greater than the values observed from homopolymer solutions (4P10000 and 10P4000). The values of E_α at the onset of transformation have implied the heterogeneous nucleation of gel crystals, which could occur at the phase boundary of low and high DP_w polymer. Although the blend of PVA-10000 and PVA-4000 was macroscopically miscible, the microscopic phase separation of polymers could have occurred in sample 4PBlend.[45]

The nucleation-and-growth of crystalline polymer has been reported to occur at the interface of phase-separated polymers within a blend. Zhang et al. proposed the mechanism of fluctuation-assisted crystallization to describe the nucleation-and-growth of crystallites within a polyolefin blend (of poly(ethylene-co-hexene and poly(ethylene-

co-butene)).[152] Nucleation sites for polymer crystallization were concentrated at the boundaries of phase separated polymer, according to AFM data. Further evidence for interfacial crystallization was observed in study of UHMWPE blended with branched PE by Xu et al., wherein DSC and optical microscopy was used to characterize the behaviors of phase separation and polymer crystallization.[20]

Portions of the E_α plots for 4PBlend, where T_{anneal}=55, 70 °C prior to cooling, were shown to exhibit values of $-dE_\alpha/dT_\alpha$ with conversion (Figure 3.4). The transition to more negative values of E_α has been associated with the initiation of gel crystals from less stable nucleation sites, namely the polymer interphase along phase boundaries.

Thus, microphase separation within sample 4PBlend (cooled from T_{anneal} =55, 70 °C) has resulted in phase boundaries, from which gel crystals could nucleate-and-grow. The mechanism of subzero transitions within 4PBlend has been likened to fluctuation-assisted nucleation-and-growth. The nucleation of PVA-4000 polymer at the interface of PVA-10000 polymer would account for the temperature ranges of exothermic and endothermic transformation (Figure 3.2b,d). Nucleation would cause the gel crystallization of PVA-4000 in sample 4PBlend to occur at temperatures higher than those reported for sample 10P4000. In spite of the high temperature melting peak (Figure 3.2c), similar behaviors of gel melting were observed between samples 4PBlend and 10P4000.

The change in conformational entropy, $S(T_f - S(T_i)$, for cryo-transformations were calculated from the values of dE_α/dT_α, (using Equation 3.7).[134-135] The reported values of $S(T_f)-S(T_i)$ versus T_{anneal} (Figure 3.5) were average values (for transformations ranging from T_i to T_f and from the data collected at β_i).

$$S(T_f) - S(T_i) = \int_{T_i}^{T_f} \frac{1}{T} \frac{dE}{dT} dT \qquad (3.7)$$

Spline fittings of $S(T_f)$-$S(T_i)$ versus T_{anneal} were given in Figure 3.5 for each sample. The values of $S(T_f)$-$S(T_i)$ for the cryo-transformations of homopolymer solutions were greatest post annealing at 30 °C. Between samples of homopolymer annealed at 30 °C, the value of $S(T_f)$-$S(T_i)$ for sample 10P4000 was greater than the value obtained from sample 4P10000. Values of $S(T_f)$-$S(T_i)$ for samples 4P10000 and 10P4000, where T_{anneal} =55, 70 °C, were similar (Figure 3.5). In consequence, the effective activation energy plots of 4P10000 were displaced to more negative values of ($-E_\alpha$) after annealing at increasingly higher temperatures (Figure 3.4).

The calculation of $S(T_f)$-$S(T_i)$ for sample 10P4000 was the greatest, followed by 4PBlend for samples annealed at 30 °C. $S(T_f)$-$S(T_i)$ for 4PBlend was slightly higher than the value reported for 4P10000. Further, the change in conformational entropy for sample 4PBlend had decreased linearly with higher annealing temperatures. Negative values of $S(T_f)$-$S(T_i)$ were reported for 4PBlend samples, where T_{anneal} =55, 70 °C. When $E_{\alpha=0} > E_{\alpha=1}$, negative values of $S(T_f)$-$S(T_i)$ were calculated (Figure 3.4 and 3.5). Conceptually, the change in conformational entropy cannot be negative; however, the calculation of negative values for $S(T_f)$-$S(T_i)$ has inferred the presence of ordered phases.[134]

The microscopic phase separation of PVA polymers within 4PBlend was believed to confine the molecular arrangement of polymer chains and create boundaries that could nucleate cryo-transformation (as depicted within Figure 3.6a). Both of these behaviors would negatively affect the values of $S(T_f)$-$S(T_i)$.

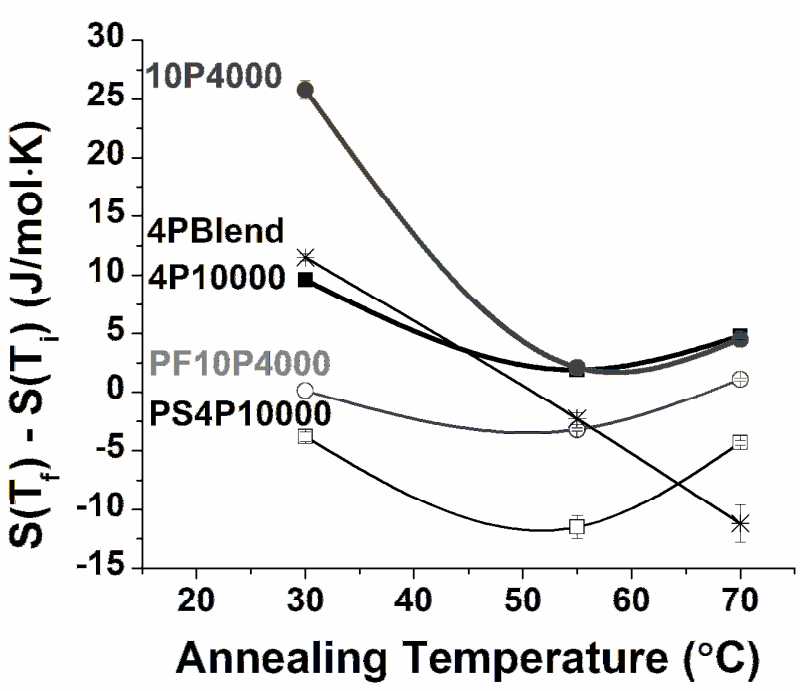

Figure 3.5. Change in the conformational entropy of cryo-transformations.

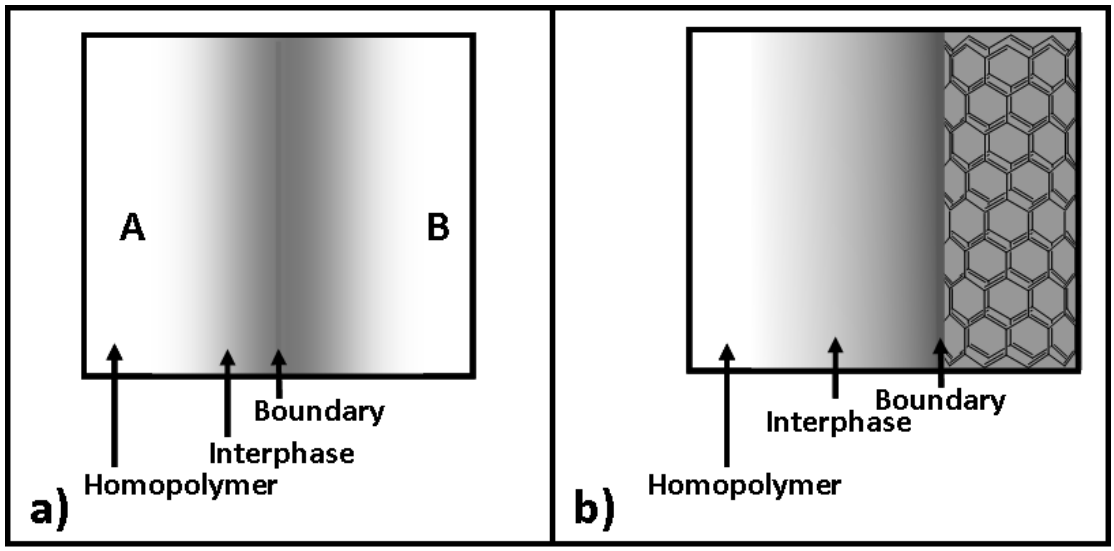

Figure 3.6. Proposed phases within a) blend of low and high *DP* polymers (A and B) and b) CNT/polymer dispersions.

3.3.6. Cryo-transformation Mechanisms of CNT Dispersions

CNT dispersions consisted of blended polymer and fillers that could nucleate gel crystallization and solvent freezing. At the onset of cryo-transformations, the effective activation energies of CNT/polymer dispersions were less negative than the values obtained from homopolymer solutions of PVA (Figure 3.4). This behavior was suspected since the nucleating effects of filler have been known to reduce the energy barrier for crystallization.[45] (Counter-intuitively, FWNTs dispersed in solvent did not nucleate the freezing of pure solvent, see Appendix B).

Since the DP_w of the PVA within sample PF10P4000 was slightly less than the value for sample 10P4000 (Table 3.1), the differences between their transformation mechanisms may be attributed to the incorporation of FWNTs and T_{anneal}. The cryo-transformation of PF10P4000 post annealing at 70 °C (Figure 3.4) exhibited higher values of E_α with conversion (see Appendix A); as discussed earlier, this behavior was indicative of a parallel transformation mechanism. The E_α plots of sample PF10P4000 annealed at 30 and 55 °C became more negative with conversion initially. The values of E_α for sample PF10P4000, after annealing at 30 °C, had increased with conversions in excess of α=0.1. This behavior was suggestive of nucleation; such that cryo-gelation would occur at surfaces and interphases up to conversions of α=0.1. Afterwards, a parallel mechanism of transformation had proceeded. The values of E_α for sample PF10P4000, where T_{anneal}=55 °C, decreased over the entire course of the transformation.

FWNTs were attributed with influencing the spatial heterogeneity of solvated polymer. Nucleation-and-growth within the homopolymer regime of Figure 3.6b was expected to proceed via increasing values of E_a, as observed for homopolymer solutions.

From the analysis of E_α plots (in Figure 3.4) and the high temperature peak of melting (in Figure 3.2c), the nucleation-and-growth of gel crystals within sample 10P4000 are believed to persist from surface of FWNTs. The polymer interphase along FWNTs was also believed to nucleate gel crystals within the PF10P4000, where T_{anneal}=30, 55 °C, (see Figure 3.6b).

The E_α plots for sample PS4P10000 were significantly different from those observed for homopolymer solutions and the PF10P4000 dispersion. The annealing of PS4P10000 at 30 °C has resulted in an irregular sinusoid for E_α values, as also observed for sample 4PBlend annealed at 70 °C. The direction of dE_α/dT_α changed at conversions of α=0.28 and α=0.76. Thus, cryo-transformation in excess of α=0.28 was believed to proceed by the nucleation-and-growth of gel crystals from spatial heterogeneities. The plots of E_α for samples PS4P10000 and 4PBlend, where T_{anneal}=55 °C, were noticeably similar. The values of dE_α/dT_α were initially negative, but the values turned positive at some value of critical conversion. The values of E_α for PS4P10000, at T_{anneal}=55 °C, increased for conversions higher than α=0.28. For T_{anneal}=70 °C, the values of E_α for sample PS4P10000 exhibited convex behavior; the positive value of dE_α/dT_α turned negative at a critical conversion of α=0.3. All in all, cryo-transformations within sample PS4P10000 were nucleated by surfaces and polymer interphases; there was also evidence of nucleation-and-growth from within solvated homopolymer (Figure 3.6b).

CNT dispersions featured significantly lower values of $S(T_f)$-$S(T_i)$ than samples of homopolymer upon cryo-transformation. Further, calculations of $S(T_f)$-$S(T_i)$ for samples of PS4P10000 were lower than those values reported for PF10P4000. Within sample PS4P10000, surfaces would exist at the interface of CNTs and phase-separated polymer.

The high value of DP_w, within sample PS4P10000, could have also reduced the value of $S(T_f)$-$S(T_i)$ (Figure 3.5).

3.3.7. Cryo-transformation Kinetics

As discussed in the Experimental Section, the value of A_α must be calculated from Equation 3.5, and then substituted into Equation 3.4 to find the experimental values of $g(\alpha)$. The values for α and t from DSC data were entered into several models for solid state transformation; the values of $\ln k(T)_i$ versus $(RT)^{-1}$ were calculated.[140] However, isoparametric constants ($\ln k_{iso}$ and T_{iso}) were only observed when the Avrami model was used (Equation 3.8).

$$\left[-\ln(1-\alpha)\right]^{1/n} = \ln k(T) \qquad (3.8)$$

Avrami nucleation-and-growth models (where n_i=1, 2, 3, 4) consistently featured a common point of intersection ($\ln k_{iso}$,T_{iso}). Examples curves were shown in Figure 3.7. The use of the Avrami model for determining isoparametric constants has implied that it may be used to model cryo-transformations; however, the exact order of the Avrami transformation model cannot be assumed from the plots represented by Figure 3.7.

The values of $\ln k_{iso}$ and T_{iso} from samples, where T_{anneal}=30, 55, and 70 ℃, were reported in Table 3.5. The cryo-transformations of sample 4P10000 occurred at higher temperatures and faster rates than those from sample 10P4000. PVA-10000 polymer in sample 4P10000 appeared to hasten the subzero association of polymer chains. The sample PF10P4000 had higher values of $\ln k_{iso}$ than sample 10P4000; the higher value of $\ln k_{iso}$ for PF10P4000 was attributed to the heterogeneous nucleation of gel crystals from the surface of FWNTs. The $\ln k_{iso}$ and T_{iso} for solvent freezing within sample PS4P10000

were lower than the values that were reported for other samples, in which polymer gelation and solvent freezing occurred.

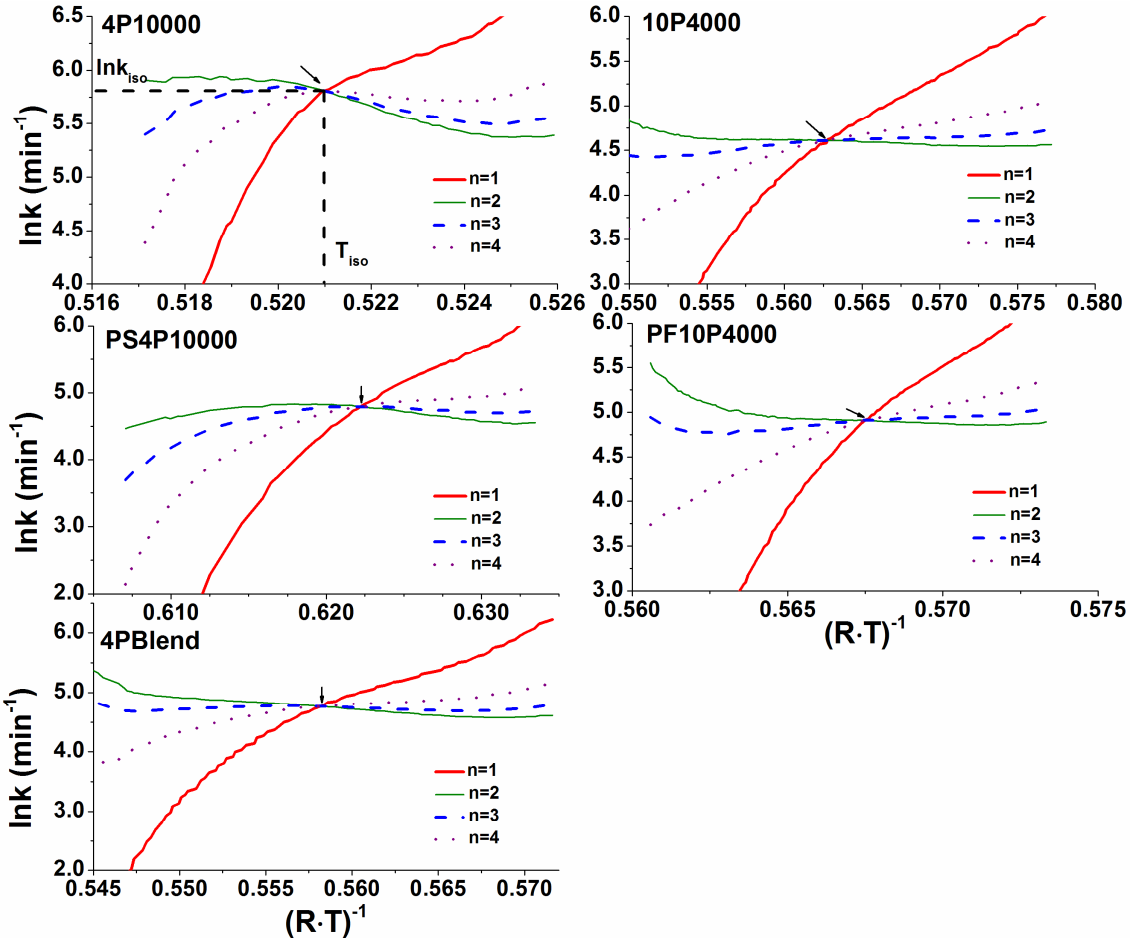

Figure 3.7. Example plots for determining isoparametric rate constant ($\ln k_{iso}$) and temperature (T_{iso}). The logarithmic isoparametric rate constants were determined by the use of Avrami reaction models, where n_i = 1, 2, 3, and 4 for samples that were annealed at 55 ℃ for 2 hrs prior to 2 ℃/min cooling.

Table 3.5. Avrami Fit Parameters to Cryo-transformations Upon Cooling at 2 °C/min.

T_{anneal} [a] (°C)	4P10000				10P4000			
	$\ln k_{iso}$ [b] (min^{-1})	T_{iso} [c] (°C)	n [d]	R^2 [e]	$\ln k_{iso}$ (min^{-1})	T_{iso} (°C)	n	R^2
30	4.9	-34	3.7	0.995	3.8	-52	3.0	0.998
55	4.8	-34	2.8	0.996	3.7	-51	2.7	0.999
70	5.5	-37	3.3	0.989	3.8	-52	2.8	0.999
T_{anneal} (°C)	PS4P10000				PF10P4000			
	$\ln k_{iso}$ (min^{-1})	T_{iso} (°C)	n	R^2	$\ln k_{iso}$ (min^{-1})	T_{iso} (°C)	n	R^2
30	3.6	-70	3.0	0.942	4.3	-47	3.3	0.998
55	3.3	-73	3.5	0.956	4.5	-53	3.0	0.999
70	3.9	-73	2.2	0.981	4.5	-47	3.5	0.999
T_{anneal} (°C)	4PBlend							
	$\ln k_{iso}$ (min^{-1})	T_{iso} (°C)	n	R^2				
30	4.8	-46	3.8	0.991				
55	4.8	-45	3.1	0.996				
70	4.8	-46	2.0	0.894				

a) T_{anneal} = annealing temperature, b) $\ln k_{iso}$ = isoparametric rate constant, c) T_{iso} = isoparametric temperature, d) n = order parameter of growth, e) R^2 = 'goodness of fit' parameter.

Equation 3.4 was simplified into Equation 3.9 to graphically represent $g(\alpha)$ with conversion, using data from a cooling rate of β_1 = -2 °C/min (Figure 3.8). The R^2 values for Avrami fits to $g(\alpha)$ were less than 0.9, which is less than ideal when ascribing a transformation model. The impingement of crystallites at higher conversions may have caused the transformations to deviate from Avrami behavior.[7] The Avrami model fitted most $g(\alpha)$ curves at conversions for $\alpha \leq 0.95$ and R^2 of ≥0.94. However, sample

4PBlend, where T_{anneal}=70 °C, and sample PS4P10000, where T_{anneal}=30 °C, did not fit the Avrami model well (Table 3.4).

$$g(\alpha) = \left(\frac{A_{\alpha,i}}{\beta_i} \cdot \frac{-E_\alpha}{R} \right) exp\left(\frac{-E_\alpha}{RT_\alpha} \right) ln \frac{T_\alpha}{T_0} \tag{3.8}$$

Since some overlap between the β_i curves was observed among homopolymer and hybrid samples (Figure 3.3), the values of n were interpreted according to heterogeneous nucleation-and-growth transformations. As obtained from Avrami fittings,[7] values of n were indicative of 2-3 dimensional growth (Table 3.4). The values of n for homopolymer solutions and 4PBlend were greatest among samples annealed at 30 °C. Interestingly, this annealing temperature of 30 °C also corresponded to the highest values of $S(T_f)$-$S(T_i)$ upon exothermic transformation (Figure 3.5). The sample of PF10P4000 had higher values of n than sample 10P4000.

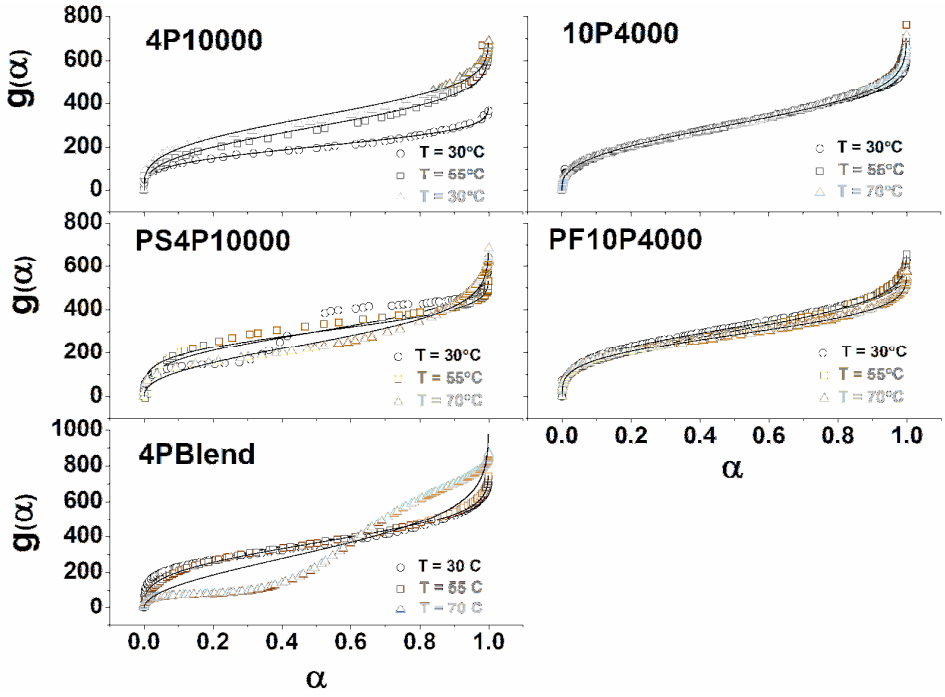

Figure 3.8. Avrami fits to $g(\alpha)$ for PVA solutions annealed at 30, 55, and 70 °C, where the cooling rate 2 °C/min.

It is worthwhile to note that the pattern of E_α plots from solutions of PVA homopolymer (in Figure 3.4) were similar to the $g(\alpha)$ plots (in Figure 3.8). The same observation has been noted for E_α plots of sample PF10P4000 and 4PBlend annealed at 70 and 30 °C, respectively. The cryo-transformation of semi-crystalline gel and solvent freezing adhered to a single Avrami nucleation-and-growth model. The freezing of solvent within a physical gel was known to exhibit Avrami nucleation-and-growth behavior, as observed in a study of cis-decalin that was frozen within amorphous matrices of physically and chemically crosslinked dimethylsiloxane.[153] Although the E_α plots for several, annealed samples PVA/CNT did not wholly exhibit increasing values for E_α, Avrami fits could be ascribed to their plots of $g(\alpha)$. Nucleation-and-growth processes that ascribe to parallel and serial transformation pathways are known to adhere to Avrami model fittings.[133] The value of E_α will steadily increase for parallel transformations; however,[133, 149-150] serial transformations can exhibit negative and positive values of dE_α/dT_α.[149] Serial transformation would imply the occurrence of interdependent processes for cryo-transformation; such that the development of interphases along filler/phase boundaries could incur cryo-gelation and/or solvent freezing.

The Avrami fits to the $g(\alpha)$ values for PS4P10000 and 4PBlend (where T_{anneal} =30 and 70 °C, respectively) did not overlay the experimental models. The irregular sinusoids for E_α plots were believed to represent changes in the mechanism of nucleation-and-growth. Therefore, the fit parameters in Table 3.5 were believed to represent the average kinetics for cryo-transformation. Further study would be required to determine the actual scheme of transformation.

3.4. Conclusions

This study has presented the use of isoconversional analysis to understand the effects of CNTs and the preparation of their dispersions on the nucleation-and-growth of PVA gel crystals and solvent freezing. The presence of CNTs, DP_w of the matrix polymer, and T_{anneal} were identified as parameters that could influence the nucleation-and-growth mechanisms of cryo-transformations. Further, the incorporation of CNTs was shown to change the pathway for exothermic transformation, as noted by plots of E_α. Parallel nucleation-and-growth mechanisms were believed to occur within regions of solvated homopolymer. The parallel pathway for transformation would suggest that the processes of gel crystallization and solvent freezing had occurred independently; such that neither phase was initiated by the other. Interdependent processes for transformation were proposed for the subzero cooling of CNT dispersion and blended PVA. The energetic responses from these systems implied the nucleation of cryo-transformation by the CNT interface, phase boundaries, polymer interphase, and within solvated homopolymer. Based on this study, the reproducibility of hybrid gel structures would be influenced by the technique for homogenizing CNT/polymer dispersions, filler loading, and thermal history. The time between sample preparation and polymer processing should also be considered for future study.

CHAPTER 4

EFFECT OF GEL AGING ON THE STRUCTURE AND PROPERTIES OF POLY(VINYL ALCOHOL)/ CARBON NANOTUBE FIBERS

4.1. Introduction

This study explores the effects of aging PVA gel fiber on the mechanical properties of CNT embedded fibers, drawing, and microstructure. The effect of gel aging on the mechanical properties of PVA gels[44] and tapes[32] has been reported in the literature but not for nanocomposites. Tanigami et al. have described the preparation of PVA cryo-gels from 10 wt. % polymer (having a *DP* of 5,000) dissolved within 80/20 v/v DMSO/water.[32] Cryo-gel films were heat pressed and aged in 10 ℃ water for 4 months, dried in a vacuum, and finally stretched by 23 X at 200 ℃. PVA tapes exhibited mechanical properties of 2.8 GPa in *TS* and 72 GPa in *TM*. The DSC thermograms of aged gels had shown low temperature endothermic peaks between 40 and 120 ℃. These transitions were noted to be crystallites which had enabled the stretching of films to high values of *DR*.

The goal of this chapter was to employ the gel aging technique and state drawing to enhance the tensile strength and modulus of PVA/CNT fibers. CNT composite and neat gel fibers were aged for several months within MeOH and MeOH/water solutions prior to gel characterization and processing. Gel aging was employed with the desire to improve the *DR* of CNT-embedded fibers at elevated temperatures. Since CNTs have

been observed to template the alignment of PVA chains through charge transfer (Chapter 2), high values of *DR* are expected to promote the molecular ordering of PVA at the interface of CNTs. The incorporation of CNTs at low loadings (of ~0.25 wt.% of the polymer) was done to aid their dispersion and molecular adhesion with matrix polymer. The structure/property/processing relationships for drawn fibers and aged gels were determined by use of mechanical, thermal, and WAXD analysis.

4.2. Experimental Section

4.2.1. Spinning dopes of PVA and PVA/CNT

Spinning dopes were prepared from a-PVA, having different values of DP_w. PVA homopolymers were termed PVA-10000 (which had a DP_w of 10,000 and 99% hydrolysis) and PVA-4000 (which had a DP_w of 4,000 and 99% hydrolysis); these polymers were made by Kuraray. PVA was dissolved in 80/20 *v/v* DMSO/water at ≈85 °C.

The concentrations of PVA-10000 and PVA-4000 in solution were optimized for gel spinning. Solutions of PVA-10000 were prepared at 3, 3.5, 4, and 5 wt.% polymer and dissolved in solvent at ≈85 °C for several hours. The circularity and diameters of fibers were used to determine the best concentration for fiber spinning. The aging technique was studied with polymer concentrations of 4 wt.% PVA-10000 and 10 wt.% PVA-4000. The sample prepared at 4 wt.% PVA-10000 was termed 4P10000. PVA-4000 solutions could not be gel-spun at concentrations < 10 wt.% polymer. Therefore, a solution was prepared at 10 wt.% PVA-4000, which was termed 10P4000.

SWNTs, having a purity >98%, came from CNI HiPCO process lot# P0247. The PVA/SWNT dispersion was prepared at 4 wt.% polymer and was referred to as

PS4P10000. FWNTs, having a purity of 99%, came from CNI lot# X0122UA. The PVA/FWNT dispersion was prepared at 10 wt.% polymer and was referred to as PF10P4000. The preparation of these dispersions was discussed in the Experimental Section of Chapter 3. Polymers within the spinning dopes of PS4P10000 and PF10P4000 were blends of sonicated and unsonicated polymer. The estimated values of relative DP_{wb}, for polymers composing CNT dispersions, were given in Table 3.1. Polymers within sample PS4P10000 have a relative DP_{wb} value of 8,900; these polymers were termed PVA-8,900. Polymers within sample PF10P4000 have a relative DP_{wb} value of 3,700; these polymers were termed PVA-3,700.

4.2.2. Fiber Gel-spinning

The syringe was heated to ≈60 ℃, and the syringe pump was set to feed spinning dope through an 18 gauge needle (of 1 mm in diameter) at 1.5 to 2 ml/min. Gel fiber was formed within spinning bath of -33 ± 7 ℃ MeOH that was chilled with dry ice. The take-up speed of gel fiber from the spinning bath ranged from 10-21 m/min. The jet stretch ratio (JSR) of gel-spun fiber was calculated from Equation 4.1, where v_{in} represented the feed velocity and v_{out} represented the output velocity.

$$JSR = \frac{v_{in}}{v_{out}} \qquad (4.1)$$

Continuous gel fiber was aged in 1 L solutions of MeOH or 50:50 (*v*/*v*) MeOH/water. Gel fibers that were aged in MeOH/water were also conditioned within 10 ℃ MeOH for 1 day; this coagulation step allowed gel fiber to be drawn at 100 ℃. Several gels that were aged in MeOH/water were also drawn cold, before they were conditioned within 10 ℃ MeOH. Fibers were drawn in stages/heating element temperatures (°C) of: S1/100, S2/160, S3/200, S4/220-250. The values of incremental

draw ratio equaled the ratio of fiber take-up rate to fiber feed rate. The cumulative draw ratio (*DR*) was the product of incremental draw ratios as from stages of cold and drawing. In summary, fibers were drawn in 4 stages, kept under vacuum for 3 days at 60 ℃, and annealed at 180 ℃ (such that the feed and take-up rates were the same) for the stage called S5/180. Select fiber of PVA/CNT was processed with an additional stage of oven drying at 85 °C under vacuum and then annealed at 220 °C. This stage was called S6/220, and it was used to stiffen the fiber.

4.2.3. Mechanical Testing

The tensile testing of drawn PVA and PVA/CNT fibers were performed at RT, using a gauge length of 25.4 mm, and at a strain rate of 0.1 %/sec. Fiber diameters and the values of circularity index (*CI*) were determined from SEM micrographs of at least 20 cross sections. *CI* was calculated from the ratio of perpendicular diameters; diameters were measured at angles of 0, 45, 90, and 135°. The calculation of *CI* was modified form the Adel version, in which the ratio of the longest to shortest diameter lengths were taken to find *CI*.[154]

The tensile testing of drawn fibers and the DMA of gel fibers were performed using the RSA III. The dynamic mechanical testing of aged gel fibers were conducted under constant strain, ambient conditions, and from 0.05 to 40 Hz. The applied load for pre-strained samples did not exceed 1 gram for testing within the linear elastic region. The storage modulus was reported as the average of two sample runs. Some drying of the sample may have occurred as the samples were tested under ambient conditions. The diameters of gel fiber, which were used for DMA testing, were obtained by optical

microscopy. Diameters were measured every 0.5 mm with optical microscopy; at least 18 measurements were taken.

4.2.4. WAXD

WAXD was performed on the Micro Max 002 X-ray generator and R-axis VI++ detector by Rigaku. Instrument settings included 45 kV power and a current of 0.66 mA. Radial scans were collected over 30 min. The values of X_c and *XS* were determined over the 10-50° range for 2θ.

The unit cell orientation for crystalline PVA (f_b) within PVA and PVA/CNT fibers was determined using the (200) and (101) diffraction planes, as described in Chapter 2.2.4).[86] The alignment of unit cell planes within aged gel fibers was analyzed qualitatively from meridonal and equatorial WAXD patterns (for *phi* angle values of 80-100° and 170-190°, respectively). Two bundles of ≥15 drawn fibers and two bundles of ≥ 5 gel fibers were used for WAXD analysis. The values of X_c, *XS*, f_c, and d-spacing were reported for each fiber bundle.

4.2.5. Thermal Analysis

MDSC experiments went as follows: sample equilibration at -20 °C, modulation of ± 0.796 °C of the average temperature every 60 s, and a temperature ramp up to 300 °C. The average rate of heating was 5 °C/min in nitrogen. The thermograms of R-heat capacity, NR-heat capacity, and total heat capacity were from the first heating cycle.

TGA measurements were performed on gel fibers that were placed within a platinum holding pan. Heating was performed at 10 °C/min in nitrogen gas.

4.3. Results and Discussion

4.3.1. Optimizing the Circularity of Gel-spun PVA-10000 Fibers

PVA solutions of 3-5 wt.% PVA-10000 were gel-spun and stretched with four stages of elevated temperature drawing (S4/200 or S4/250). The as-spun gels of homopolymer were noted to be transparent. The drawing conditions and geometries of these fibers were described in Table 4.1. Samples were labeled according to the weight fraction of PVA-10000 in the spinning dope.

Fibers prepared from 3.5 and 4 wt.% PVA had similar diameters sizes; however the fiber cross sections of the 4P10000 fibers were more uniform and circular (Table 4.1 and Figure 4.1). The circularity indices for fibers of 3P10000 and 3.5P10000 were *CI*=0.7. The value of *CI* for 4P10000 was 0.9. Sample 5P10000, from 5 wt.% PVA-10000, had a smooth but oval cross section. The diameters of 5P10000 fibers were considerably larger than fibers produced from solutions of 3-4 wt.% PVA-10000. Therefore, a concentration of 4 wt.% PVA-10000 was used to test the processing/structure/property relationships of PVA and PVA/CNT fibers.

Table 4.1. PVA-10000 Fiber Cross-sections.

Sample Designation	**3.5P10000**	**4P10000**	**5P10000**
Total Draw Stages/ Final Draw Temp (°C)	**S4/220**	**S4/220**	**S4/250**
PVA (wt.%)[a)]	3.5	4	5
JSR[b)]	5.3	5.3	5.3
DR[c)]	5.0 X	5.2 X	5.4 X
φ_f[d)] **(µm)**	29 ± 3	29 ± 3	43 ± 3
CI[e)]	0.72 ± 0.16	0.91 ± 0.07	0.78 ± 0.07

a) wt.% = weight percent, b) *JSR* = jet stretch ratio, c) *DR* = cumulative draw ratio, d) φ_f = the diameters of drawn fibers according to SEM micrographs, and e) *CI* = circularity index of drawn fibers according SEM micrographs.

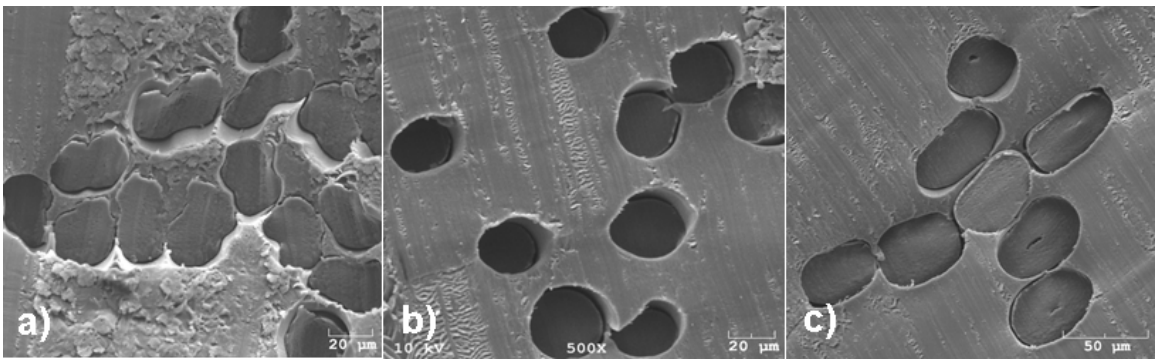

Figure 4.1. Cross-sections of fibers spun from solutions of a) 3.5, b) 4, and c) 5 wt.% PVA-10000.

Fibers of 4P10000 (in Table 4.1 and Figure 4.1) were drawn at S4/220 and S5/180. The values of *TS* and *TM* for 4P10000 fibers had improved after S5/180 processing. The values of *TS*=0.92 ± 0.02 GPa and *TM* =18 ± 5 GPa were reported for S4/220 fibers. The values of *TS*=1.01 ± 0.07 GPa and *TM* =36 ± 4 GPa were reported for S5/180 fibers. The tensile strain values were the same for both samples: 6 ± 1%.

4.3.2. Aging Gels of PVA-10000

Gel fibers were prepared from solutions of PVA-10000 and aged in MeOH or MeOH/water at 10 ℃. The properties and microstructures of S5/180 drawn fibers and precursor gels were described herein.

4.3.2.1. Drawn 4P10000 Fibers from Gels Aged in MeOH

Fibers drawn from gels aged in MeOH for 1 and 22 days were termed 4P10000-1MeOH and 4P10000-22MeOH, respectively. Sample 4P10000-1MeOH was drawn to a higher value of *DR* than sample 4P10000-22MeOH (6.1 X versus 4.1 X in Table 4.2). The cross sections of 4P10000-22MeOH fiber had varied more in size and their geometries were more irregular (Table 4.2 and Figure 4.2). The diameter of 4P10000-1MeOH fiber was 22 ± 2 μm, and the diameter of 4P10000-22MeOH fiber was 34 ± 10

μm. The *TS* of drawn 4P10000-1MeOH fibers was ~9 X the strength of drawn 4P10000-22MeOH fibers and the *TM* of drawn 4P10000-1MeOH fiber was twice the value of drawn 4P10000-1MeOH fiber. Therefore, the mechanical properties of drawn 4P10000 fibers had decreased with MeOH aging time. A similar behavior was reported in Minus; such that the tensile strengths of PVA fibers had decreased from ~0.9 to 0.5 GPa with gel aging in -30 ℃ MeOH for 1-8 days.[42]

Table 4.2. Mechanical Properties of Drawn 4P10000 Fibers from Gels Aged in MeOH.

Sample Designation	**4P10000-1MeOH**	**4P10000-22MeOH**
MeOH Aging Time (Days)	1	22
JSR [a)]	8.1 X	8.1 X
DR [b)]	6.1 X	4.1 X
φ_f [c)] **(μm)**	22 ± 2	34 ± 10
CI [d)]	0.83 ± 0.08	0.79 ± 0.09
TS [e)] **(GPa)**	1.15 ± 0.15	0.13 ± 0.02
Maximum *TS* (GPa)	1.37	0.16
TM [f)] **(GPa)**	19 ± 2	8 ± 1
Maximum *TM* (GPa)	22	9
Strain at Break (%)	5.5 ± 0.8	5.3 ± 0.4

a) *JSR* = jet stretch ratio b) *DR* = cumulative draw ratio for drawing past coagulation, c) φ_f = diameters of drawn fibers according to SEM micrographs, d) *CI* = circularity index of drawn fibers according SEM micrographs, e) *TS* = tensile strength, and f) *TM* = tensile modulus.

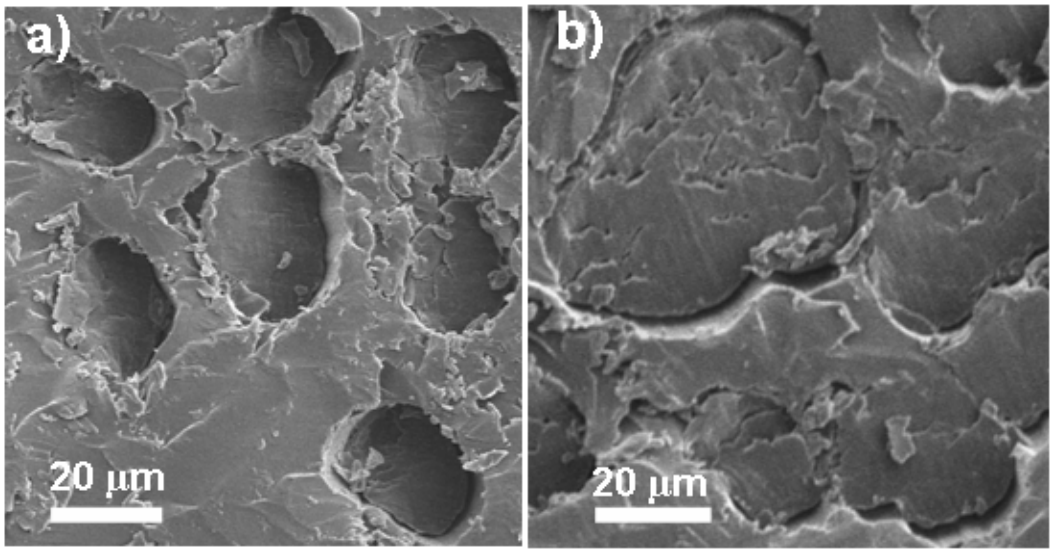

Figure 4.2. Cross-sections of drawn 4P10000 fibers from gels aged in MeOH for a) 1 and b) 22 days.

MeOH aging has influenced the behavior of solvent imbibed within drawn fibers (Figure 4.3a). The NR-heat capacity curve for drawn 4P10000-1MeOH fiber has revealed the presence of water-rich and DMSO-rich phases in the fiber microstructure. Similar thermal events were observed among the drawn fibers of PVA and PVA/SWNT (Figure 2.3). As discussed in Chapter 2, solvent evaporation was accompanied by the molecular relaxation of solvated polymer. The peak temperature for water evaporation (T_{evap1} = 75 ℃) from drawn 4P10000-1MeOH fiber were slightly lower than the water evaporation temperature for 4P10000-22MeOH (T_{evap1} = 87 ℃). The value of T_{evap1} of drawn fibers had shifted to temperatures above 100 ℃ after aging gel fiber in MeOH for 22 days. Therefore, molecular impurities were removed from the water-rich phase of the MeOH aged gel fiber.

Hydrogen bonding between water molecules and PVA hydroxyl groups are expected to reduce the evaporation temperature of water, which occurs at 100 ℃. The

debonding of PVA hydroxyl groups from water molecules must have occurred upon the phase separation of water from PVA. There was further evidence of unbound water (where evaporation occurred at temperatures greater than 100 °C) and water bonded to PVA (where evaporation occurred at temperatures less than 100 °C) in Figure 4.3a. The TGA of 4P10000 gels aged in MeOH will be discussed in an upcoming section.

The DMSO-rich phase within 4P10000-22MeOH fiber was negligible; however, the evaporation of DMSO from drawn fibers of 4P10000-1MeOH was apparent (Figure 4.3). Although fibers were prepared from a greater volume fraction of DMSO than water, MeOH aging had favored the removal of DMSO from precursor gel. This behavior will be discussed in further detail.

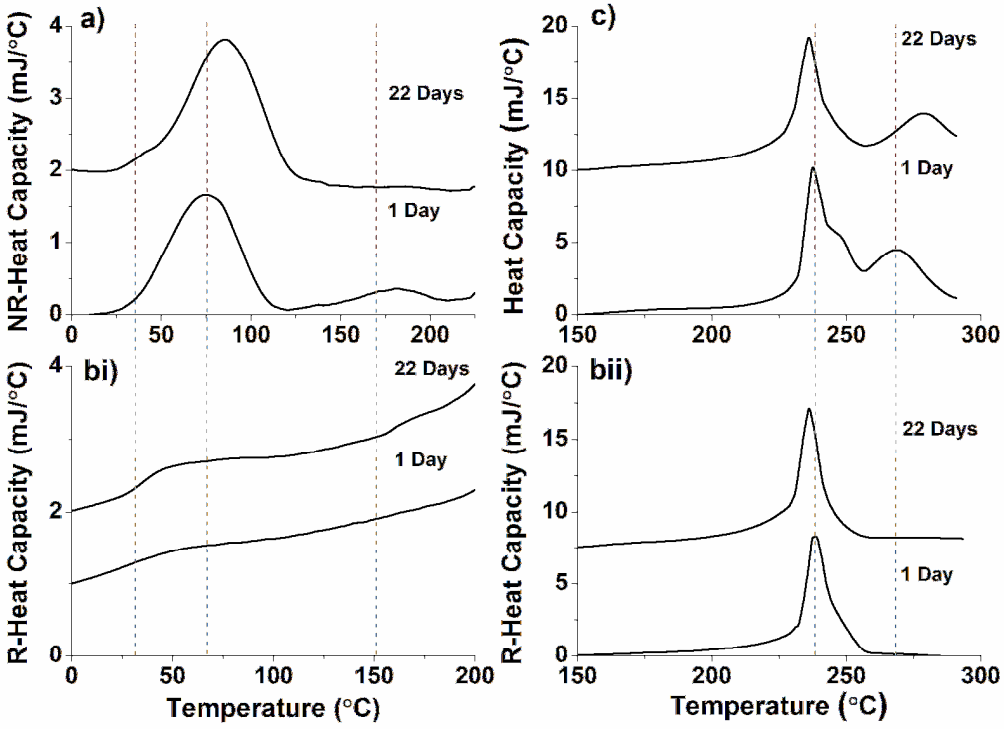

Figure 4.3. MDSC thermograms of drawn 4P10000 fibers from gels aged in MeOH: a) NR-heat capacity, b) R-heat capacity for i) 0-200 °C and ii) 150-300 °C, and c) total heat capacity from tests in nitrogen.

The temperature range for water evaporation had overlapped the T_g of 4P10000 fibers that were drawn from gels aged in MeOH (Figure 4.3a,bi). Dried PVA has a T_g of 85 ℃;[35] therefore, the observed T_g values were indicative of solvated polymer. After 22 days of MeOH aging, a low temperature shoulder was observed along T_{evap1}; this shoulder coincided with the T_g of those 4P10000-22MeOH fibers. Aged polymers are known to exhibit enthalpic relaxation peaks within the DSC thermogram. Peaks indicative of enthalpic relaxation have occurred in the vicinity of the T_g and within the total and NR-heat capacity thermograms.

Gel aging affected the drawing and melting behaviors of 4P10000 fibers. The melting temperature of drawn 4P10000 fibers was the highest after 1 day of gel aging in MeOH (Figure 4.3b); furthermore, a high temperature shoulder was observed along the dominate melting peak at ~230 ℃. The drawing of 4P10000 fiber to higher values of *DR* was shown to aid the formation of higher melting temperature crystals. The thermal degradation of PVA was represented by the high temperature transition that began at ~260 ℃. Interestingly, the degradation of PVA in sample 4P10000-1MeOH began at lower temperature than for sample 4P10000-22MeOH. The conformations of crystalline PVA residing in sample 4P10000-1MeOH were believed to be more conducive to high temperature degradation.

The WAXD analysis of drawn 4P10000 fibers was shown in Figure 4.4 and Table 4.3. Drawn 4P10000-1MeOH fibers were more crystalline than the 4P10000-22MeOH fibers; the values of X_c for these fibers were ~63 % and ~44%, respectively. The orientation of PVA crystals (f_b) within drawn 4P10000 fibers was not significantly affected by differences in *DR* (Table 4.3); f_b values were ~0.88. Incremental increases in

the orientation of PVA crystals seem to require larger increases between the *DR* of fiber. (Similarly, PVA fibers that were drawn by 5.2 and 7.5 X had f_b values of 0.88/0.89, according to Table 2.4).

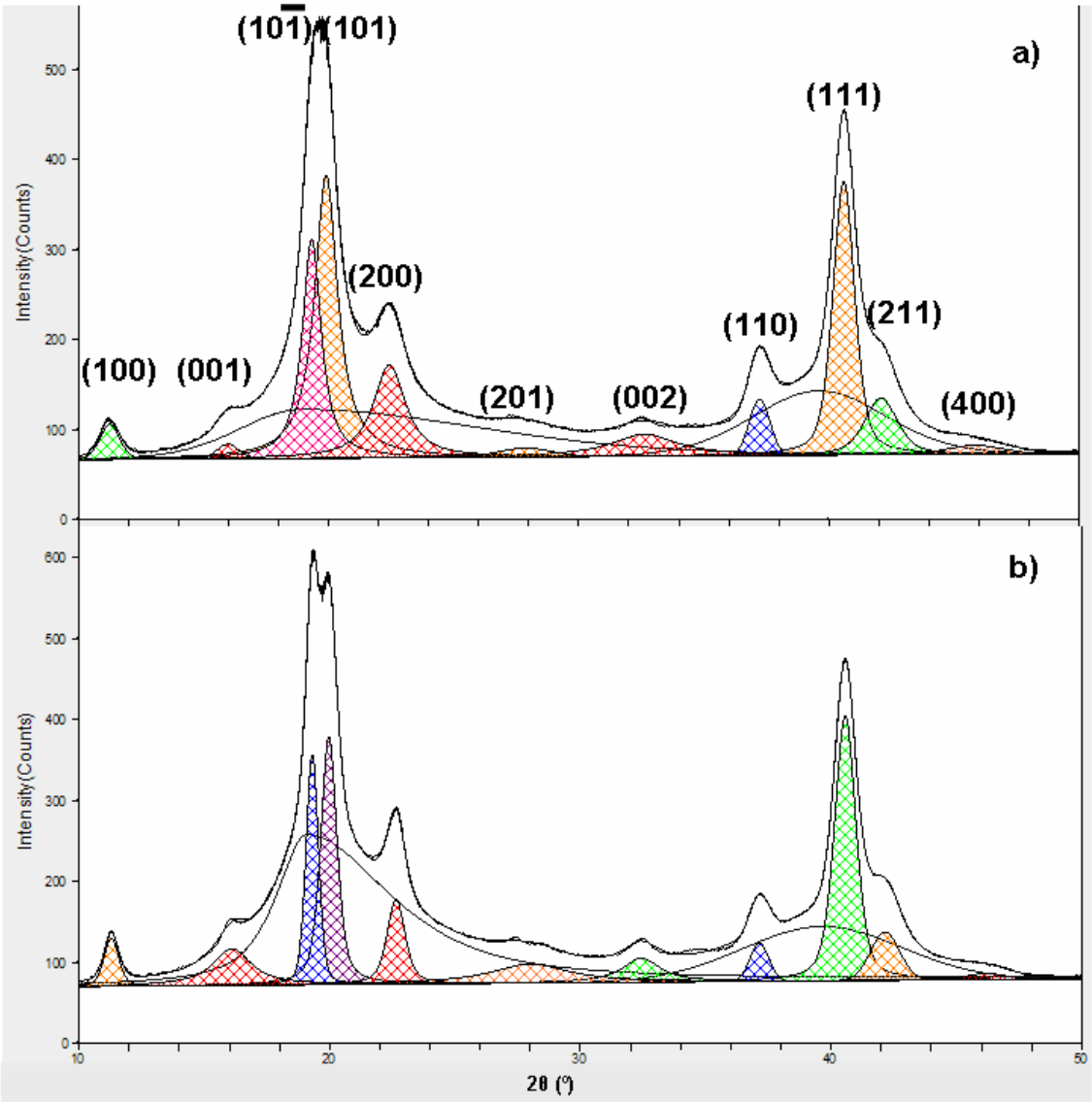

Figure 4.4. WAXD analysis from radial scans of drawn 4P10000 fibers from gels aged in MeOH for a) 1 and b) 22 days. Scattering from amorphous polymer was represented by unfilled peaks; diffraction from planes of the PVA unit cell was represented by filled peaks.[30, 42, 97]

Table 4.3. WAXD Characterization of Drawn 4P10000 Fibers from Gels Aged in MeOH.

Sample Designation		**4P10000-1MeOH**	**4P10000-22MeOH**
MeOH Aging Time		**1 Day**	**22 Days**
JSR [a)]		8.1 X	8.1 X
DR [b)]		6.1 X	4.1 X
X_c [c)] **(%)**		64, 62	42, 45
f_b [d)]		0.88, 0.89	0.88, 0.87
XS [d)] **(nm)**	**(100)**	8, 8	11, 11
	(001)	9, 8	5, 5
	(110)	9, 9	9, 9
	(111)	8, 8	8, 8
d-spacing (nm)	**(100)**	0.79, 0.79	0.78, 0.78
	(001)	0.55, 0.55	0.55, 0.55
	(110)	0.24, 0.24	0.24, 0.24
	(111)	0.22, 0.22	0.22, 0.22

a) *JSR* = jet stretch ratio b) *DR* = cumulative draw ratio, c) X_c = crystallinity of polymer, d) f_b = orientation of PVA unit cell crystals along the molecular *b*-axis, and e) *XS* = crystal size.

The d-spacings and crystal sizes of the 100, 001, 110, and 111 planes of the PVA unit cell are given in Table 4.3. These planes of diffraction represented the strongest peaks (Figure 4.4), and the 2θ values of these planes are illustrated within Figure 4.4. The d-spacing of prominent planes within the PVA unit cell did not vary between drawn fibers of 4P10000-1MeOH and 4P10000-22MeOH (Table 4.3). However, the crystal sizes of PVA along the *a*-axis were slightly larger within the 4P10000-22MeOH fibers than for the 4P10000-1MeOH fibers. The crystal sizes of 110 planes, which are perpendicular to the molecular axis, were similar for these fibers. The $(10\bar{1})$ and (101)

planes represented intermolecular hydrogen bonding between the monomer units of two different PVA chains.

4.3.2.2. 4P10000 Gel Fiber Aged in MeOH

This section has described the mechanical and structural properties of gel fibers that were derived from solutions of 4P10000 and aged in 10 ℃ MeOH. Storage modulus ($E'(f)$) was observed to increase with gel aging time in MeOH (Figure 4.5). $E'(f)$ values were observed to increase gradually with frequency; whereas, a fully developed network would exhibit a plateau modulus over several magnitudes of oscillation.[26] The loss modulus ($E''(f)$) of 4P10000 gel fiber aged in MeOH is reported in Appendix C.

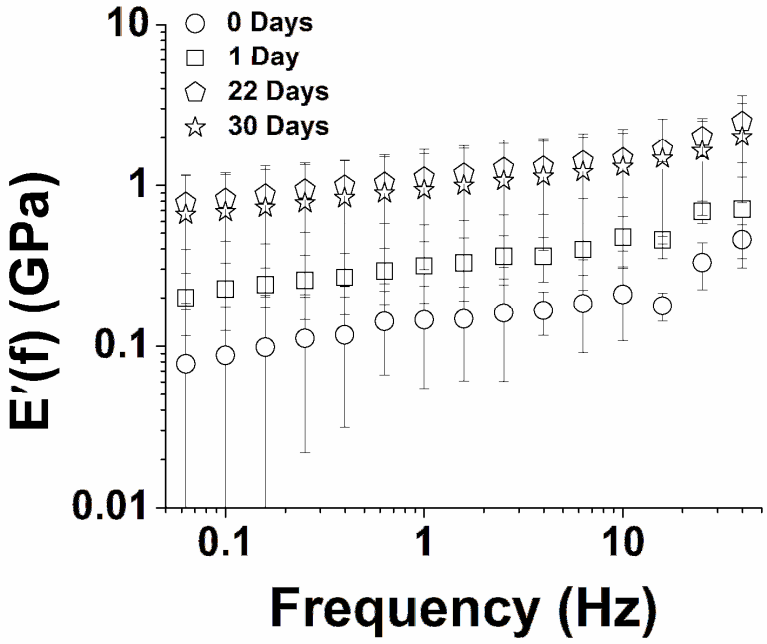

Figure 4.5. Storage modulus of 4P10000 gel fibers aged in MeOH.

A temperature range of RT to 200 ℃ was used to characterize the behavior of solvent imbibed within gel-spun fibers (Figure 4.6). (The same range of temperatures were used for the TGA analysis of solvent contained within stage drawn fibers, in Figure 2.4). More than 80% of the unaged, as spun gel fiber was composed of solvent (Figure 4.6a). After 1 day of MeOH aging, this value was significantly reduced to 5% solvent.

According to Equation 1.2-1.4, the weight fraction of imbibed solvent (parameter Q) will affect the storage modulus of gels. Solvent swelling was expected to decrease $E'(f)$, but the removal of solvent was expected to increase the value of $E'(f)$. Parameter v_{2r} would be the same for each sample of gel since each sample came from the same batch of as-spun gel fiber. The $E'(f)$ increased with MeOH aging up to 22 days; such that the coagulation of PVA polymer would be represented by an increase in v_2 and the removal of solvent. Therefore, the trends observed from DMA and TGA qualitatively support the structure/property relationships that were given by Equations 1.2-1.4. The coagulation of 4P10000-22 MeOH-Gel was also believed to have reduced its drawability.

The DTGA analysis of 4P10000 gel fibers (Figure 4.6b) was suggestive of changes to the composition of DMSO/water within the gel fiber. According to Figure 2.4b2, an 80/20 mixture of DMSO/water had fully evaporated at a temperature of 150 ℃. The DTGA plot of unaged gel fibers showed differential weight loss at temperatures >150 ℃. DMSO appeared to phase separate from water within the spinning bath and during the process of MeOH aging. The Hildebrand solubility parameters (δ_t) for DMSO, water, and MeOH were 26.7, 47.8, and 29.6 $MPa^{1/2}$, respectively.[155] Since the values of δ_t for DMSO was most similar to the value for MeOH, DMSO was expected to readily diffuse into MeOH from the mixture of DMSO/water.

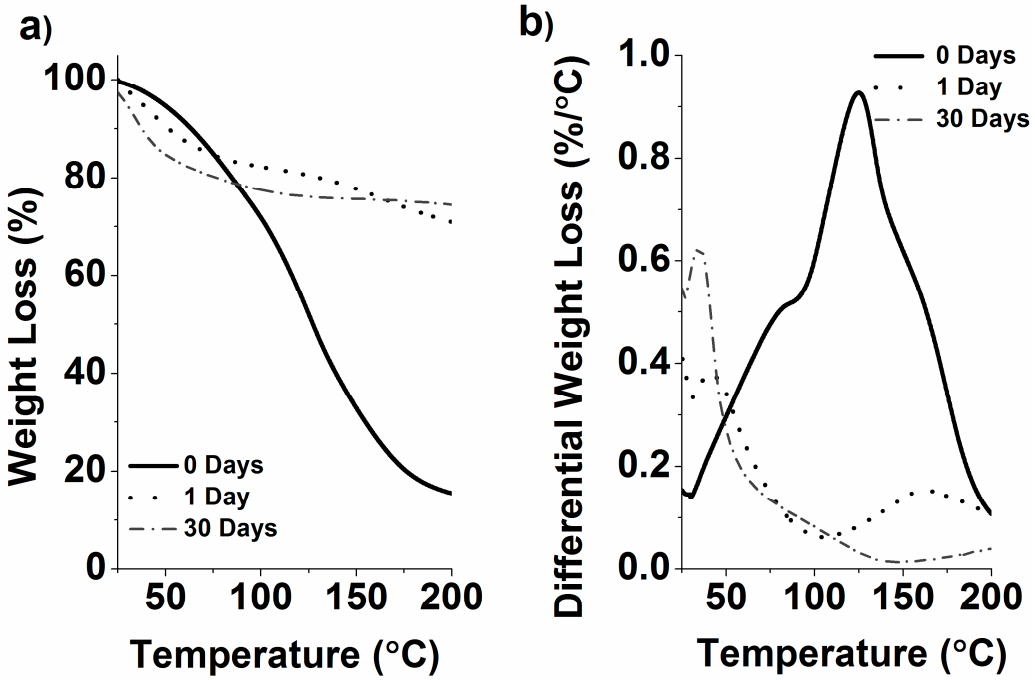

Figure 4.6. 4P10000 gel fibers aged in MeOH: a) TGA and b) DTGA at 10 ℃/min in nitrogen.

Between 22-30 days of MeOH aging, the weight fraction of imbibed solvent had increased slightly to 10 %. This increase in solvent swelling was likely due to the influx of water or MeOH/water. The DTGA plot of 4P10000 gel after 30 days of aging showed a lower peak temperature for differential weight loss. This behavior was attributed to the counter-diffusion of MeOH into gel fiber. The phenonmeon of solvent diffusion and counterdiffusion with aging time will be discussed for other PVA gels and MeOH/water aging.

The WAXD analysis of 4P10000 gels was reported in Table 4.4 and Figure 4.7. Gel samples were designated by MeOH aging time and the word 'gel' in Table 4.4. A significant increase in the percent crystallinity of gel fibers was observed after 1 day of MeOH aging. The initial crystallnity of as-spun gel fiber was 5%; this value increased to

~46 % upon aging. Differences between the X_c of gels aged for up to 30 days were neglibile (based on the error associated with its mode of determination). The process of stage drawing had a considerable influence on the overall crystallinity of fibers drawn from 4P10000-1MeOH-Gel; the X_c increased by ~16 % (Table 4.3 and 4.4). In contrast, the X_c values of drawn and gel fibers of 4P10000-22MeOH were similar.

Table 4.4. WAXD Characterization of 4P10000 Gel Fibers Aged in MeOH.

Sample Designation		**4P10000-0MeOH-Gel**	**4P10000-1MeOH-Gel**	**4P10000-22MeOH-Gel**	**4P10000-30MeOH-Gel**
Gel Fiber Aging Time (Days)		0	1	22	30
X_c [a] (%)		5, 5	48, 46	47, 46	48, 43
XS [b] (nm)	**(100)**	3, 3	5, 5	5, 5	5, 5
	(111)	5, 5	5, 5	5, 5	5, 5
d-spacing	**(100)**	0.68, 0.68	0.76, 0.76	0.76, 0.76	0.76, 0.76
	(110)	-	0.24, 0.24	0.24, 0.24	0.24, 0.24
	(111)	0.22, 0.22	0.22, 0.22	0.22, 0.22	0.22, 0.22

Crystal sizes were not reported for the 110 planes of low peak intensity. a) X_c = crystallinity of gel fiber and b) *XS* = crystal size.

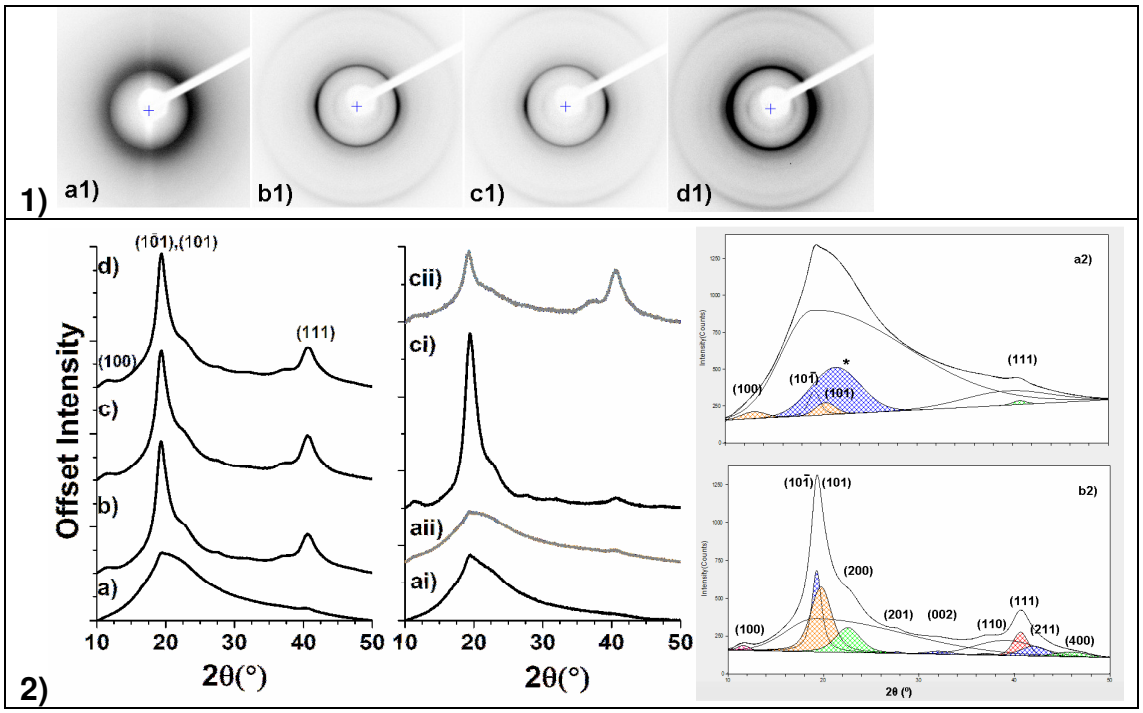

Figure 4.7. WAXD analysis of 4P10000 gel fibers with aging time a) 0, b) 1, c) 22, and d) 30 days in MeOH: 1) diffraction patterns, 2) integrated radial scans, equatorial scans (ai and ci), and meridonal scan (aii and cii). (*) in a2) represents solvent scattering.

Parameters of crystal size and d-spacing were reported for the (001) planes of fibers that were drawn from gels aged in MeOH (Figure 4.4); however, a diffraction peak from (001) planes was not detected among gel fiber. Since diffraction from (100) and (110) planes (perpendicular to the molecular axis) were detected, PVA chains were believed to initially organize into two-dimensional sheets along the *a*- and *b*-axis upon gelation. The dimensionality of organized PVA chains increased from a two to three dimensional form upon elevated temperature drawing (Figure 4.4). The crystal size and d-spacing increased along the *a*-axis after 1 day of aging, but these values did not change upon aging after 22 and 30 days (Table 4.4). The d-spacing between *a*-axis planes increased from 0.68 to 0.76 nm after 1 day of aging and remained at 0.76 nm within gel

fibers aged for 22 and 30 days of MeOH aging. After stage drawing, the d-spacing between *a*-axis planes equaled 0.79 nm.

Hydrogen bonding between PVA chains and organized molecules of water were believed to occur between associated chains of PVA. Based on the bond length distance between the oxygen and hydrogen atom of water, several molecules of water could organize between two monomer units of PVA. The deconvoluted diffraction pattern of as-spun gel fiber featured a broad peak at $2\theta \approx 21.7$ (Figure 4.7a2). This peak was attributed to scattering by solvent. Interestingly, this peak was only present within the WAXD analysis of as-spun gel fiber and not for the aged gel or drawn fiber. The ordered PVA within as-spun gel polymer was therefore believed to configure according to the Sakurada model, in which the disruption of intermolecular hydrogen bonding occurred along the *a*-axis; however, van der Waals bonding along the *c*-axis was not observed (Figure 1.1).[29] Nevertheless, the unit cell configuration of PVA within aged gels and drawn fiber is believed to adhere to the Bunn model, wherein the intermolecular hydrogen bonding that occurs along the *c*-axis was influenced by the solvent (Figure 1.1).[29]

Since the (101) and $(10\bar{1})$ planes overlapped, the d-spacing was reported as the average distance between their deconvoluted peaks. The d-spacing characteristics of $(10\bar{1})$/(101) planes were ~0.45 nm for the as-spun gel, aged gel, and even the drawn fibers. The study of PVA gelation by Hoshino et al. had shown the d-spacing of the $(10\bar{1})$/(101) peaks to be equal to 0.43 nm, after 96 hours of aging cryogel that was prepared from 80/20 v/v DMSO/water.[24] These values were believed to represent the intercalation of water within ordered PVA. The infusion of water within the crystal

structure of PVA was reported to enlarge the d-spacing of the $(10\bar{1})$/(101) planes from that of an unsaturated crystals.[156] The effects of water on the ordering of PVA chains in the gel state will be discussed in this study for other PVA gels.

Upon drawing aged gel fibers, the crystal size along the *a*-axis became larger (to values greater than 5 nm), and d-spacing was increased by a few angstroms (from 0.76 to 0.78/0.79 nm) (Table 4.3 and 4.4). The d-spacing of the (100) planes is comparable to the lengths reported by Bunn, where the *a*-axis d-spacing equals 0.778 nm.[29] PVA crystals grew along the *c*-axis upon fiber drawing; whereas, their growth was none existent within the gel fiber.

After 22 days of MeOH aging, the (111) plane was preferentially oriented along the meridonal axis and the $(10\bar{1})$/(101) planes were preferentially oriented along the equatorial axis (Figure 4.7). However, diffracting planes within the as-spun gel fiber did not exhibit any preferential alignment. In Tanigami et al, the WAXD analysis was reported for a dried aged film. The process of drying was believed to cause film shrinkage, which had caused the mild orientation of the (101) plane along the film axis.[29] Similarly, the changing volume fraction and swelling behavior of polymer within aged gels may have incurred the preferrential alignment of these diffracting planes.

4.3.2.3. Drawn 4P10000 Fibers from Gels Aged in MeOH/Water

The mechanical properties of drawn fibers that were prepared from gels aged in 50:50 MeOH/water at 10 ℃ were recorded in Table 4.5. Fiber drawn from gel that was aged for 1 day in MeOH/water had the highest *TS* of 0.90 ± 0.10 GPa, and the highest *TM* of 13 ± 1 GPa. The process of gel aging for ≥1 day in MeOH/water had produced PVA fibers with lower mechanical properties. The *TS* and *TM* values of fibers drawn from gels aged for 120-155 days in MeOH/water were significantly lower than those values reported for gel aged for up to 69 days. Also, 4P10000-1MeOHWater fiber was less drawable than 4P10000-1MeOH fiber (Table 4.3 and 4.5).

The circularity of drawn fibers that were drawn from gels aged in MeOH/water for ≥69 days was influenced by thick-and-thin areas along the fiber's length. The dynamic process of solvent diffusion may have resulted in these irregularities among the diameters of drawn fibers (Table 4.5 and Figure 4.8).

The NR-heat capacities from the first endothermic peaks of drawn 4P10000-MeOH/Water fibers had increased significantly with gel fiber aging for 120-155 days (Figure 4.9a). This increase has been attributed to the counter-diffusion of pure water into the precursor gel fiber. Phases of unbound water and solvated polymer were believed to impair the mechanical performance of fibers drawn from gels aged for 120 and 155 days in MeOH/water. DMSO was more readily removed from the fiber structure after 1 day of MeOH/water aging (Figure 4.9b) in comparison to fibers drawn from gels aged in MeOH for 1 day (Figure 4.3b). The composition of imbibed solvent, as a function of MeOH/water aging time, was also investigated from the TGA of aged gel fibers.

Table 4.5. Mechanical Properties of Drawn 4P10000 Fibers from Gels Aged in MeOH/Water.

Sample Designation	**4P10000-1MeOH/ Water**	**4P10000-69 MeOH/ Water**	**4P10000-120 MeOH/ Water**	**4P10000-155 MeOH/ Water**
MeOH/Water Aging Time (Days)	1	69	120	155*
JSR [a)]	8.1 X	8.1 X	8.1 X	8.1 X
DR [b)]	4.2 X	4.2 X	3.7 X	4.0 X
φ_f [c)] **(μm)**	26 ± 2	30 ± 2	30 ± 7	29 ± 5
CI [d)]	0.76 ± 0.15	0.84 ± 0.12	0.64 ± 0.18	0.73 ± 0.12
TS [e)] **(GPa)**	0.90 ± 0.10	0.73 ± 0.12	0.49 ± 0.03	0.54 ± 0.06
Maximum *TS* (GPa)	1.07	0.97	0.54	0.64
TM [f)] **(GPa)**	13 ± 1	11 ± 2	12 ± 1	9 ± 1
Maximum *TM* (GPa)	16	16	13	11
Strain at Break (%)	5.8 ± 0.7	7.1 ± 2.2	4.7 ± 0.3	5.4 ± 0.5

a) *JSR* = jet stretch ratio, b) *DR* = cumulative draw ratio for drawing past coagulation, c) φ_f = diameters of drawn fibers according to SEM micrographs, d) *CI* = circularity index of drawn fibers according SEM micrographs, e) *TS* = tensile strength, and f) *TM* = tensile modulus. *Samples drawn with 4 stages of elevated temperature drawing; all other samples were drawn cold, coagulated in MeOH for 1 day, and then drawn in stages.

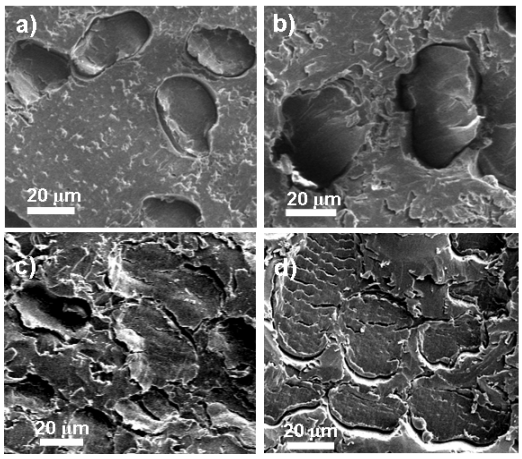

Figure 4.8. Cross-sections of 4P10000 fibers drawn from gels aged in MeOH/water for a) 1, b) 69, c) 120, and d) 155 days.

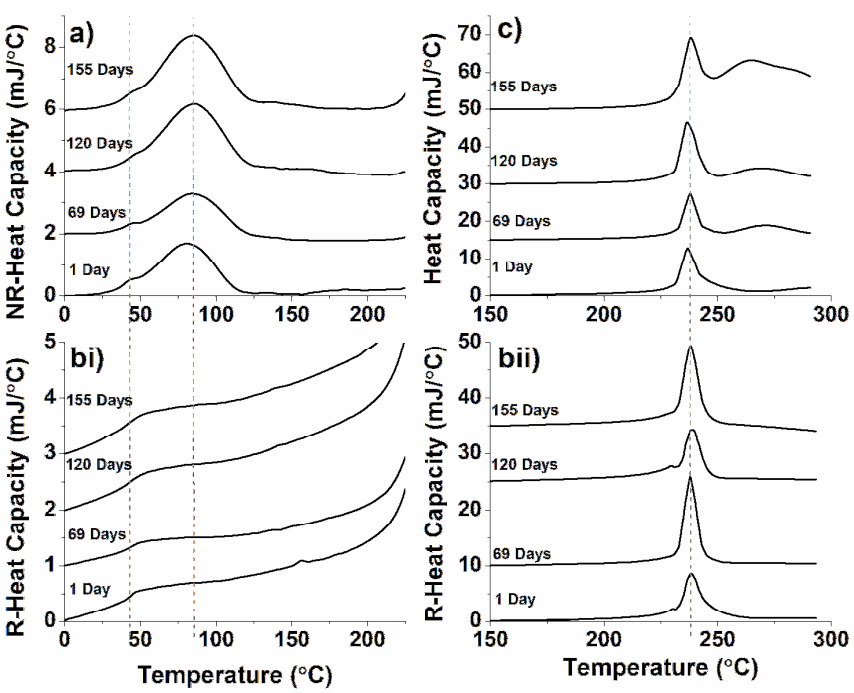

Figure 4.9. MDSC thermograms of drawn 4P10000 fibers from gels aged in MeOH/water: a) NR-heat capacity, b) R-heat capacity for i) 0-200 °C and ii) 150-300 °C, and c) total heat capacity from tests in nitrogen.

Polymer within drawn 4P10000-1MeOHWater fiber had expressed enthalpic relaxation. This behavior was previously exhibited by drawn 4P10000-22MeOH fibers but not from drawn 4P10000-1MeOH fibers. The low temperature shoulder occurred between 25-50 °C and shifted to slightly higher temperatures after 120 days of gel fiber aging (Figure 4.9a).

The range of crystalline melting for drawn 4P10000-1MeOH fiber was similar to the melting behavior from drawn 4P10000-1MeOH/Water fibers; nevertheless, the 4P10000-1MeOH/Water fiber was less crystalline than the 4P10000-1MeOH fiber (63% versus ~57 %, respectively in Table 4.3 and 4.6). The dimensions of PVA crystals within 4P10000-1MeOH/Water fibers were shown to be similar to those within 4P10000-1MeOH fibers.

Table 4.6. WAXD Characterization of Drawn 4P10000 Fibers from Gels Aged in MeOH/Water.

Sample Designation		**4P10000-1MeOH/ Water**	**4P10000-69MeOH/ Water**	**4P10000-122MeOH/ Water**	**4P10000-155MeOH/ Water**
MeOH/Water Aging Time (Days)		**1**	**69**	**122**	**155**
JSR [a]		8.1 X	8.1 X	8.1 X	8.1 X
DR [b]		4.2 X	4.2 X	3.7 X	4.0 X
X_c [c]		58, 55	52, 54	51, 50	52, 60
f_b [d]		0.87, 0.87	0.87, 0.88	0.83, 0.84	0.88, 0.86
***XS* (nm)**	**(100)**	9, 9	8, 8	7, 7	9, 8
	(001)	9, 6	5, 5	4, 3	6, 3
	(010)	9, 9	7, 7	7, 7	9, 8
	(111)	8, 8	7, 7	7, 7	8, 7
d-spacing (nm)	**(100)**	0.78, 0.78	0.78, 0.79	0.78, 0.78	0.78, 0.78
	(001)	0.55, 0.55	0.56, 0.56	0.55, 0.55	0.55, 0.55
	(110)	0.24, 0.24	0.24, 0.24	0.24, 0.24	0.24, 0.24
	(111)	0.22, 0.22	0.22, 0.22	0.22, 0.22	0.22, 0.22

a) *JSR* = jet stretch ratio, b) *DR* = cumulative draw ratio for drawing past coagulation, c) X_c = crystallinity of polymer, d) f_b = orientation of PVA unit cell crystals along the molecular *b*-axis, and e) *XS* = crystal size

4.3.2.4. 4P10000 Gel Fiber Aged in MeOH/Water

The mechanical properties and microstructure of 4P10000 gels that were aged in MeOH/water are discussed in this section. $E'(f)$ values for 4P10000 gels aged in MeOH/water had increased gradually with frequency, as was observed for gels aged in MeOH (Figure 4.5 and 4.10). Therefore, the gel network was not fully developed. The stiffest gels were observed after 120 days of MeOH/water aging; gels aged for 155 days were slightly less stiff. The stiffening of gels with aging time was also observed among samples aged in MeOH for up to 22 days.

The counter-diffusion of solvent into the gel structure had weakened 4P10000 gels in instances of MeOH aging for 30 days and MeOH/water aging for 155 days (Figure 4.5 and 4.10). DMSO readily diffused from the gel after 1 day of MeOH/water aging; the total solvent content had been reduced by 65%. After 120 days of aging, the counter-diffusion of water had swelled the PVA gel. MeOH/water aging between 120-155 days had resulted in further swelling and the infusion of pure water. As a result, the *E′(f)* for gel aged for 155 days in MeOH/water had decreased slightly from the values reported for gel that was aged for 120 days (Figure 4.10). (The loss modulus (*E″(f)*) of 4P10000 gel fiber aged in MeOH/water is reported in Appendix C.)

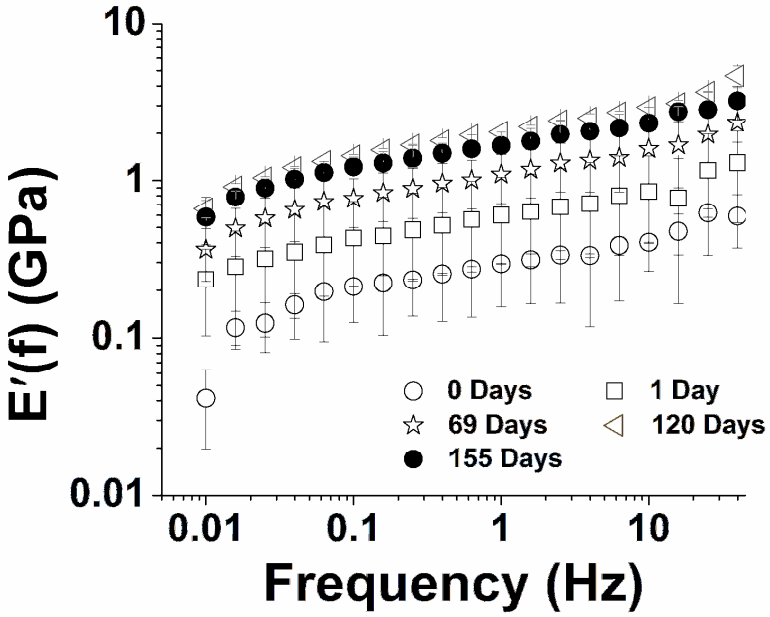

Figure 4.10. Storage modulus of 4P10000 gel fibers aged in MeOH/water.

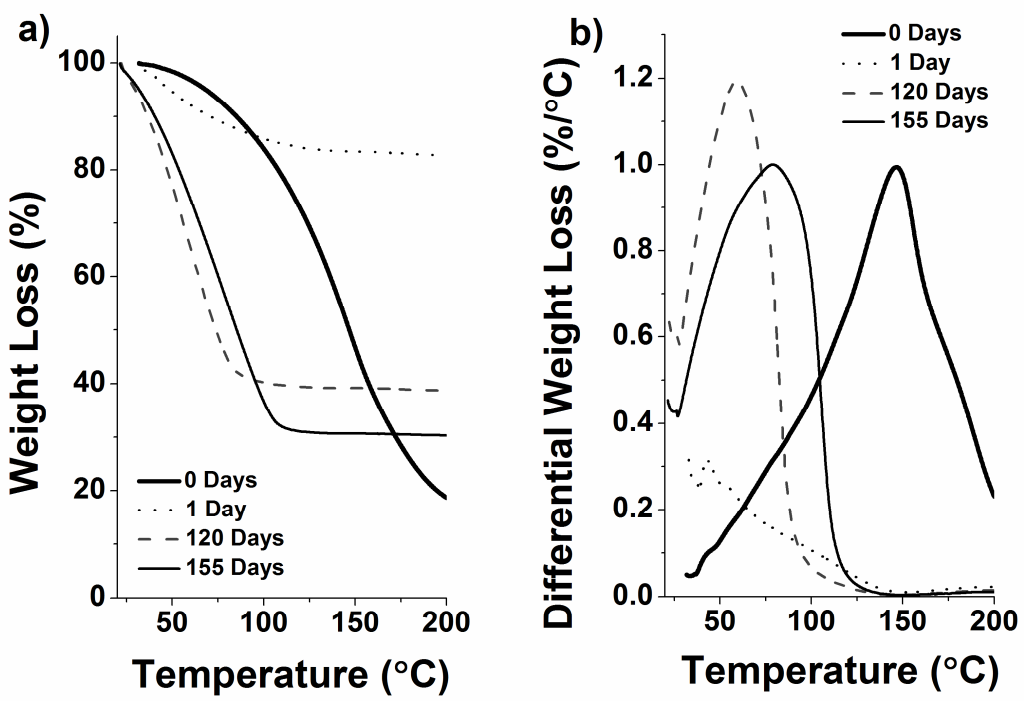

Figure 4.11. 4P10000 gel fibers aged in MeOH/water: a) TGA and b) DTGA at 10 °C/min in nitrogen.

The X_c of 4P10000 gels that were aged in MeOH/water was characterized in Table 4.7 and Figure 4.12. After 1 day of MeOH/water aging, the X_c of gel fibers increased from 8 to 44%; additional aging did not influence the crystallinity of gel fibers. In both instances, gel fibers were rich in water after 1 day of aging and onward. The ordering of PVA chains within gels aged in MeOH and in MeOH/water was similar as well. The WAXD analysis of gels aged in MeOH/water and their fibers (Table 4.6 and 4.7) was further evidence that the three dimensional crystals within drawn PVA fibers had come from ordered sheets of PVA chains, wherein water molecules were intercalated between the chains. The d-spacing of $(10\bar{1})/(101)$ (~0.45 nm) was also suggestive of water bound to ordered PVA within the gel and drawn fiber.

Table 4.7. WAXD Characterization of 4P10000 Gel Fibers Aged in MeOH/Water.

Sample Designation		**4P10000-0MeOH/ Water-Gel**	**4P10000-1MeOH/ Water-Gel**	**4P10000-69MeOH/ Water-Gel**	**4P10000-120MeOH/ Water-Gel**	**4P10000-155MeOH/ Water-Gel**
MeOH/Water Aging Time (Days)		0	1	69	120	155
X_c **(%)**		8, 8	43, 46	44, 48	43, 45	46, 46
***XS* (nm)**	**(100)**	3, 3	5, 5	5, 5	5, 5	5, 5
	(111)	5, 5	5, 5	5, 5	5, 5	5, 5
d-spacing (nm)	**(100)**	0.69, 0.69	0.76, 0.76	0.76, 0.76	0.76, 0.76	0.76, 0.76
	(110)	-	0.24, 0.24	0.24, 0.24	0.24, 0.24	0.24, 0.24
	(111)	0.22, 0.22	0.22, 0.22	0.22, 0.22	0.22, 0.22	0.22, 0.22

Crystal sizes were not reported for the 110 planes of low peak intensity. a) X_c = crystallinity of gel fiber and b) *XS* = crystal size.

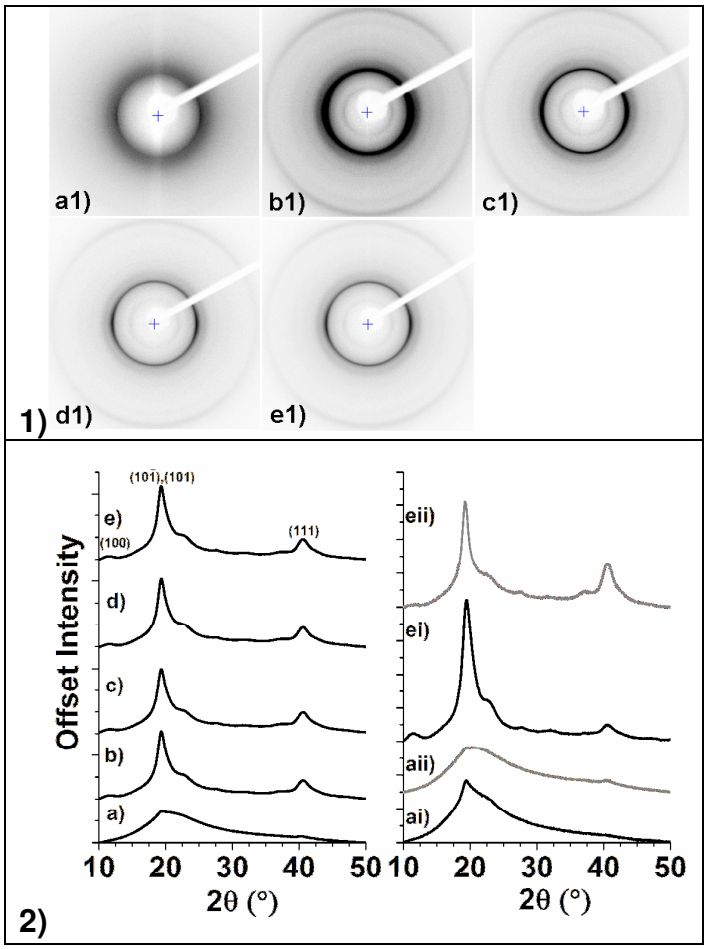

Figure 4.12. WAXD analysis of 4P10000 gel fibers with aging time a) 0, b) 1, c) 69, d) 122, and e) 155 days in MeOH/water: 1) diffraction patterns, 2) integrated radial scans, equatorial scans (ai and ei), and meridonal scans (aii and eii).

The type of aging solvent was observed to affect the diffusion and counter-diffusion of solvent within the gel over time. The mechanical properties of precursor gel and drawn fibers were influenced by the solvent phase, namely water. Ordered PVA chains, within as-spun and aged gels, had exhibited scattering that was mostly diffuse; nevertheless, the (10$\bar{1}$)/(101) and (111) planes of 4P10000/155MeOH/Water-Gel had exhibited preferential alignment, as observed for gel aged in MeOH (Figure 4.7 and 4.12).

4.3.2.5. Drawn 4P10000 Fibers after Extensive Gel Aging in MeOH/Water

4P10000 gel was aged extensively in 50:50 MeOH/water at 10 ℃. Fiber was drawn from gels that were aged for 1 day and 18 months in MeOH/water. *DR* for the as-spun 4P10000 fiber had increased by a factor of two after 18 months of MeOH/water aging (Table 4.8 and Figure 4.13). Further, the *TS* of the fibers had increased by one-third, and these drawn fibers were more than twice as stiff after extensive gel aging.

The average diameter of 4P10000-18Ext fibers was smaller than the 4P10000-1Ext fibers. As observed in Figure 4.14, the circularity of drawn fibers had improved upon extensive gel aging in MeOH/water. *CI* for drawn fibers increased from 0.76 to 0.89.

Table 4.8. Mechanical Properties of Drawn 4P10000 Fibers from Gels Extensively Aged in MeOH/Water.

Sample Designation	**4P10000-1Ext**	**4P10000-18Ext**
MeOH/Water Aging Time	**1 Day**	**18 months**
JSR [a)]	5.3 X	5.3 X
DR [b)]	4.0 X	8.0 X
φ_f [c)] **(μm)**	30 ± 3	26 ± 4
CI [d)]	0.76 ± 0.07	0.89 ± 0.05
TS [e)] **(GPa)**	0.85 ± 0.05	1.19 ± 0.09
Maximum *TS* (GPa)	0.91	1.33
TM [f)] **(GPa)**	10 ± 3	26 ± 4
Maximum *TM* (GPa)	13	34
Strain at Break (%)	7.3 ± 0.5	5.3 ± 1.1

a) *JSR* = jet stretch ratio, b) *DR* = cumulative draw ratio for drawing past coagulation, c) φ_f = diameter of drawn fibers according to SEM micrographs, d) *CI* = circularity index of drawn fibers according SEM micrographs, e) *TS* = tensile strength, and f) *TM* = tensile modulus.

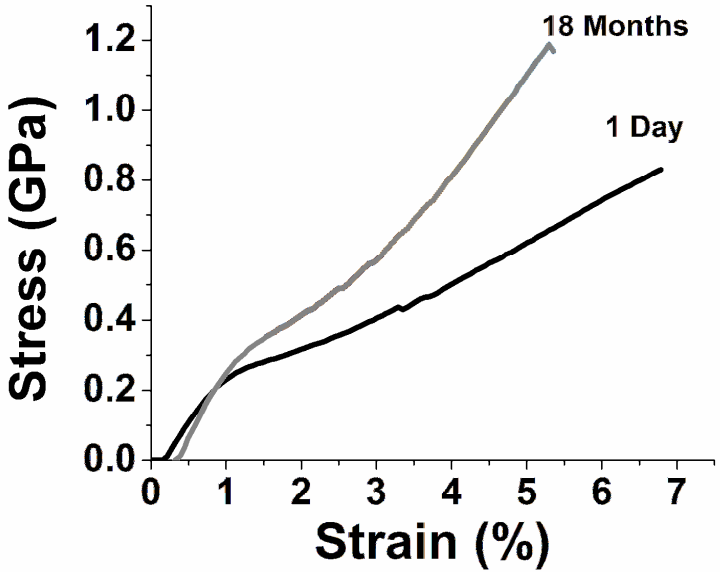

Figure 4.13. Stress-strain curves of drawn 4P10000 fibers from gels aged in MeOH/water for 1 day and extensively aged for 18 months.

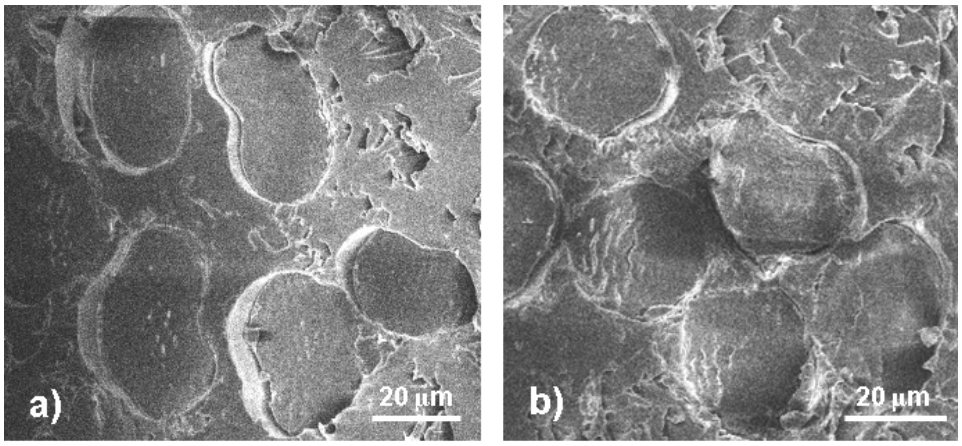

Figure 4.14. Cross-sections of drawn 4P10000 fibers from gels aged in MeOH/water for a) 1 day and b) extensively aged for 18 months.

The X_c of drawn 4P10000-Ext fibers had increased by ≈6% as a result of gel fiber aging for 18 months (Table 4.9). The orientation of PVA crystals and their planar spacings within drawn fibers were not influenced by gel aging.

Table 4.9. WAXD Characterization of Drawn 4P10000 Fibers from Gels Extensively Aged in MeOH/Water.

Sample Designation		**4P10000-1Ext**	**4P10000-18Ext**
MeOH/Water Aging Time		**1 Day**	**18 months**
JSR [a]		5.3 X	5.3 X
DR [b]		4.0 X	8.0 X
X_c [c] **(%)**		56, 57	61, 63
f_b [d]		0.93, 0.92	0.92, 0.91
XS [e] **(nm)**	**(100)**	9, 9	9, 8
	(001)	4, 4	5, 8
	(110)	9, 9	9, 9
	(111)	8, 8	8, 8
d-spacing (nm)	**(100)**	0.78, 0.78	0.78, 0.78
	(001)	0.55, 0.55	0.55, 0.55
	(110)	0.24, 0.24	0.24, 0.24
	(111)	0.22, 0.22	0.22, 0.22

a) *JSR* = jet stretch ratio, b) *DR* = cumulative draw ratio for drawing past coagulation, c) X_c = crystallinity of polymer, d) f_b = orientation of PVA unit cell crystals along the molecular *b*-axis, and e) *XS* = crystal size.

4.3.3. Aging PVA/SWNT Gel of PVA-8900

4.3.3.1. Drawn PS4P10000 Fibers from Gel Aged in MeOH

PS4P10000 fiber was drawn from gel aged in 10 ℃ MeOH for 1 day. The mechanical properties and geometry of fiber that was drawn from gel aged for 1 day will be discussed. The *TS* and *TM* of drawn PS4P10000 fiber, having an average diameter of 32 ± 2 μm, were 0.67 ± 0.05 GPa and 17 ± 1 GPa, respectively. The *DR* for that fiber was 4.7 X. The *CI* of the drawn PS4P10000-1MeOH fiber was 0.79 ± 0.09; fiber cross sections were shown in Figure 4.15.

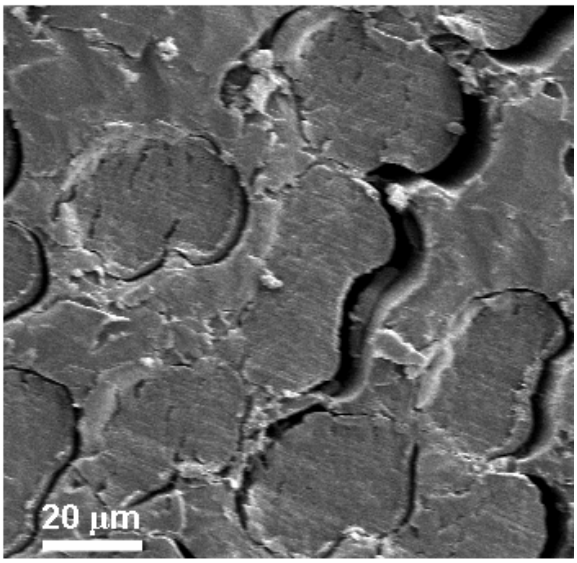

Figure 4.15. Cross-sections of drawn PS4P10000 fibers from gels aged in MeOH for 1 day.

4.3.3.2. PS4P10000 Gel Fiber Aged in MeOH

The mechanical and thermal properties of PS4P10000 gels aged for 0, 1, and 30 days in MeOH were included in this study. This section has reported on the mechanical and thermal properties of those gels. The structure of PVA crystals, composing those gels, has also been described.

The *E'(f)* of as-spun PS4P10000 gels increased after 1 day of aging in 10 ℃ MeOH (Figure 4.16). (The loss modulus (*E''(f)*) of PS4P10000 gel fiber aged in MeOH is reported in Appendix C.) Because as-spun PS4P10000 gel was prepared from polymer having a lower *DP*, its *E'(f)* was lower than the value reported for 4P10000, in spite of SWNT incorporation (Figure 4.5 and 4.16). The weight ratio of SWNTs to PVA was much less than the DP_w ratio of low DP_w to high DP_w PVA (0.25:99.75 and 1:1, respectively). In studying the mechanical behavior of 4P10000 gels as a function of

MeOH aging time, the weight fraction of imbibed solvent appeared to influence the storage modulus of gel fibers. TGA of PS4P10000 gels had revealed that the weight fraction of solvent within the gels aged for 1 and 30 days were simlar (Figure 4.17); as a result, the *E'(f)* of PS4P10000 gels were unaffected by gel aging time, and the values of v_2 must be similar. According to the DTGA of aged PS4P10000 gels, the composition of solvent within both gels differed, which was the result of DMSO diffusion from the gel and the counter-diffusion of MeOH into the gel.

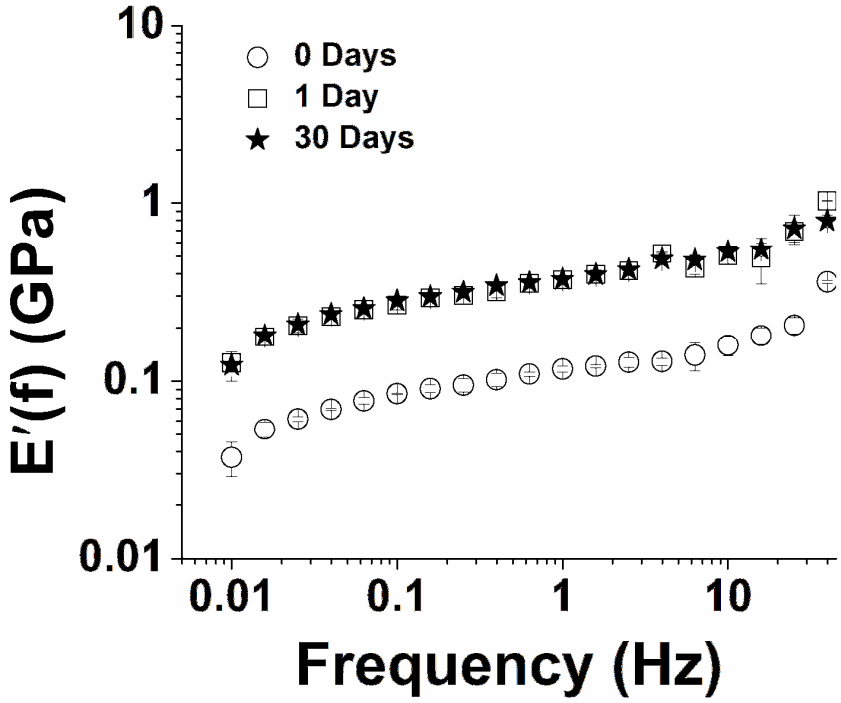

Figure 4.16. Storage modulus of PS4P10000 gel fibers aged in MeOH.

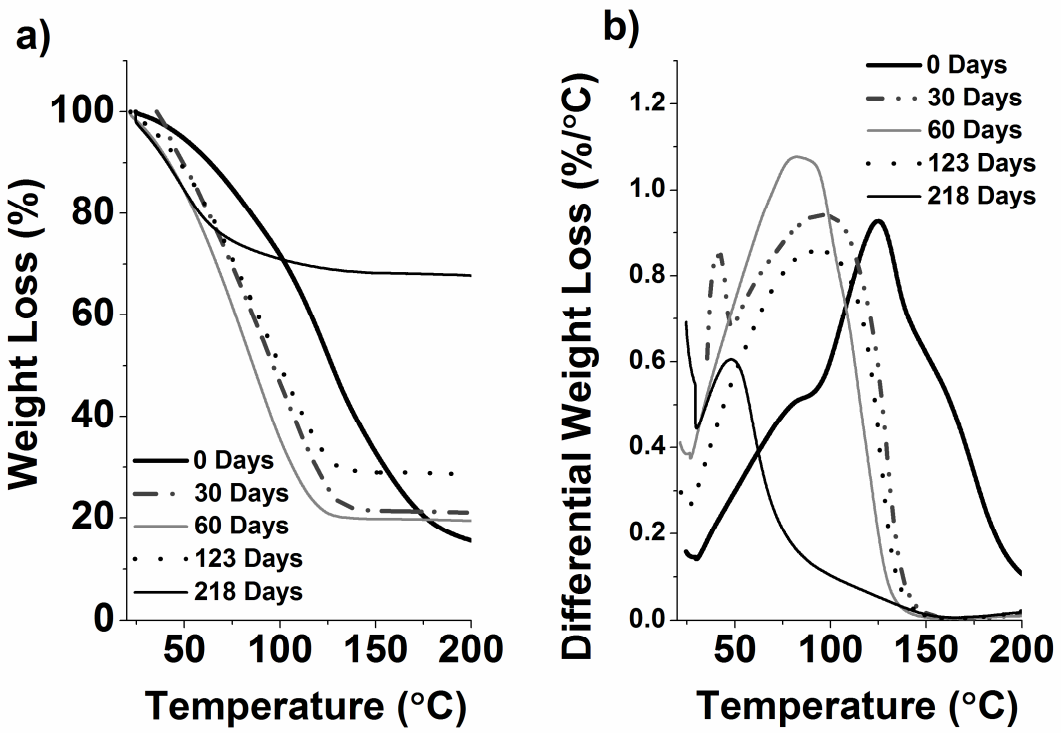

Figure 4.17. PS4P10000 gel fibers aged in MeOH: a) TGA and b) DTGA at 10 °C/min nitrogen.

It was further observed that the error associated with repeat tests of *E'(f)* were negligible for these PS4P10000 gels, in comparison to the error reported for 4P10000 gels aged in MeOH (Figure 4.5 and 4.16). The dispersion of CNTs within the gel microstructure appeared to aid the reproducibility of its dynamic mechanical behavior. As such, the mechanical behaviors of 4P10000 gels were less reproducible than composite gels of PS4P1000. This cause of this behavior has been discussed in more detail and with the aid of WAXD analysis of PS4P10000 gels.

The X_c of PS4P10000 gels increased from ~8% to a range of 42 to 47% upon MeOH aging (Table 4.10). These values of X_c were similar to those of 4P10000 gels that were aged in MeOH for up to 22 days (Table 4.4). The ordering of PVA chains within PS4P10000 gels was also similar to those formed in 4P10000 gel upon MeOH aging.

Evidence for sheets of ordered PVA chains, having solvent intercalated between the monomer units of PVA, was also interpreted from the WAXD analysis of these PS4P10000 gels. The packing of water molecules that have hydrogen bonded to PVA chains appeared to be denser within the as-spun PS4P10000 gel than for the as-spun 4P10000 gel. Therefore, SWNTs were believed to nucleate the ordering of PVA chains upon gelation within the spinning bath. The ordering of PVA chains at the surface of SWNTs would also explain the improved reproducibility of composite gels over that of unfilled gels upon DMA testing (Figure 4.5 and 4.16).

Table 4.10. WAXD Characterization of PS4P10000 Gel Fibers Aged in MeOH.

Sample Designation		**PS4P10000-0MeOH**	**PS4P10000-1MeOH**	**PS4P10000-30MeOH**
MeOH Aging Time (Days)		0	1	30
X_c [a] **(%)**		7, 9	45, 47	42, 45
XS [b] **(nm)**	**(100)**	2, 2	5, 5	5, 5
	(111)	4, 3	5, 5	5, 5
d-spacing	**(100)**	0.65, 0.64	0.77, 0.77	0.77, 0.77
	(110)	-	0.24, 0.24	0.24, 0.24
	(111)	0.22, 0.22	0.22, 0.22	0.22, 0.22

Crystal sizes were not reported for the 110 planes of low peak intensity. a) X_c = crystallinity of gel fiber and b) *XS* = crystal size.

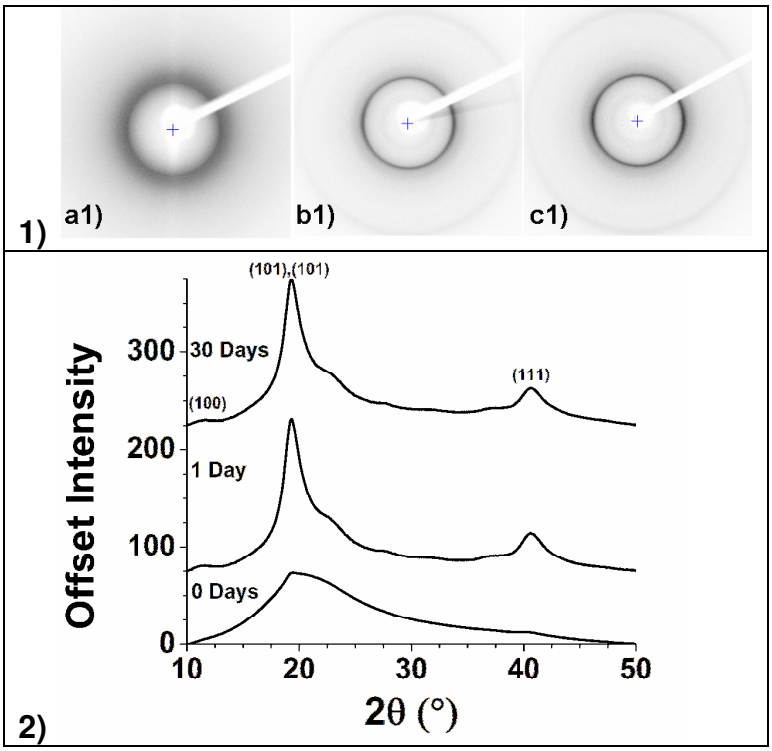

Figure 4.18. WAXD analysis of PS4P10000 gel fibers with aging time a) 0, b) 1, and c) 30 days in MeOH: 1) diffraction patterns and 2) integrated radial scans.

4.3.3.3. Drawn PS4P10000 Fibers from Gels Aged in MeOH/Water

Both the *TS* and *TM* of drawn PS4P10000 fibers had increased with gel aging for up to 219 days in 50:50 MeOH/water at 10 ℃. Drawn fiber of PS4P10000-123MeOH/Water fibers was 66% stronger than drawn PS4P10000-1MeOH/Water fiber (Table 4.11). The opposite behavior was observed among 4P10000 fibers aged in MeOH/water for 155 days; fiber became weaker with gel aging time (Table 4.5). The *DR* of drawn PS4P10000-155MeOH/Water fiber (*DR*=6 X) was higher than value for drawn 4P10000-155MeOH/Water fiber (*DR*=4 X). The presence of SWNTs in aged gels had structurally reinforced MeOH/water aged gels and allowed drawing at higher *DR* values.

Table 4.11. Mechanical Properties of Drawn PS4P10000 Fibers from Gels Aged in MeOH/Water.

Sample Designation	**PS4P10000-1MeOH/ Water**	**PS4P10000-30MeOH/ Water**	**PS4P10000-60MeOH/ Water***	**PS4P10000-123MeOH/ Water***	**PS4P10000-219MeOH/ Water***
MeOH/Water Gel Aging Time (Days)	1	30	60	123	219
JSR [a)]	5.6 X	5.6 X	5.6 X	5.6 X	5.6 X
DR [b)]	3.9 X	4.3 X	4.7 X	6.1 X	5.5 X
φ_f [c)] **(µm)**	37 ± 3	33 ± 3	34 ± 3	29 ± 4	29 ± 2
CI [d)]	0.64 ± 0.09	0.70 ± 0.12	0.76 ± 0.08	0.84 ± 0.09	0.83 ± 0.07
TS [e)] **(GPa)**	0.54 ± 0.03	0.70 ± 0.10	0.54 ± 0.05	0.95 ± 0.06	0.87 ± 0.10
Maximum *TS* (GPa)	0.63	0.82	0.60	1.06	1.12
TM [f)] **(GPa)**	13 ± 1	11 ± 1	11 ± 1	19 ± 2	22 ± 3
Maximum *TM* (GPa)	14	13	13	22	26
Strain at Break (%)	5.4 ± 0.5	4.4 ± 0.6	5.1 ± 0.5	5.9 ± 0.7	5.0 ± 0.6

a) *JSR* = jet stretch ratio, b) *DR* = cumulative draw ratio for drawing past coagulation, c) φ_f = diameters of drawn fibers according to SEM micrographs, d) *CI* = circularity index of drawn fibers according SEM micrographs, e) *TS* = tensile strength, and f) *TM* = tensile modulus. *Samples drawn with 4 stages of elevated temperature drawing; all other samples were drawn cold, coagulated in MeOH for 1 day, and then drawn at elevated temperatures.

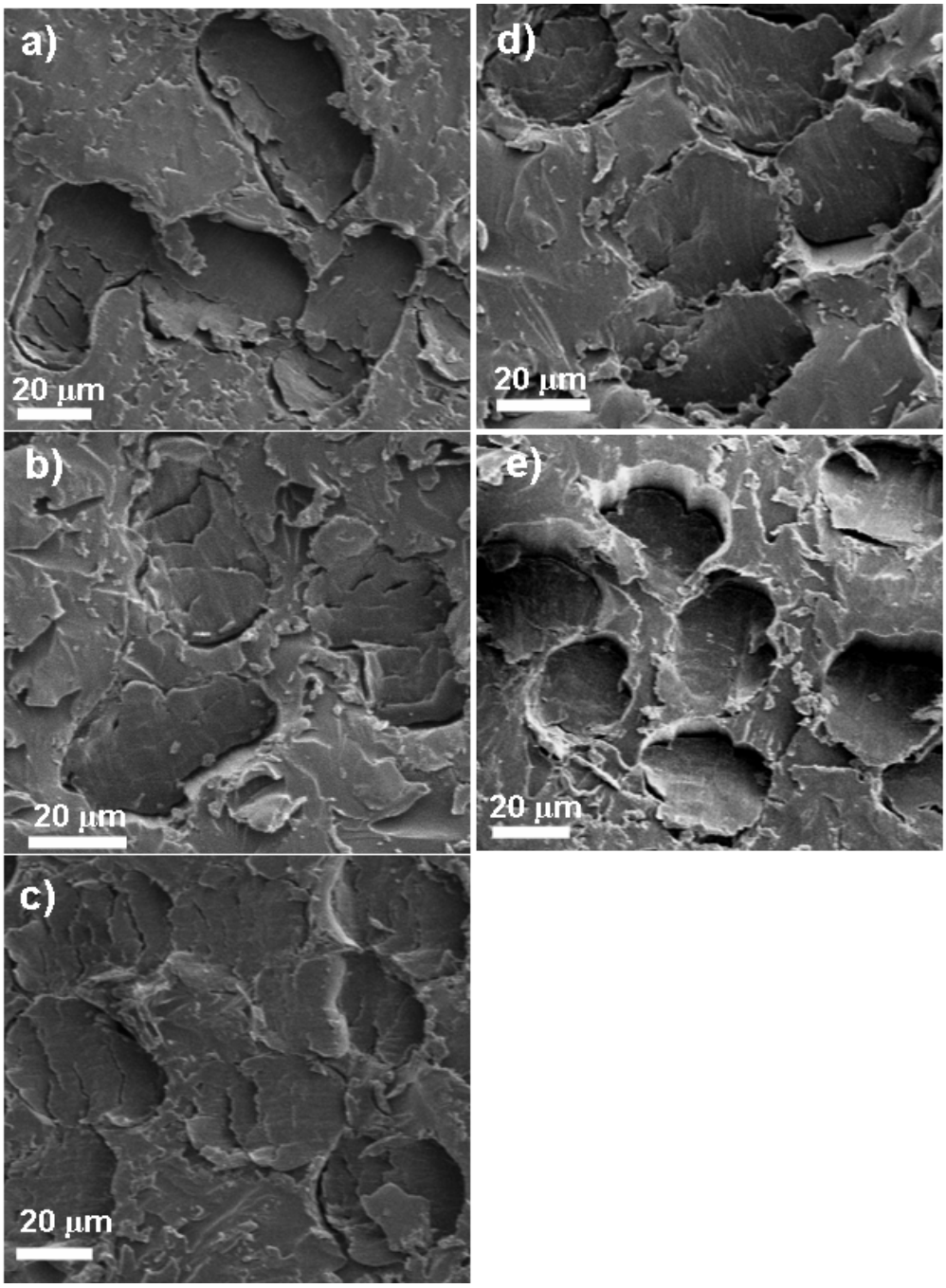

Figure 4.19. Cross-sections of drawn PS4P10000 fibers from gels aged in MeOH/water for a) 1, b) 30, c) 60, d) 123 days with cold drawing, and e) 219 days without cold drawing.

The diameter of drawn PS4P10000 fibers decreased from 37 μm to 29 μm as the *DR* increased (from 4 to 6 X) with aging time up to 123 days. The error associated with *CI* values for drawn PS4P10000-MeOH/Water fibers (Table 4.11) was much less than the error observed for drawn 4P10000-MeOH/Water fibers (Table 4.5).

Thermograms of drawn PS4P10000 fibers (Figure 4.20) had also revealed the enthalpic relaxation of PVA subsequent to solvent evaporation, as observed for 4P10000 fibers (Figure 4.9). The enthalphic relaxation of polymer chains had occurred at increasingly higher temperatures with aging time. Furthermore, the breath and height of the first endothermic peak increased with aging up to 219 days (Figure 4.20a).

The T_m values of drawn PS4P10000 fibers were lower than those observed for drawn 4P10000 fibers. The PS4P10000 dispersion contained polymer that had a lower value of DP_w, as discussed in Chapter 3. The DP_w of the polymer may have reduced the T_m. As the *DR* of PS4P10000 fibers had improved with gel aging, the peak melting temperature of drawn fibers had also increased. The T_m of fibers that were drawn from gels aged for 123-219 days had shifted to higher temperatures. Broad peaks for crystalline melting were observed; a high temperature shoulder along the prominent peak could be observed in most instances of drawn PS4P10000 fiber (Figure 4.20).

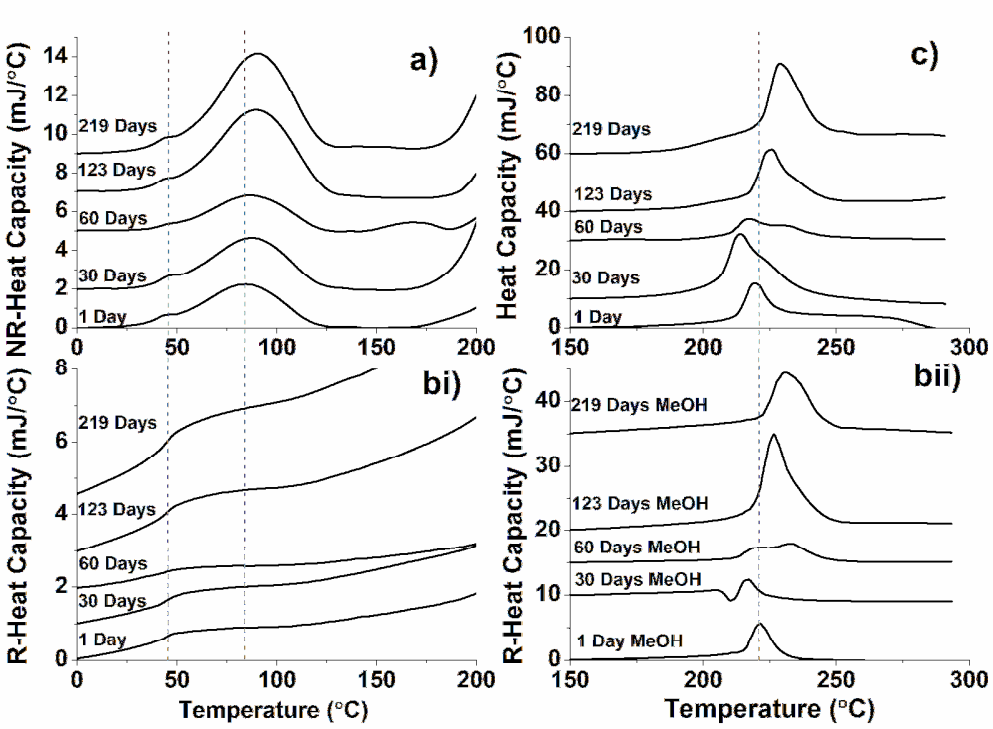

Figure 4.20. MDSC thermograms of drawn PS4P10000 fibers from gels aged in MeOH/water: a) NR-heat capacity, b) R-heat capacity for i) 0-200 °C and ii) 150-300 °C, and c) total heat capacity from tests in nitrogen.

The orientation of PVA crystals along the fiber axis had increased slightly with the value of *DR* for PS4P10000 fibers (Table 4.12). Drawn PS4P10000 fibers exhibited X_c values of 55-60%. The dimensions of ordered PVA, along the (001) and (110) planes, had enlarged with aging time. Drawn PS4P10000 fibers, from gels aged for 123 and 219 days in MeOH/water, exhibited the greatest amount of crystal growth along the (100), (110), and (111) planes (Table 4.12). These fibers also exhibited the highest T_m values and range of high temperature melting.

Table 4.12. WAXD Characterization of Drawn PS4P10000 Fibers from Gels Aged in MeOH/Water.

Sample Designation		**PS4P10000-1MeOH/ Water**	**PS4P10000-30MeOH/ Water**	**PS4P10000-60MeOH/ Water**	**PS4P10000-123MeOH/ Water**	**PS4P10000-219MeOH/ Water**
MeOH/Water Gel Aging Time (Days)		1	30	60	123	219
JSR [a]		5.6 X	5.6 X	5.6 X	5.6 X	5.6 X
DR [b]		3.9 X	4.3 X	4.7 X	6.1 X	5.5 X
f_b [c]		0.85, 0.84	0.84, 0.85	0.85, 0.86	0.86, 0.88, 0.88	0.87, 0.87
X_c [d] **(%)**		57, 56	55, 57	55, 57	56, 55	57, 60
XS [e] **(nm)**	**(100)**	8, 8	7, 7	7, 8	9, 9	9, 9
	(001)	8, 8	7, 6	7, 7	5, 5	6, 6
	(110)	8, 7	7, 7	7, 8	10, 9	9, 9
	(111)	7, 7	6, 6	6, 7	8, 8	8, 8
d-spacing (nm)	**(100)**	0.78, 0.78	0.78, 0.78	0.78, 0.78	0.79, 0.79	0.79, 0.78
	(001)	0.56, 0.56	0.56, 0.56	0.56, 0.56	0.55, 0.55	0.55, 0.55
	(110)	0.24, 0.24	0.24, 0.24	0.24, 0.24	0.24, 0.24	0.24, 0.24
	(111)	0.22, 0.22	0.22, 0.22	0.22, 0.22	0.22, 0.22	0.22, 0.22

a) *JSR* = jet stretch ratio, b) *DR* = cumulative draw ratio, c) X_c = crystallinity of polymer, d) f_b = orientation of PVA unit cell crystals along the molecular *b*-axis, and e) *XS* = crystal size.

4.3.3.4. PS4P10000 Gels Aged in MeOH/Water

The *E'(f)* of PS4P10000 gels were reported in Figure 4.21 as a function of gel aging time in 10 °C MeOH/water. (The loss modulus (*E''(f)*) of PS4P10000 gel fiber aged in MeOH/water is reported in Appendix C.) After 1 day of gel fiber aging, *E'(f)* had increased. Additional aging in MeOH/water did not influence the storage modulus of gel fibers.

Although the composition of solvent within PS4P10000 gels had varied significantly with MeOH/water aging (Figure 4.22); however, the *E'(f)* did not exhibit any dependency with aging for >1 day. The error between repeat DMA runs was less for PS4P10000 as-spun and MeOH/water aged gels than for gels of 4P10000 (Figure 4.10 and 4.21). Therefore, the incorporation of SWNTs added stability to as-spun and aged gels. In spite of SWNT incorporation at 0.25 wt.%, network formation within PS4P10000 gel was not improved, as noted by the increasing values *E'(f)* with frequency.

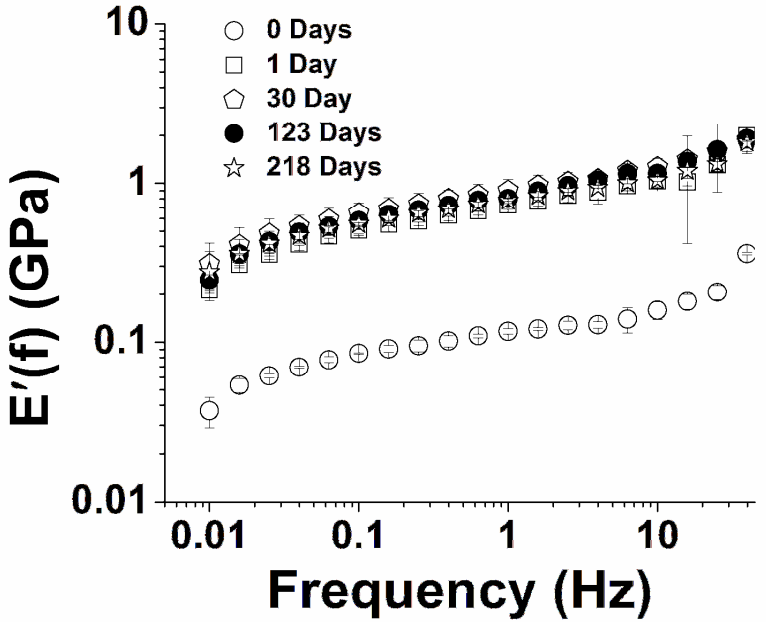

Figure 4.21. Storage modulus of PS4P10000 gels aged in MeOH/water.

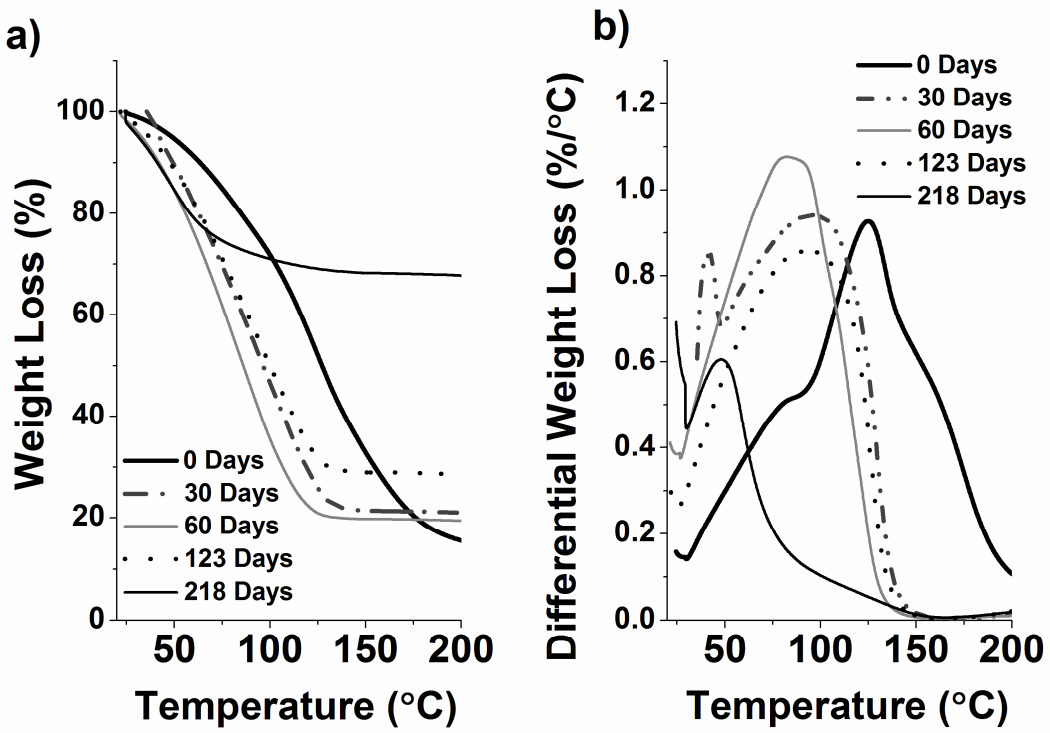

Figure 4.22. PS4P10000 gel fibers aged in MeOH/water: a) TGA and b) DTGA at 10 ℃/min in nitrogen.

As observed for 4P10000 as-spun gel, ~85 % of the PS4P10000 gel was solvent (Figure 4.11a and 4.22a). Upon gel aging in MeOH/water, pure DMSO of high evaporation temperature (189 ℃) had readily left the microstructure of PS4P10000 gel. Nevertheless, weight loss between 125-150 ℃ (Figure 4.22b) was representative of DMSO/water complexes (Figure 2.4). As gel fiber was aged from 30-123 days in MeOH/water, DMSO/water complexes had diffused in and out of the gel microstructure. After 219 days of MeOH/water aging, the weight fraction of solvent was reduced to 30% of the PS4P10000 gel. Most of the DMSO/water phase had diffused out of the gel microstructure, and the water-rich phase had remained.

Table 4.13. WAXD Characterization of PS4P10000 Gel Fibers Aged in MeOH/Water.

Sample Designation		**PS4P1000-0MeOH/ Water-Gel**	**PS4P1000-1MeOH/ Water-Gel**	**PS4P1000-30MeOH/ Water-Gel**	**PS4P1000-60MeOH/ Water-Gel**	**PS4P1000-123MeOH/ Water-Gel**	**PS4P1000-219MeOH/ Water-Gel**
MeOH/Water Gel Aging (Days)		0	1	30	60	123	219
X_c [a] **(%)**		7, 9	44, 42	41, 39	45, 47	40, 43	46, 46
XS [b] **(nm)**	**(100)**	2, 2	5, 5	5, 5	5, 5	4, 5	5, 5
	(111)	4, 3	5, 5	5, 5	6, 4	5, 5	5, 5
d-spacing	**(100)**	0.65, 0.64	0.76, 0.76	0.76, 0.76	0.77, 0.77	0.77, 0.77	0.77, 0.77
	(110)	-	0.24, 0.24	0.24, 0.24	0.24, 0.24	0.24, 0.24	0.24, 0.24
	(111)	0.22, 0.22	0.22, 0.22	0.22, 0.22	0.22, 0.22	0.22, 0.22	0.22, 0.22

Crystal sizes were not reported for the (110) planes of low peak intensity. a) X_c = crystallinity of gel fiber and b) *XS* = crystal size.

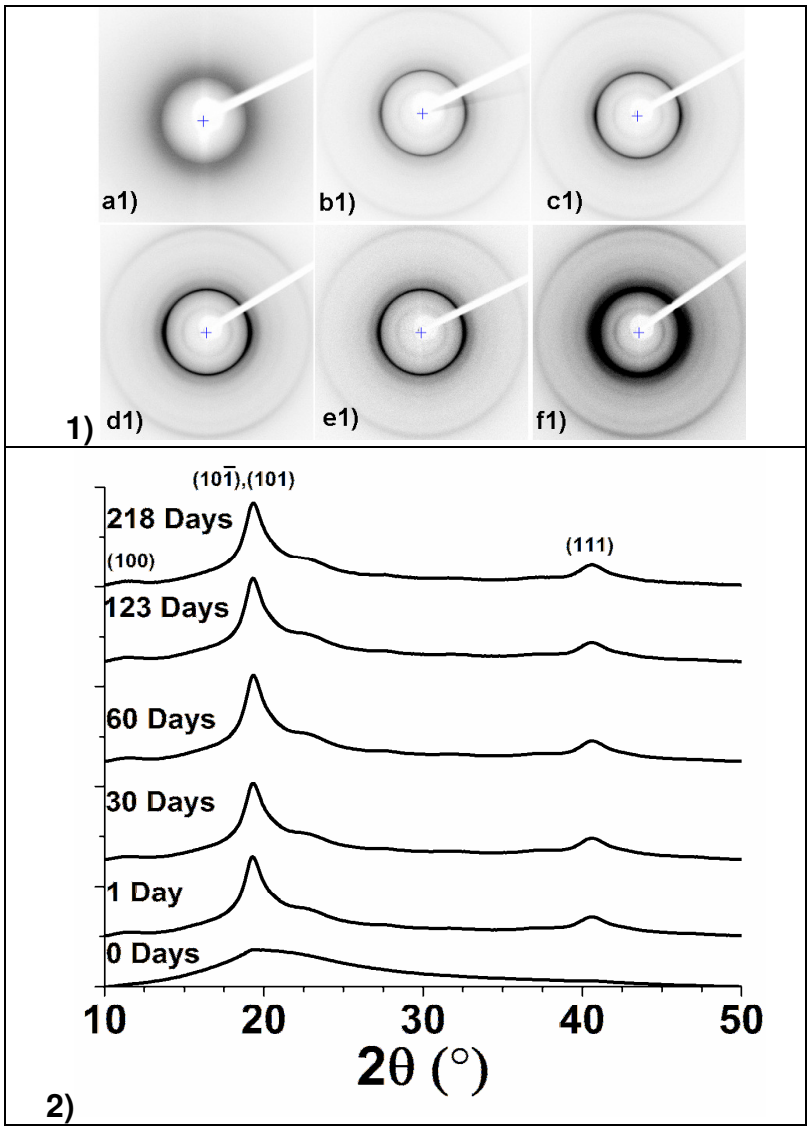

Figure 4.23. WAXD analysis of PS4P10000 gel fibers with aging time a) 0, b) 1, c) 30, d) 60, e) 123, and f) 218 days in MeOH/water: 1) diffraction patterns and 2) integrated radial scans.

The values of X_c within PS4P10000 gel fibers were similar to the values from 4P10000 gels that were aged in MeOH/water (Table 4.7 and 4.13). In both cases, the overall crystallinity did not change with aging time; rather these values remained between 40-46% up to 219 days of aging. The geometry of ordered PVA within these PS4P10000 gels was similar to those within 4P10000 gels that were also aged in MeOH/water.

The WAXD analysis, of these gels was suggestive of ordered PVA chains that had hydrogen bonded to water. The d-spacing values for the (100) planes had increased from 0.65 to 0.76 upon MeOH/water aging. The d-spacing values for the $(10\bar{1})$/(101) planes in gel (Figure 4.23) and drawn fibers (not shown) was ~0.45 nm. Therefore, the PVA within the crystalline phase of drawn fibers must also exhibit hydrogen bonding with water, as well.

4.3.4. Aging Gels of PVA-4000

4.3.4.1. Drawn 10P4000 Fibers from Gels Aged in MeOH/Water

The tensile properties of 10P4000 fibers that were drawn from gels aged in 50:50 MeOH/water at 10 ℃ are reported in Table 4.14. After 1 day of gel aging, the *TS* of drawn fiber equaled 0.7 GPa. Fibers drawn from gels that were aged for 16-120 days in MeOH/water had exhibited *TS* values of 1-1.5 GPa. No further improvement in the *TS* of drawn 10P4000 fibers was observed after 152 days of gel aging. The morphologies of fibers that were drawn from 10P4000 had the appearance of ovals or circles (Figure 4.24). The *CI* values of the strongest fibers were ≈0.9 (Table 4.14).

MDSC thermograms of drawn 10P4000 fibers had revealed the enthalpic relaxation of polymer chains; this transition was observed among fibers that were drawn from gels aged for at least 16 days in MeOH/water (Figure 4.25a). Enthalpic relaxation was recognized as the low temperature shoulder along the prominent endothermic peak that ranged between 25-150 ℃. This behavior of enthalpic relaxation was also observed among fibers that were drawn from 4P10000 and PS4P10000 gels.

Table 4.14. Mechanical Properties of Drawn 10P4000 Fibers from Gels Aged in MeOH/Water.

Sample Designation	**10P4000-1MeOH/ Water**	**10P4000-16MeOH/ Water**	**10P4000-46MeOH/ Water**	**10P4000-60MeOH/ Water**	**10P4000-120MeOH/ Water**	**10P4000-120MeOH/ Water***	**10P4000-152MeOH/ Water***
MeOH/Water Aging Time (Days)	1	15	46	60	120	120	152
JSR [a)]	11.5 X	11.5 X	11.5 X	11.5 X	11.5 X	11.5 X	11.5 X
DR [b)]	4.5 X	5.9 X	6.0 X	5.4 X	5.5 X	5.3 X	5.6 X
φ_f [c)] **(μm)**	33 ± 3	36 ± 5	32 ± 5	34 ± 5	30 ± 4	32 ± 4	33 ± 6
CI [d)]	0.92 ± 0.05	0.84 ± 0.04	0.88 ± 0.06	0.83 ± 0.06	0.88 ± 0.05	0.91 ± 0.05	0.93 ± 0.04
TS [e)] **(GPa)**	0.58 ± 0.06	0.84 ± 0.14	1.11 ± 0.12	0.79 ± 0.12	1.15 ± 0.22	0.89 ± 0.15	0.65 ± 0.10
Maximum *TS* (GPa)	0.68	0.98	1.26	0.96	1.46	1.19	0.78
TM [f)] **(GPa)**	19 ± 5	15 ± 2	19 ± 2	14 ± 2	14 ± 2	12 ± 3	12 ± 2
Maximum *TM* (GPa)	24	18	21	18	17	20	16
Strain at Break (%)	6.2 ± 1.7	6.2 ± 1.0	4.6 ± 0.5	4.8 ± 0.6	5.8 ± 1.0	6.0 ± 0.6	6.1 ± 0.4

a) *JSR* = jet stretch ratio, b) *DR* = cumulative draw ratio, c) φ_f = diameters of drawn fibers according to SEM micrographs, d) *CI* = circularity index of drawn fibers according SEM micrographs, e) *TS* = tensile strength, and f) *TM* = tensile modulus. *Samples drawn with 4 stages of elevated temperature drawing; all other samples were drawn cold, coagulated in10 °C MeOH for 1 day, and then drawn in stages.

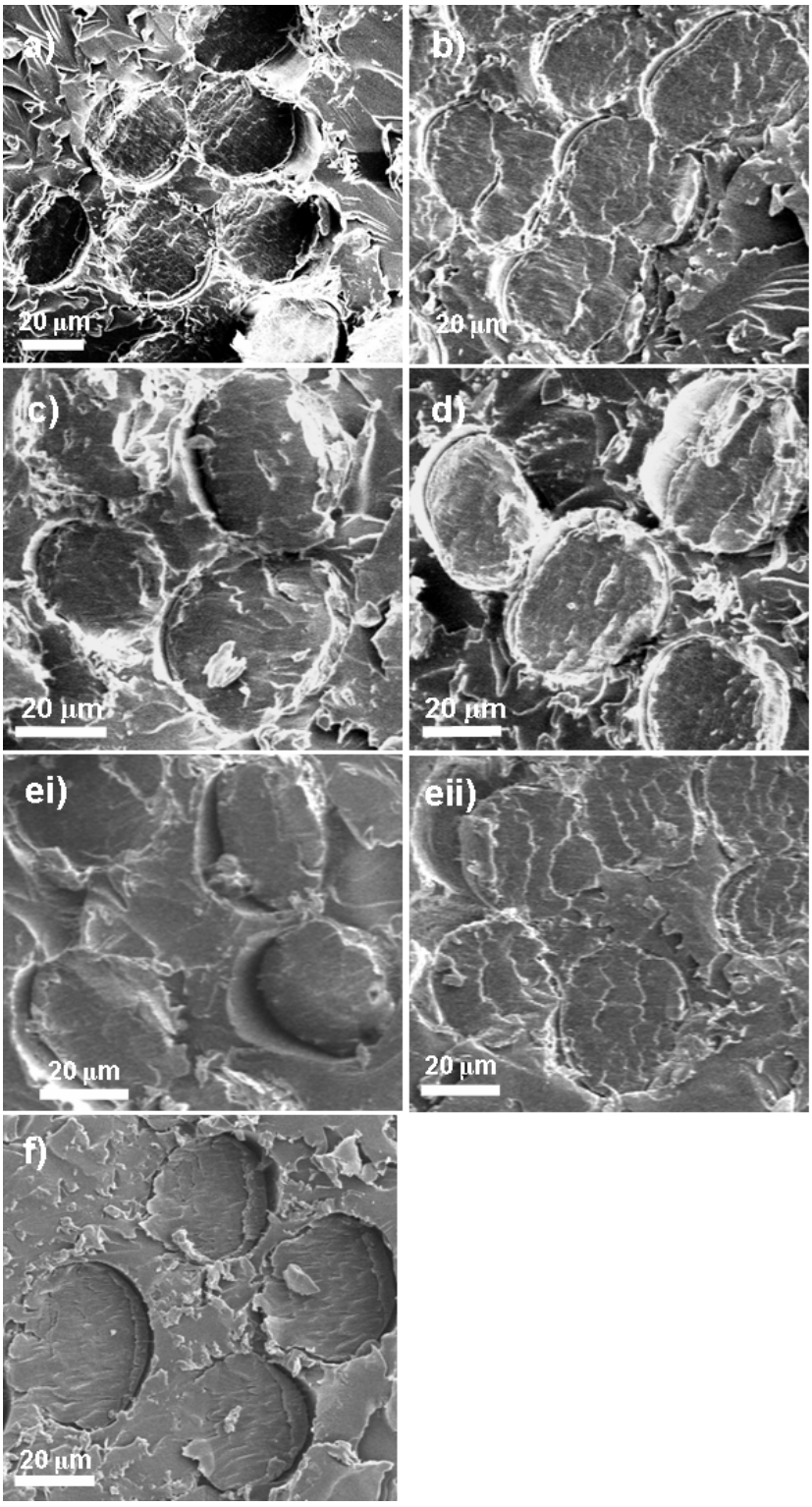

Figure 4.24. Cross-sections of drawn 10P4000 fibers from gels aged in MeOH/water for a) 1, b) 16, c) 46, d) 60, and ei) 120 days with cold drawing, eii) 120 and f) 152 days without cold drawing stage.

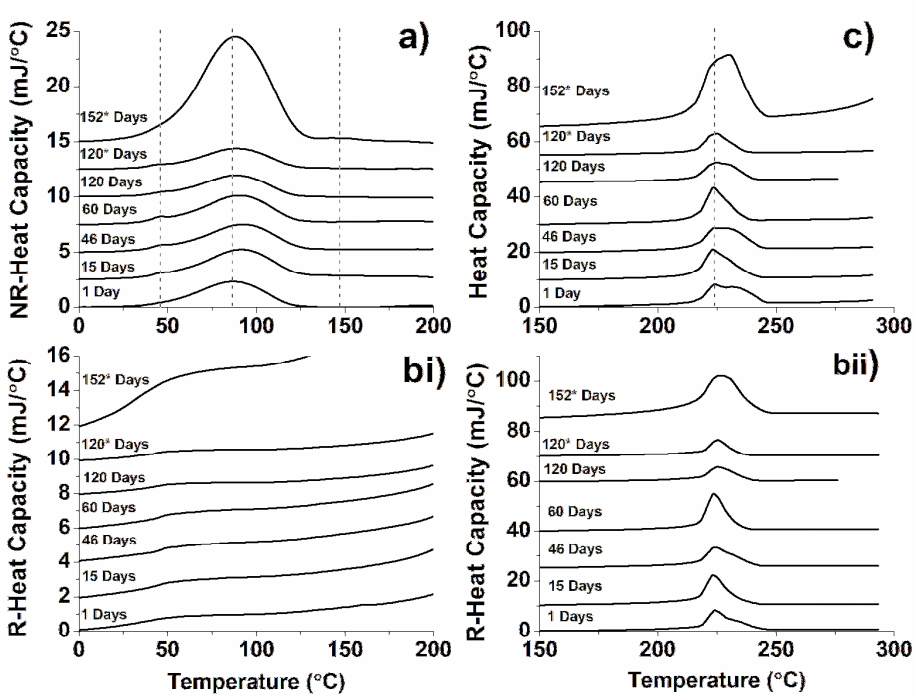

Figure 4.25. MDSC thermograms of drawn 10P4000 fibers from gels aged in MeOH/water: a) NR-heat capacity, b) R-heat capacity for i) 0-200 °C and ii) 150-300 °C, and c) total heat capacity from tests in nitrogen. *Samples drawn with 4 stages of elevated temperature drawing; all other samples were drawn cold, coagulated in MeOH for 1 day, and then drawn at elevated temperatures.

The prominent T_{evap1} peak resulted from the evaporation of water from PVA-based fibers (as discussed previously in Chapter 2). Although the fibers were spun from PVA solutions of DMSO/water, most of the thermograms did not give much evidence of a DMSO-rich phase (Figure 4.25a). Fiber drawn from 10P4000 gel that was aged for 152 days in MeOH/water had the most intense peak for water evaporation. This transition implied the presence of pure water within the drawn fiber, which had not hydrogen bonded with PVA and exhibited water evaporation at temperatures >100 °C. The excess of unbound water within sample 10P4000-152MeOH/water would explain the low values of *TS* and *TM* that were reported for that fiber (Table 4.14).

Table 4.15. WAXD Characterization of Drawn 10P4000 Fibers from Gels Aged in MeOH/Water.

Sample Designation		**10P4000-1MeOH/Water**	**10P4000-16MeOH/Water**	**10P4000-46MeOH/Water**	**10P4000-60MeOH/Water**	**10P4000-120MeOH/Water**	**10P4000-120MeOH/Water***	**10P4000-152MeOH/Water**
MeOH/Water Gel Aging Time (Days)		1	16	46	60	120	120	152
JSR [a]		11.5 X	11.5 X	11.5 X	11.5 X	11.5 X	11.5 X	11.5 X
DR [b]		4.5 X	5.9 X	6.0 X	5.4 X	5.5 X	5.3 X	5.6 X
f_b [c]		0.86, 0.87	0.85, 0.84	0.86, 0.86	0.87, 0.85	0.85, 0.85	0.84, 0.85	0.85, 0.85
X_c [d] **(%)**		53, 52	52, 52	58, 61	56, 57	55, 54	56, 52	56, 56
XS [e] **(nm)**	**(100)**	8, 8	7, 7	7, 7	7, 7	7, 7	7, 7	7, 7
	(001)	9, 9	8, 7	7, 7	6, 7	7, 5	9, 8	6, 8
	(110)	9, 9	8, 8	8, 8	7, 7	8, 8	8, 8	5, 7
	(111)	8, 8	7, 7	7, 7	7, 7	7, 7	7, 7	7, 7
d-spacing	**(100)**	0.79, 0.79	0.78, 0.78	0.79, 0.79	0.78, 0.78	0.78, 0.78	0.78, 0.78	0.78, 0.78
	(001)	0.55, 0.55	0.55, 0.55	0.56, 0.56	0.56, 0.56	0.55, 0.55	0.56, 0.56	0.56, 0.56
	(110)	0.24, 0.24	0.24, 0.24	0.24, 0.24	0.24, 0.24	0.24, 0.24	0.24, 0.24	0.24, 0.24
	(111)	0.22, 0.22	0.22, 0.22	0.22, 0.22	0.22, 0.22	0.22, 0.22	0.22, 0.22	0.22, 0.22

a) *JSR* = jet stretch ratio, b) *DR* = cumulative draw ratio for drawing past coagulation, c) X_c = crystallinity of polymer, d) f_b = orientation of PVA unit cell crystals along the molecular *b*-axis, and e) *XS* = crystal size.

Broad peaks, in the range of 210-225 °C, represented the melting of crystalline PVA (Figure 4.25b). The most intense peak was observed among fibers that were drawn from gels aged for 152 days. The heat capacity of crystalline melting within 10P4000-152MeOH/Water fiber was suggestive of a high degree of crystallinity, even more than within other samples of drawn 10P4000 fiber. Based on the WAXD analysis, this sample was observed to have a X_c value that was similar to other drawn fibers (52-59% in Table 4.15). The drying of this fiber within the DSC instrument was believed to have prompted the crystallization of PVA. The overall crystallinity of PVA is known to increase upon drying.[36, 157] The transition for crystalline melting began at ~175 °C (in Figure 4.25).

The orientation of PVA crystals ranged between f_b values of 0.84-0.86; f_b did not vary with MeOH/water aging time or *DR*.

The as-spun 10P4000 gels were not as stiff as the as-spun 4P10000 gels (Figure 4.10 and 4.26). Therefore, the *E'(f)* of PVA gel was influenced by the polymer's *DP*. The *E'(f)* of 10P4000 gels did not plateau with frequency, which was indicative of an imperfect network. The *E'(f)* values for gels aged from 1-45 days were similar, but the values of *E'(f)* increased gradually with MeOH/water aging from 45-60 days (Figure 4.26). From 60-122 days of MeOH/water aging, the values of *E'(f)* had decreased. (The loss modulus (*E''(f)*) of 10P4000 gel fiber aged in MeOH/water is reported in Appendix C.)

According to the TGA plots in Figure 4.27a, the overall mass of imbibed solvent had decreased with MeOH/water aging up to 60 days; this behavior coincided with the gradual increase in gel stiffness (Figure 4.26). The mass of solvent within the gel microstructure had increased by ~25% between 60-120 days of MeOH/water aging. Water had diffusion back into the gel microstructure, as determined from the DTGA plots (Figure 4.27b). As discussed earlier, the storage modulus of gels aged for 120 days was not as high as for gels that were aged for 60 days.

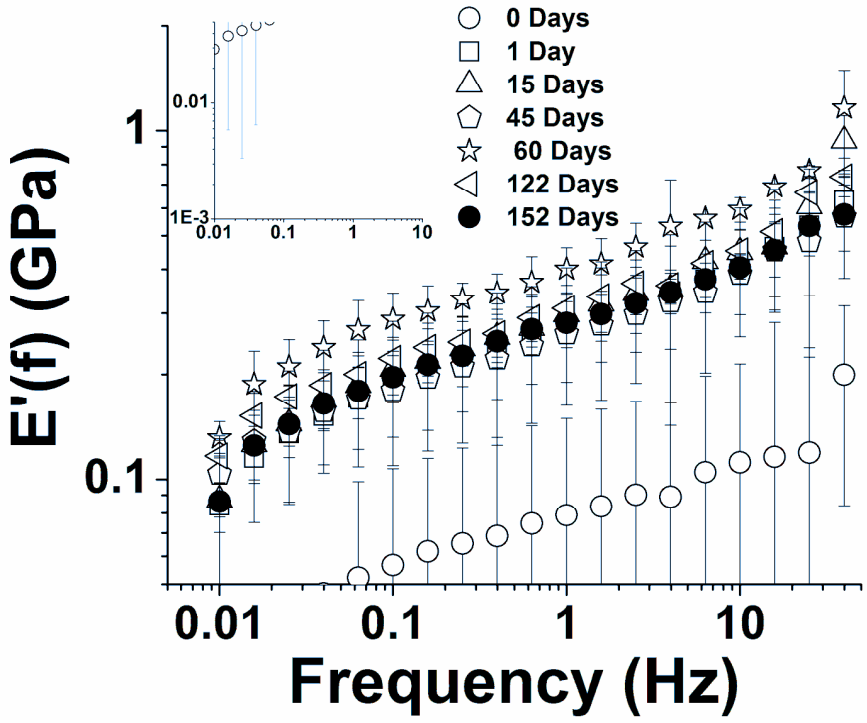

Figure 4.26. Storage modulus of 10P4000 gel fibers aged in MeOH/water.

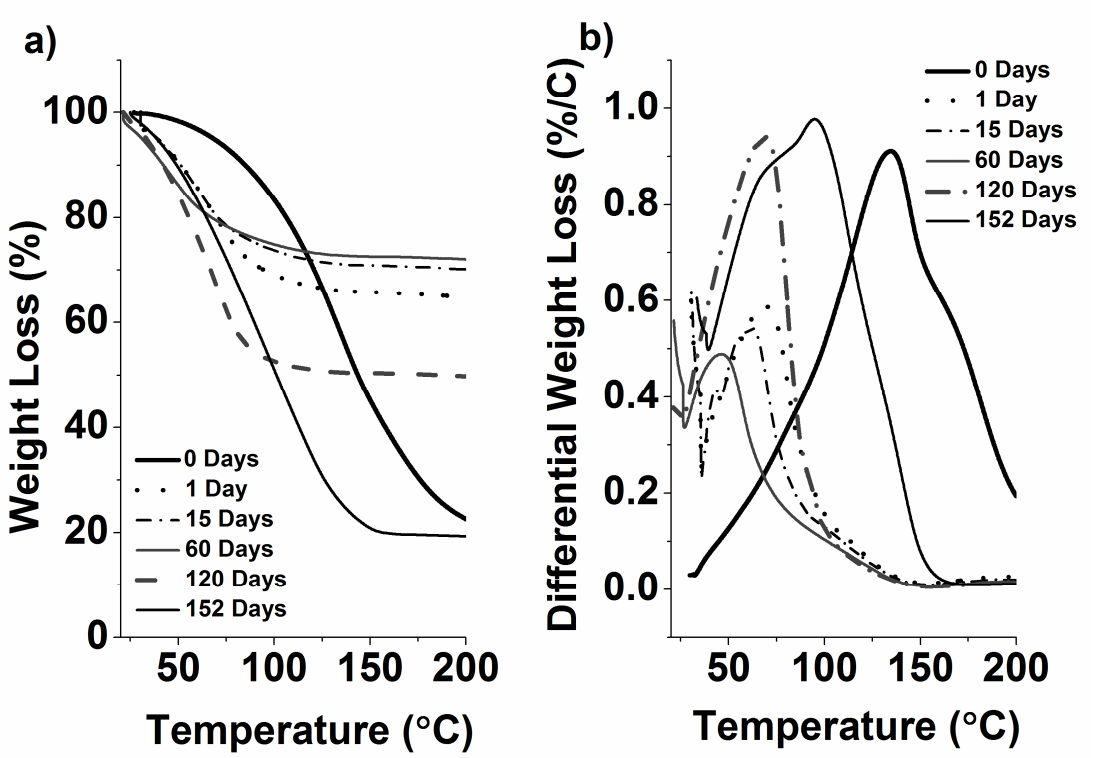

Figure 4.27. 10P4000 gel fibers aged in MeOH/water: a) TGA and b) DTGA at 10 °C/min in nitrogen.

The differential weight loss curves had shifted to the left with aging times up to 60 days (Figure 4.27); this behavior was indicative of DMSO diffusion from the gel microstructure. The counter-diffusion of DMSO/water into the gel microstructure occurred between 120-152 days of MeOH/water aging. Interestingly, the NR-heat capacity curve of drawn 10P4000-155MeOH/Water fiber did not exhibit transitions that were indicative of DMSO/water and/or DMSO evaporation from drawn fibers (130-200 °C in Figure 4.25a). DMSO/water complexes were probably removed during the process of placing gels aged in MeOH/water into MeOH for 1 day before heat-drawing (see Experimental Section). Since DMSO/water complexes were not bound to the PVA chain by hydrogen bonding, they were easily removed from the microstructure of 10P4000.

The ordering of PVA chains within 10P4000 gels was similar to that within 4P10000 gels that were also aged in MeOH/water (Table 4.7 and 4.16). The crystal sizes of gels along the (100) planes were $XS \approx 2$ nm in the as-spun gel and $XS \approx 5$ nm for MeOH/water aged gels. As in 4P10000 and PS4P10000 gel structures, PVA chains within sample 10P4000 were organized into two-dimensional sheets. Diffraction has been detected from (100) planes and the (110) plane, which was perpendicular to the molecular axis of PVA chains. The d-spacing of (100) plane in as-spun gel fiber was ~0.66 nm. Within aged gels, the d-spacing of the (100) plane was 0.76 nm. Organized chains were hydrogen bonded to solvent rather than other chains of PVA within the as-spun gel. After 1 day of aging, intermolecular bonding had occurred between the PVA chains. The d-spacing for $(10\bar{1})$/(101) was represented by values of ~0.45 nm within the gel (Figure 4.28) and drawn fibers (not shown); this value of d-spacing was indicative of solvent within the PVA lattice. The intercalating solvent was likely to be water since it is a hydrogen donor and acceptor. DSC thermograms (Figure 4.23a) confirmed the presence of water, but not DMSO. This behavior suggests DMSO was not bound to amorphous or ordered polymer but rather water.

According to Figure 4.28, upon 10P4000 aging in MeOH/water, the $(10\bar{1})$/(101) and (111) planes within gel fiber that was aged for 122 days had exhibited preferential alignment along the equatorial and meridonal planes, respectively. This behavior was also attributed to changes in the v_2 and Q parameters of gels (as also observed for 4P10000 gels in Figure 4.7 and 4.12).

Table 4.16. WAXD Characterization of 10P4000 Gel Fibers Aged in MeOH/Water.

Sample Designation		**10P4000-0MeOH/ Water-Gel**	**10P4000-1MeOH/ Water-Gel**	**10P4000-15MeOH/ Water-Gel**	**10P4000-46MeOH/ Water-Gel**	**10P4000-60MeOH/ Water-Gel**	**10P4000-122MeOH/ Water-Gel**	**10P4000-152MeOH/ Water-Gel**
MeOH/Water Gel Aging Time (Days)		0	1	15	46	60	122	152
X_c [a] (%)		10, 11	42, 43	39, 41	38, 43	40, 44	39, 39	46, 44
XS [b] (nm)	**(100)**	2, 3	5, 5	5, 5	5, 5	5, 5	5, 5	5, 5
	(111)	2, 5	5, 5	5, 5	5, 5	5, 5	5, 5	5, 5
d-spacing (nm)	**(100)**	0.63, 0.70	0.76, 0.76	0.76, 0.76	0.76, 0.76	0.76, 0.76	0.76, 0.76	0.77, 0.77
	(110)	-	0.24, 0.24	0.24, 0.24	0.24, 0.24	0.24, 0.24	0.24, 0.24	0.24, 0.24
	(111)	0.22, 0.22	0.22, 0.22	0.22, 0.22	0.22, 0.22	0.22, 0.22	0.22, 0.22	0.22, 0.22

Crystal sizes were not reported for the (110) planes of low peak intensity. a) X_c = crystallinity of gel fiber and b) *XS* = crystal size.

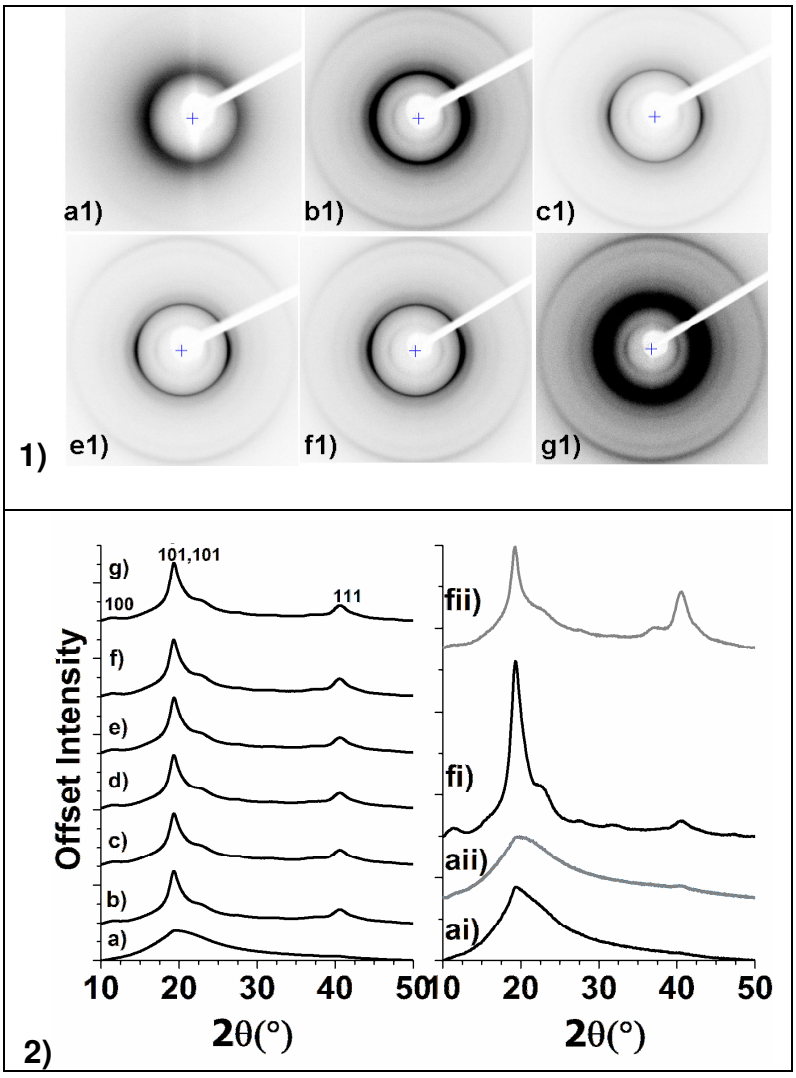

Figure 4.28. WAXD analysis of 10P4000 gel fibers with aging time a) 0, b) 1, c) 15, d) 46, e) 60, f) 122, and g) 152 days in MeOH/water: 1) diffraction patterns, 2) integrated radial scans, equatorial scans (ai and fi), and meridonal scans (aii and fii).

4.3.5. Aging PVA/FWNT Gels of PVA-3700

4.3.5.1. Drawn PF10P4000 Fibers from Gels Aged in Solvent

Composite gels were spun from PF10P4000 and aged in 10 ℃ solvents of MeOH and 50:50 MeOH/water. The mechanical properties of PF10P4000 fibers that were drawn from gels aged in both solvents were described in Figure 4.29, Table 4.17, and Table 4.18. The strongest fibers were drawn from PF10P4000 gels that were aged in either MeOH or MeOH/water for ≥215 days (Figure 4.29). The highest values of *TS* were 1.0 ± 0.08 and 1.3 ± 0.11 GPa for fibers drawn from gels aged in MeOH and MeOH/water, respectively. The *TS* of fibers that were drawn from gels aged for 264 days in MeOH had drastically decreased to 0.58 ± 0.06 GPa. The *TM* of PF10P4000 fibers that were drawn from gels aged in MeOH/water had increased from 12 to 28 GPa, as the aging time increased from 122 to 265 days.

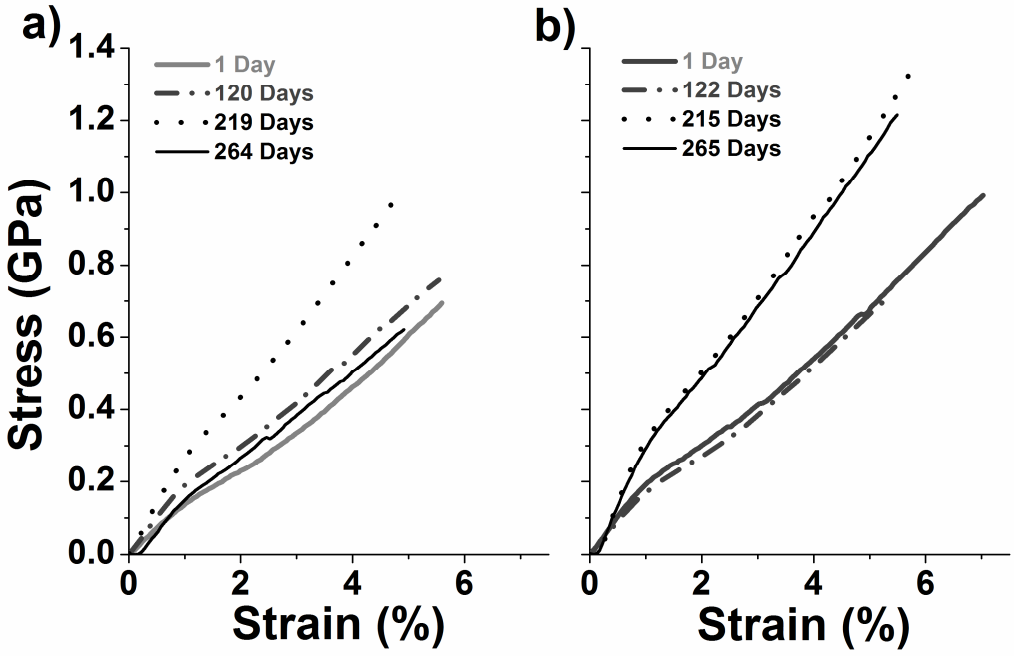

Figure 4.29. Stress-strain curves of PF10P4000 fibers drawn from gels aged in a) MeOH and b) MeOH/water.

Table 4.17. Mechanical Properties of Drawn PF10P4000 Fibers from Gels Aged in MeOH.

Sample Designation	**PF10P4000 1MeOH**	**PF10P4000 120MeOH**	**PF10P4000 219MeOH**	**PF10P4000 264MeOH**
MeOH/Water Aging Time (Days)	1	120	219	264
JSR [a)]	10.6 X	10.6 X	10.6 X	10.6 X
DR [b)]	7.3 X	7.0 X	8.7 X	8.0 X
φ_f [c)] **(μm)**	31 ± 2	33 ± 3	26 ± 3	33 ± 3
CI [d)]	0.93	0.94	0.88	-
TS [e)] **(G Pa)**	0.70 ± 0.07	0.75 ± 0.07	1.01 ± 0.08	0.58 ± 0.06
Maximum *TS* (GPa)	0.81	0.83	1.21	0.71
TM [f)] **(GPa)**	13 ± 1	20 ± 1	22 ± 3	14 ± 2
Maximum *TM* (GPa)	15	22	27	18
Strain at Break (%)	5.6 ± 1.7	5.3 ± 0.5	5.3 ± 0.4	4.8 ± 0.3

Table 4.18. Mechanical Properties of Drawn PF10P4000 Fibers from Gels Aged in MeOH/Water.

Sample Designation	**PF10P4000 1MeOH/ Water**	**PF10P4000 122MeOH/ Water***	**PF10P4000 215MeOH/ Water***	**PF10P4000 265MeOH/ Water***
MeOH/Water Aging Time (Days)	1	122	215	265
JSR [a)]	10.6 X	10.6 X	10.6 X	10.6 X
DR [b)]	6.9 X	4.9 X	8.4 X	8.0 X
φ_f [c)] **(μm)**	29 ± 3	32 ± 8	23 ± 2	25 ± 3
CI [d)]	0.74	0.90	0.83	0.92
T [e)] **(GPa)**	0.87 ± 0.10	0.70 ± 0.11	1.33 ± 0.11	1.24 ± 0.11
Maximum *TS* (GPa)	1.02	0.92	1.50	1.40
TM [f)] **(GPa)**	12 ± 2	12 ± 2	21 ± 2	28 ± 2
Maximum *TM* (GPa)	15	17	24	32
Strain at Break (%)	6.1 ± 0.5	5.3 ± 1.8	5.8 ± 0.5	5.5 ± 0.5

a) *JSR* = jet stretch ratio, b) *DR* = cumulative draw ratio, c) φ_f = diameters of drawn fibers according to SEM micrographs, d) *CI* = circularity index of drawn fibers according SEM micrographs, e) *TS* = tensile strength, and f) *TM* = tensile modulus. *Samples drawn with 4 stages of elevated temperature drawing; all other samples were drawn cold, coagulated in 10 °C MeOH for 1 day, and then drawn at elevated temperatures.

The geometries of drawn PF10P4000 fibers were described in Table 4.17, 4.18, and Figure 4.30. The geometry of fibers drawn from gels aged in MeOH were fairly circular; CI indexes were consistently around 0.9 for those prepared from gels aged in MeOH for up to 215 days. Drawn fibers of PF10P4000-263MeOH featured a void, which had likely formed within the aging bath. The outer diameter of these fibers was larger than those from fibers prepared from other gels aged in MeOH, which resulted in low tensile properties.

The circularity of fibers that were drawn from gels aged for 122 days in MeOH/water had improved from 0.76 to 0.90; however, the distribution of fiber cross sections were less uniform. Peppas et al. have attributed this phenonmenon of anomaolous swelling within PVA hydrogels to the occurrence of solvent diffusion juxtaposed to polymer relaxation.[36] The *DR* of fibers drawn from aged gels increased from 5 to 8 X after 122 to 215 days of MeOH/water aging. Drawn PF10P4000-215MeOH/Water fibers were fairly circular (having a CI of 0.83), and their diameters were smaller than that of the drawn PF10P4000-122MeOH/Water fibers. The resulting *TS* and *TM* of fiber drawn from gel that was aged for 215 days in MeOH/water were 1.33 GPa and 22 GPa, repectively (Table 4.18). The *TM* of drawn PF10P4000-265MeOH/Water fibers was 28 GPa although its *TS* was slightly less than the value reported for PF10P4000-215MeOH/Water. The CI index of PF10P4000-265MeOH/Water fibers was 0.92; these circular cross sections are shown in Figure 4.30dii.

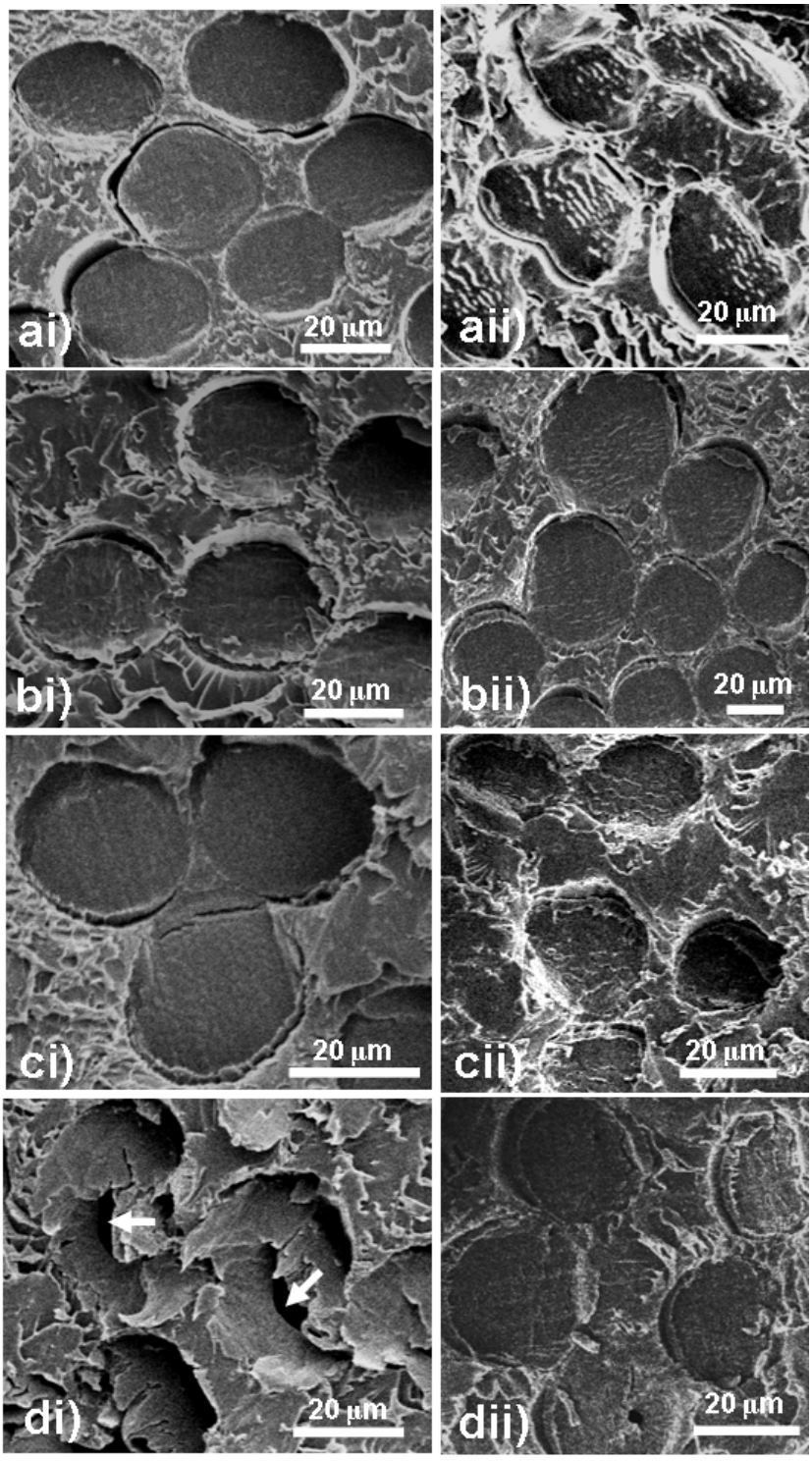

Figure 4.30. Cross-sections of PF10P4000 fibers drawn from gels aged in MeOH for a1) 1, b1) 120, c1) 218, d1) 263 days and MeOH/water for a2) 1, b2) 122, c2) 215, d2) 265 days.

The distribution of carbon nantoubes, within the fracture tip and cross section of PF10P4000-215MeOH/Water fiber, is shown in Figure 4.31. FWNTs appeared to be well distributed within the matrix polymer, which is an important feature for polymer reinforcement. FWNTs, protruding from the cross section of drawn PF10P4000-215MeOH/Water fiber, lay in the direction of shearing. Fibrils of coated FWNTs had a thickness of 22 ± 5 nm (Figure 4.31aii).

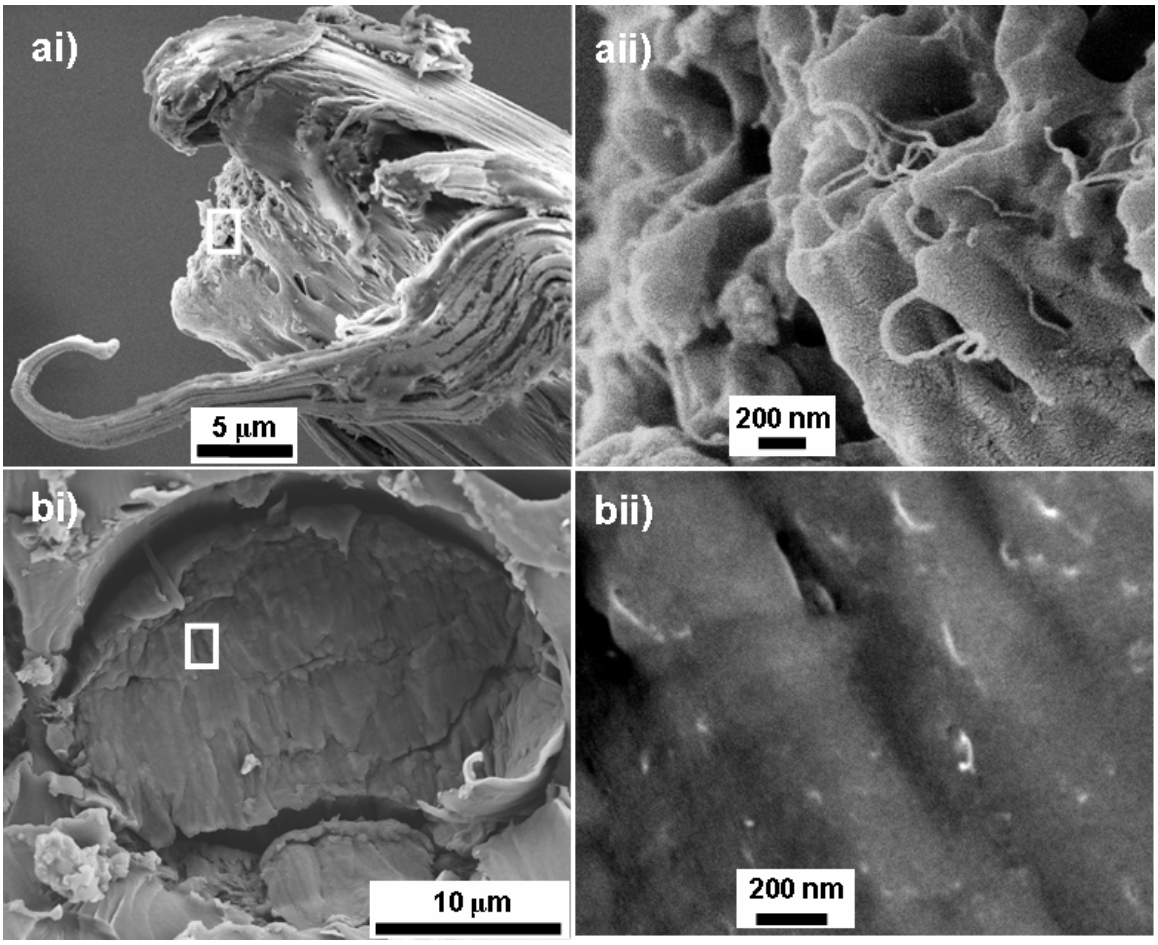

Figure 4.31. SEM characterization of FWNTs within PF10P4000 fiber drawn from gel aged in MeOH/water for 219 days at the a) fracture tip and b) microtomed fiber cross section; aii) and bii) are high resolution images of areas shown in ai) and bi), respectively.

Fibers drawn from PF10P4000 gels were also characterized with MDSC. Thermograms of fibers drawn from gels that were aged in MeOH and MeOH/water solutions were shown in Figure 4.32. The behaviors of solvent evaporation and chain relaxation were observed in the NR-heat capacity thermograms. The prominent peaks within the NR-heat capacity thermograms were due to the evaporation of water-rich phases. Peaks associated with T_{evap1} shifted to lower temperatures and/or had reduced in size as fibers were drawn from gels aged in MeOH or MeOH/water for ≥120 days. The content of unbound water was also reduced upon solvent aging for ≥120 days. Evidence of the DMSO-phase, having temperatures ranging between 125-200 ºC, was observed at a far lesser extent. Enthalpic relaxation was observed among fibers that were drawn from gels aged in MeOH for up to 263 days and in MeOH/water for 215-265 days. This behavior was represented by the low temperature shoulder along peak T_{evap1}.

Fibers that were drawn from gels aged for ≥215 days in solvent exhibited a double melting peak or a high temperature shoulder along the more prominent melting peak (Figure 4.32aii and bii). Fibers that were drawn from gels aged for ≤122 days in solvent exhibited a single melting peak, whose T_m was lower than that of the high temperature shoulders/peaks observed in the aforementioned fibers. The peaks and shoulders that were indicative of high melting temperature crystals were indicative of two different phases of crystalline polymer. The drawing of PVA composites to higher values of *DR* and along FWNT-templates was believed to induce PVA conformations that were conducive to high melting temperatures.

Drawn PF10P4000 fibers exhibited values of X_c between 53-58%, according to Tables 4.19 and 4.20. The largest PVA crystals were among PF10P4000 fibers that were

drawn from gels aged for 215 and 265 days in either MeOH or MeOH/water. The *DR* values of those fibers ranged from 8.0 to 8.7 X. The orientation of PVA crystals within PF10P4000 fibers that were drawn from gels aged in MeOH/water was consistently higher than those reported from gels aged in MeOH (~0.9 and 0.83-0.86, respectively).

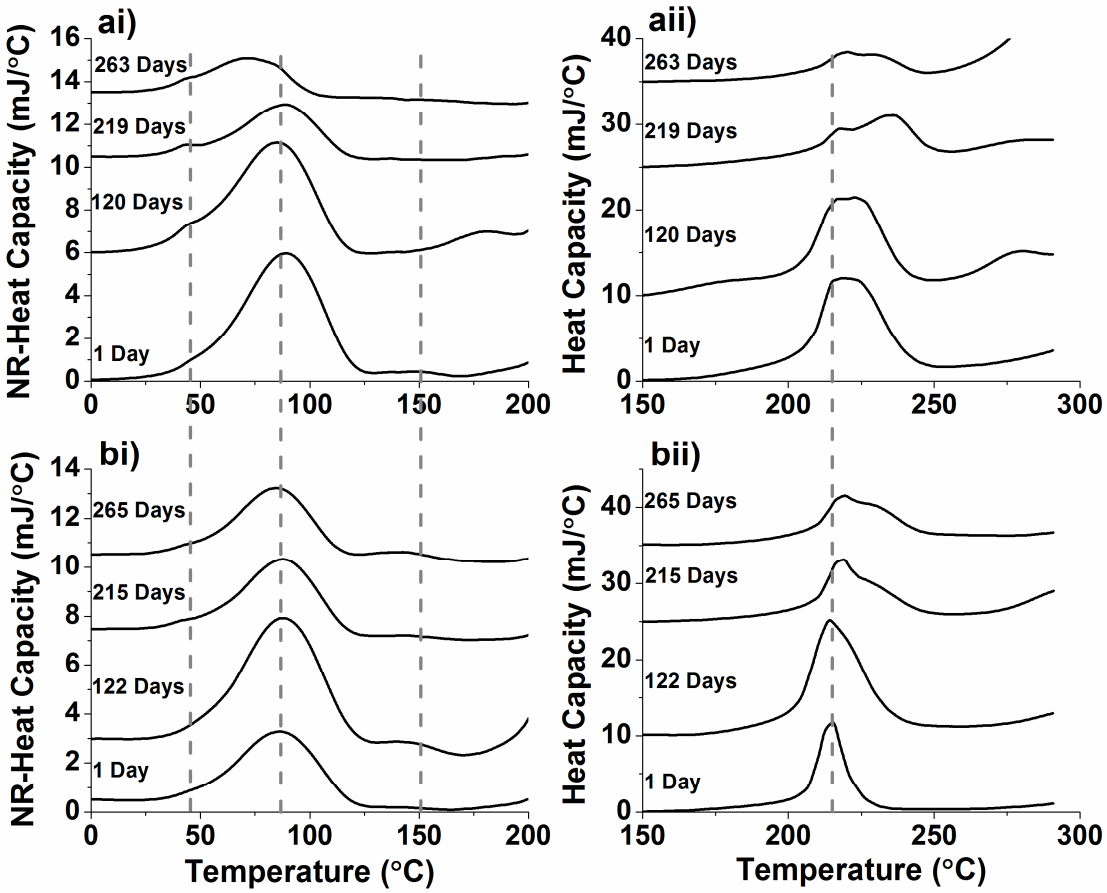

Figure 4.32. MDSC thermograms of PF10P4000 fibers drawn from gels aged in a) MeOH and b) MeOH/water: i) NR-heat capacity and ii) total heat capacity from tests in nitrogen.

Table 4.19. WAXD Characterization of Drawn PF10P4000 Fibers from Gels Aged in MeOH.

Sample Designation		**PF10P4000 1MeOH**	**PF10P4000 120MeOH**	**PF10P4000 219MeOH**	**PF10P4000 264MeOH**
MeOH/Water Aging Time (Days)		1	122	215	265
JSR [a]		10.6 X	10.6 X	10.6 X	10.6 X
DR [b]		7.3 X	7.0 X	8.7 X	8.0 X
X_c [c] **(%)**		53, 56	53, 53	56, 52	54, 53
f_b [d]		0.87, 0.87	0.84, 0.83	0.85, 0.86	0.83, 0.83
XS [e] **(nm)**	**(100)**	8, 7	7, 7	9, 9	9, 8
	(001)	6, 8	8, 7	8, 9	9, 10
	(110)	8, 8	7, 7	9, 9	9, 10
	(111)	7, 7	6, 6	8, 8	8, 8
d-spacing (nm)	**(100)**	0.78, 0.78	0.78, 0.78	0.78, 0.78	0.78, 0.78
	(001)	0.56, 0.56	0.56, 0.56	0.56, 0.56	0.56, 0.56
	(110)	0.24, 0.24	0.24, 0.24	0.24, 0.24	0.24, 0.24
	(111)	0.22, 0.24	0.22, 0.22	0.22, 0.22	0.22, 0.22

a) *JSR* = jet stretch ratio, b) *DR* = cumulative draw ratio, c) X_c = crystallinity of polymer, d) f_b = orientation of PVA unit cell crystals along the molecular *b*-axis, and e) *XS* = crystal size.

Table 4.20. WAXD Characterization of Drawn PF10P4000 Fibers from Gels Aged in MeOH/Water.

Sample Designation		**PF10P4000 1MeOH/ Water**	**PF10P4000 122MeOH/ Water**	**PF10P4000 215MeOH/ Water**	**PF10P4000 265MeOH/ Water**
MeOH/water Aging Time (Days)		1	122	215	265
JSR [a)]		10.6 X	10.6 X	10.6 X	10.6 X
DR [b)]		6.9 X	4.9 X	8.4 X	8.0 X
X_c [c)](%)		58, 58	56, 58	56, 59	57, 57
f_b [d)]		0.91, 0.89	0.90, 0.91	0.90, 0.91	0.90, 0.90
XS [e)] **(nm)**	**(100)**	8, 9	7, 7	8, 8	8, 8
	(001)	5, 4	4, 6	4, 4	10, 7
	(110)	8, 9	7, 7	9, 9	9, 9
	(111)	8, 7	6, 6	8, 8	8, 8
d-spacing (nm)	**(100)**	0.78, 0.78	0.78, 0.78	0.79, 0.79	0.79, 0.79
	(001)	0.55, 0.55	0.56, 0.56	0.55, 0.55	0.55, 0.55
	(110)	0.24, 0.24	0.24, 0.24	0.24, 0.24	0.24, 0.24
	(111)	0.22 ± 0.22	0.22 ± 0.22	0.22 ± 0.22	0.22, 0.22

a) *JSR* = jet stretch ratio, b) *DR* = cumulative draw ratio, c) X_c = crystallinity of polymer, d) f_b = orientation of PVA unit cell crystals along the molecular *b*-axis, and e) *XS* = crystal size.

4.3.5.2. PF10P4000 Gels Aged in Solvent

PF10P4000 gels were aged in solvents of MeOH and MeOH/water. Aging times within both solvents were similar to compare the effects of solvent aging on mechanical performance (Figure 4.33) and gel structure.

The *E'(f)* of gels aged in MeOH and MeOH/water is reported in Figure 4.33. The loss modulus (*E''(f)*) of PF10P4000 gel fiber aged in MeOH and in MeOH/water is reported in Appendix C. The error that has been observed between repeat tests was much less for PF10P4000 gels than for 10P4000 gels that were aged in MeOH/water (Figure

4.26 and 4.33). Similar behaviors were observed for the mechanical responses of PS4P10000 gels versus that of the 4P10000 gels (Figure 4.10 and 4.21). The presence of FWNTs in gels (at 0.24 wt.% of the polymer) appeared to stabilize the gel structures and make them more reproducible. PF10P4000 was a blend of sonicated and unsonicated PVA-4000. Since the DP_{wb} for PF10P4000 was less than the DP_{wb} for 10P4000, the as-spun gel of PF10P4000 was not as stiff as-spun gel 10P4000. The *E'(f)* of PF10P4000 gels had increased by several orders of magnitude after 1 day of solvent aging. Overall, gels that were aged in MeOH were stiffer than gels aged in MeOH/water for similar periods of time. The *E'(f)* from PF10P4000 gels that were aged in MeOH had increased with aging time. In contrast, the *E'(f)* from gels that were aged in MeOH/water for up to 218 days had mostly overlapped, except at high frequencies. Between 218-264 days, the storage modulus of gel aged in MeOH/water decreased slightly.

The solvent content decreased with MeOH aging time (Figure 4.34a), but *E'(f)* had increased (Figure 4.33a). As-spun gel consisted of ~85% solvent, which had reduced to ~12% after 1 day of MeOH aging. Gels aged in MeOH for 218-263 days contained 8 % solvent. The *E'(f)* for PF10P4000 gel that was aged for 263 days was slightly higher than the value reported for gels that were aged in MeOH for 218 days. Therefore, the volume fraction of polymer was expected to be slightly higher within the gel aged for 263 days in MeOH.

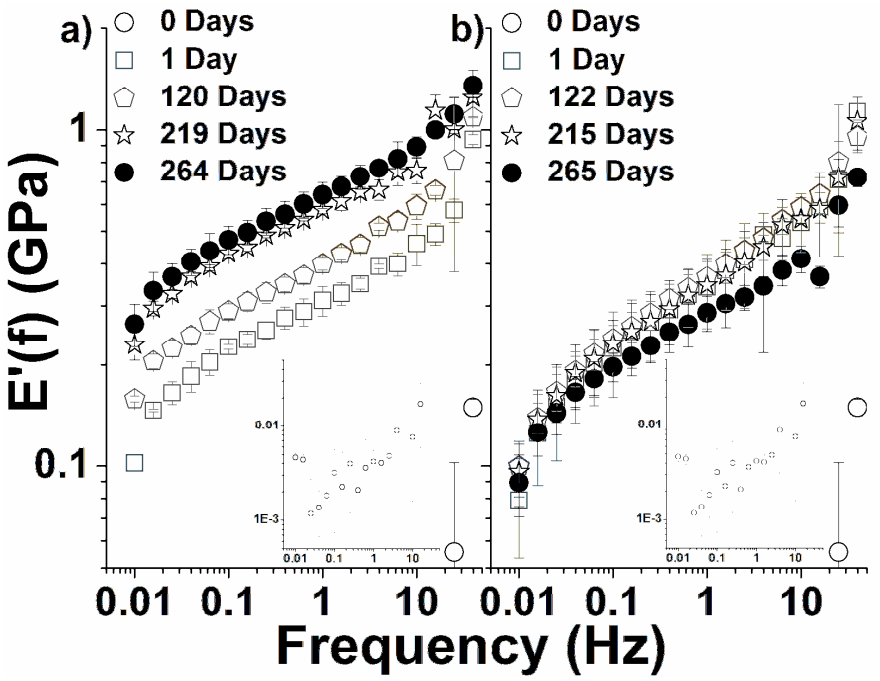

Figure 4.33. Storage modulus of PF10P4000 gel fibers aged in a) MeOH and b) MeOH/water.

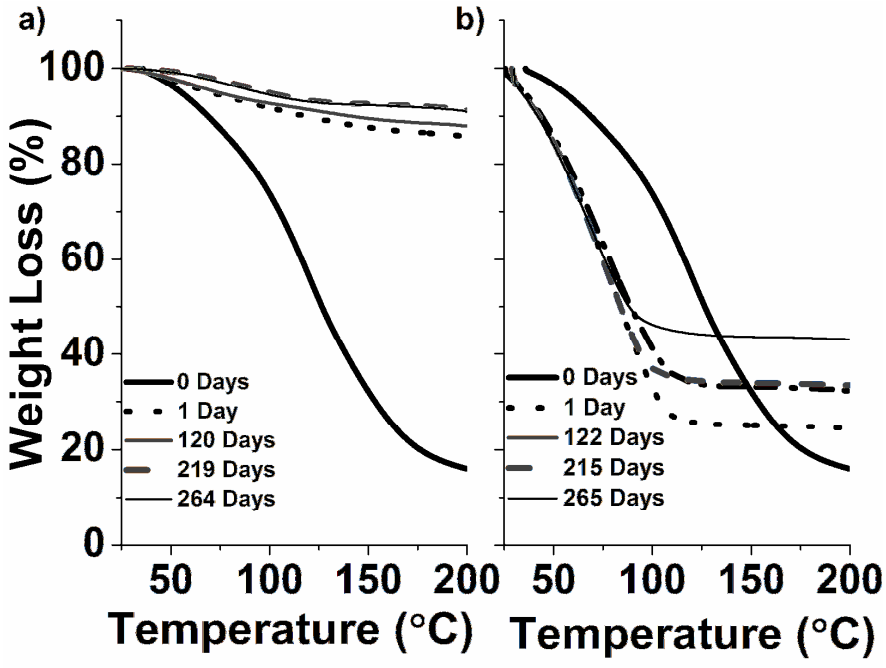

Figure 4.34. TGA of PF10P4000 gel fibers aged in a) MeOH and b) MeOH/water at 10 °C/min in nitrogen.

Overall, the weight fraction of solvent within gels aged in MeOH/water was considerablly more than the amount of solvent remaining in gels aged in MeOH. As discussed in Chapter 1, the swelling ratio (Q in equation 1.2-1.4) influenced the storage modulus of gel fiber, such that increasing amounts of imbibed solvent would adversely influence the storage modulus of gel fiber. In agreement with this relationship, the values of $E'(f)$ for gels aged in MeOH/water was less than the value reported for gels that were aged in MeOH and for a similar period of time. The content of solvent within as-spun PF10P4000 gels was reduced by only 10% after 1 day of MeOH/water aging. The weight fraction of unbound water within the PF10P4000 gels was shown to increase upon gel aging from up to 120 days in MeOH/water. The increase of unbound water was also observed within T_{evap1} peak for drawn fibers (in Figure 4.32b1). The weight fraction of solvent had decreased from 33 to 44 % with additional aging from 215-265 days (Figure 4.34b). As a result, the storage modulus of PF10P4000 gels had decreased with aging from 215-264 days; this behavior was most obvious at higher frequencies.

PVA crystals within PF10P4000 gels are described in Table 4.21 and 4.22 and Figure 4.35 and 4.36. The PF10P4000 gels aged in MeOH/water were slightly less crsytalline (38-42%) than gels aged in MeOH (44-47%). Drawn fibers were 10-12% more crystalline than aged gel fibers and 45% more crystalline than as-spun gel fibers. The ordering of PVA chains within PF10P4000 gels was independent of aging solvent.

Table 4.21. WAXD Characterization of PF10P4000 Gel Fibers Aged in MeOH.

Sample Designations		**PF10P4000-0MeOH-Gel**	**PF10P4000-1MeOH-Gel**	**PF10P4000-120MeOH-Gel**	**PF10P4000-219MeOH-Gel**	**PF10P4000-264MeOH-Gel**
MeOH Aging Time (Days)		0	1	122	219	263
X_c [a] **(%)**		5, 5	46, 48	47, 41	47, 48	44, 46
XS [b] (nm)	**(100)**	2, 2	5, 5	5, 5	5, 5	5, 5
	(111)	5, 5	5, 5	5, 4	5, 5	5, 5
d-spacing (nm)	**(100)**	0.62, 0.62	0.76, 0.76	0.76, 0.76	0.76, 0.76	0.76, 0.76
	(110)	-	0.24, 0.24	0.24, 0.24	0.24, 0.24	0.24, 0.24
	(111)	0.22, 0.22	0.22, 0.22	0.22, 0.22	0.22, 0.22	0.22, 0.22

Crystal sizes were not reported for the (110) planes of low peak intensity. a) X_c represents the crystallinity of gel fiber and b) *XS* stands for crystal size

Table 4.22. WAXD Characterization of PF10P4000 Gel Fibers Aged in MeOH/water.

Sample Designations		**PF10P4000-0MeOH/ Water-Gel**	**PF10P4000-1MeOH/ Water-Gel**	**PF10P4000-122MeOH/ Water-Gel**	**PF10P4000-215MeOH/ Water-Gel**	**PF10P4000-265MeOH/ Water-Gel**
MeOH/Water Aging Time (Days)		0	1	122	215	265
X_c [a] **(%)**		5, 5	37, 39	38, 40	43, 41	40, 40
XS [b] (nm)	**(100)**	2, 2	5, 5	5, 5	5, 5	5, 5
	(111)	5, 5	5, 6	6, 6	5, 5	5, 5
d-spacing (nm)	**(100)**	0.62, 0.62	0.76, 0.76	0.76, 0.76	0.76, 0.76	0.77, 0.77
	(110)	-	0.24, 0.24	0.24, 0.24	0.24, 0.24	0.24, 0.24
	(111)	0.22, 0.22	0.22, 0.22	0.22, 0.22	0.22, 0.22	0.22, 0.22

Crystal sizes were not reported for the (110) planes of low peak intensity. a) X_c represents the crystallinity of gel fiber and b) *XS* stands for crystal size.

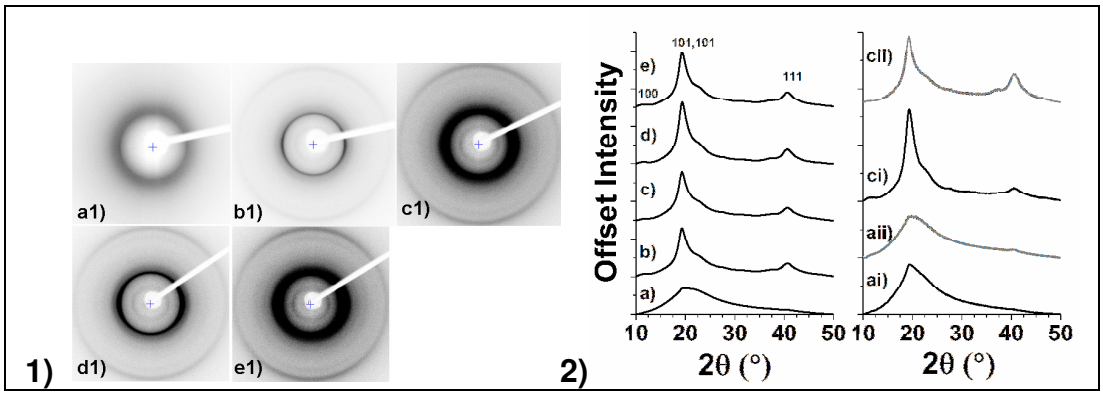

Figure 4.35. WAXD analysis of PF10P4000 gels aged in MeOH for a) 0, b) 1, c) 15, d) 122, e) 215, and f) 256 days: 1) diffraction patterns, 2) integrated radial scans, equatorial scans (ai and ci) and meridonal scans (aii and cii).

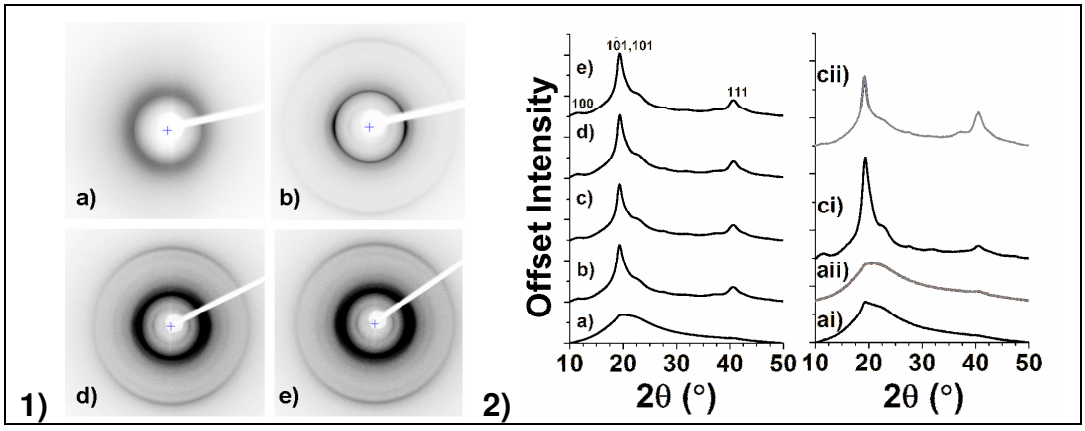

Figure 4.36. WAXD analysis of PF10P4000 gels aged in MeOH/water for a) 0, b) 1, c) 122, d) 215, and e) 256 days: 1) diffraction patterns, 2) integrated radial scans, equatorial scans (ai and ci), and meridonal scans (aii and cii).

The dimensions of ordered PVA, along the *a*-axis and planes perpendicular to the *b*-axis of PF10P4000 gels, were independent of aging solvent. The *XS* for (100) planes were ~5 nm for aged PF10P4000 gels. As observed in the study of other gels, the d-spacing for (100) planes gradually increased from 0.62 to ~0.76 nm after ≥1 day of gel aging. Diffraction from (001) planes was not detected; therefore, PF10P4000 gels were also believed to consist of PVA chains that were arranged in the form of ordered sheets.

The hydrogen bonding of PVA chains to solvent molecules would hinder inter-chain hydrogen bonding (along the *c*-axis of the Bunn unit cell in Figure 1.1). The d-spacing within the as-spun gel was suggestive of solvent molecules that were tightly bounded to PVA chains within CNT composite gels than within neat gels. The d-spacing of (100) planes within as-spun gels of 10P40000 and PF104000 was 0.62 nm and 0.68 nm, respectively. The d-spacing for (100) planes had increased to 0.76-0.79 nm within aged gels and drawn fibers. Values that were closer to 0.79 nm were indicative of hydrogen bonding between PVA chains. The d-spacing for the $(10\bar{1})$/(101) diffraction peak was ≈0.45 nm for organized PVA in PF10P4000 gels (Figure 4.35 and 4.36) and fibers drawn from aged gels. These widths were indicative of solvent within the PVA lattice and hydrogen bonding between PVA chains and solvent, namely water. As a result of PF10P4000 gel aging in MeOH and MeOH/water, the $(10\bar{1})$/(101) and (111) planes had a slight preference for alignment along the equatorial and meridonal planes.

4.3.6. Stiffening of 10P4000 and PF10P4000 Fibers

Samples of drawn 10P4000-120MeOHWater and PF10P4000-215MeOHWater fiber were vacuum dried at 85℃ for 1 day and then annealed at 210 and 220 ℃, respectively, at feed and take-up rates of 5 m/min. The objective of this trial was to improve the modulus of fibers having residual solvent. As a result of further processing, the *TS* of 10P4000-120MeOH/water fiber had decreased from 0.89 ± 0.15 to 0.59 ± 0.05 GPa, but the *TM* of that fiber had increased from 12 ± 3 to 17 ± 2 GPa. A similar behavior was observed for drawn PF10P4000-215MeOH/Water fiber after processing, in which the *TS* had decreased, but the *TM* had increased. The *TS*, *TM*, and strain at break for drawn PF10P4000-215MeOH/Water fibers, after further processing, was 1.06 ± 0.08

GPa, 33 ± 2 GPa, and 5.1 ± 0.4%. The representative stress-strain behaviors for PF10P4000 fibers (before and after stiffening) are featured in Figure 4.37.

The X_c of PF10P4000 fiber was not affected by processing; the reported value was X_c=55%. Nevertheless, the crystalline orientation for PF10P4000 fiber decreased after the heat treatment from ~0.91 to 0.88. The relaxation of crystalline polymer had likely occurred upon the use of the high temperature treatment. As a result, the *TS* value of the PVA/FWNT fiber decreased slightly. Although *TM* values of the 10P4000 and PF10P4000 fibers increased after processing, the PVA/FWNT fiber exhibited a greater level of stiffening. FWNTs were believed to restrict the thermal relaxation of polymer within the composite fiber; such that the modulus improved and the strength of the composite fiber was not compromised to the same extent as that of the neat fiber upon heating. As observed in Figure 2.2., the presence of CNTs can restrict thermal shrinkage.

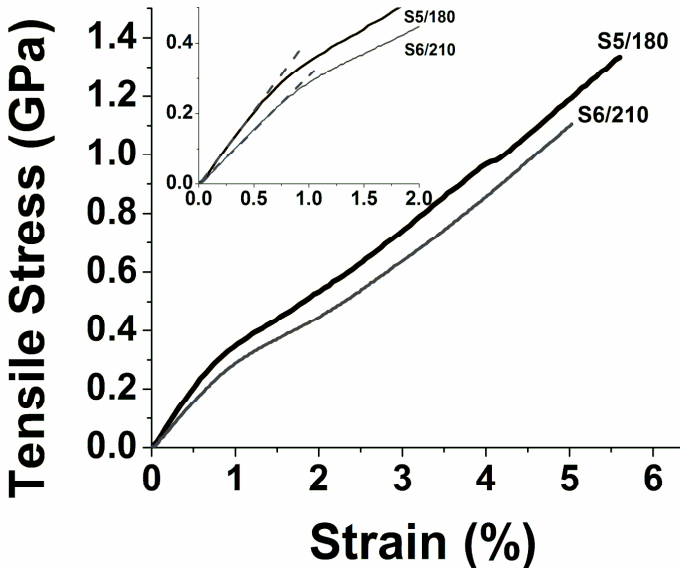

Figure 4.37. Stress-strain curves of drawn PF10P4000-215 fiber at S5/180 and S6/210.

4.4. Conclusions

The aging technique was used to increase the drawability of CNT composite fibers and to aid the nucleation of ordered PVA along CNTs. The values of *DR* for 99.75:0.25 PVA/SWNT fibers increased from 4 to 6 X, and the tensile strength of drawn fibers had increased from 0.6 to 1.1 GPa. The values of *DR* for 99.76:0.24 PVA/FWNT fibers increased from 7 to 8 X, and the mechanical strength of drawn fibers increased from 0.9 to 1.3 GPa. These PVA/CNT fibers that were drawn from gels aged in MeOH/water for ≥215 days exhibited higher tensile strength values than fibers drawn from gels that were aged for lesser time. The aging process invoked the enthalpic relaxation of polymer chains at ~50 °C. This process of molecular relaxation is believed to have increased the drawability of matrix polymer. The strongest of the fibers drawn from aged gels exhibited the highest melting temperatures and some exhibited a second peak/shoulder of high temperature melting. The shifting of T_m to higher temperatures of melting was attributed to the ordering of PVA along CNTs.

The unfilled PVA fiber that was drawn from gel aged in MeOH/water for 18 months yielded fiber of 1.2 GPa. Nevertheless, the optimum conditions for PVA fiber spinning utilized PVA-10000 polymer and the aging of gel in 10 ℃ MeOH for 1 day. The reported *TS* and *TM* values of that fiber were 1.2 GPa and 36 GPa, respectively. Therefore, the aging technique appears to be beneficial to the process of spinning PVA/CNT fibers.

CNTs were shown to behave as structural supports within as-spun and aged gel fiber. The values of *E'(f)* from PVA/CNT gels were more reproducible than for unfilled gels, especially after aging. The incorporation of ~0.25 wt.% CNTs in PVA improved

the uniformity of most gels; however, gels still exhibited the behavior of a loose network. This behavior has also provided evidence that CNTs have nucleated the ordering of PVA chains in the gel state. As-spun and aged gels consisted of ordered regions of polymer chains that have the form of two-dimensional sheets, along the *a*- and *b*-axis. As-spun gels have low values for 100 planar spacing (<0.78 nm). This observation suggests that the PVA chains were hydrogen bonded to solvent molecules rather than each other. Hydrogen bonding between PVA chains and solvent within as-spun gel fibers had occurred along the *a*-axis, as represented by the Sakurada unit cell model.

Tanigami et al. had reported the fabrication of high strength and high modulus tapes of PVA from gels aged in 10 °C water for 4 months. After gel aging, films (of 20 mm X 2 mm) were dried before drawing them at 200 °C.[32] In comparison to their method, swollen gels of continuous filament were drawn in this study. The surface of gel fiber was kept from sticking together since fibers were drawn from spools of swollen gel filaments. The removal of solvent imbibed within amorphous and ordered chains of PVA is necessary to improve the ultimate strength and modulus of PVA/CNT fibers that have been drawn from aged gels.

Through the application of additional heating, the *TM* of PVA/FWNT was increased from 24 to 33 GPa although the *TS* decreased from 1.33 to 1.06 GPa. Therefore, the process of high temperature annealing and fiber tensioning should be optimized for fiber stiffening. The relaxation of crystalline polymer at higher temperatures, which would enable the drawing of ECC phase, must be balanced with the relaxation and melting of crystalline PVA. Nevertheless, the mechanical properties of the final PVA/FWNT fiber were similar to the properties of the PVA/SWNT fibers that were

prepared by Zhang et al.[158] In that study, PVA/SWNT fiber (from the same PVA-4000 polymer and 3 wt.% SWNTs) had properties of *TS*=1.1 GPa and *TM*=35.8 GPa.

CHAPTER 5

CONCLUSIONS AND RECOMMENDATIONS

5.1. Conclusions

The section will highlight the conclusions from each chapter.

5.1.1. Chapter 2

The mechanical and thermal properties of PVA and PVA/SWNT composite fibers were influenced by the following phases: crystalline polymer, amorphous polymer, and imbibed solvent. After stage-4 fibers were drawn at 220 °C and then treated at 180 °C, the *TS* of PVA fibers increased from 0.81 to 1 GPa, and the *TM* increased from 26 to 31 GPa. Drawing induced crystal growth along the *b*-axis. As the value of *DR* increased from 4.1 X to 7.5 X, crystal sizes determined from the (110) plane increased from 5 nm to 12 nm.

The physical properties of composite fibers were further influenced by the draw-induced alignment of embedded SWNTs. Drawn PVA/SWNT fibers were less susceptible to thermal shrinkage at temperatures below 200 °C than neat PVA fibers. As a result of drawing, a SWNT interphase of polymer side groups and solvent molecules had exhibited preferential orientation. In contrast, the consecutive drawing of neat PVA fibers did not induce any preferential orientation among hydroxyl groups and water molecules within those fibers. Matrix moieties were engaged in charge transfer between themselves and SWNTs, as confirmed by molecular modeling. 10% of the PVA hydroxyl groups were aligned in response to SWNT alignment. 40% the water molecules had aligned in response to SWNT alignment. The alignment of solvent and other

impurities along SWNTs poses a concern for improving the polymer interface between embedded SWNTs and bulk polymer.

5.1.2. Chapter 3

The bulk heterogeneity of PVA/CNT dispersions and PVA homopolymer solutions were similar. Values of $G'(\omega)/G'(\omega)\approx1.5$ were reported for PVA/CNT dispersions and PVA solutions alike. Plots of $\eta^*(\omega)$ have shown measurements from filled and unfilled samples to be reproducible, which would suggest the SWNTs were well dispersed in polymer.

The sonication of polymer with CNTs has reduced the *DP* of that polymer. PVA/DMSO solutions of 0.5 g/dL were sonicated and tested using the Ubbelohde viscometer. The capillary elution time decreased with sonication time. PVA/SWNT and PVA/FWNT dispersions had calculated DP_w values of 8,900 and 3,700, respectively. PVA solutions had DP_w values of 10,000, 7,000 and 4,000. The solution of PVA-7000 was a blend of polymers having DP_w values of 10,000 and 4,000.

DP_w seemed to have the greatest effect on complex viscosity trends. Plots of $\eta^*(\omega)$ were fitted with the modified Carreau model. At loadings of ~0.25 wt.% CNTs, the dispersion of CNTs in polymer had a lesser effect on the overall rheology of these samples. Samples 4P10000, PS4P10000, and 4PBlend were all composed of 4 wt.% PVA, and samples 10P4000 and PF10P4000 were composed of 10 wt.% PVA. The values of η^0 and λ decreased with decreasing values of DP_w. The b increased as the DP_w decreased. The shear thinning behaviors for all of these samples were the same, where values of m=1 were reported.

CNTs influenced the nucleation-and-growth of cryo-transformations, such as polymer gelation and solvent freezing. The mechanisms and kinetics of cryo-transformation were obtained from an isoconversional analysis of DSC data. The value of E_a gradually increased with the conversion of homopolymer solutions; this behavior for E_a has been associated with the parallel mechanism of transformation. E_a trends for CNT dispersions and for the polymer blend were different from those occurring within homopolymer; the value of E_a at the onset of conversion was suggestive of heterogeneous nucleation. The polymer interphase along CNTs and the boundary between blended polymers were proposed as other sources of heterogeneous nucleation.

The incorporation of CNTs, the polymer's DP_w, and annealing temperature were shown to influence the change in conformational entropy for cryo-transformation. The values of $S(T_f)$-$S(T_i)$ were plotted against T_{anneal}. Samples containing CNTs had shown lower values of $S(T_f)$-$S(T_i)$ than homopolymer solutions, for each value of T_{anneal}. When T_{anneal}=30 °C, homopolymer sample 10P4000 had the highest values of $S(T_f)$-$S(T_i)$. Low values of $S(T_f)$-$S(T_i)$ were attributed to the chain mobility that was constrained by surfaces and/or molecular ordering.

Avrami nucleation-and-growth models fitted most of the experimentally determined models of cryo-transformation, except for 4PBlend annealed at 70 °C and PS4P10000 annealed at 30 °C.

5.1.3. Chapter 4

The gel aging technique was shown to increase the drawability and mechanical properties of fibers drawn from PVA/CNT gels. The *DR* increased from 4 to 6 X for PVA/SWNT fibers that were drawn from gels aged for up to 219 days in 10 °C

MeOH/water. The *TS* of these fibers increased from 0.63 GPa to 1.1 GPa, and the *TM* increased from 13 to 22 GPa. Drawn PVA/SWNT fibers, having a tensile strength of >1 GPa, had circular cross sections; the values of *CI* ranged from 0.87 to 0.95.

DR had increased from 7.3 to 8.7 X for PVA/FWNT fibers that were drawn from gels aged in 10 °C MeOH for up to 219 days. The *TS* increased from 0.70 to 1.0 GPa, and the *TM* increased from 13 to 22 GPa. These PVA/FWNT fibers were fairly circular for MeOH aging up to 219 days; the *CI* values ranged from 0.88 to 0.94.

The *DR* increased from 5 to 8 X for PVA/FWNT fibers that were drawn from gels aged in 10 °C MeOH/water for 122-265 days. The *TS* increased from 0.7 to ≥1.2 GPa. The highest reported value of *TM* was 28 GPa. The *CI* values of drawn PVA/FWNT fiber were 0.83 and 0.92.

Gel aging was believed to have enhanced the relaxation of polymer chains within precursor PVA/CNT fibers during elevated temperature drawing. MDSC thermograms, of fibers drawn from aged gels, shows transitions that are indicative of enthalpic relaxation.

As a result of drawing PVA/CNT fibers to higher *DR*, the melting temperature of crystalline PVA had increased. PVA/CNT fibers, having *TS* values ≥1 GPa, manifested a high temperature shoulder along the more prominent melting peak or two melting peaks. The melting of crystalline PVA at the higher temperature was attributed to the molecular chain extension of ordered PVA along CNT templates. The crystal sizes of the (110) planes, which were perpendicular to the molecular axis of PVA chains, were the largest for these fibers.

The highest values of *TM* were achieved for unfilled PVA fibers (at 36 GPa). PVA fiber (having a *DP* of 10,000) was drawn from gel that was aged for 1 day in 10 °C MeOH. Long term aging was not shown to improve the mechanical properties of neat fibers; instead the mechanical properties were shown to decrease. Since PVA gels were comprised of loose networks (where the storage modulus was a function of frequency), the density of physical crosslinks or chain entanglements may not have been sufficient for drawing at high draw ratios. Therefore, CNTs were believed to reinforce the network of composite gels, so that fibers could be drawn to higher draw ratios with aging time.

The *E'(f)* values for PVA/CNT gels were more reproducible than those obtained from unfilled gels of PVA. The DMA testing of as-spun and aged gel fibers further confirmed the ability of CNTs to stabilize the loose gel network.

As-spun gels consisted of ordered PVA chains that appeared bound to the solvent. The WAXD analysis shows diffraction peaks from *a*-axis planes and planes perpendicular to the molecular axes of PVA chains. In the absence of diffraction peaks indicative of *c*-axis planes, a sheet structure was determined. The values of d-spacing suggested intermolecular bonding between PVA chains and the solvent, rather than bonding between PVA chains. The (100) d-spacing should be equal to 0.778 nm according to the Bunn unit cell model of PVA, but instead the (100) d-spacing of ≤0.68 nm was observed from as-spun PVA. This reduction in d-spacing was presumed the effect of hydrogen bonding between PVA chains and an intercalated layer of water molecules.

The Sakurada unit cell model was used to describe the ordering of PVA in as-spun gel fibers. The Bunn unit cell models seemed to describe the ordering of PVA within aged gel fibers and drawn fibers.

The composition and weight fraction of solvent in the aged gels were influenced by the aging time and the bath composition. DMSO readily diffused from the gel microstructure with solvent aging at 10 °C; however, water and DMSO/water complexes were found to infuse the gel at longer aging times. Solvent, namely water, was found to exist in the following phases: solvated amorphous polymer, bound to ordered chains of PVA, and as pure solvent.

5.2. Recommendations

The aging of gel fiber in solvent was used to increase the fiber draw ratio of composite fibers and to promote the structural reinforcement of PVA by CNTs. This study has provided indirect evidence of structural reinforcement; such as higher Tm, CNTs coated with polymer, and CNT nucleation of gel crystals. Evidence of molecular adhesion between CNTs and polymer could also be provided by the TEM analysis of drawn fibers and of PVA/CNT dispersions. TEM analysis would also give an idea of CNT exfoliation within the drawn fibers. Furthermore, the loading of well-dispersed CNTs at higher weight fractions may improve the mechanical properties of composite fibers produced by the gel aging technique.

Although gel fiber aging in MeOH/water was shown to enhance the tensile properties of drawn PVA/CNT fibers, residual water was believed to have prohibited the achievement of higher properties. Solvent was shown to reside within the crystalline and amorphous phases of PVA polymer. In an attempt to reduce the content of residual water

in PVA-based fibers, the use of PVA/CNT/DMSO dispersions is recommended for the aging study. Further, aging baths having a lower volume fraction of water may help to reduce the fraction of water bound to PVA.

APPENDIX A

RESCALED PLOTS OF THE EFFECTIVE ACTIVATION ENERGY

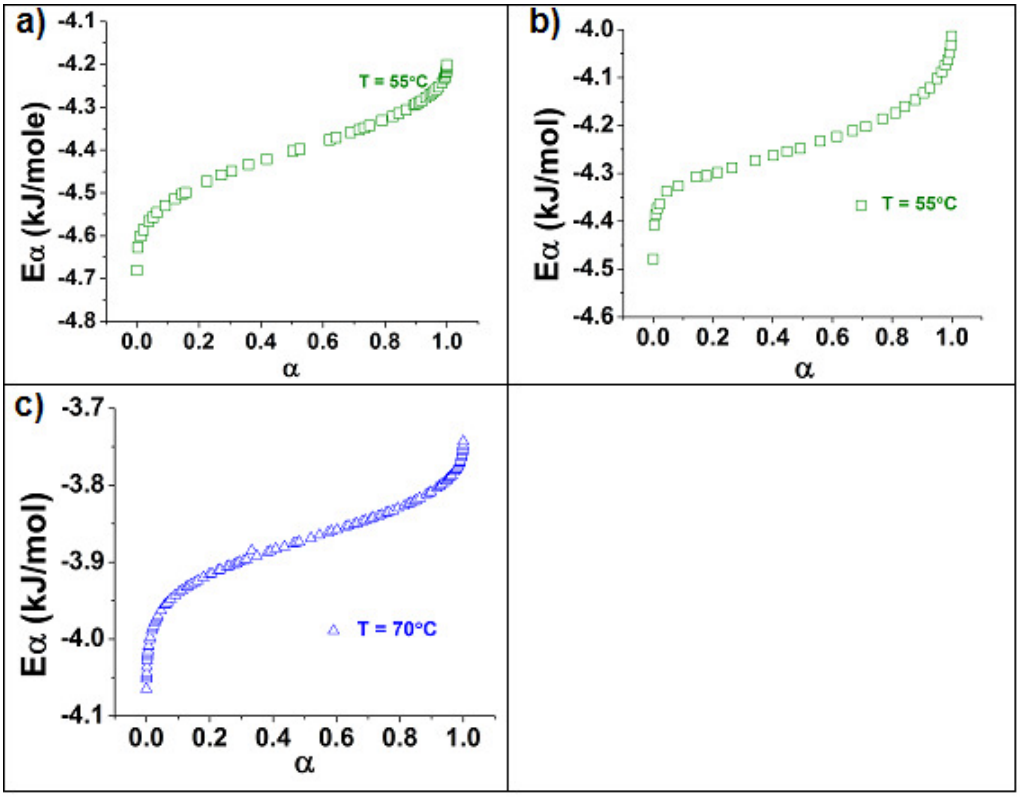

Figure A.1. Rescaled E_α plots for select samples to demonstrate nonlinear increases in E_α with conversion: a) 4P10000 annealed at 55℃, b) 10P40000 annealed at 55℃, and c) PF10P4000 annealed at 70℃.

APPENDIX B

FWNT SOLVENT DISPERSIONS

B.1. Experimental Procedure

FWNTs (X0122UA) were dispersed in organic solvents to see the effects of FWNTs on the freezing and melting behavior of solvent. The preparation of FWNTs in DMAc, DMSO, and the 80/20 (*v/v*) of DMSO/deionized water is summarized in Table B1. The total sonication time for each sample containing FWNTs was 24 hrs.

Table B.1. Preparation of FWNT/Solvent Dispersions.

Sample	Concentration of CNTs in Solvent	Procedure
D1	10 mg/L	1. Add 0.1 mg of CNT to 10 ml of solvent. 2. Then sonicate for 5 hours before making D2. 3. Sonicate 9 ml of solution for 20 hours before testing to compare with other dispersions.
D2	1 mg/L	1. Add 9 ml of solvent to 1 ml of D1. 2. Then sonicate for 5 hours before making D3. 3. Sonicate 9 ml of solution for 16 hours before testing to compare with other dispersions.
D3	0.1 mg/L	1. Add 9 ml of solvent to 1 ml of D2. 2. Then sonicate for 5 hours before making D4. 3. Sonicate 9 ml of solutions for 8 hours before testing to compare with other dispersions.
D4	0.01 mg/L	1. Add 9 ml of solvent to 1 ml of D1. 2. Then sonicate for 5 hours before removing 1 ml. 3. Sonicate 9 ml of solutions for 4 hours before testing to compare with other dispersions.

B.2. Results and Discussion

The images of FWNTs dispersed in DMAc, DMSO and an 80:20 DMSO/water are shown in Figure B.1. Homogeneous dispersions of FWNTs in DMAc (at 10 mg/L) were obtained immediately after sonication. Swollen aggregates of FWNTs were observed in DMSO; however, dense aggregates of FWNTs formed within DMSO/water. Ham et al. likewise observed the swollen state of CNTs immersed in DMSO; the sedimentation of SWNTs was observed in water.[73]

The melting temperatures of DMAc and DMSO are -19 and 18 °C, respectively (CRC Handbook). Experimentally obtained melting temperatures agreed with these reported values; supercooled liquid froze below their melting temperatures (Table B.2). The freezing temperature of 80:20 DMSO/water was -55 ± 1 °C for cooling rates of 10 C°/min. Therefore, FWNTs did not influence the temperatures of solvent melting and freezing; the surface tensions of the solvent remain unchanged as well (Table B.2).

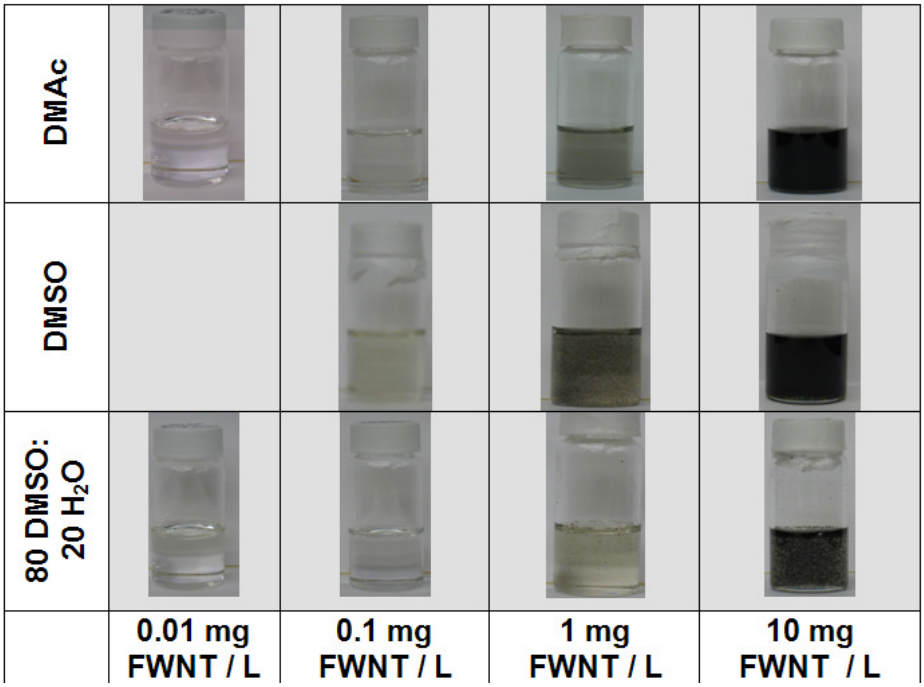

Figure B.1. FWNTs sonicated in organic solvent for a total of 24 hrs.

Table B.2. Thermal Properties of FWNTs Dispersed in Solvents.

	FWNT (mg/L)	Surface Tension (mN/m)	T_f [a] (°C)	ΔH_f [b] (J/g)	T_m [c] (°C)	ΔH_m [d] (J/g)	ΔT [e] (°C)
DMAc	0	36.0 ± 0.3	-60 ± 1	142 ± 31	-22 ± 1	95 ± 7	38 ± 3
	0.01	36.0 ± 0.1	-51 ± 7	113 ± 4	-24 ± 1	97 ± 6	27 ± 8
	0.1	36.1 ± 0.2	-58 ± 4	93 ± 33	-23 ± 4	94 ± 4	35 ± 8
	1	35.7 ± 0.1	-64 ± 6	67 ± 5	-28 ± 4	56 ± 11	36 ± 1
	10	35.9 ± 0.9	-63 ± 2	87 ± 6	-27 ± 1	76 ± 2	36 ± 2
DMSO	0	44.3 ± 0.4	8 ± 2	-	18 ± 4	-	10 ± 1
	0.1	42.2 ± 0.8	11 ± 1	174 ± 14	16 ± 1	155 ± 8	6 ± 1
	1	44.1 ± 0.3	9 ± 0	154 ± 4	15 ± 1	142 ± 4	6 ± 1
	10	44.1 ± 0.5	11 ± 0	181 ± 2	18 ± 0	155 ± 1	7 ± 0
80/20 DMSO/Water	0	49.1 ± 0.2	-55 ± 1	43 ± 1	-29 ± 1	38 ± 3	26 ± 0
	0.01	49.4 ± 0.1	-58 ± 4	45 ± 2	-30 ± 1	36 ± 2	29 ± 5
	0.1	49.2 ± 0.1	-55 ± 3	43 ± 1	-29 ± 1	38 ± 1	26 ± 3
	1	49.2 ± 0.1	-54 ± 1	38 ± 1	-30 ± 1	36 ± 1	24 ± 1
	10	49.1 ± 0.2	-48 ± 2	37 ± 1	-30 ± 1	35 ± 3	18 ± 2

a) T_f = temperature of solvent freezing, b) ΔH_f = enthalpy of freezing, c) T_m = solvent melting upon heating, d) ΔH_m = enthalpy of melting, and e) ΔT = difference between peak temperatures of solvent freezing and solvent melting. Samples were prepared in hermetically sealed T-zero pans and run at 5 °C/min.

APPENDIX C

LOSS MODULUS OF AGED GEL FIBERS

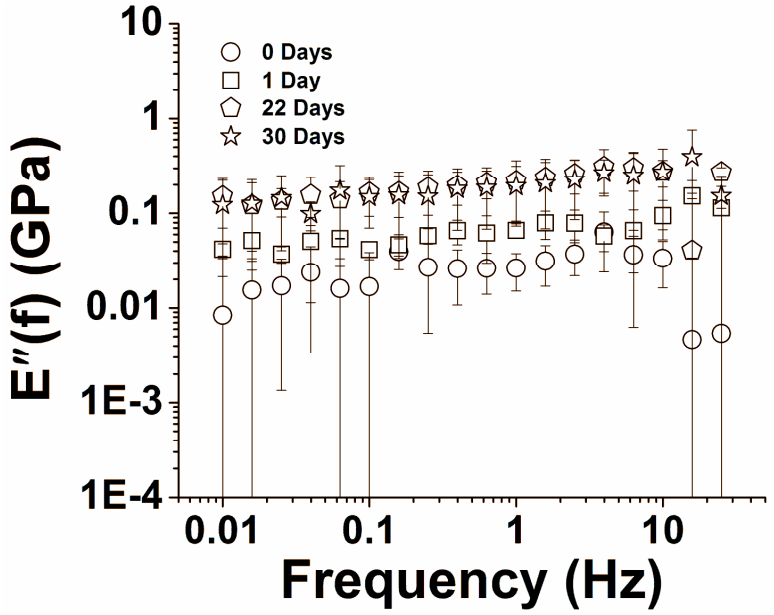

Figure C.1. Loss modulus of 4P10000 gel fibers aged in MeOH.

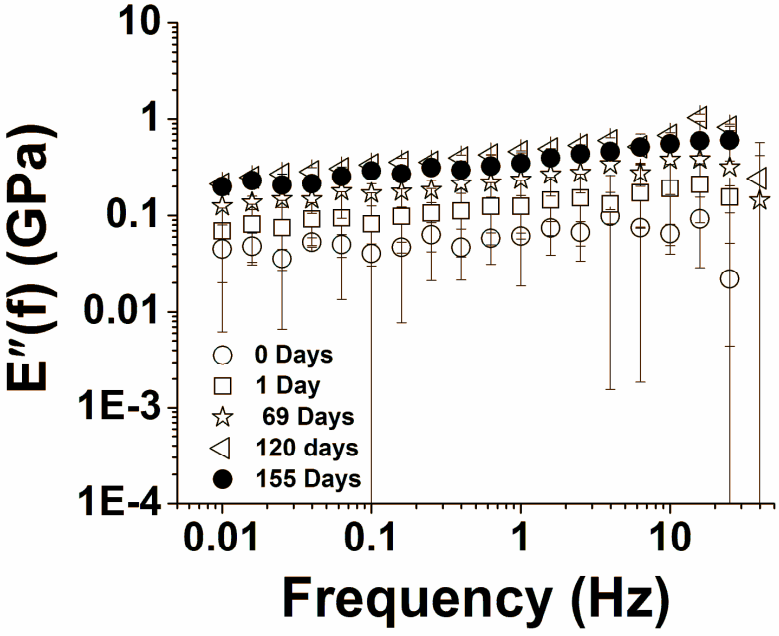

Figure C.2. Loss modulus of 4P10000 gel fibers aged in MeOH/water.

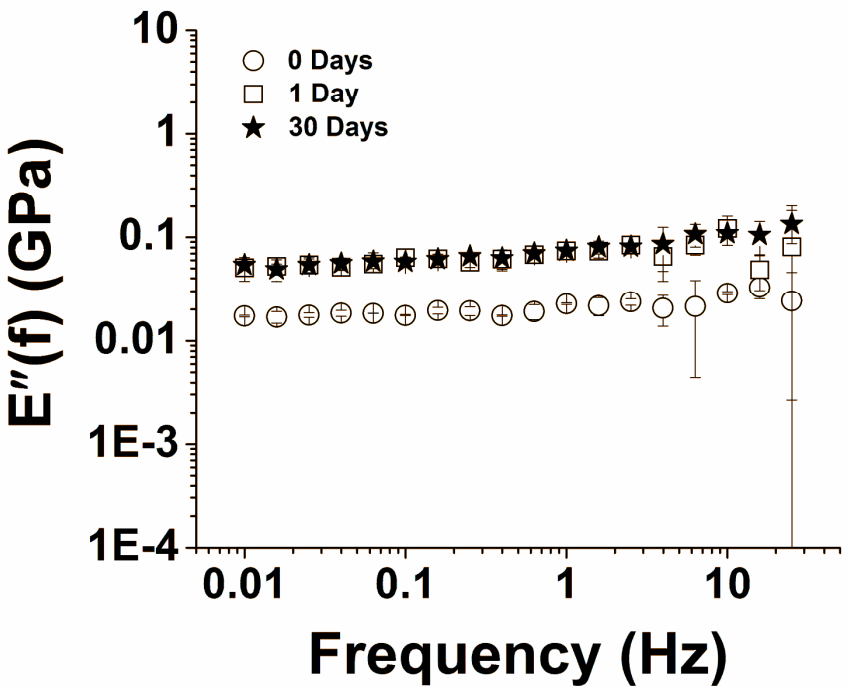

Figure C.3. Loss modulus of PS4P10000 gel fibers aged in MeOH.

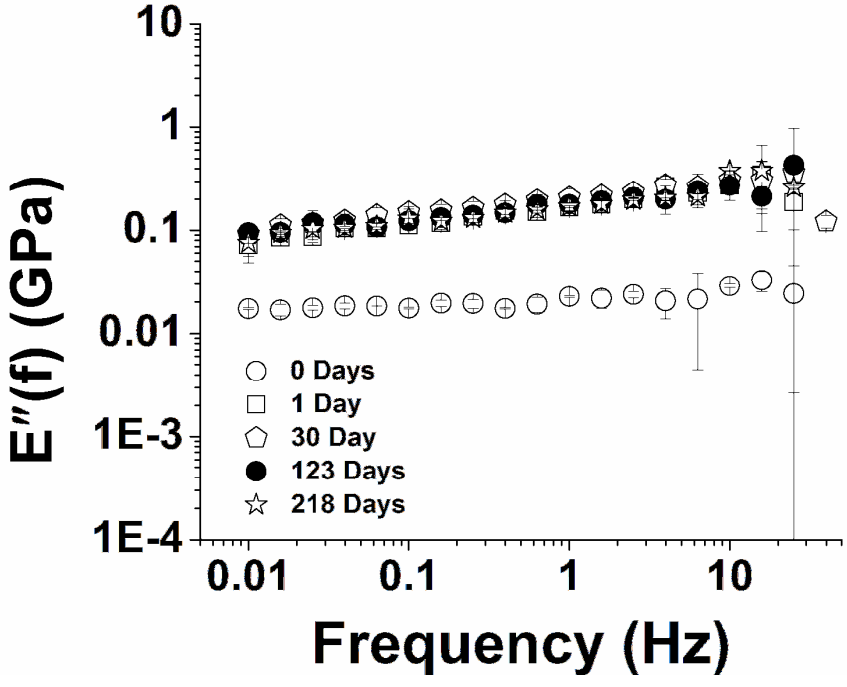

Figure C.4. Loss modulus of PS4P10000 gel fibers aged in MeOH/water.

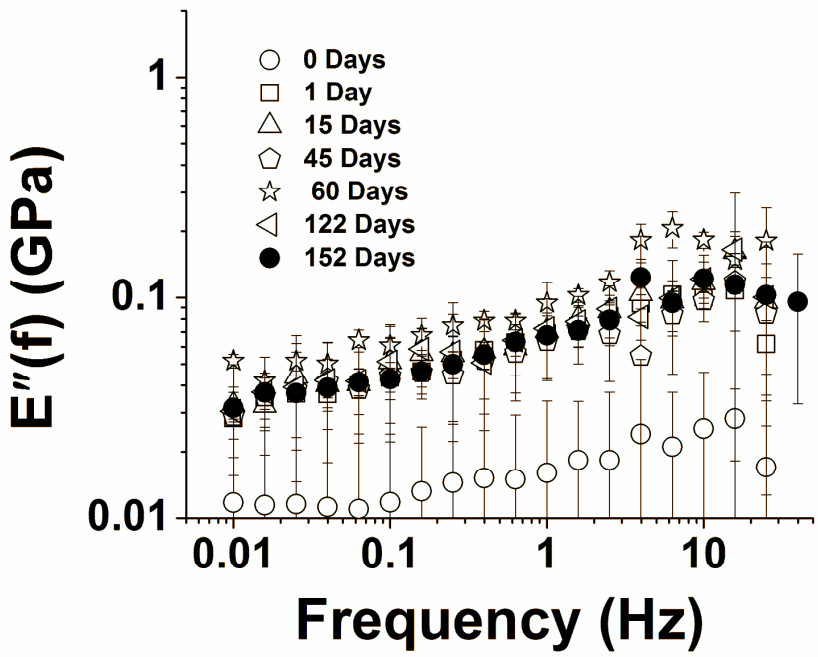

Figure C.5. Loss modulus of 10P4000 gel fibers aged in MeOH/water.

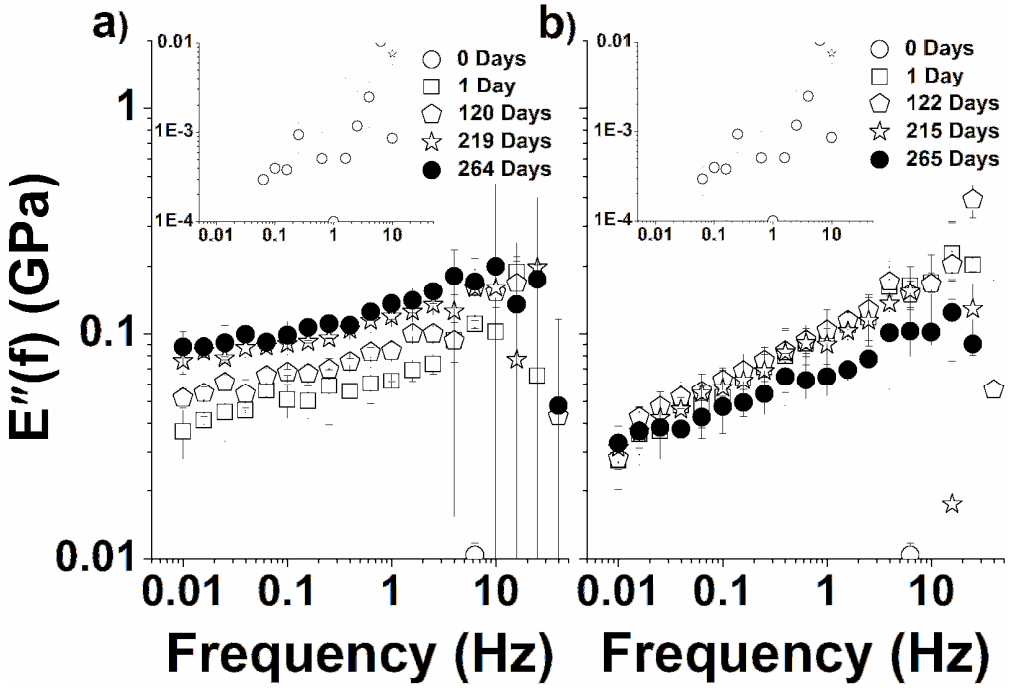

Figure C.6. Loss modulus of PF10P4000 gel fibers aged in a) MeOH and b) MeOH/water.

REFERENCES

1. Hearle, J.W.S., ed. *High-performance Fibres*. Woodhead Publishing Limited series on fibres, ed. J.E. McIntyre. 2001, The Textile Institute Woodhead Publishing Limited: Boca Raton. 329.

2. Nalankilli, G., *Gel Spinning- A Promising Technique for the Production of High Performance Fibres.* Man-Made Textiles in India, 1997. **40**(6): p. 237-242.

3. Smith, P., P.J. Lemstra, and J.P.L. Pijpers, *Tensile Strength of Highly Oriented Polyethylene. II. Effect of Molecular Weight Distribution.* Journal of Polymer Science Part B: Polymer Physics, 1982. **20**: p. 2229-2241.

4. Chae, H.G. and S. Kumar, *Making Strong Fibers.* Science, 2008. **319**(5865): p. 908-909.

5. *Kevlar Aramid Fiber Technical Guide*, Dupont, Editor.

6. Rubinstein, M. and R.H. Colby, *Polymer Physics*. 2003, Oxford: Oxford University Press. 440.

7. Gedde, U.W., *Polymer Physics*, ed. 1st. 1995, London: Chapman & Hall.

8. Hikosaka, M., et al., *Topological Mechanism of Polymer Nucleation and Growth - The Role of Chain Sliding Diffusion and Entanglement.* Advanced Polymer Science 2005. **191**: p. 137-186.

9. Qian, B., et al., *The Role of Macromolecular Entanglements in the Gel Spinnning Process and Properties of High Performance Polyacrylonitrile Fibers.* Journal of Polymer Engineering, 1995/1996. **15**: p. 327-345.

10. Rees, D.V. and D.C. Bassett, *Origin of Extended-chain Lamellae in Polyethylene.* Nature, 1968. **219**(5152): p. 368-370.

11. Smith, P. and P.J. Lemstra, *Ultra-high-strength Polyethylene Filaments by Solution Spinning/Drawing.* Journal of Materials Science, 1980. **15**(2): p. 505-514.

12. Cha, W.I., S.H. Hyon, and Y. Ikada, *Gel Spinning of Poly(vinyl Alcohol) from Dimethyl Sulfoxide/Water Mixture.* Journal of Polymer Science: Part B: Polymer Physics, 1994. **32**(2): p. 297 - 304.

13. Rubinstein, M. and A.N. Semenov, *Thermoreversible Gelation in Solutions of Associating Polymers. 2. Linear Dynamics.* Macromolecules, 1998. **31**(4): p. 1386-1397.

14. Kumar, S.K. and J.F. Douglas, *Gelation in Physically Associating Polymer Solutions.* Physical Review Letters, 2001. **87**(18): p. 188301(4).

15. Michael Rubinstein, R.H.C., *Polymer Physics*. 2003, Oxford: Oxford University Press. 440.

16. Berghmans, H. and F. Deberdt, *Phase Behavior and Structure Formation in Solutions of Vinyl Polymers.* Philosophical Transactions of the Royal Society of London, Series A: Mathematical, Physical and Engineering Sciences, 1994. **348**(1686): p. 117-130.

17. Hong, P.-D. and C.-M. Chou, *Effects of Phase Separation on Structural Characteristics of Poly(vinyl chloride) Physical Gels.* Macromolecules, 2000. **33**: p. 9673-9681.

18. Auriemma, F., C. De Rosa, and R. Triolo, *Slow Crystallization Kinetics of Poly(vinyl alcohol) in Confined Environment during Cryotropic Gelation of Aqueous Solution.* Macromolecules, 2006. **39**: p. 9429-9434.

19. Takahashi, N., et al., *Gelation-Induced Phase Separation of Poly(vinyl alcohol) in Mixed Solvents of Dimethyl Sulfoxide and Water.* Macromolecules, 2007. **40**: p. 8750-8755.

20. Xu, D., Y. Bin, and P. Tang, *Crystallization and Phase Separation of Branched Low Molecular Weight Polyethylene/Ultrahigh Molecular Weight Polyethylene Blend Under a Controlled Temperature Gradient.* Macromolecules, 2010. **43**(12): p. 5323-5329.

21. Berghams, H., et al., *Thermoreversible Gelation of Syndiotactic Poly(methyl methacrylate).* Polymer, 1987. **28**(1): p. 97-102.

22. Berghmans, M., et al., *Study of Polymer Gelation by Fluorescence Spectroscopy.* Polymer Engineering and Science, 1992. **32**(20): p. 1466-1470.

23. Liu, M., R. Cheng, and R. Qian, *Effect of Solution Concentration on the Gelation of Aqueous Poly(vinyl Alcohol) Solution.* Journal of Polymer Science, Part B: Polymer Physics, 1995. **33**(12): p. 1731-1735.

24. Hoshino, H., et al., *Gelation of Poly(vinyl alcohol) in Dimethyl Sulfoxide/Water Mixtures.* Polymer Bulletin, 1996. **37**(2): p. 237-244.

25. Yamaura, K., et al., *Gelation of Poly(vinyl Alcohol) Solutions at Low Temperatures (20 to -78C) and Properties of Gels.* Journal of Applied Polymer Science, 1994. **51**: p. 2041-2046.

26. Almdal, K., et al., *Towards a Phenomenological Definition of the Term 'Gel'.* Polymer Gels and Networks, 1993. **1**: p. 5-17.

27. Isabel E Pacios, I.F.P., *Discrimination of the Roles of Crosslinking Density and Morphology in the Swelling Behavior of Crosslinked Polymers: Poly(N-vinylimidazole) Hydrogels.* Journal of Applied Polymer Science, 2009. **112**: p. 1579-1586.

28. Joaquin Valencia, J.B., Ines F Pierola, *Compression Elastic Modulus of Neutral, Ionic, and Amphoteric Hydrogels Based on N-Vinylimidazole.* Journal of Polymer Science Part B: Polymer Physics, 2009. **47**: p. 1078-1087.

29. Sakurada, I. and T. Okaya, *Vinyl Fibers*, in *Handbook of Fiber Chemistry*, M. Lewin and E.M. Pearce, Editors. 1998, Marcel Dekker, Inc.: New York. p. 292-293,298-299,302-306,308-309, 313,317-322, 325-331

30. Bunn, C.W., *Crystal Structure of Polyvinyl Alcohol.* Nature, 1948. **161**(4102): p. 929-930.

31. Sakurada, I., T. Ito, and K. Nakamae, *Elastic Moduli of the Crystal Lattices of Polymers.* Journal of Polymer Science, Polymer Symposia, 1967. **15**: p. 75-91.

32. Tanigami, T., et al., *High Strength and High Modulus Poly(vinyl alcohol) by the Gel Ageing Method.* Journal of Materials Science, 1995. **30**(20): p. 5110-5120.

33. Suzuki, M., et al., *Influence of Molecular Weight and Syndiotacticity on the Structure of High-Performance Poly(vinyl alcohol) Fibers Prepared by Gel Spinning.* Journal of Applied Polymer Science, 2002. **86**(8): p. 1970-1977.

34. Endo, R., S. Amiya, and M. Hikosaka, *Conditions for Melt Crystallization Without Thermal Degradation and Equilibrium Melting Temperature of Atactic Poly(Vinyl Alcohol).* Journal of Macromolecular Science, Physics, 2003. **B42**(3&4): p. 793-820.

35. Cheng, S.Z.D., ed. *Handbook of Thermal Analysis and Calorimetry*. Applications to Polymers and Plastics, ed. P.K. Gallagher. Vol. 3. 2002, Elsevier: Amsterdam. 462-463.

36. Hassan, C. and N.A. Peppas, *Structure and Application of Poly(vinyl alcohol) Hydrogels Produced by Conventional Crosslinking or by Freezing/Thawing Methods.* Advances in Polymer Science, 2000. **153**: p. 37-65.

37. Ricciardi, R., et al., *X-ray Diffraction Analysis of Poly(vinyl alcohol) Hydrogels, Obtained by Freezing and Thawing Techniques.* Macromolecules, 2004. **37**(5): p. 1921-1927.

38. *Nycon.* http://www.nycon.com/ncwp (8/30/2012).

39. *Kuraray.* http://www.kuraray.co.jp/en/products, (8/30/2012).

40. Murahashi, S., et al., *The Preparation and Some Properties of Highly Stereoregular Poly(vinyl alcohol)s.* Polymer Letters, 1966. **4**(1): p. 59-63.

41. Lyoo, W.S., et al., *Effect of Stereosequences on Crystallinity and Properties of Zone-Drawn Poly(vinyl alcohol) Microfibrils.* Journal of Polymer Science Part B: Polymer Physics, 2001. **39**(12): p. 1263 - 1271

42. Minus, M.L., *The Study of Crystallization and Interfacial Morphology in Polymer/Carbon Nanoutbe Composites*, in *School of Polymer Textile, and Fiber Engineering*. 2008, Georgia Institute of Technology: Atlanta. p. 206.

43. Kunugi, T., T. Kawasumi, and T. Ito, *Preparation of Ultra-High Modulus Polyvinyl Alcohol Fibers by the Zone-Drawing Method.* Journal of Applied Polymer Science 1990. **40**(11-12): p. 2101-2112.

44. Tanigami, T., et al., *Ageing of Poly(vinyl alcohol) Gels Prepared from Dimethylsulfoxide/Water Solutions.* Polymer, 1994. **35**(12): p. 2573-2578.

45. Lipatov, Y.S. and I.S. Lipatov, *Polymer Reinforcement*. 1995, Toronto: ChemTec Publishing.

46. Shia, D., et al., *An Interface Model for the Prediction of Young's Modulus of Layered Silicate-Elastomer Nanocomposites.* Polymer Composites, 1998. **19**(5): p. 608-617.

47. Nakane, K., et al., *Properties and Structure of Poly(vinyl alcohol)/Silica Composites.* Journal of Applied Polymer Science, 1999. **74**: p. 133-138.

48. Choi, J.H., et al., *Preparation and Characterization of Syndiotacticity-rich Ultra-high Molecular Weight Poly(vinyl alcohol)/Imogolite Blend Film.* Polymer International 1998. **47**(2): p. 237-242.

49. Strawhecker, K.E. and E. Manias, *Structure and Properties of Poly(vinyl alcohol)/Na^+ Montmorillonite Nanocomposites.* Chem. Mater., 2000. **12**: p. 2943-2949.

50. Tanigami, T., et al., *Melting of the Blends Between Syndiotacticity-rich and Atactic Poly(vinyl alcohol)s.* European Polymer Journal, 19999. **35**: p. 1165-1171.

51. Chuangchote, S., A. Sirivat, and P. Supaphol, *Mechanical and Electro-rheological Properties of Electrospun Poly(vinlyl alcohol) Nanofibre Mats Filled With Carbon Black Nanoparticles.* Nanotechnology, 2007. **18**: p. 145705/1-8.

52. Baughman, R.H., A.A. Zakhidov, and W.A. deHeer, *Carbon Nanotubes- the Route Toward Applications.* Science, 2002. **297**(5582): p. 787-792.

53. Kroto, H.W., et al., *C60: Buckminsterfullerene.* Nature, 1985. **318**(6042): p. 162-163.

54. Iijima, S. and T. Ichihashi, *Single-shell carbon nanotubes of 1-nm diameter.* Nature, 1993. **363**(6430): p. 603-605.

55. Treacy, M.M.J., T.W. Ebbesen, and J.M. Gibson, *Exceptionally High Young's Modulus Observed for Individual Carbon Nanoutbes.* Nature, 1996. **381**(658): p. 678.

56. Dresselhaus, M.S., et al., *Raman spectroscopy of carbon nanotubes.* Physics Reports, 2008. **409**: p. 83-108.

57. Thayer, A.M., *Carbon Nanotubes by the Metric Ton*, in *Chemical & Engineering News*. 2007, American Chemical Society. p. 29-35.

58. *Cheap Tubes.com.* http://www.cheaptubesinc.com, 10/21/2012.

59. Kataura, H., et al., *Optical Properties of Single-Wall Carbon Nanotubes.* Synthetic Metals, 1999. **103**(1-3): p. 2555-2558.

60. Frogley, M.D., Q. Zhao, and H.D. Wagner, *Polarized Resonance Raman Spectroscopy of Single-wall Carbon Nanotubes Within a Polymer Under Strain.* Physical Review B, 2002. **65**(11): p. 113413/1 - 113413/4.

61. Wang, T., *Electrospun Carbon Nanofibers for Electrochemical Capacitor Electrodes*, in *School of Polymer, Textile Fiber Engineering*. 2007, Georgia Institute of Technology: Atlanta. p. 186.

62. Liu, J., *Carbon Nanotube/Polymer Composites and Novel Micro- and Nano-Structured Electrospun Polymer Materials*, in *School of Polymer, Textile & Fiber Engineering*. 2007, Georgia Institute of Technology: Atlanta. p. 219.

63. Shin, H., et al., *Tailoring Electronic Structures of Carbon Nanotubes by Solvent with Electron-Donating and -Withdrawing Groups.* Journal of the American Chemical Society, 2008. **130**(6): p. 2062-2066.

64. Bose, S., R.A. Khare, and P. Moldenaers, *Assessing the Strengths and Weaknesses of Various Types of Pre-treatments of Carbon Nanotubes on the Properties of Polymer/Carbon Nanotubes Composites: A Critical Review*. Polymer, 2010. **51**(5): p. 975-993.

65. Grady, B.P., *The Use of Solution Viscosity to Characterize Single-Walled Carbon Nanotube Dispersions.* Macromolecular Chemistry and Physics, 2006. **207**(23): p. 2167-2169.

66. Weisman, R.B. and S. Subramoney, *Carbon Nanotubes.* The Electrochemical Society Interface, 2006. **Summer**: p. 42-26, http://www.electrochem.org/d/interface/sum/sum06_p42.pdf.

67. Zhang, X., et al., *Poly(vinyl alcohol)/SWNT Composite Film.* Nano Letters, 2003. **3**(9): p. 1285-1288.

68. Chae, H.G., M.L. Minus, and S. Kumar, *Oriented and Exfoliated Single Wall Carbon Nanotubes in Polyacrylonitrile.* Polymer, 2006. **47**(10): p. 3494-3504.

69. Liu, T. and S. Kumar, *Quantitative Characterization of SWNT Orientation by Polarized Raman Spectroscopy.* Chemical Physics Letters, 2003. **378**(3,4): p. 257-262.

70. Perez, R., S. Banda, and Z. Ounaies, *Determination of the Orientaiton Distribution Function in Aligned Single Wall Nanotube Polymer Nanocomposites by Polarized Raman Spectroscopy.* Journal of Applied Physics, 2008. **103**(7, Pt. 1): p. 074302/1 - 074302/9.

71. Bhattacharyya, A.R., et al., *Crystallization and Orientation Studies in Polypropylene/Single Wall Carbon Nanotube Composite.* Polymer, 2003. **44**(8): p. 2373-2377.

72. Moore, V., et al., *Individually Suspended Single-Walled Carbon Nanotubes in Various Surfactants.* Nano Letters, 2003. **3**(10): p. 1379-1382.

73. H. Ham, Y. Choi, and I. Chung, *An explanation of dispersion states of single-walled carbon nanotubes in solvents and aqueous surfactants solutions using solubility parameters.* Journal of Colloid and Interface Science, 2005. **286**: p. 216-223.

74. Ham, H.T., Y.S. Choi, and I.J. Chung, *An Explanation of Dispersion States of Single-walled Carbon Nanotubes in Solvents and Aqueous Surfactant Solutions Using Solubility Parameters.* Journal of Colloid and Interface Science, 2005. **286**(1): p. 216-223.

75. Yang, D., J. Rochette, and E. Sacher, *Spectroscopic Evidence for π-π Interaction Between Poly(diallyl dimethylammonium) Chloride and Multiwalled Carbon Nanotubes.* Journal of Physical Chemistry B, 2005. **109**(10): p. 4481-4484.

76. R. Foster, *Organic Charge-Transfer Complexes*. Organic Chemistry, ed. A.T. Blomquist. 1969, London: Academic Press. 470.

77. A. Rao, et al., *Evidence for charge transfer in doped carbon nanotube bundles from Raman scattering.* Nature, 1997. **388**(6639): p. 257-259.

78. W. Zhou, et al., *Single-Walled Carbon Nanotube-Templated Crystallization of H_2SO_4": Direct Evidence for Protonation.* Journal of American Chemical Society, 2005. **127**: p. 1640-1641.

79. G. Voyiatzis, et al., *Polarized Resonance Raman and FTIR Reflectance Spectroscopic Investigation of the Molecular Orientation in Industrial Poly(Vinyl Chloride) Specimens.* Macromolecules, 2000. **33**(15): p. 5613-5623.

80. K. Tashiro, M. Kobayashi, and H. Tadokoro, *Polarized Raman Spectra of Doubly Oriented Poly(vinyl alcohol).* Polymer Bulletin, 1978. **1**(1): p. 61-66.

81. N. Everall, J. Chalmers, and P. Mills, *Use of Polarized Resonance Raman Spectroscopy of a Polyene Probe, and FT-IR Dichroism, to Probe Amorphous-Phase Orientation in Uniaxially Drawn Poly(ethylene).* Applied Spectroscopy, 1996. **50**(10): p. 1229-1234.

82. L. Cho, et al., *A New Method for Fiber Comparison Using Polarized Infrared Microspectroscopy.* Journal of Forensic Sciences, 1999. **44**(2): p. 275-282.

83. Yuan, C., et al., *Insight Into Carbon Nanotube Effect on Polymer Molecular Orientation: An Infrared Dichroism Study.* Chemical Communications, 2011. **47**(3): p. 899-901.

84. Chen, G., et al., *An Attenuated Total Reflection FT-IR Spectroscopic Study of Polyamide 6/Clay Nanocomposite Fibers.* Molecular Rapid Communications, 2004. **25**: p. 1121-1124.

85. Chen, Q., Y. Bin, and M. Matsuo, *Characteristics of Ethylene-Methyl Methacrylate Copolymer and Ultrahigh Molecular Weight Polyethylene Composite Filled with Multiwall Carbon Nanotubes Prepared by Gelation/Crystallization from Solutions.* Macromolecules, 2006. **39**(19): p. 6528-6536.

86. Minus, M.L., H.G. Chae, and S. Kumar, *Single Wall Carbon Nanotube Templated Oriented Crystallization of Poly(vinyl alcohol).* Polymer, 2006. **47**(11): p. 3705-3710.

87. Bin, Y., et al., *Development of Highly Oriented Polyethylene Filled with Aligned Carbon Nanotubes by Gelation/Crystallization from Solutions.* Macromolecules, 2003. **36**(16): p. 6213-6219.

88. Coleman, J.N., et al., *Reinforcement of polymers with carbon nanotubes. The role of an ordered polymer interfacial region. Experiment and modeling.* Polymer, 2006. **47**: p. 8556-8561.

89. Karevan, M., et al., *Effect of Interphase Modulus and Nanofiller Agglomeration on the Tensile Modulus of Graphite Nanoplatelets and Carbon Nanotube Reinforced Polypropylene Nanocomposites.* Carbon Letters, 2010. **11**(4): p. 325-331.

90. van Hutten, P.F., C.E. Koning, and A.J. Pennings, *The Deformation Behavior of Polyethylene Shish-kebab Produced by Stirring Induced-crystallization.* Colloid and Polymer Science, 1984. **262**: p. 521-525.

91. Li, C.Y., et al., *Nanohybrid Shish-Kebabs: Periodically Functionalized Carbon Nanotubes.* Advanced Materials, 2005. **17**: p. 1198-1202.

92. Li, L., et al., *Carbon nanotube induced polymer crystallization: The formation of nanohybrid shish-kebabs.* Polymer, 2009. **50**(4): p. 953-965.

93. Brosse, A.-C., et al., *Effect of multi-walled carbon nanotubes on the lamellae morphology of polyamide-6.* Polymer, 2008. **49**: p. 4680-4686.

94. Probst, O., et al., *Nucleation of Polyvinyl Alcohol Crystallization by Single-walled Carbon Nanotubes.* Polymer, 2004. **45**(13): p. 4437-4443.

95. Wang, Z. and Y. Chen, *Supramolecular Hydrogels Hybridized with Single-walled Carbon Nanotubes.* Macromolecules, 2007. **40**(9): p. 3402-3407.

96. Matsuo, M., A. Yamanaka, and Y. Nakano, *Gelation Mechanism of Ultra-high-molecular-weight Polyethylene (UHMWPE) Chains in Dispersion Solutions Contaning Multiwall Carbon Nanotubes (MWNTs) Analyzed in Terms of Liquid-liquid Phase Separation.* Pure and Applied Chemistry, 2009. **81**(3): p. 513-524.

97. Minus, M., H.G. Chae, and S. Kumar, *Interfacial Crystallization in Gel-spun Poly(vinyl alcohol)/Single-Wall Carbon Nanotube Composite Fibers.* Macromolecular Chemistry and Physics, 2009. **210**(21): p. 1799-1808.

98. Xu, X., et al., *Fabrication of High Strength PVA/SWCNT Composite Fibers by Gel Spinning.* Carbon 2010. **48**(7): p. 1977-1984.

99. Zhang, X., et al., *Gel Spinning of PVA/SWNT Composite Fiber.* Polymer, 2004. **45**(26): p. 8801 - 8807.

100. Gill, P.S., S.R. Sauerbrunn, and M. Reading, *Modulated Differential Scanning Calorimetry.* Journal of Thermal Analysis, 1993. **40**(3): p. 931-939.

101. Reading, M., D. Elliott, and V.L. Hill, *A New Approach to the Calorimetric Investigation of Physical and Chemical Transitions.* Journal of Thermal Analysis, 1993. **40**(3): p. 949-955.

102. Fornasiero, F., et al., *Glass-transition Temperatures for Soft-contact-lens Materials. Dependence on Water Content.* Polymer, 2005. **46**(13): p. 4845-4852.

103. Wilchinsky, Z.W., *Measurement of Orientation in Prolypropylene Film.* Journal of Applied Physics, 1960. **31**(11): p. 1969-1972.

104. Tasumi, I.M., et al., *Infrared Spectra of Normal Higher Alcohols.* Spectrochimica Acta 1974. **20**(4): p. 629-666.

105. Fraser, R.D.B., *The Interpretation of Infrared Dichroism in Fibrous Protein Structures.* The Journal of Chemical Physics 1953. **21**(9): p. 1511-1515.

106. Perdew, J.P., K. Burke, and M. Ernzerhof, *Generalized Gradient Approximation Made Simple.* Physical Review Letters, 1996. **77**(18): p. 3865-3868.

107. Delley, B., *An All-electron Numerical Method for Solving the Local Density Functional for Polyatomic Molecules.* Journal of Chemical Physics, 1990. **92**(1): p. 508-517.

108. Delley, B., *From molecules to solids with the DMol^3 approach.* Journal of Chemical Physics, 2000. **113**(18): p. 7756-7764.

109. Mulliken, R.S., J. Chem. Phys., 1955. **23**: p. 1833.

110. Capaccio, G., *Structural Changes in the Preparation of Ultra-high Modulus Polyethylene.* Pure and Applied Chemistry, 1983. **55**(5): p. 869-872.

111. Thomas, P., et al., *FTIR Study of the Thermal Degradation of Pol(vinyl alcohol).* Journal of Thermal Analysis and Calorimetry, 2001. **64**(2): p. 501-508.

112. Guerrini, L.M., et al., *Thermal and Structural Characterization of Nanofibers of Poly(Vinyl Alcohol) Produced by Electrospinning.* Journal of Applied Polymer Science, 2009. **112**(3): p. 1680-1687.

113. Brandup, J., E.H. Immergut, and W. McDowell, *Polymer Handbook*, ed. 2d. 1975, New York: John Wiley & Sons.

114. Shimanouchi, T., *Normal Vibrations of Polyethylene and Some Vinyl Polymers.* Journal of Polymer Science Part C, 1964. **7**: p. 85-97.

115. Tashiro, K., M. Kobayashi, and H. Tadokoro, *Polarized Raman Spectra of Doubly Oriented Poly(vinyl alcohol).* Polymer Bulletin, 1978. **1**(1): p. 61-66.

116. White, R.G., *Handbook of Industrial Infrared Analysis*. 1964, New York: Plenum Press. 440.

117. Kim, E., et al., *Characterization of Poly(vinyl alcohol) Films with Various Molecular Parameters.* Journal of Applied Polymer Science, 2007. **106**(5): p. 3259-3267.

118. Dai, L. and L. Ying, *Infrared Spectroscopic Investigation of Hydrogen Bonding in EVOH Containing PVA Fibers.* Macromolecular Materials and Engineering, 2002. **287**(8): p. 509-514.

119. Banno, M., K. Ohta, and K. Tominaga, *Ultrafast Vibrational Dynamics and Solvation Complexes of Methyl Acetate in Methanol Studied by Sub-picosecond Infrared Spectroscopy.* Journal of Raman Spectroscopy, 2008. **39**: p. 1531-1537.

120. Awadhia, A. and S. Agrawal, *Structural, Thermal and Electrical Characterizations of PVA:DMSO:NH4SCN Gel Electrolytes.* Solid State Ionics, 2007. **178**: p. 951-958.

121. Takei, K., R. Takahashi, and T. Noguchi, *Correlation between the Hydrogen-Bond Structures and the C=O Stretching Frequencies of Carboxylic Acids as Studied by Density Functional Theory Calculations: Theoretical Basis for Interpretation of Infrared Bands of Carboxylic Groups in Proteins.* Journal of Physical Chemistry, 2008. **112**: p. 6725-6731.

122. Paul, S.O. and T.A. Ford, *Infrared Spectroscopic Studies of Hydrogen-bonded Complexes of Water with Oxygen Bases. III. The HOH-bending Region of the Spectra of Water Molecules Dissolved in Some Ketones and Ethers.* Journal of Crystallographic and Spectroscopic Research, 1986. **16**: p. 811-821.

123. Bertoluzza, A., et al., *Raman and Infrared Study on the Effects of Dimethylsulphoxide (DMSO) on Water Structure.* Journal of Raman Spectroscopy, 1979. **8**(5): p. 231-235.

124. Shimanouchi, T., *Stable Conformations of Syndiotactic and Isotactic Vinyl Polymers and Their Two-unit and Three-unit Model Molecules.* Pure and Applied Chemistry, 1966. **12**(1-4): p. 287-309.

125. Nakamoto, K., ed. *Infrared and Raman Spectra of Inorganic and Coordination Compounds*. 1986, John Wiley & Sons: New York. 484.

126. Foster, R., *Organic Charge-Transfer Complexes*. Organic Chemistry, ed. A.T. Blomquist. 1969, London: Academic Press.

127. Speakman, J.C., *The Hydrogen Bond and Other Inter-molecular Forces*. Vol. 27. 1975, London: Chemical Society. 33.

128. Smith, M.B. and J. March, eds. *March's Advanced Organic Chemistry: Reactions, Mechanisms, and Structure*. 5th ed. March's Advanced Organic Chemistry. 2001, John Wiley & Sons, INC. 16-18, 102-104, 363-367.

129. Lirova, B., A.L. Smolyanskii, and A.A. Tager, *Infared Absorption Study of the Molecular Interactions in Solutions of Poly(vinyl alcohol) and its Low-molecular Analogs.* Zhurnal Prikladnoi Spektroskopii, 1971. **15**(3): p. 491-497.

130. Vyazovkin, S. and N. Sbirrazzuoli, *Mechanism and Kinetics of Epoxy-Amine Cure Studied by Differential Scanning Calorimetry.* Macromolecules, 1996. **29**: p. 1867-1873.

131. Zhou, D., et al., *Crystallization Kinetics of Amorphous Nifedipine Studied by Model-Fitting and Model Free Approaches.* Journal of Pharmaceutical Sciences, 2003. **92**(9): p. 1779-1792.

132. Guigo, N., N. Sbirrazzuoli, and S. Vyazovkin, *Gelation on Heating of Supercooled Gelatin Solutions.* Macromolecular Chemistry and Physics, 2012: p. DOI: 10.1002/marc.201100748.

133. Svec, P., K. Kristiakov A, and M. Deanko, *Cluster structure of the amorphous state and (nano)crystallization of rapidly quenched iron and cobalt based systems*, in *NATO Science Series II: Mathematics, Physics and Chemistry*, T. Tsakalakos, I.A. Ovid'ko, and A.K. Vasudevan, Editors. 2003, Springer. p. 275,280,286-287.

134. Reynier, Y.F., R. Yazami, and B. Fultz, *Thermodynamics of Lithium Intercalation into Graphites and Disordered Carbons.* Journal of Electrochemical Society, 2004. **151**(3): p. A422-A426.

135. Vink, R.L.C. and G.T. Barkema, *Configurational Entropy of Network-Forming Materials.* Physical Review Letters, 2002. **87**(7): p. 076405-1/4.

136. *Mowiol: Poly(vinyl alcohol).* [cited 2012; Available from: http://www.kuraray-am.com/pvoh-pvb/downloads/Mowiol_brochure_en_KSE.pdf.

137. Cotiuga, I., et al., *Block-Copolymer-Assisted Solubilization of Carbon Nanotubes and Exfoliation Monitoring Through Viscosity.* Macromolecular Rapid Communications, 2006. **27**: p. 1073-1078.

138. Yasuda, K., R.C. Armstrong, and R.E. Cohen, *Shear Flow Properties of Concentrated Solutions of Linear and Star Branched Polystyrenes.* Rheol Acta, 1981. **20**: p. 163-178.

139. Irabien, A., C. Santiago, and A. Arnaiz, *Kinetic Interpretation of the Thermal Decomposition of Anilinium Octamolybdate at Differenting Heat Rate.* Journal of Thermal Analysis, 1984. **29**(4): p. 1131-1137.

140. Vyazovkin, S. and C.A. Wight, *Kinetics in Solids.* Annual Review of Physical Chemistry, 1997. **48**: p. 125-149.

141. Vyazovkin, S. and A.I. Lesnikovich, *Estimation of the Pre-exponential Factor in the Isoconversional Calculation of Effective Kinetic Parameters.* Thermochimica Acta, 1988. **128**: p. 297-300.

142. Maroto, J.A., M. Quesada-Perez, and A.J. Ortiz-Hernandez, *Use of Kinematic Viscosity Data for the Evaluation of the Molecular Weight of Petroleum Oils.* Journal of Chemical Education, 2010. **87**(3): p. 323-325.

143. Nichetti, D. and I. Manas-Zloczower, *Viscosity Model for Polydisperse Polymer Melts.* Journal of Rheology, 1998. **42**(4): p. 951-969.

144. Huang, Y.Y., S.V. Ahir, and E.M. Terentjev, *Dispersion Rheology of Carbon Nanotubes in a Polymer Matrix.* Physical Review B, 2006. **73**: p. 125422/1-9.

145. Han, C.D., *Rheology and Processing of Polymeric Materials*. Vol. 1 - Polymer Rheology. 2007, Oxford: Oxford University Press.

146. Lee, S.J., et al., *Rheological Properties of High Molecular Weight Poly(vinyl alcohol)/Dimethyl Sulfoxide/Water Concentrated Solutions.* Polymers and Polymer Composites, 2004. **12**(7): p. 561-567.

147. Dealy, J.M. and K.F. Wissbrun, *Melt Rheology and its Role in Plastic Processing*. 1995, London: Chapman & Hall.

148. Tubbs, R.K., *The Melting Point and Heat of Fusion of Poly(vinyl alcohol).* J. Polym. Sci. Part A. , 1965. **3**: p. 4181-4189.

149. Burnham, A.K. and L.N. Dinh, *A Comparison of Isoconversional and Model-fitting Approaches to Kinetic Parameter Estimation and Application Predictions.* Journal of Thermal Analysis and Calorimetry, 2007. **89**(2): p. 479-490.

150. Vyazovkin, S. and A.I. Lesnikovich, *An Approach to the Solution of the Inverse Kinetic Problem in the Case of Complex Processes. Part 1. Methods Employing a Series of Thermoanalytical Curves.* Thermochimica Acta, 1990. **165**: p. 273-280.

151. House, J.E., *Principles of Chemical Kinetics*. 2nd ed. 2007, Boston: Academic Press. 326.

152. Zhang, X., et al., *Fluctuation-Assisted Crystallization: In a Simultaneous Phase Separation and Crystallization Polyolefin Blend System.* Macromol Rapid Commun, 2005. **26**: p. 1285-1288.

153. Markovic, N., M. Ginic-Markovic, and N.K. Dutta, *Mechanism of Solvent Entrapment Within the Network Scaffolding in Organogels: Thermodynamic and Kinetic Investigations.* Polymer International, 2003. **52**: p. 1095-1107.

154. Adel, G., F. Faten, and A. Radhia, *Assessing Cotton Fiber Maturity and Fineness by Image Analysis.* Journal of Engineered Fabrics and Fibers 2011. **6**(2): p. 50-60.

155. Barton, A.F.M., *CRC Handbook of Solubility Parameters and Other Cohesion Parameters*. 1991, Boca Raton: CRC Press.

156. M. Nagura, M. Nagura, and H. Ishikawa, *State of water in highly elastic poly(vinyl alcohol) hydrogens by repeated freezing and melting.* Polymer Communications, 1984. **25**: p. 313-314.

157. Wong, S.-S., A. Altinkaya, and S.K. Mallapragada, *Drying of Semicrystalline Polymers: Mathematical Modeling and Experimental Characterization of Poly(vinyl alcohol) Films* Polymer, 2004. **45**: p. 5151-5161.

158. Zhang, X., *Studies on Single Wall Carbon Nanotubes and Polymer Composite Films and Fibers*, in *School of Polymer, Textile and Fiber Engineering*. 2004, Georgia Institute of Technology: Atlanta. p. 135.